

Innovative Bidirectional Video-Goniophotometer for Advanced Fenestration Systems

THÈSE N° 2941 (2004)

PRÉSENTÉE À LA FACULTÉ ENVIRONNEMENT NATUREL, ARCHITECTURAL ET CONSTRUIT

Institut des infrastructures, des ressources et de l'environnement

SECTION D'ARCHITECTURE

ÉCOLE POLYTECHNIQUE FÉDÉRALE DE LAUSANNE

POUR L'OBTENTION DU GRADE DE DOCTEUR ÈS SCIENCES

PAR

Marilyne ANDERSEN

ingénieure physicienne diplômée EPF
de nationalité suisse et originaire de Wallenried (FR)

acceptée sur proposition du jury:

Prof. J.-L. Scartezzini, directeur de thèse

M. C. Roecker, rapporteur

Dr J.L.J. Rosenfeld, rapporteur

Dr M. Rubin, rapporteur

Prof. R.P. Salathé, rapporteur

Lausanne, EPFL

2004

*To Igor,
with all my love*

Acknowledgements

I am extremely grateful to the many people who made the completion of this PhD thesis possible. In particular, I would like to address my warmest thanks to:

Prof. Jean-Louis Scartezzini for his steady support, his scientific rigor and the independence he allowed me to benefit from during the whole duration of this work.

The jury members Christian Roecker, Dr Jean L.J. Rosenfeld, Dr Michael Rubin and Prof. René Salathé for the attention with which they read this thesis and for their helpful questions, comments and suggestions, as well as Prof. Luca Ortelli for having kindly accepted the role of President of the jury and having carried it out with charisma and professionalism.

The Swiss Federal Institute of Technology in Lausanne (EPFL) for having provided financial and human support.

The Commission for Technology and Innovation (CTI) of the Swiss Federal Government, who financed the institutional part of this project, and more particularly Dr Paul-Eric Gygax, member of the CTI commission, who ensured its follow-up.

The Swiss National Science Foundation and the Lawrence Berkeley National Laboratory for their joint financial support in my one year stay at LBNL as a visiting scholar.

Steve Selkowitz and Michael Rubin for their invitation to work in the Building Technologies Department at LBNL, their support and scientific guidance and the welcoming atmosphere they offered.

Our industrial partners Baumann-Hüppe AG, Relux Informatik AG and Regent Appareils d'Eclairage for providing manpower, for their helpful feedbacks about the use of bidirectional data and the numerous fenestration systems prototypes they provided for BT(R)DF characterization.

Christian Roecker and Pierre Loesch, without whom the goniophotometer could not have been materialized, for their inventiveness, conscientiousness and efficiency.

Dr Laurent Michel for his fruitful advice and essential involvement in the early stages of the goniophotometer's design, for his preliminary work on image acquisition and processing and on graphical BTDF representation.

Laurent Deschamps for his kind dedication to solving our computer-related problems in a friendly and efficient manner and François Leresche for the implementation of the first command routines.

Dominique Glauser and Serge Bringolf for their contribution to the goniophotometer's robotic and mechanical design.

Lambda Research Corporation for having provided me with a license of TRACEPRO® to complete the ray-tracing-based validation approach for BT(R)DF measurements.

Antoine Guillemin for his enjoyable companionship during all these years sharing the same office room, his wholehearted support and his precious friendship.

Martin Gonzenbach, Jessen Page and my dear Igor for having carefully and patiently reread some chapters of this thesis.

And all members of the LESO-PB at EPFL and the Building Technologies Department at LBNL for the very friendly working environment they made me benefit from.

My very special thanks go to my beloved husband Igor, who has accompanied me throughout this long-term work with extreme kindness and patience, invaluable advice and unwavering support. They also go to my family, my dearest parents, sisters and brother-in-law, as well as to Igor's family that has supported me likewise with a touching care and interest.

*The frightening thought that what you draw may become a building
makes for reasoned lines.*

Saul Steinberg, cartoonist.

Abstract

Efficient collection and redistribution of the direct and diffuse components of daylight in buildings remains a major objective of advanced fenestration systems. Such systems, including novel solar blinds, new glazing or coating materials and daylight-redirecting devices, can improve significantly the penetration of daylight in deep rooms to reduce electricity consumption while improving visual comfort conditions greatly; at the same time, they can lead to larger solar gains in winter combined with lower solar loads in summer.

To allow their integration in buildings and benefit from their potential as energy-efficient strategies, an in-depth and accurate knowledge of their directional optical properties is necessary. These properties are described by Bidirectional Transmission (or Reflection) Distribution Functions, abbreviated BT(R)DF, that express the emerging light flux distribution for a given incident direction.

Such detailed transmission or reflection functions are intended to be used by the building industry to optimize the luminous performances of innovative solutions for windows and to describe photometric properties of complex glazing and shading materials according to a common format. On the other hand, they will allow daylighting simulation tools to improve their potentialities and integrate complex fenestration systems reliably in the simulation models.

Their accurate assessment requires an appropriate experimental equipment. An innovative bidirectional goniophotometer, based on digital imaging techniques, was designed and set up for that purpose: instead of scanning the emerging light flux distribution by moving a sensor from point to point, an original method was used that comprises a rotating diffusing screen on which the emerging light flux is reflected towards a digital video-camera, used as a multiple-points luminance-meter.

This novel approach significantly reduces the time needed to monitor BT(R)DF data, lowering it down to a few minutes per incident direction instead of several hours for conventional assessment methods, which is a critical parameter in BT(R)DF assessment as about a hundred incident directions are usually required. At the same time, it allows the gathering of continuous transmitted (reflected) light distribution figures, only limited in resolution by the pixellisation of the digital images. Moreover, by taking advantage of the considerable luminance range reached when images are captured and superposed at different integration intervals, combined to the appreciable flexibility in the data processing offered by digital imaging-based techniques, a remarkable accuracy can be achieved when assessing BT(R)DF data.

This PhD thesis explains the different conception, calibration and processing stages that were necessary to develop the bidirectional goniophotometer into a functioning, validated measurement device. Its design for combining BTDF and BRDF assessments is described, the various calibration procedures for converting the CCD camera into a reliable multiple-points luminance-meter are detailed, as well as the image and data processing phases. An in-depth validation of the performed measurements was realized based on different approaches and led to a relative error on BT(R)DF data of only 10%, allowing to confirm the high accuracy and reliability of this novel device.

Version abrégée

Contrôler et redistribuer efficacement les composantes directe et diffuse de la lumière du jour dans les bâtiments fait partie des objectifs majeurs à remplir par les systèmes de fenêtre innovants. Ces systèmes comprennent à la fois les protections solaires, les nouveaux types de vitrage ou de revêtement et les dispositifs de captage de lumière naturelle et peuvent contribuer à d'importantes économies d'énergie: d'une part, les gains thermiques peuvent être augmentés en hiver et diminués en été; d'autre part, en améliorant la pénétration de la lumière du jour dans des pièces profondes, les consommations électriques peuvent être réduites de manière significative, tout en améliorant notablement les conditions de confort visuel.

Pour intégrer ces systèmes dans les bâtiments et utiliser leur potentiel en économie d'énergie de manière effective, une connaissance précise et approfondie de leurs propriétés optiques directionnelles est indispensable. Celles-ci sont décrites par les fonctions bidirectionnelles de distribution en transmission (ou réflexion) - abrégées BT(R)DF -, qui décrivent la distribution dans l'espace du flux lumineux émergent pour une direction d'incidence donnée.

De telles fonctions sont destinées à être utilisées par l'industrie du bâtiment afin d'optimiser les performances lumineuses de vitrages ou protections solaires innovants et de décrire leurs propriétés photométriques selon un format commun. Par ailleurs, les prestations des outils de simulation pour l'éclairage naturel pourront être élargies par la modélisation fiable de la propagation de la lumière naturelle en présence de systèmes complexes de fenêtre.

Cette caractérisation précise requiert un équipement expérimental approprié. Un goniophotomètre bidirectionnel innovant, basé sur des techniques d'imagerie numérique, a été conçu et développé dans ce but: la conception classique d'un détecteur mobile se déplaçant d'une position à l'autre est remplacée par une méthode originale, qui consiste à analyser la lumière émergente après réflexion sur un écran diffusant rotatif à l'aide d'une caméra vidéo digitale, utilisée comme luminance-mètre à points multiples.

Cette approche nouvelle réduit le temps de mesure de manière significative, ramenant celui-ci à quelques minutes par direction d'incidence au lieu de plusieurs heures; ce paramètre est particulièrement critique compte tenu que plus de cent directions d'incidence sont généralement requises pour caractériser un système. En outre, elle permet d'obtenir une mesure continue de la distribution de flux lumineux transmis (réfléchi), limitée en résolution uniquement par la pixellisation de l'image. De plus, en profitant de la dynamique de luminances considérable obtenue en superposant des images prises à différents temps d'exposition et de la grande flexibilité offerte par l'imagerie numérique dans le traitement des données, une précision et une efficacité remarquables peuvent être atteintes dans la mesure de fonctions BT(R)DF.

Ce travail de thèse explique les différentes phases de développement, calibrage et traitement qui ont été nécessaires pour réaliser et valider un tel appareil de mesure. Les étapes de sa conception pour combiner des mesures en transmission et en réflexion sont décrites, ainsi que les nombreuses procédures d'étalonnage, d'acquisition et de traitement des images permettant de convertir la caméra CCD en un luminance-mètre à points multiples fiable. Une validation exhaustive des mesures a été réalisée en se basant sur différentes approches permettant de déterminer une erreur relative de seulement 10% sur les données BT(R)DF, confirmant ainsi la grande précision et fiabilité de cet appareil.

Contents

1	Introduction	1
1.1	Daylight in buildings	1
1.2	Characterization of light distribution	3
1.3	Structure of thesis	5
2	Bidirectional photometric measurements	7
2.1	The Bidirectional Transmission (Reflection) Distribution Function	7
2.2	Configuration of existing goniophotometers throughout the world	9
2.2.1	Characterization based on a scanning process	9
2.2.2	Video-based time-efficient approaches	17
2.3	Use of digital imaging techniques in photometric measurements	18
2.4	Innovation and advantages of the adopted approach	19
3	Digital imaging goniophotometer for transmission and reflection	23
3.1	Functioning principle	23
3.1.1	Transmission measurements (BTDF)	24
3.1.2	Reflection measurements (BRDF)	25
3.2	Construction of the transmission device	25
3.2.1	Major structural components	25
3.2.2	Mechanical developments	27
3.2.3	Light source	28
3.2.4	Sample holder	29
3.2.5	Diffusing projection screen	31
3.2.6	CCD video camera	34
3.3	Design of the transmission / reflection device	35
3.3.1	Physical constraints	35
3.3.2	Pre-design concepts	35
3.3.3	Final concept	40
3.4	Modification of components	41
3.4.1	Light source	41
3.4.2	Measurement space envelope	46
3.4.3	Main platform and rotating ring	50
3.4.4	Diffusing projection screen	52
4	Calibration procedures	57
4.1	CCD camera	57
4.1.1	Spectral calibration	57
4.1.2	Photometric calibration	61
4.2	Spatial calibration	63
4.2.1	Screen image position adjustment	63
4.2.2	Reference situation	65

4.2.3	Spatial referential variations	67
4.2.4	Obstruction of emerging light	72
4.3	Additional corrections	74
4.3.1	Incident beam collimation	75
4.3.2	Image uniformity	77
4.3.3	Parasitic light	79
5	Command and processing	81
5.1	Characterization process for bidirectional measurements	81
5.1.1	Command interface	81
5.1.2	Program structure	82
5.2	Averaging grid for BT(R)DF data	85
5.2.1	Pixel gathering according to angular grid	86
5.2.2	Grid assembling	87
5.3	Image acquisition and processing	89
5.3.1	Image capture and illuminance measurement	89
5.3.2	Image correction and composition	89
5.3.3	Global visualization through recombined screen images	92
5.4	BT(R)DF data extraction	94
5.4.1	Conversion from screen luminance to BT(R)DF	94
5.4.2	Simultaneous assessment of specular and diffuse components	97
5.4.3	Weighted averaging and association to polar angles	102
5.5	Bidirectional data for photometric performances assessment	102
5.5.1	Graphical representations	103
5.5.2	Application of photometric solids	106
5.5.3	Visual comfort assessment based on bidirectional data	108
5.5.4	Description of complex glazings in building simulations	111
6	Validation	115
6.1	Experimental error	115
6.1.1	Calibration error sources	115
6.1.2	Inaccuracies due to processing or mechanical constraints	117
6.1.3	Mechanical components adjustment	120
6.1.4	Global relative error	120
6.2	Analytical verification	121
6.2.1	Symmetry-based comparisons	121
6.2.2	Theoretical bidirectional functions	124
6.3	Empirical validation	124
6.3.1	Inter-laboratory comparison for opalescent glazing	125
6.3.2	Comparison of diffuse components in a complex BTDF figure	126
6.4	Directional-hemispherical transmittance (reflectance) comparisons	127
6.4.1	Integration of BT(R)DF over emerging hemisphere	128
6.4.2	Comparisons with Ulbricht sphere measurements	130
6.4.3	Ray-tracing based model	133
6.5	Detailed BT(R)DF comparisons with ray-tracing simulations	134
6.5.1	Systems description and modeling	135
6.5.2	Simulation model of experimental set-up	138
6.5.3	Virtual model of ideal set-up	143
6.5.4	Simulation error estimation	144
6.5.5	Results comparisons	147

7 Conclusion	153
7.1 Achievements	153
7.2 Perspectives of application and use	157
7.3 Outlook	158
Appendices	161
A Mechanical components specifications	161
A.1 Main platform and rotating ring	161
A.2 Quarter-circular support frame	162
A.3 Motorized screen	163
A.4 Sample mounting	164
B Command interface and monitoring procedure	167
B.1 Determination of the BT(R)DF monitoring parameters	168
B.1.1 Incident directions set	168
B.1.2 Sample properties	173
B.1.3 Emergence parameters	173
B.2 BT(R)DF assessment deliverables	174
B.2.1 Format of BT(R)DF data files	175
B.2.2 Recombined image and photometric solids	178
C List of BTDF and BRDF measurements	179
C.1 Diffusing materials	179
C.1.1 White opalescent plexiglas	180
C.1.2 White opalescent plastic	180
C.1.3 Diffusing paint	181
C.2 Sunlight redirecting systems	181
C.2.1 Laser Cut Panel	182
C.2.2 Sun directing glass	183
C.2.3 Holographic film	183
C.2.4 Adjacent curved mirrors	185
C.3 Prismatic panels	185
C.3.1 Acrylic prisms	186
C.3.2 3M prismatic film	188
C.4 Fabric blinds	189
C.4.1 Baumann-Hüppe prototypes	189
C.4.2 Fabric blinds with reflective coating	192
C.5 Venetian blinds	195
C.5.1 Mirror blind between glass layers	196
C.5.2 Curved slats with mirror coating	197
C.5.3 Köster blinds	197
C.5.4 Metallic slats	198
D Nomenclature	201
Bibliography	207

Chapter 1

Introduction

“We shape our buildings; thereafter they shape us.” (Winston Churchill)

1.1 Daylight in buildings

Through the ages, light has remained an object of fascination to mankind. To the Egyptians, it represented the relationship between a man and the God Ra, and they hence searched for a spiritual answer to what its nature was; to the medieval mind, light passing through the glass and stone structures of cathedrals dignified not only the sacred edifice, but the whole town (Zajonc, 1993). Although scientists have elaborated more and more in-depth theories to describe light, its essence has remained an enigma ever since. Einstein’s declaration in 1951, quoted in Wolf (1979), underlines the limitations of quantum optics in creating a faithful model for the photons: “All the fifty years of conscious brooding have brought me no closer to the question, ‘What are light quanta?’ Of course today every rascal thinks he knows the answer, but he is deluding himself.”

In architecture, it is not so much the mystery around the nature of light that plays the prominent part than the one encompassing its distribution in space, how it will affect the objects and structure the built volumes. “Architecture is the masterly, correct and magnificent play of volumes brought together in light” says Le Corbusier (1923). Beyond the purely architectural point of view, a planned use of daylight is also essential at more rational levels, and the visual comfort of occupants needs to be combined with a strong ecological concern.

The protection of the environment indeed appears as a major issue of our present society; in this context, the necessity to reduce energy use in buildings positions itself as a priority. As a consequence of this larger consensus regarding the concept of sustainable development in buildings (Council for Sustainable Development, 1997), daylight and solar radiation control through fenestration systems receive a growing attention both in research and practice; advanced strategies have been developed at different levels to improve energy efficiency by minimizing electric lighting as well as heating and cooling loads of buildings.

Furthermore, observations of human behaviour outline the importance of daylight in buildings (Boyce, 1998): on one hand, windows are needed to provide a connection with the outside environment; on the other hand, natural light permits excellent colour discrimination and rendering, while providing high illuminance dynamics.

Of course, the way daylight is delivered is crucial for the visual comfort it produces (Fontoynt, 2002): high luminance contrasts or glaring sources alter greatly with good vision (Commission Internationale de l’Eclairage, 1983b; Nazzal, 2001). Moreover, as shown by a recent project on

users acceptance of automatic shading control systems (Guillemin, 2003), energy efficient strategies for controlling solar gains in buildings need to be adapted to users wishes in order to be fully accepted, which is the primary condition for them to be functional.

Many studies about the impact of a daylit environment on its users have shown that human productivity could be significantly increased when benefiting from natural light: a recent study realized amongst 20,000 students in California, Colorado and Massachusetts showed that standardized test scores among comparable students could be increased by 26% when they attended classes in buildings mainly relying on natural light (Libby, 2003). Other studies conducted on commercial retail centers showed that a 30% to 40% increase in sales could be observed if a special emphasis was placed on the use of daylight, while at the same time reducing electric lighting costs by 38% (Hubbard et al., 2003; Libby, 2003).

Indeed, when observing the energy consumption of non-residential buildings in Switzerland e.g. (Scartezzini, 2003), it appears that about 15% to 20% is provided for electric lighting for average office buildings and commercial retail centers (Figure 1.1), the needs being of course larger for the latter. An efficient collection and redistribution of direct sunlight for optimal visual and thermal comfort conditions (Programme d'action RAVEL, 1995; Wirth et al., 1997) can significantly improve the penetration of daylight into deep rooms (Wilson et al., 2002) and thus reduce electricity consumption. As pointed out by Bodart and De Herde (2002), the many studies conducted on the integration of daylighting availability in the electric lighting management (Lee et al., 1999; Li and Lam, 2000) stress the high potential of energy savings, with predictable values of lighting energy consumption varying from 20% to 80%, depending on the authors. At the same time, it can also lead to larger solar gains in winter and lower solar loads in summer, which again reduces non renewable energy consumption (Klems et al., 1995; Friedman and Cammalleri, 1997; Rubin et al., 1998; Dubois, 2000a; Karlsson et al., 2001; Greenup et al., 2001; Li et al., 2002). Trying to optimize the daylight distribution in spaces therefore appears as an option that cannot be overlooked to reduce a building's environmental impact while improving its visual performances (Moore, 1985; Swiss Federal Office of Conjonctural Problems, 1995; Baker et al., 1997; Selkowitz and Lee, 1998; International Energy Agency, 2000).

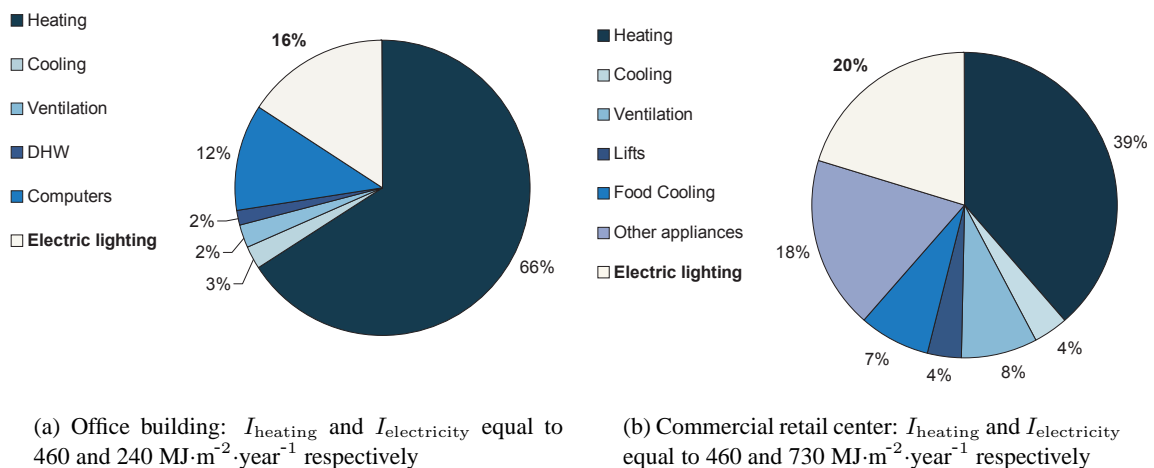


Figure 1.1: Typical energy consumption of Swiss non-residential buildings: relative distribution (%) and energy consumption indexes (I_{heating} and $I_{\text{electricity}}$).

This effort in optimization has led to the development of a large variety of innovative fenestration systems (Ballinger and Lyons, 1998; International Energy Agency, 2000; Kischkoweit-Lopin, 2002). Amongst the daylight redirecting and shading devices, optimized coatings have been developed for light shelves and louvers (Beltran et al., 1997; Pohl and Scheiring, 1998),

shading prototypes with improved geometry and slats surface manufacturing have been designed (Köster, 1989; Hunn et al., 1996; Hüppe-Form, 1988) and anidolic systems (Courret, 1999) based on non-imaging optics (Welford and Winston, 1989) have shown a high efficiency under over-cast skies. Various advanced glazing materials have proven their potentialities, such as: laser-cut panels (Edmonds, 1993), whose effect can be observed on Figure 1.2(a), holographic optical elements or sun-directing glass (Müller, 1994, 1996; Beck et al., 1999), prismatic panels and films (Holmes, 1988; Siemens AG, 1996; Lorenz, 2001), as for the building shown in Figure 1.2(b) and switchable “smart” windows (electro-, photo-, piezo- or thermochromic glazing (Greenberg, 1994), gasochromic and thermotropic layers (Georg et al., 1998; Inoue, 2003)).

More recently, further advances in materials developments, that improve the luminous efficacy, visual comfort and color management, have taken place, such as transparent and translucent polymers or glass sheets (Reim et al., 2002) and light pipes or colour mixers (Smith, 2003); other innovative components are phase change materials (PCM) combined to double glazing (Weinläder et al., 2003) or microstructured surfaces for glazings (Bläsi et al., 2003).



(a) Sunlight deflection through Laser Cut Panels installed in awning of classroom windows (Brisbane, Australia)



(b) Structure with movable prismatic panels (SBV building in Biel, Switzerland)

Figure 1.2: Advanced fenestration systems in existing buildings (International Energy Agency (2000)).

1.2 Characterization of light distribution

To allow the integration of such daylighting systems in buildings and to benefit from their potential as energy-efficient strategies enhancing the occupants’ comfort and performance, a detailed knowledge of their properties appears as a major issue (International Energy Agency, 2000). More specifically, as pointed out by Dubois (1997), not only need optical properties of window-shade and glazing systems to be determined for normal incidence, but also for varying impinging directions, as an angle dependent characterization is essential to accurately predict their performances for variable climatic conditions and sun courses (Wirth, 2000).

Furthermore, many applications, and in particular complex or heterogeneous fenestration systems, also require a precise characterization of the spatial distribution of emerging light, in a similar way as for lighting fixtures (Illuminating Engineering Society of North America, 1993; Schweizerische Lichttechnische Gesellschaft, 1992; Commission Internationale de l’Eclairage, 1996). This will help manufacturers to develop and optimize such products, and provide guidelines to architects in their judicious selection already at the project’s level (Fontoynt, 1995; Scartezini and Paule, 1994; Dubois, 2000b). Such a detailed characterization is also necessary for daylighting simulation programs to improve their performances (Scartezini et al., 1994; Rein-

hart and Herkel, 2000; Roy, 2000; International Energy Agency, 2000; Mitanchey et al., 2002; Mitchell et al., 2003) and achieve a reliable modeling of light propagation in rooms using advanced fenestration systems.

The quantity used to describe these photometric properties, that are angle-dependent at both the incidence and the emerging levels, is called Bidirectional Transmission (or Reflection) Distribution Function, abbreviated BTDF (or BRDF). This function is defined by Commission Internationale de l'Eclairage (1977) as “the quotient of the luminance of a surface element in a given direction, by the illuminance incident on the sample” and is described in details in Section 2.1.

It expresses the emerging light distribution for a given incident direction, as schematized in Figure 1.3 for the Laser Cut Panel illustrated in Figure 1.2(a). The incident directions chosen for this example are based on realistic sun positions for a south-oriented façade at latitude 47°N, at 8h, 10h and 12h solar time on March 21st (equinox); the emerging light distributions are represented as two highly directional luminous peaks: one part of the incident flux is transmitted regularly (directly); another part is reflected on the parallel laser cuts and redirected upwards, leading to a partially altered view of the outside environment. These properties are verified in practice for this glazing, as the schematic illustrations of Figure 1.3 are based on actual bidirectional measurements (listed in Appendix C).

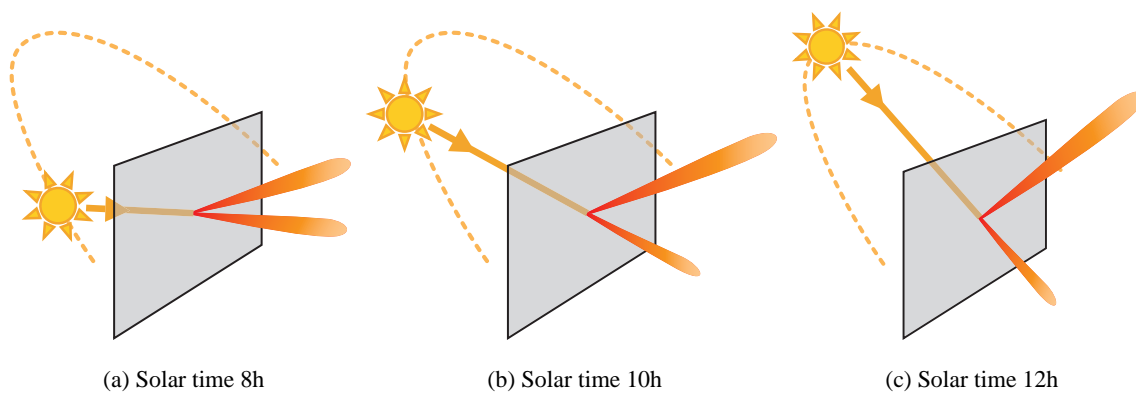


Figure 1.3: Bidirectional transmission figures for the Laser Cut Panel for different incident directions.

The aim of this project is to set up an experimental equipment (a bidirectional goniophotometer) for an efficient measurement and characterization of light transmission and reflection properties of such building components.

Several bidirectional goniophotometers have been developed to perform BT(R)DF measurements of glazing and shading systems (International Energy Agency, 2000; Papamichael et al., 1988; Apian-Bennewitz, 1994; Bakker and van Dijk, 1995; Breitenbach and Rosenfeld, 1998); they are described in more details in Section 2.2. Most are based on a conventional design using a movable photo-sensor to track and measure in all possible directions the outgoing luminance of the light flux emerging from the sample, after either transmission or reflection (see Figure 1.4).

Their performance is accurate and reliable, but they show two significant drawbacks: on one hand they are time consuming because numerous movements of the mobile photo-sensor are required to achieve an appropriate angular resolution, and these movements increase tremendously with a finer resolution; on the other hand, the risk of missing a narrow light peak with a large gradient in the space left between two measurement points can never be avoided. Materials with a high dynamical luminance range can cause serious technical difficulties, and require local refinements of the angular resolution.

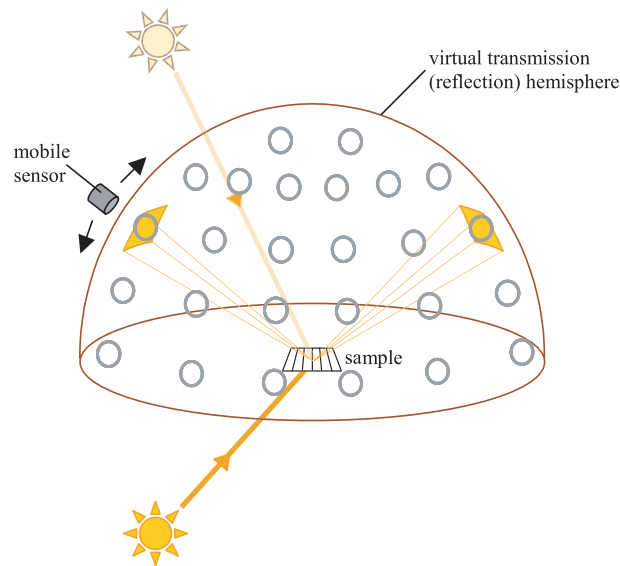


Figure 1.4: Detection principle for conventional goniophotometers: the photo-sensor moves from one position to the other.

To overcome these problems, a novel type of bidirectional goniophotometer was developed, using advanced digital imaging techniques and based on the projection of emerging light on a diffusing screen before being detected; its functioning principle is explained in details in Section 3.1. Several major advantages are thus obtained: a significant reduction of the BT(R)DF data assessment time (a few minutes instead of hours per incident direction) and a continuous information about the transmission (reflection) hemisphere, whose resolution is only limited by the pixellisation of the images. The use of digital imaging also allows to handle material samples showing large range of luminances without any loss of accuracy, while offering appreciable flexibility in the data processing. However, as the light distribution assessment is not based on the direct measurement of a photometric quantity, several critical calibration procedures, described in Chapter 4, are necessary before the goniophotometer is operational, mainly to convert the Charge-Coupled Device (CCD) camera into a reliable multiple-points luminance-meter.

1.3 Structure of thesis

The following chapters sequence the thesis according to the main phases of development of the goniophotometer, from its design to the validation of its results.

Chapter 2 gives an overview of the configuration of existing bidirectional goniophotometers, that are almost all based on a conventional point-per-point investigation, but can differ greatly in the chosen detection system: luminancemeter, luxmeter, optical fiber system, mobile CCD camera. Their innovations and draw-backs are analyzed, together with the contribution of digital imaging techniques in assessing optical properties of materials. A definition of the photometric quantities involved in the experimental procedures is given as well.

Chapter 3 presents the functioning principle and describes the design process of the achieved bidirectional goniophotometer, relying on digital imaging and allowing the combination of transmission and reflection measurements. Chronologically, it was first set up as full, functioning transmission version, and only then converted into a double version. However, as the calibration procedures and data processing are similar, they are described together throughout the thesis. In this chapter, the equipment's concept is presented with the early and final stages of design for the double version, whose components properties (materials, geometry, installation) are described in details: light source, structural components, projection screen, CCD camera.

Chapter 4 provides a clear understanding of the calibration procedures used to set up the different operating functions of the device: conversion of the CCD camera into a luminance-meter, relation between image pixels and direction in space, correction of several parameters.

Chapter 5 details the different phases necessary to process raw images into a complete set of BT(R)DF values. The major steps in a system's characterization are described, and the analytical developments on which this processing is based are outlined. Different graphical representations of BT(R)DF data are then proposed, as well as application examples for assessing the performances of a fenestration system.

Chapter 6 presents a detailed investigation of the different potential error sources in a BT(R)DF assessment and the various methods used to validate the results: comparisons with analytical or ray-tracing based models and with other goniophotometric data; calculation of the directional-hemispherical transmittance (reflectance) gauged against measurements of the same systems with Ulbricht (integrating) spheres (Commission Internationale de l'Eclairage, 1998).

Chapter 7 concludes the thesis by summarizing the main achievements; it suggests different application fields or directions for bidirectional photometric data and contains recommendations for future research to enhance their potentialities.

Appendix A adds to the mechanical components description given in Chapter 3 in providing details about the geometry of the structure, and the constraints and specifications for samples to be characterized.

Appendix B describes the command interface in more details than Chapter 5, reviews the different parameters for a characterization process and outlines the input and actions needed from the user.

Appendix C contains an exhaustive list of the BT(R)DF measurements performed on various advanced fenestration systems, and provides some examples of their photometric features, that illustrate the suitability of the new device for practical applications.

Appendix D provides a nomenclature list for all the parameters and variables used throughout the thesis.

Chapter 2

Bidirectional photometric measurements

“I switch off the light, where does it go ?” (Koan zen)

2.1 The Bidirectional Transmission (Reflection) Distribution Function

The concept of bidirectional distribution function was first introduced by Nicodemus (1970) and Nicodemus et al. (1977) for directional reflectance in radiometric units, where it was defined as the scattered surface radiance ($\text{W}\cdot\text{m}^{-2}\cdot\text{sr}^{-1}$) divided by the incident surface irradiance ($\text{W}\cdot\text{m}^{-2}$).

As a photometric quantity¹, the *Bidirectional Transmission* - respectively *Reflection - Distribution Function*, abbreviated *BTDF* - respectively *BRDF* - (sometimes also named luminance coefficient q) is defined in Commission Internationale de l’Eclairage (1977) as the “quotient of the luminance of the medium by the illuminance on the medium”. It is illustrated in Figure 2.1 and expressed by Equation (2.1) in $\text{Cd}\cdot\text{m}^{-2}\cdot\text{lux}^{-1}$ or sr^{-1} :

$$BT(R)DF(\theta_1, \phi_1, \theta_2, \phi_2) = \frac{L_2(\theta_1, \phi_1, \theta_2, \phi_2)}{L_1(\theta_1, \phi_1) \cdot \cos \theta_1 \cdot d\omega_1} = \frac{L_2(\theta_1, \phi_1, \theta_2, \phi_2)}{E_1(\theta_1)} \quad (2.1)$$

where the corresponding symbols are defined as follows:

- (θ_1, ϕ_1) and (θ_2, ϕ_2) are the polar co-ordinates of the incoming and emerging (either transmitted or reflected) light flux, expressed in ($^\circ$) for convenience²;
- $L_1(\theta_1, \phi_1)$ and $L_2(\theta_1, \phi_1, \theta_2, \phi_2)$ are the luminances of an element of incoming and emerging light flux ($\text{Cd}\cdot\text{m}^{-2}$);
- $d\omega_1$ is the solid angle subtended by the incoming light flux (sr);
- $E_1(\theta_1)$ is the illuminance on the sample plane due to the incident light flux (lux).

The characterization of a daylighting system with respect to the different incident and emerging angles is based on a spherical co-ordinate system, defined on an international basis within Task 21 of the International Energy Agency (2000).

¹More details about photometric quantities terminology can be found in references: Commission Internationale de l’Eclairage (1983a), Association Française de l’Eclairage (1991), Schweizerische Lichttechnische Gesellschaft (1992), Illuminating Engineering Society of North America (1993).

²In further expressions, whenever radians units are required, they will be specified explicitly.

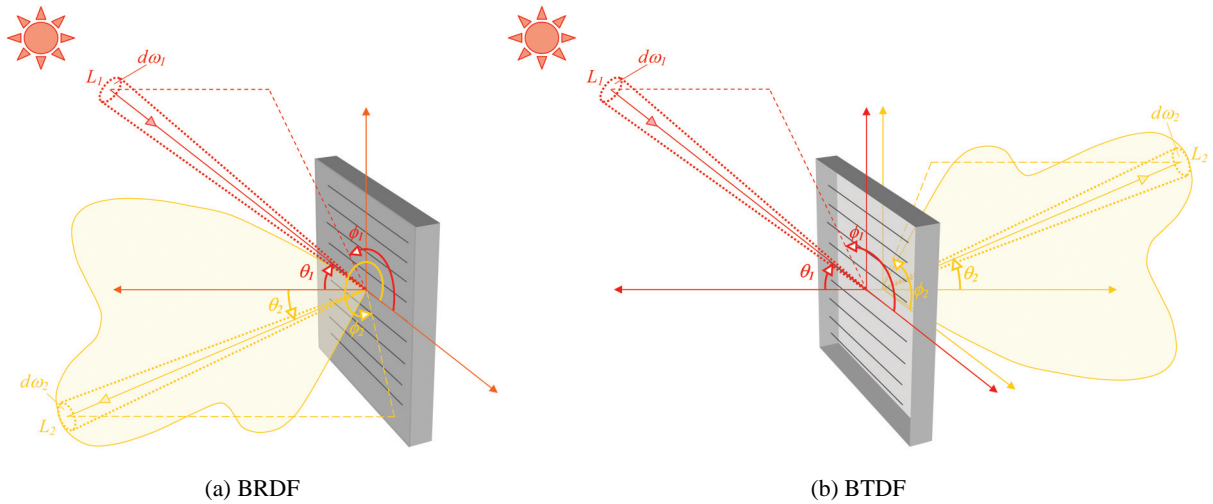


Figure 2.1: Photometric and geometric quantities used to define the Bidirectional Reflection (a) and Transmission (b) Distribution Functions of a fenestration material.

As shown on Figure 2.1, its origin is placed on the characterized component itself and the directions are defined by their respective altitude and azimuth angles: θ_i is comprised between 0° and 90° and ϕ_i is comprised between 0° and 360° , where index i indicates whether the angle is related to the incident ($i = 1$) or emerging ($i = 2$) direction (either transmitted or reflected). Both are integer numbers.

The base plane for incidence (i.e. where $\theta_1 = 90^\circ$, $\phi_1 \in [0^\circ; 360^\circ]$) is given by the external sample interface, which is fixed; as far as the base plane for emerging light is concerned ($\theta_2 = 90^\circ$, $\phi_2 \in [0^\circ; 360^\circ]$), it coincides with the former for reflected light, but is given by the internal sample interface for transmitted light, that will thus be shifted according to the sample thickness. The induced referential adaptations are explained in Section 4.2.3.

Bidirectional distribution functions are formally only applicable in reference to scattered radiation and should be assessed separately from the possible regular (specular) component of transmitted (reflected) light flux (Commission Internationale de l'Eclairage, 1977). This restriction makes it quite laborious to characterize a system properly, as two full investigations are hence required; furthermore, the distinction between highly directional scattering and true specular peaks becomes difficult to establish when dealing with real - thus imperfect - experimental conditions: the incident beam is not perfectly collimated, which induces that even regular transmittance (or specular reflectance) will have a non-zero spread.

As detailed in Section 5.4.2, the measurement conditions and principle of this particular assessment technique based on digital imaging allow to take both components into account without involving a significant loss in accuracy as long as certain restrictive conditions are respected (given by Equation (5.17) in the same section). Regular (specular) as well as diffuse components will, in consequence, be considered when defining and assessing BT(R)DFs within the framework of this research project.

It is important to note that, although the BT(R)DF appears as a four dimensional function (Equation (2.1)), it is, when considered from the most general point of view, dependent on several additional parameters: the polarization vector and wavelength of the incoming and outgoing light, and the exact position on the sample.

However, as we are here interested in characterizing photometric properties of daylighting systems, the energetic light fluxes will be integrated according to the human eye's sensitivity to colors

$V(\lambda)$ (defined in Commission Internationale de l’Eclairage (1932) and given in Figure 4.2); on the other hand, the incoming beam will be unpolarized white light, of properties (spectrum, color temperature) as close as possible to sunlight. Finally, the aim being to determine how transmitted or reflected light is distributed in space, we choose to average the sample’s heterogeneities over the considered illuminated area (that would therefore typically encompass at least one period of a recurrent structure).

2.2 Configuration of existing goniophotometers throughout the world

The range of applications for bidirectional goniophotometers has broadened increasingly since the early nineties, especially with the strong progress made in computer graphics rendering. These applications include the characterization of ground surfaces as well as microscopic interactions between layers of different components, of luminaires and lamps or of details about surface texture. A serious effort has been made as well in developing accurate and efficient bidirectional goniophotometric devices for detailed studies of fenestration systems, capable of measuring BTDFs and/or BRDFs in an appropriate way for such materials.

These instruments are described in the following section, with a special emphasis on the characteristics of devices for daylighting systems measurement. They are almost all based on a scanning process, i.e. on relative individual movements of the sample, detector, and/or source to monitor all incoming and outgoing light flux directions for which BT(R)DF data are needed. Some of them propose a way to reduce this onerous scanning process, although not significantly in the fenestration systems characterization field so far. In Section 2.2.2, two video-based approaches are spotted because of their strong time-efficiency combined to a potential applicability to daylighting components assessment; however, as detailed in that section, they also present significant draw-backs.

2.2.1 Characterization based on a scanning process

The main part of this section aims to provide a good overview of the different existing goniophotometers that were developed more specifically to characterize advanced glazing and shading systems. Other applications, not as close to the aims of this project but using similar assessment techniques, are then outlined more briefly.

Goniophotometers for advanced fenestration systems

The first bidirectional goniophotometer designed for BT(R)DF measurements of fenestration materials, shown on Figure 2.2(a), was developed at the *Lawrence Berkeley National Laboratory (LBNL)*, USA, in the late eighties (Papamichael et al., 1988). Not in use anymore, it consisted of a fixed light source, a sample holder with two rotational degrees of freedom (see Figure 2.2(b)) to determine direction (θ_1, ϕ_1) and of a photopically corrected silicon sensor moving on a semicircular track, pointing at the illuminated sample from the different outgoing directions (θ_2, ϕ_2) . It was able to handle samples of about $40 \times 40 \text{ cm}^2$.

The measured luminance, as well as the emerging direction, were here average values obtained over the whole sample area. As long as the detection method is coherent with this approximation, it is not by itself a draw-back of the device. What needs to be guaranteed is that the detection surface is able to encompass the possible divergence of the rays that reach it, either choosing a sensor element of appropriate dimensions, or compensating a too small or too close detector by averaging data obtained at different positions within the target space portion. A significant draw-back of this assessment method, however, is the considerable time required to gather a full set of BTDF data, as all possible incident and emerging directions need to be scanned individually, which

generally leads to far more than 50'000 discrete values to be assessed. Besides, a reduction of the processing time inevitably leads to a stronger use of interpolation techniques to guess the missing information, as the angular resolution is poorer; therefore, a lower accuracy is reached and the risk of missing transmission (reflection) features between two detection positions increases. These facts are of course true for any scanning-based assessment method, although not repeated in each of the following facility descriptions.

Achieved BTDFs were used to predict the performances of multi-layer fenestration systems, and were implemented in matrix-layer calculations to validate this analytical approach against measured solar heat gain values (Klems, 1994; Klems and Warner, 1995; Klems et al., 1997). An attempt of comparing BTDFs to ray-tracing calculations was made later but proved unsuccessful, the discrepancies between measurements and simulations remaining very important from both the quantitative and qualitative points of view (McCluney and Sung, 1999).

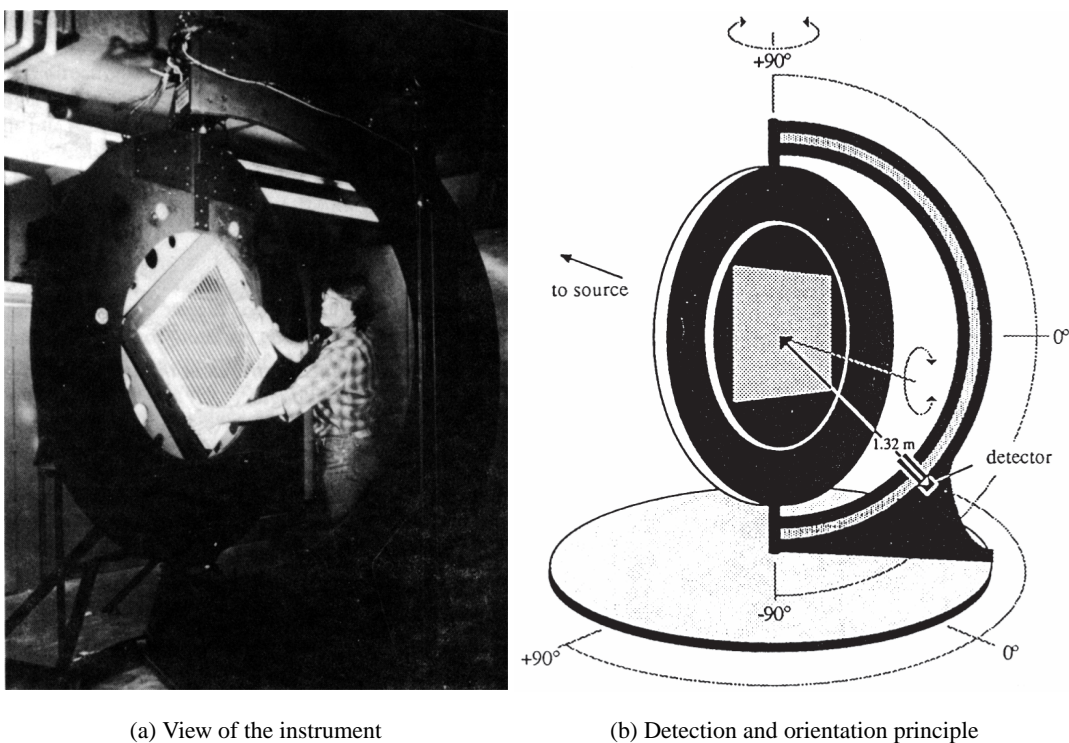


Figure 2.2: Original concept of a bidirectional goniophotometer for fenestration systems, developed at LBNL, California.

At the *Fraunhofer Institute for Solar Energy Systems (ISE)*, Freiburg, Germany, Apian-Bennewitz (1994) designed a goniophotometer allowing flexible sample dimensions, which was an innovation in regard to LBNL's device. It included two fixed light sources: a halogen lamp with parabolic mirror, intended for large samples characterization (up to $40 \times 40 \text{ cm}^2$), and a 1 kW Xenon lamp with collimating lens and varying diaphragms, for small samples (down to about $4 \times 4 \text{ cm}^2$). An automated solar cell ($2 \times 2 \text{ cm}^2$) with green $V(\lambda)$ filter was used as the detector, and moved on a linear rail; it viewed the complete $40 \times 40 \text{ cm}^2$ sample, fixed on an adjustable holder presenting two degrees of freedom. From a relative point of view, the detector was quite close to the sample (only at about twice its dimensions), and it therefore becomes difficult to assess BT(R)DF values without assumptions on emission, especially as the restrictions on detection areas, mentioned above, remain applicable. Two important innovations are to be underlined: an adaptive refinement in angular resolution was developed to concentrate detection positions inside interesting areas

(typically presenting high luminance gradients), unfortunately requiring a two-steps investigation to locate these areas; on the other hand, the results were integrated and validated against Ulbricht integrating sphere measurements performed on the same materials for the first time in 1993.

In 1998, Apian-Bennewitz and von der Hardt (1998) upgraded the device by replacing the linear detector rail with a semi-circular rail of 1 m radius, so that its distance to the sample remains constant (see Figure 2.3(a)); a silicon photodiode was chosen as the detector, with a green $V(\lambda)$ filter to correct the sensitivity in the IR range to a photometric response; interchangeable diaphragms can be placed in front of the detector (for the standard diameter 5 mm, the opening angle is 0.28°). The signal range is $1:10^7$, allowing the detection of both specular and low scattering components, and an angular resolution as fine as 0.1° can be achieved for the detector if necessary. A reference solar-cell had to be added to account for Xenon source fluctuations, which makes the assessment process heavier; on the other hand, the light source being of diameter often smaller than the sample itself, it can be viewed through the latter by the detector. This device was validated again with directional-hemispherical comparisons with integrating spheres.

Currently, a further upgrade of this device is under way, with an improved light source and, more importantly, a calibrated and movable CCD camera as the detector, that will thus also be used to identify details on the surface of façade elements, like localized peaks possibly responsible for glare effects (Apian-Bennewitz and von der Hardt, 1998).

A new goniophotometer has been designed recently by Apian-Bennewitz (2003), as part of his *pab[®]-opto* consultancy company activities, that is primarily designed for in-house use and consulting. It will allow both transmission and reflection measurements, as well as a flexibility in the sample size (up to $30 \times 30 \text{ cm}^2$). Either a Xenon lamp or a laser will be used as the incident light source, and a jointed arm will ensure the automated movements of the detector over the emerging hemisphere (see Figure 2.3(b)), according to an angular resolution up to 0.1° for both sample and detector, where the latter can be chosen amongst different types and spectral ranges depending on the application (IR, visible, multi channel), optionally adaptable to far infrared measurements.

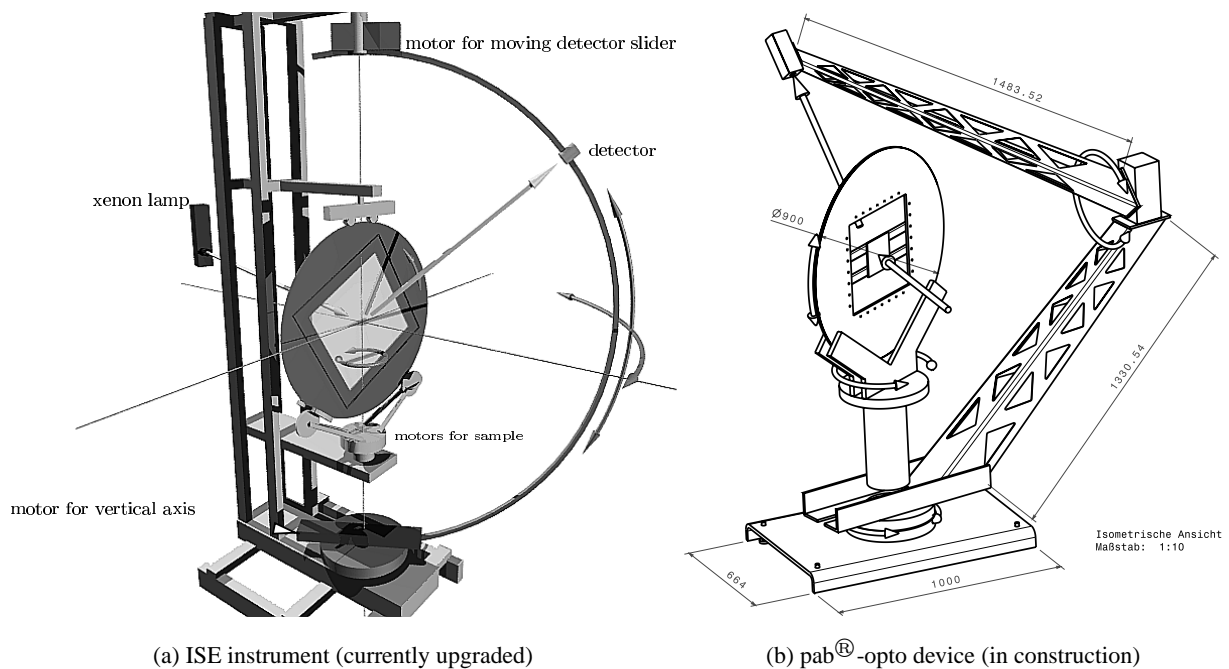


Figure 2.3: Mechanical components and movements of the bidirectional goniophotometers developed at ISE and pab[®]-opto in Freiburg, Germany.

At the *TNO Building and Construction Research*, Delft, The Netherlands, Bakker and van Dijk (1995) have developed a goniophotometric design very similar to the former concept at ISE (Apian-Bennewitz, 1994), also combining transmission and reflection measurements, a flexibility to the sample size and positioning the detector by the way of adjustable arms; it was validated against integrating spheres as well (van Dijk, 2001). More specifically, a wide bundle light source is combined to a small opening angle ($\sim 1^\circ$) sensor (silicon photodiode with green $V(\lambda)$ filter) that can be positioned every 0.1° if necessary. The combination of a wide incident beam with a narrow detection angle allows the observation of a restricted sample area without needing to account for border effects; at the same time, however, it supposes a sufficient homogeneity of the material for a 1° aperture to represent it appropriately; furthermore, having a large illuminated area induces a poor collimation of the incident beam. The chosen small light source (2 cm, Xenon 2.5 kW stage light, 100 Hz frequency), placed at 5 m, requires a hundred measurements at frequency 10,000 Hz to be realized and averaged for each incident or emerging direction. The distance from sensor to sample is of 1.2 m, with a maximal sample area of $80 \times 80 \text{ cm}^2$, and the sample holder turns around two perpendicular axes. This device was at first developed to characterize transparent-insulating (TI) materials; in 2000, it was adjusted to measure other systems as well (van Dijk, 2001), like simple and complex glazing, plastics and shading fabrics.

Aydinli (1996) describes the characteristics of the goniophotometer developed at the *Berlin University of Technology (TUB)*, Germany: capable of measuring transmitted light distribution only, it is based on a spiral scanning, achieved by manual movements of a 100 W incandescent light source on a semi-circular arc, that are combined to a manual rotation of the sample to determine the incident direction. This source and sample system is in turn rotated as a whole to determine the transmitted direction thanks to an automated rotation of the detector. Typical sample diameters stay around 7 cm, but a certain flexibility is allowed. Like at TNO and ISE, Ulbricht sphere measurements were used to validate integrated BTDF values.

It is currently upgraded as well, and will be based on a different mechanical principle, close to the one currently used at ISE (Apian-Bennewitz and von der Hardt, 1998), with a rotating arc on which the detector is moved; however, the latter will not be unique anymore, but will consist of several sensors distributed on the arc, undergoing small movements within the gap to their neighbor. This principle guarantees a complete arc investigation with a number of scanning positions reduced by a factor equal to the number of sensors; the reduction of the measurement time is of course significant but does unfortunately not prevent the scanning process to be laborious for a full BT(R)DF characterization. The light source will be a halogen lamp with reflector, and the sample diameter will be freely chosen amongst 5, 10 or 15 cm.

The *Institute for Light and Building technique (ILB)*, Cologne, Germany, also documents two different concepts. A former design, described in Kischkoweit-Lopin (1996), allowed transmission measurements only, and consisted of a fixed 50 W halogen lamp - thus of non-optimal spectrum -, placed at the focal point of a Fresnel lens. The beam was reflected by two redirecting planar mirrors before reaching the mobile detector, a 5 mm^2 photodiode with a green $V(\lambda)$ filter placed at 0.5m from sample. The incident, respectively transmitted, angular range could be chosen inside a 60° , respectively 80° , half-angle cone from the sample centre; only small samples ($5 \times 5 \text{ cm}^2$) could be characterized. Some measurements were performed on pressed glass, a 3M film and a diffusing material, although the obtained results were very poor for the latter, the transmission being too low for the signal to be properly detected.

Upgraded into a new concept two years later (Kischkoweit-Lopin, 1998), it was then capable of handling transmission as well as reflection characterizations; as the addition of a photomultiplier to the photodiode did not prove successful, a Zeiss[®] spectrometer for adaptable spectral analysis was used instead, moved on a semi-circular rail (80° half-angle movement) in a vertical

plane, itself rotating around a vertical axis. A halogen lamp with photopic filter remained at a constant distance of 1 m from the sample by being moved on a second semi-circular rail (80° half-angle movement), in a plane rotating around a horizontal axis. The same positioning accuracy of 0.1° as for the previous devices could be reached, but only small samples were allowed still ($\leq 7.5 \times 7.5 \text{ cm}^2$). An interesting new feature was the use of a non-calibrated monochrome CCD camera, that was added as a receiver option for qualitative analyzes of surface inhomogeneities; integration times could be varied from 10 ms to $10 \mu\text{s}$.

At *Cardiff University*, UK, Breitenbach and Rosenfeld (1998) developed a very innovative goniophotometer, now owned by the *Technical University of Denmark (DTU)* and illustrated in Figure 2.4. Designed for transmission measurements only, it is capable of collecting angle- as well as wavelength-dependent optical properties, thanks to a detector comprising a light collection system and an optical spectrum analyzer. This detector is placed at 2 m from the sample on a rotating arc (goniometer) and moved with a precision of 1° . The light collection system consists of an off axis parabolic mirror that focuses the transmitted light onto the end of an optical fiber bundle; the spectrum analyzer is either a silicon detector (from 300 to 1100 nm) or a InGaAs detector (900 to 2100 nm), with respective resolutions of 5 and 10 nm. Having access to the spectral properties of transmitted light is not only useful for describing visual properties in more details, but is also necessary for the data to be relevant for solar heat gain performances assessment.

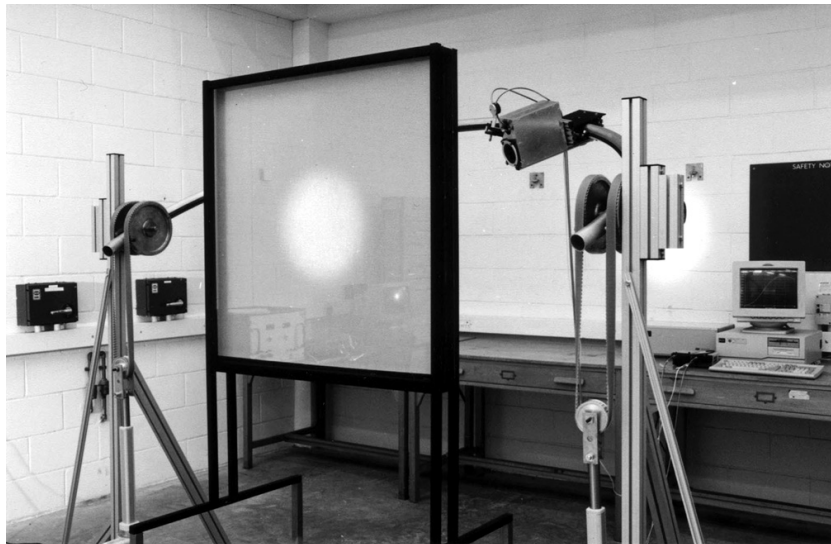


Figure 2.4: Goniophotometer developed at Cardiff University, United Kingdom.

The sample is rotated to determine the incident direction with a precision of 0.1° ; a tungsten halogen lamp (250 W) with parabolic aluminium reflector is fixed on a tripod at 2 m from the sample. This makes the alignment with the latter quite laborious, especially as a high precision is needed in the adjustment because of the detection method. A good uniformity of the incident beam is achieved ($<1\%$ below 60° from the beam axis); sample sizes can range from 2 to 9 cm in diameter, which remains restrictive for fenestration systems applications.

As for all the other instruments based on a scanning process, the complete BTDF characterization of a system remains very time-consuming: typically 5 to 10 hours are required for one incident direction (Breitenbach and Rosenfeld, 2000), as about 100 spectral scans (achieved in ~ 8 s) are necessary at each outgoing direction to get a satisfactory signal to noise ratio (>4), and these 5 to 10 hours still need to be multiplied by the number of incident directions for which BTDF data are needed. However, thanks to the chosen detection system, there is a noticeable advantage of this device compared to the others, apart from its capability to characterize the spectrum of

the transmitted light only shared with few: the optical fiber diameter determines very precisely the maximal divergence of rays that will be detected, which in this case is $\pm 0.5^\circ$; this divergence should be greater or equal - but preferably as close as possible - to the beam divergence in the sampled region itself, that is $< 1^\circ$ and thus of optimal concordance. Such a system therefore allows to ensure an optimal accuracy in the spatial characterization of transmitted light, which was not yet achieved by the other instruments.

As far as BTDF validation is concerned, directional-hemispherical transmittance were again compared to integrating sphere results (Breitenbach and Rosenfeld, 1998), but also to analytic model predictions (Rosenfeld, 1996; Breitenbach et al., 2001).

Finally, another goniophotometer based on a scanning process was realized at the *University of Technology Sydney (UTS)*, Australia (Smith, 1999; Smith et al., 2001). Of mechanical concept close to the upgraded facility at ISE (Apian-Bennewitz and von der Hardt, 1998), and also allowing transmission and reflection measurements, it differentiates itself by the two chosen light sources, one of which being a laser, used for detailed studies. This represents the only occurrence of lasers for fenestration systems assessment, apart from the not yet completed *pub[®]-opto* device (Apian-Bennewitz, 2003); these sources are indeed suitable for specular light analysis and offer an almost perfect collimation, but they also present the significant draw-backs of proposing only pulsed and monochromatic signals, that are too low for diffuse materials, and too narrow for large samples. The other source is an arc lamp, used for larger sample areas, with a beam splitter and a collimator. The sample rotates around a vertical axis, and the detector is moved on a quarter-circular arc turning around both horizontal and vertical axes; its distance to the sample is 60 cm at most, but can be varied according to the signal level: when scattering occurs, it needs to be brought closer, which also implies that the angular resolution will be coarser (a 0.002° resolution in altitude or azimuth is the finest reachable, but is rarely necessary). It was also validated against integrating sphere measurements Smith et al. (2001).

Table 2.1 summarizes the main features of these different instruments: research institute, detection device, measurement type, sample size and date (based on the associated documentation's publishing year(s)) are provided.

Institute	Sensor	BTDF	BRDF	Sample (cm ²)	Date
LBNL, USA	silicon photodiode	✓	-	40 × 40	1988/94/95/97
ISE, Germany	silicon photodiode	✓	✓	≤ 40 × 40	1994/98
TNO, The Netherlands	silicon photodiode	✓	✓	≤ 80 × 80 (only ≈ 1 cm observed)	1995/2001
TUB, Germany	photoelement	✓	-	∈ [5 × 5 ; 15 × 15]	1996/98
ILB, Germany	spectrometer	✓	✓	≤ 7.5 × 7.5	1996/98
Cardiff, United Kingdom	optical fiber + silicon / InGaAs	✓	-	≤ 9 × 9	1996/98 2000/01
UTS, Australia	radiometer	✓	✓	≤ 40 × 40	1999/2001
LESO, Switzerland	CCD camera	✓	✓	≤ 40 × 40	1999 2000/01/02/03

Table 2.1: Main features of existing bidirectional goniophotometers for the assessment of fenestration systems.

Many other applications are found for goniophotometric measurements. An overview of the broad range of existing devices is here given according to three main categories: instruments for assessing BTDFs or BRDFs of surfaces smaller than a few cm, directional goniophotometers for luminaires, and devices developed for the detailed analysis of surface texture or local variations in luminance, often aiming at image rendering applications.

Bidirectional transmittance and reflectance properties of small surfaces

Several instruments have been designed for analyzing samples of a few cm only.

Murray-Coleman and Smith (1990) in Boulder, Colorado, developed such a device for luminaire modeling applications; it uses an incandescent light source and silicon photodiodes to detect the emerging radiation, and allows sample sizes of 6.5 cm diameter. It was used for reflection measurements, although the principle remains viable in transmission as well. Another apparatus was designed by Hunn et al. (1991), based on the LBNL goniophotometer principle (Papamichael et al., 1988), to measure the transmittance properties of small fabric composite samples.

At Cornell University, NY, Foo (1997) developed a bidirectional gonireflectometer for surface texture characterization; the sample size is limited to about 5 cm. A rotating Quartz-halogen source is combined to an opal glass diffuser for depolarization; the incident beam then passes through a condenser lens, an adjustable iris and a Nikon camera lens. The sample can be rotated around two perpendicular axes to determine the incident and reflected directions; a fixed commercial spectroradiometer manufactured by Kodak is used as the detector, where light scattered from the sample is focused after passing through a dichroic polarizer and being reflected on a folding mirror.

Proctor (2000) uses a tunable laser source, whose beam goes through a large set of optical components (beamsplitter, mirrors, filters, monochromator, polarizer) before reaching the photodiode detector. Milandri et al. (2002) designed an instrument for assessing BT(R)DFs of silica wool samples, using a bolometer mounted on a goniometer as detector.

The Belgian Building Research Institute (BBRI) owns a commercial double beam spectrophotometer (Perkin-Elmer model Lambda 900) with angular accessory (PELA 130) (Barthel et al., 2002), very similar to the customized Perkin-Elmer goniospectroradiometers at LBNL (Rubin and Powles, 2001): it allows transmission and reflection measurements from 175 to 3300 nm, and creates two symmetric mirror paths (reference and measurement beams), that are each collected in a small integrating sphere. Likewise, van Nijnatten (2002, 2003) developed a measurement device for BT(R)DFs with a fixed 2 cm light source, a rotating sample, and an integrating sphere mounted on a goniometer for detection, combined to a polarizer to measure s- and p- polarizations separately. Other commercially available spectro-radiometers with goniometric accessory are marketed by Schmitt Industries (2003) and Surface Optics (2003), and are using a laser source for BT(R)DF assessment.

Characterization of lighting fixtures

The principle remains the same as for bidirectional measurements, but the aim is to determine how the light emitted from lamps or luminaires is distributed in space, so there is no incident direction to account for.

Several assessment methods rely on a scanning along section views (Grundmann et al., 1993; PRC Krochmann GmbH, 1996), or on the positioning of the detector by robots and a similar adjustment of the analyzed incandescent lamp (Sauter, 1996). More recently, methods allowing to investigate the whole luminaire have been developed, that can differ whether they aim at investigating detailed properties over the luminaire's surface or only the globally emitted light flux in each direction. West and Pearce (1998) chose to collect the light emitted from the whole luminaire with a mirror, and to redirect it towards a notional sphere that maps the luminous intensity

distribution; the same option was taken by Lighting Sciences Inc. (1999), yet with a photodetector as the final target.

The preferred technique for luminance field goniophotometry remains however the use of a calibrated CCD camera as the detector, to avoid a scanning over the luminaire (Ashdown, 1993; Ashdown and Rykowski, 1998; Rykowski, 1994; Lewin and O'Farrell, 1999; Whitehead et al., 1999; Jenkins and Mönch, 2000; Deniel, 2002; TechnoTeam Bildverarbeitung GmbH, 2003); both CCD camera and photosensor can also be placed on a ring moving around the luminaire (Kloss, 2001); finally, to analyze very small light sources (LED's), the Katholieke Hogeschool Sint-Lieven (2003) resorts to fiber optics connected to a spectroheliograph in addition to the CCD camera system.

Investigation of texture or local luminance variations on the surface of an object

Local variations in microgeometry and in reflectance are not represented in sufficient details by a BRDF, which typically integrates a sample area over a period of heterogeneity. For such detailed analyses, an investigation of the characterized surface becomes necessary. The use of a CCD camera to perform this investigation in an efficient way appears as the most commonly used option, as it allows to reduce the number of scanned dimensions greatly, without any loss of accuracy if appropriately calibrated. Formally, such a function was defined in Dana et al. (1999) as the "Bidirectional Texture Function (BTF)", which is a six dimensional function, extending the BRDF concept by allowing reflectance to vary spatially along the surface.

At macroscopic levels, gonioradiometers were developed to describe the reflectance properties of ground or vegetation, as by Coulomb and Brusque (1996) for roads, Bicheron et al. (1997) on boreal forests and fen, Nandy et al. (1998) on test sites in Nevada and New Mexico, Tsuchida et al. (1999), Demircan et al. (2000) and Sandmeier (2000) on fields and land surfaces, and Georgiev and Butler (2002) on planet Mars. On the other side, surface texture scattering patterns are investigated at microscopic levels to characterize tapered roller bearings (Huynh and Wong, 1993), ink-paper interactions (Arney and Hung-Tran, 1998), or the scattering properties of velvet and shot fabrics wrapped around a right-circular cylinder for a more convenient collecting of radiances by the digital camera (Lu et al., 1998, 2000)

Bidirectional reflectance functions of visual display screens were also studied to assess the parasitic reflections of the ambient light sources in a room (Becker, 1998): it must be noted that this approach presented an interesting 2-D BRDF concept using a conoscopic receiver and a specific illumination technique ('Focal Plane Illumination[®]'). Fusco et al. (1999) from the IEN Istituto Elettrotecnico Nazionale in Turin, Italy developed a bidirectional assessment method for transmission and reflection, where small samples (5 cm diameter) are analyzed by a rotating, spectrally corrected CCD camera, with a resolution up to 40 μm .

At a larger scale, the Katholieke Hogeschool Sint-Lieven (2002) designed a photogoniometer primarily for traffic lights and variable message signs, thus including a large rotating sample holder; the detection technique is based on a radianceprobe combined to a CCD-spectroheliograph.

Amongst the different instruments developed for a detailed characterization of objects texture for image rendering applications (Karner et al., 1996; Dana et al., 1999; Ke, 1999; Marschner et al., 1999, 2000; Nadal, 2000; Goesele et al., 2000; Lensch et al., 2003; Han and Perlin, 2003), almost all of which use an imaging detector (CCD camera), two approaches can be distinguished for their much better time-efficiency: Marschner et al. (1999, 2000) and Lensch et al. (2003) consider curved test samples, like in Lu et al. (1998), and thus capture light reflected from many differently oriented parts of the surface at the same time; this method significantly accelerates the investigation process by eliminating the mechanisms of detector and source positioning, the latter being determined by automated photogrammetry. Han and Perlin (2003) use a tapered kaleidoscope; it allows, on one hand, a camera to view the same surface from many directions simultaneously; on

the other hand, the surface can be illuminated from many different directions using a structured light source.

2.2.2 Video-based time-efficient approaches

Whether developed for small or large scale elements, all the approaches based on a scanning process prove to be extremely time-consuming. Experiment planning techniques can be used to refine the angular resolution of BT(R)DF data assessment around directions of high luminance dynamical range (“peaks” of transmission or reflection), and to lower it in smoother areas. However, a full pre-scanning of the outgoing rays hemisphere is then required to identify the corresponding “light peaks”, which increases again the time requested for a BT(R)DF data processing (Apian-Bennewitz, 1994).

The use of CCD cameras allows a fine investigation of the materials and an appreciable flexibility in the luminance dynamics if different integration intervals are used. One of its greatest advantages is to allow the visualisation of many directions or locations at the same time. It has been used so far mostly to investigate details on materials. However, the projection of the light emerging from the sample on a surface that could be more easily viewed by the camera would allow to prevent the latter from having to move from one acquisition position to the next one.

Two examples of instruments using digital imaging combined to this projection principle were designed for photo-realistic rendering of lighting in interior spaces, allowing to lower the processing time needed to perform a full BRDF measurement in a remarkable way.

Ward (1992), at the Lawrence Berkeley National Laboratory, designed an original and extremely time-efficient approach for reflection measurements, schematized in Figure 2.5(a): the sample and a CCD camera equipped with a fish-eye lens are each positioned at the two focal points of a hemi-ellipsoidal, semi-transparent mirror. The light source, always pointing towards the sample, can be moved. The light rays emerging from the sample are reflected on the interior face of the mirror, and redirected towards the camera. Thus, basically only one image is needed to investigate the whole reflected light distribution; as a consequence, only a few minutes are required to achieve a complete sample characterization, e.g. for about a hundred incident angles. What is more, even reflected directions coincident with the illumination direction are permitted.

However, using a specular surface to redirect the light towards the detector can induce polarization problems, as the reflection index of a mirror depends on the polarization state of the incoming light; even if the light reflected on the sample is unpolarized, its reflection on the mirror could create a partial polarization. Besides, due to practical and mechanical constraints, it was not possible to build an ellipsoid, and a half-silvered hemispherical mirror was designed instead, which induces that the two focal points become one, although sample and camera of course cannot be placed at exactly the same position.

A 3 W quartz-halogen lamp with parabolic reflector was chosen as the light source, moved automatically. Incident rays are transmitted regularly through the hemispherical mirror, and reflected on the 3 cm diameter sample, manually rotated. After undergoing a second reflection on the mirror, they meet at the mirror’s focal distance, i.e. at half its radius, wherever the sample is placed (as long as it stays close to the mirror center). Yet, as the camera needs to be positioned symmetrically to the sample regarding the mirror center in order to collect the mirror reflected rays, it will not be able to focus at exactly the rays’ intersection points but only on a half radius hemisphere slightly shifted from these points: geometrical approximations become necessary to recover the reflected angles from pixel locations. Apart from that, the main limitations of this device are the measurement of polished surfaces presenting sharp specular peaks, and of reflectance near grazing angles, because the hemisphere is not of perfect shape and the incident beam is not

parallel enough. This device could in principle be used for transmission measurements as well, by moving the light source on the other side of the sample, but 3 cm is too small an area to achieve an accurate assessment of the transmitted light distribution for usual optical systems' thickness because of the important edge effects.

A similar measurement device, based on Ward's work, was developed recently by Deniel (2002) at the Université de Rennes 1, in France, together with a more conventional approach using of a jointed device and a mobile spectrophotometer. It consists of a digital camera equipped with a fish-eye lens as well, that is placed at the bottom of a cube coated with a diffuse grey painting (see Figure 2.5(b)), replacing Ward's hemispherical mirror. This allows to avoid problematic polarization effects due to specular reflections, but induces many parasitic inter-reflections that are difficult to assess and control.

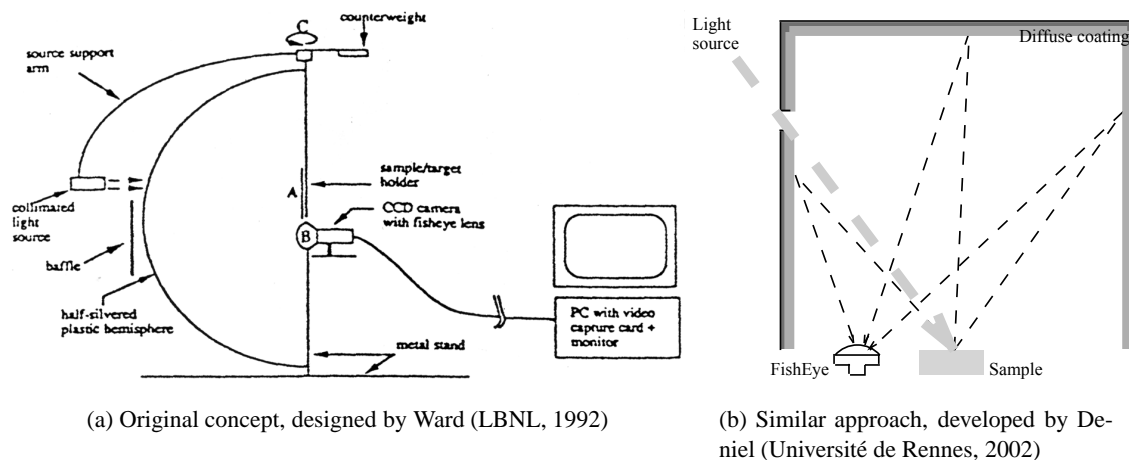


Figure 2.5: Time-efficient video-reflectometers developed for photo-realistic rendering of interior spaces.

Although extremely time-efficient, these two propositions show important draw-backs mainly because either the projection surface is specular and induces potentially significant polarization effects, or because with a concave diffuse one, inter-reflections cannot be avoided. In this project, we also use a CCD camera combined to a projection screen, but a flat and diffusing one in order to avoid the two undesirable effects mentioned above. The functioning principle is explained briefly in Section 2.4, and in more details in Chapter 3.

2.3 Use of digital imaging techniques in photometric measurements

The use of video techniques, together with digital image handling software, has proven to be a very fruitful and encouraging approach in the field of photometry, especially since the advent of CCD image sensors (Ochi and Lizuka, 1996).

We have seen in the previous section that CCD cameras were already widely used for assessing luminance distributions on surfaces and reflectance properties of objects at very different scales; they allow to reduce the scanning process and achieve high spatial accuracy in the results. Many other photometric measurement facilities take benefit from digital imaging techniques as well, and the latter have proven to be efficient and reliable, allowing considerable improvements in speed and flexibility.

Several video-photometers or mapping luminancemeters were designed (Rea and Jeffrey, 1990; Lewin et al., 1992; Song et al., 1994; Pasini and Transley, 1994; Berrutto, 1996; Tansley et al., 1999), as well as CCD camera-based instruments for the modeling of lighting conditions in a

given environment (Loscos, 1999) or for road lighting assessment (Glenn et al., 1999). Michel and Andersen (1999) developed a sky luminance scanner, using the reflection of the sky vault on a spherical mirror, captured by a calibrated CCD camera.

More recent works confirmed the adequacy of this technique for the assessment of the luminous performance of buildings (Dittmar et al., 2003); a more specific application was ergonomic evaluation, achieved through the use of a black and white CCD camera as a visual comfort meter (Berrutto and Fontoynt, 1995; Kondo et al., 1997), or a color digital camera (Michel et al., 2001; Francioli and Meyer, 2003). Dennis (2003) chose to resort to video capture for a time-efficient determination of the horizon obstruction.

For all these devices, the overall video digital system must follow detailed calibration and correction procedures, which probably makes up the main difficulty of this approach compared to the conventional acquisition method using radio- or photometers providing directly the desired output. The reliability of the data assessment and its related accuracy depend on the execution of these procedures, explained in more details in Chapter 4. Generally, they are defined in three steps (Andersen, 1998; Bellia et al., 2002): the CCD video camera has first to be calibrated spectrally, in order that its response becomes as close as possible to the human eye's spectral sensitivity $V(\lambda)$ (Illuminating Engineering Society of North America, 1993); thereafter, greyscale levels (or more generally speaking the pixel values) have to be converted into luminance values, these conversions depending on the integration interval chosen for each captured image; finally, the relation between the pixel co-ordinates of the image and the corresponding light ray direction must be determined.

Besides, apart from controlling that a uniform luminance distribution produces an image of equal pixel values (CCD component sensitivity and lens effects), as detailed in Section 4.3.2, additional possible sources of error due to the camera itself must be checked, including the stability of the electronic circuit responsible for the gain of the CCD camera, the sensitivity of the CCD sensor to ambient temperature and the degree of reliability of the main function parameters control (exposure time, aperture diameter, etc.). Andersen (1998) gives a detailed description of the handling of these sources of error for the camera used in this project.

2.4 Innovation and advantages of the adopted approach

As mentioned above, one of the main draw-backs of scanning processes is the considerable measurement time needed for a BT(R)DF assessment, which is further increased when finer angular resolutions are required, as the latter are directly linked to the number of investigated directions. Besides, several difficulties appear when the emerging light presents high luminance gradients, that go beyond problems of accuracy upholding as well for the lowest as for the strongest emerging luminance values: the luminous peaks - especially the narrow ones - need to be located precisely beforehand to ensure their inclusion in the investigation, which requires a preliminary characterization. Yet, the risk of missing some feature can still never been put aside completely.

In such regions where the luminances vary rapidly, a tightening of the measured directions is often necessary because interpolation becomes uncertain. However, apart from being time-consuming, this makes it not only more difficult for simulation programs to implement the BT(R)DF data afterwards, but the estimation of the global (directional-hemispherical) transmittance or reflectance also becomes delicate (see Section 6.4.1): a weighting of data is then necessary, based on the areas associated to each point that are difficult to determine as the latter are distributed irregularly (Apian-Bennewitz et al., 1994).

Finally, the necessary interpolation between measured directions remains problematic even for smoother luminance distribution parts, as it is difficult to evaluate how different the resulting approximation is from the actual distribution, the material being a priori of unknown properties.

The resort to digital imaging techniques combined to using a projection principle close to the time-efficient approaches of Ward (1992) and Deniel (2002) (actually not as time-efficient but avoiding their main draw-backs) allows to overcome these difficulties.

The measurement principle is the following, illustrated by Figure 2.6: the light emerging from the sample is reflected by a diffusing triangular panel towards a CCD camera, which provides a picture of the screen in its entirety; the camera is used as a multiple-points luminance-meter and calibrated accordingly. Within six positions of the screen and camera around the sample (each separated by a 60° rotation from the next one), a complete investigation of the transmitted or reflected light is achieved.

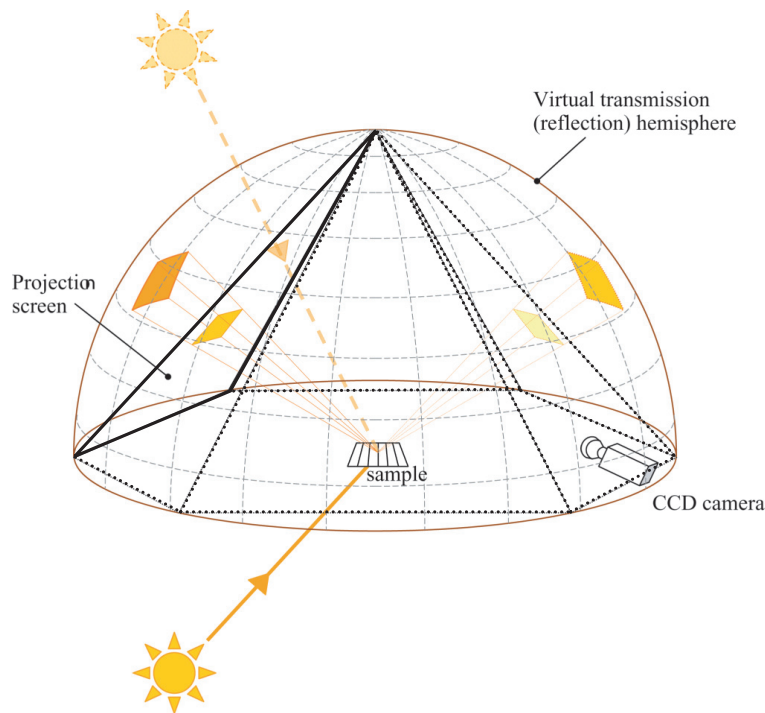


Figure 2.6: Detection principle of the bidirectional goniophotometer using a CCD camera combined to a flat and diffuse projection screen, allowing a continuous investigation of emerging light.

Thanks to this novel approach, the transmission (reflection) hemisphere no longer needs to be scanned along every emerging light direction, which in consequence tremendously decreases the processing time: instead of several hours of scanning for one incident direction, it was reduced to a few minutes, and could be lowered to less than a minute with a more powerful computer system. Indeed, only six movements of the screen and camera are necessary to gather a complete, and what is more, continuous information about the emerging light distribution.

As the six screen positions (and therefore their six captured images) are adjacent, there can be no gap or missed feature for this type of investigation; on the other hand, for a given screen image, the luminance map is provided by the calibrated (and corrected: see Section 5.4.1) pixel values, that cover the whole screen area in a continuous way as well. The only parameter that limits the angular resolution is actually the pixels size, which leads to a limit angular definition of about 0.1° in altitude and 0.3° in azimuth.

In order to provide a set of BT(R)DF data flexible to the user's wishes, the considerable information contained in the achieved calibrated images is averaged according to an angular grid of freely chosen intervals in altitude and azimuth (see Section 5.2), represented on Figure 2.6 as well. This grid therefore allows to subdivide the emerging hemisphere into contiguous sectors where the BT(R)DF can be averaged, without any loss of precision as each mean value will truly represent the angular interval it is associated to. For materials that don't present perfectly diffusing

properties, such BT(R)DF data will obviously be different from goniophotometric measurements based on a scanning process, where the obtained values are associated to a given direction (θ , ϕ_2) and not to the hemisphere portion around it.

Furthermore, by taking advantage of digital imaging potentialities, and in particular of the possibility of capturing several images of the same luminous situation but at different integration intervals, very large dynamics in luminance can be assessed with constant accuracy; at the same time, a high quality of measurements can be maintained for low luminance investigation as well as strong peaks in transmission or reflection, even if they are close to each other. Indeed, as explained in Section 5.3.2, individual 8 bits images can be combined to form a complete 32 bits floating point image, whose pixels are thus each calibrated according to the most suitable integration time specifically. Fontoynt (1995) defines the signal range needed for BT(R)DF assessment to be of 10^7 ; with this method, a 2^{32} range can be achieved (500 times larger) when taking full advantage of the floating-point image format, confirming that this approach is reliable to handle high gradients in luminance and prevent saturation or under-exposure effects.

As mentioned above, these advantages are only accessible at the expense of numerous and careful calibration procedures as well as heavy image and data processing, explained in Chapters 4 and 5. However, once all the intermediate stages leading from raw digital images to accurate BT(R)DFs have been completed successfully, the measurement facility becomes again as easy to use as any instrument of the kind.

Choosing to point an imaging detector towards a projection screen to assess BT(R)DFs in a time-efficient and continuous way unfortunately prevents from being able to achieve a spatial accuracy as optimal as for the instrument developed at Cardiff University (Breitenbach and Rosenfeld, 1998), that remains the only one capable to distinguish outgoing directions with a high level of precision for samples larger than a few cm. The measured luminances and emerging directions are instead average values for the sampled region; thus, as mentioned for LBNL's device, it is important to subdivide the emerging hemisphere according to an averaging grid in agreement with the possible divergence of rays reaching a given point on the screen, as explained in more details in Section B.1.3.

Chapter 3

Digital imaging goniophotometer for transmission and reflection

“Two ways to shine: reject light or produce it.” (Paul Claudel)

3.1 Functioning principle

The functioning principle of the bidirectional goniophotometer is based on the collection of the light flux emerging from the investigated sample by a diffusing flat screen, at which a calibrated Charge-Coupled Device (CCD) camera is aiming.

To cover all possible emerging directions (2π steradian), the camera and the screen perform rotations of a 60° angle magnitude to make up a virtual 6-faced pyramid, shown on Figure 2.6, while the sample remains unmoving. This leads to the visualization of the whole transmitted (reflected) hemisphere in a continuous way. The orthogonal projection of these six screen positions on the sample plane is illustrated in Figure 3.1(a).

A perfectly flat projection screen is chosen to avoid inter-reflections from one screen point to another, that would not be prevented with a hemisphere (although the latter might have appeared a more natural alternative for symmetry reasons). On the other hand, a diffusing coating is required for two reasons: to allow light reflected by any part of the screen to be observable likewise by the camera and to avoid any correlation between the camera's position and the measurements. Strong constraints are in consequence imposed on the paint covering the triangular panel, as detailed in Section 3.2.5.

In order to be used as a multiple-points luminance-meter, the camera carries out a luminance mapping of the projection screen by capturing images of it at different integration intervals, thus avoiding over and under-exposure effects (Section 5.3). The latter are then treated appropriately to extract BT(R)DF data: the emerging direction and luminance to which each pixel is associated are determined and, based on these parameters, the corresponding BT(R)DF values are calculated at the pixel level and gathered according to a suitable averaging grid (see Section 5.4).

The measurements are performed in a $15 \times 7 \times 8$ m dark chamber made of black velvet curtains and carpet showing reflection factors inferior to 1%; besides, a light-proof cap protects the measurement space against parasitic light. On the other hand, all internal elements are covered with highly absorbing material. Appropriate experimental conditions are thus achieved, preventing any disturbance of measurements due to external light penetration or parasitic internal reflections.

The light source remaining fixed, the incident direction (θ_1, ϕ_1) is determined by inclining the sample plane around a horizontal axis at altitude θ_1 , and by rotating the sample around its normal to reach azimuth ϕ_1 , as illustrated in Figure 3.1(b). The origin axes for azimuth are in consequence bound to the sample itself; a rotation of the latter will thus induce a change in the referential, discussed in Section 4.2.3.

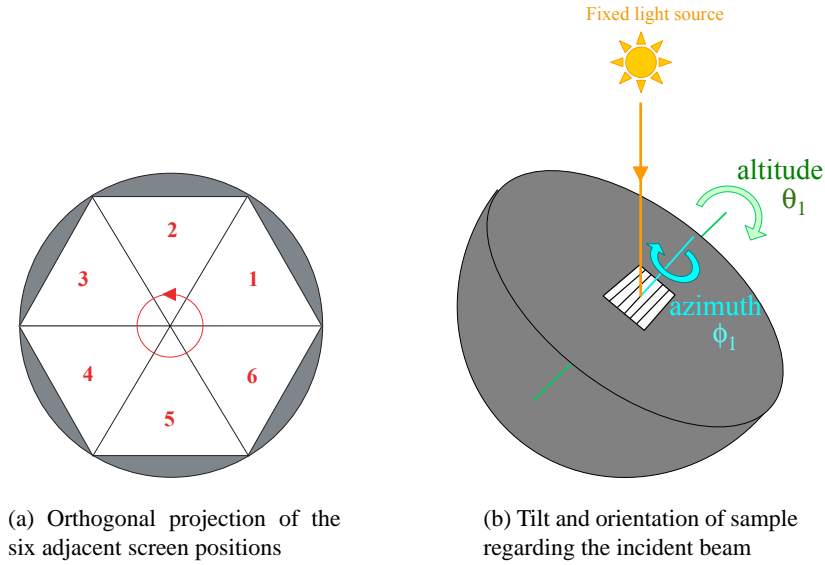


Figure 3.1: Light collection principle and determination of incident direction for the goniophotometer.

Whether used for transmission or reflection measurements, these components remain identical, yet with some additional mechanisms necessary for investigating reflected light, outlined below. Overall, the time needed to perform a BT(R)DF characterization is only of a few minutes per incident direction.

3.1.1 Transmission measurements (BTDF)

As can be seen on Figure 3.2, BTDF assessments (transmission measurements) only require the screen and the camera to move from one position p to the next one $p+1$ ($p = 1 \dots 6$), where pictures can be taken to assess the spatial distribution of transmitted light flux.

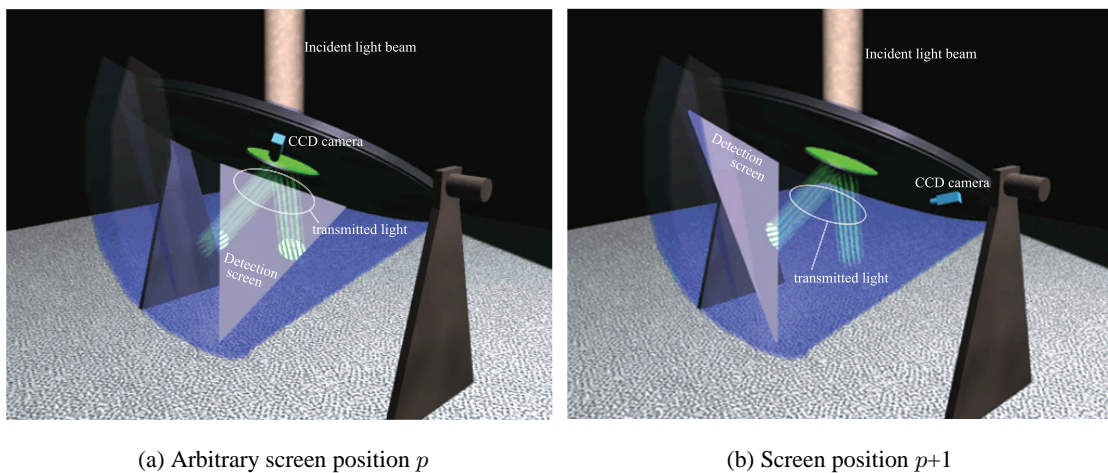


Figure 3.2: Detection of transmitted light flux.

3.1.2 Reflection measurements (BRDF)

For BRDF assessment (reflection measurements), however, some additional constraints appear due to the conflict of the incident and emerging light flux. For five out of the six screen positions (unless incidence is normal), the detection principle can be kept identical as in transmission mode (Figure 3.3(a)), except that light flux must penetrate the measurement space in a way that the beam is restricted to the sample area only. As there is one position (all six for normal incidence) where the screen obstructs the incoming light flux, a special opening in the latter is required to let the beam reach the sample, producing a blind spot at that specific screen position (and only in reflection mode), as illustrated in Figure 3.3(b). The practical answer to these constraints is detailed in Section 3.3.3.

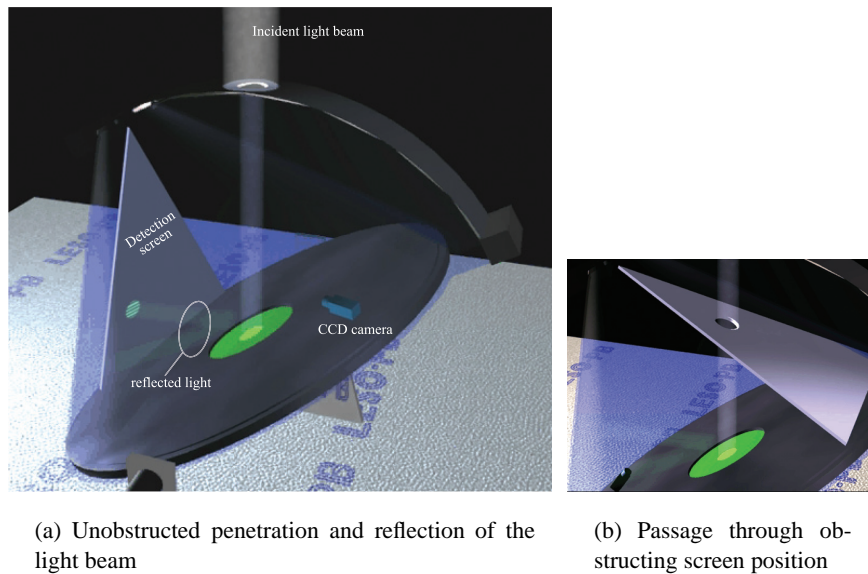


Figure 3.3: Detection of reflected light flux.

3.2 Construction of the transmission device

Prior to the PhD project itself, an extensive feasibility study was realized about this innovative measurement principle for bidirectional transmission measurements, and several major mechanical components were designed and constructed (main platform, rotating ring, supporting structure, light-proof cap). Section 3.2.1 describes the main achievements of this work; further information can be found in Scartezzini et al. (1997b).

The final design of the goniophotometer (computer controlled movements of all axes, mechanical adjustments), the adaptation of the sample holder and the addition of the light detection system (diffusing screen, CCD camera) took place as first stages of this PhD project; they are explained in the subsequent sections, together with the characteristics of the light source that was used until the device was, in a second phase of development, converted into a double BTDF and BRDF measurement facility, as detailed in Sections 3.3 and 3.4.

3.2.1 Major structural components

The subdivision of a hemisphere into six parts to reduce material costs was already used for another daylighting device developed at the Solar Energy and Building Physics Laboratory (LESO-PB) at EPFL: the sky scanning simulator (Michel et al., 1995). Besides, the mechanical concept of

the goniophotometer benefited from the development of the automated heliodon (sun simulator) (Rhyner et al., 1991) associated to it, that also uses DC motors to achieve the rotations of the two main movable axes.

With the aid of CAD representations of the device (cf. Figure 3.4), a final concept for the bidirectional goniophotometer was established for BTDF measurements (more details about the structural components geometry can be found in Appendix A).

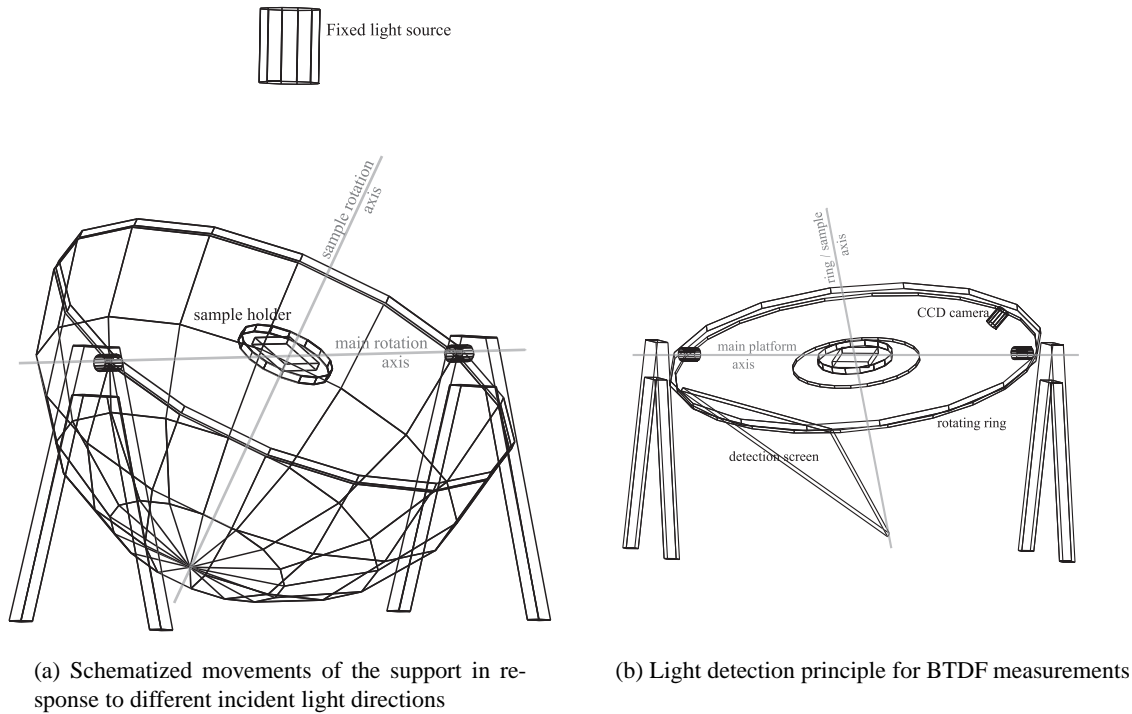


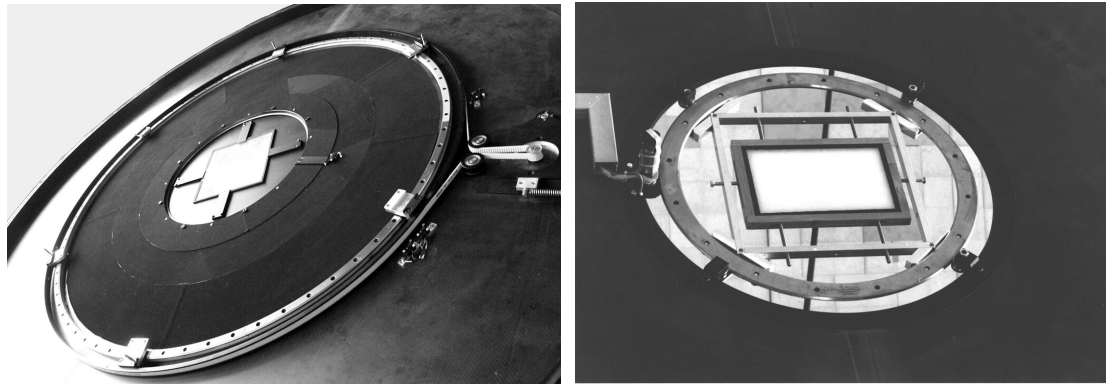
Figure 3.4: Virtual representations of the goniophotometer for BTDF characterization.

A first axis controls the main platform tilt (used as the primary support to all other mechanical elements), that defines incident altitude θ_1 . It moves within a 90° range, from horizontal to vertical (i.e. from normal to grazing incidence). This axis is computer controlled via a two-axes Creonics motion control card driving a DC motor with a high reduction (1:160) Harmonic Drive gear.

A second axis, driven with the same Creonics technology, controls the movement of the light detection system, consisting of a triangular projection screen and a CCD camera both fixed on a rotating ring. Within six positions of this system separated by 60° rotations, the light distribution emerging from the sample is intercepted in its entirety. The supporting ring's rotation is in fact limited to 330° because of the belt system used to achieve these movements, shown on Figure 3.5(a) (where the ring itself has been removed). This is however widely sufficient to cover the whole emerging hemisphere, as to get from the screen position $p = 1$ to $p = 6$ on Figure 3.1(a) only a 300° rotation is required.

A third axis controls the sample holder orientation, shown on Figure 3.5(b), that determines incident azimuth ϕ_1 . This axis can move over 360° and is controlled by an external Creonics motion control card, driven from the PC through a RS-232 link (COM Port).

All three motors are connected to DC amplifiers controlled by the Creonics cards and located in the main electronic command unit.



(a) Indented belt control system

(b) Original sample holding structure

Figure 3.5: Details of mechanisms for ring and sample movements.

The overall equipment existing at this stage of design is shown on Figure 3.6: one recognizes the main platform and the moving plate for light detection rotating underneath it, on which the support for the diffusing screen is fixed. All three are made of carbon fiber to achieve maximal strength at minimal momentum of inertia; the light-proof conic cap encompassing the measurement space is made of the same material, disassembled on the picture for a better vision; the inside of this cap is covered with a black foam, of 2.2% reflection coefficient.

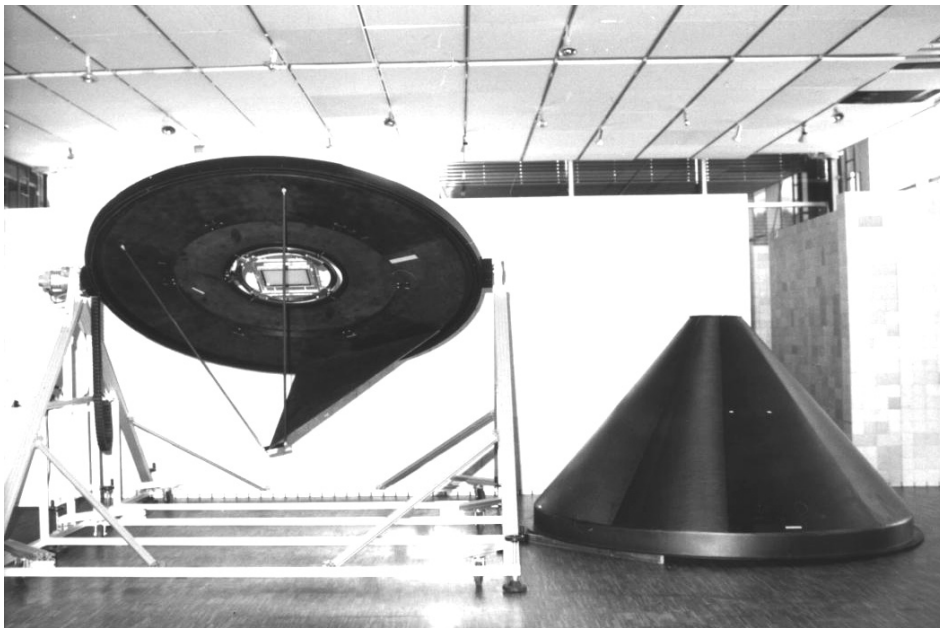


Figure 3.6: Early stage of the goniophotometer mechanical development: main structural components and support.

3.2.2 Mechanical developments

Command routines (in machine language) for the computer to send orders to the motors were implemented. The home positions of the three axes (main platform, rotating ring, sample holder) could then be defined. This was achieved on the basis of the relation between motor units and angular degrees; as a second step, geometric criteria and spirit level measurements were used for an accurate determination of the “zero” positions.

Precise investigations were undertaken to check - and if necessary correct - diverse slight modifications in positioning due to mechanical constraints. The latter were explained by the following reasons:

- Because of the important unbalanced weight on the emerging light detection side of the device's platform, the elasticity of the main axle caused an insufficiently accurate positioning of the latter, and therefore θ_1 values were slightly incorrect. In consequence, an additional compensation of the target position was applied, based on a linear interpolation of positions between the vertical and horizontal configurations, determined thanks to spirit level adjustments; this correction proved to be accurate at $\pm 0.1^\circ$.
- Another strong mechanical constraint due to unbalanced weight is undergone by the rotating ring, especially when both the camera and the screen are in place, the screen being much heavier.

This constraint caused two problems: a bending of the ring visible when observing images of the screen at different platform inclinations, and jolts in its rotation movement.

To avoid the flexing, rigid bars were fixed on the ring itself; the relative position, the material and dimensions of these bars were determined based on a compromise between mechanical and disturbance criteria (prevention of internal reflections). Aluminium bars of dimensions 5×3 cm (cf. Figure 3.10) were positioned in a parallel to the triangular screen's symmetrical axis, both at 65 cm from the device's central axis (sample rotation axis). On the other hand, to ensure smooth movements of the ring, counterweights were placed on both sides of the camera.

Finally, to reduce internal reflections as much as possible, a black paper of velvet appearance (named "velvetine") was stuck up on all internal surfaces: its light reflection factor lies underneath 1%.

3.2.3 Light source

Although replaced later with a more efficient source, the light source installed for the sun simulator (Rhyner et al., 1991) was used during an important phase of development of the device and even for a substantial set of BTDF measurements. It consists of a short arc discharge lamp (OSRAM 2.5 kW HMI metallogen light bulb), which combines high luminous efficacy (96 Lm W^{-1}), a spectrum consistent with daylighting analysis (see Figure 3.7) and of color temperature 5600 K. Its optical system is made of a spotlight projector, characterized by a hyperbolic mirrored reflector, a Fresnel front lens and a supplementary conic optical element, to improve beam light collimating and illuminance uniformity on beam cross-sections. The light source is located 6.5 m above the main platform of the goniophotometer, which thus determines the distance from the source to the sample.

Illuminance $E_1(\theta_1)$ in Equation (2.1) has to be uniform over the whole section of the fenestration material sample for a given incident angle θ_1 . This was checked by moving an illuminance meter over the concerned region. To account for the relative temporal fluctuations of 2% to 6% observed for the light source, the results were normalized with the simultaneous measurements of a second sensor, that was fixed. The resulting standard deviation in illuminance was found equal to 1.8% in relative terms.

The large distance separating the source from the sample compared to its size and cross section reduces the effect of inverse-square law (Bouguer law) on the sample illuminance: the maximum relative deviation reaches 3.7% for a movement from horizontal to fully vertical. This result

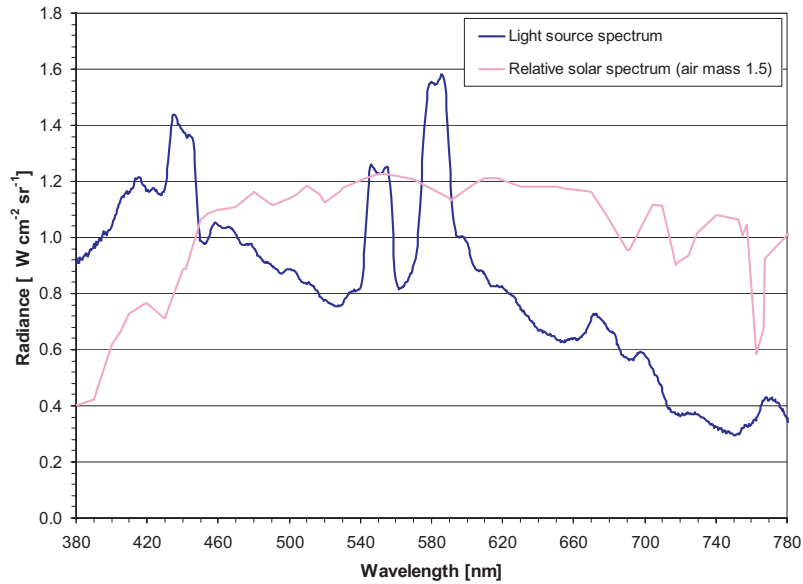


Figure 3.7: Spectral characteristics of light beam emitted by the HMI discharge lamp with Fresnel lens and comparison to the solar spectral distribution (air mass 1.5, divided by a factor $9 \cdot 10^{-5}$ for better display).

revealed an acceptable quality in the sample's illuminating homogeneity and was improved further with the new light source, described in Section 3.4.1.

As the light beam collimation has a large impact on the measurements, it required a detailed assessment, presented in Section 4.3.1.

3.2.4 Sample holder

The sample holder needs to be designed in order to ensure that the external sample interface remains coplanar with the rotation axis of the main platform for any sample thickness.

A first concept of sample holding system was realized, illustrated in Figure 3.8. To fill in the open gap region around the sample rotation mechanism (visible on Figure 3.5(b)), an opaque disk presenting a squared aperture, laid out according to the rotating frame, was fixed on the inner side of the main platform. The parasitic light infiltrations induced by the inevitable residual space between the platform and the disk were prevented with a light trap fixed around the latter. To control the illuminated area and restrict it to a circular region of defined dimensions (a rectangular area would produce corner effects on the transmission figures), thin opaque square diaphragms of different aperture diameters (10 cm, 17 cm, 24 cm and 30 cm) were made to be easily and precisely set on the sample holder, as shown by Figure 3.8(b).

Unfortunately, the disk and light trap arrangement were making up too large obstacles: light emerging at grazing angles could not reach the projection screen properly, especially for thin samples and large illuminated areas where problematic altitudes θ_2 could start at 75° already.

A new design was therefore imagined and materialized, that would also be compatible with reflection measurements, and installed in place of the former system.

As illustrated in Figure 3.9, this new fixing system sandwiches a thin circular diaphragm between the sample and a rigid mounting piece; the latter consists of a ring with four protruding parts, each one presenting two holes to screw the sample tight. For reflection measurements, the sample is simply placed on the other side and secured with fixing legs of appropriate design. The whole arrangement can then be mounted on the rotating system thanks to the eight large screws placed regularly on the ring. More details about sample mounting can be found in Section A.4.

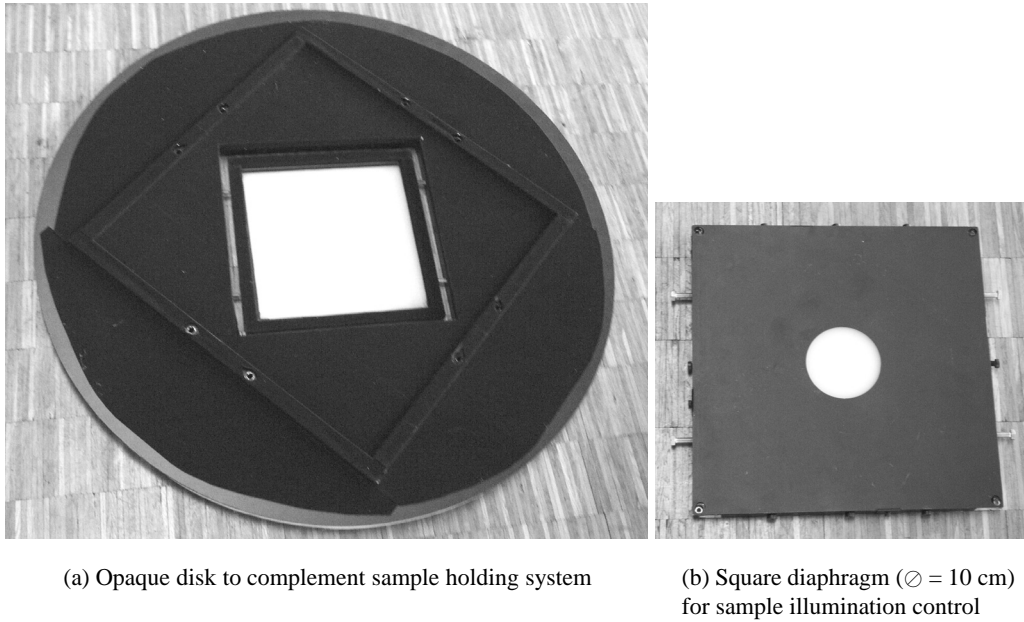


Figure 3.8: Former sample holder components.

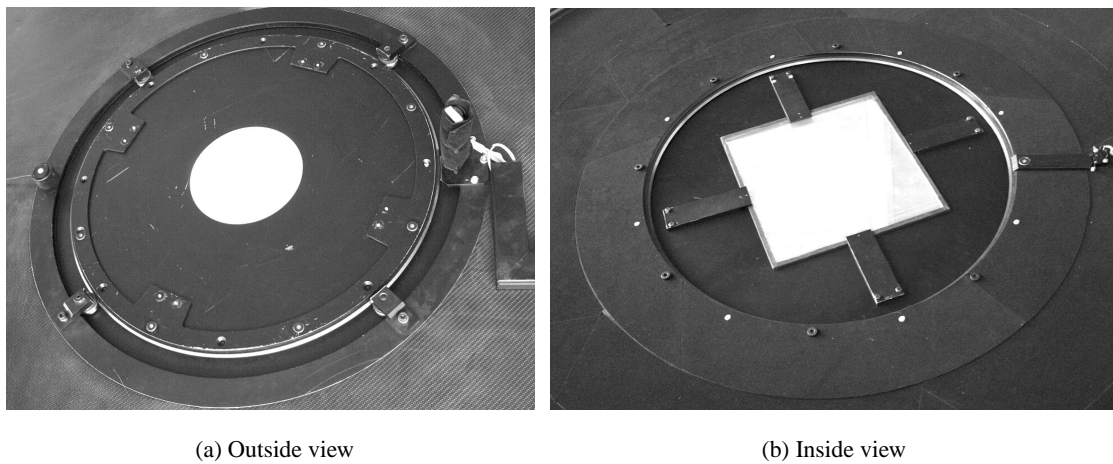


Figure 3.9: Actual sample holder configuration.

This new concept has several advantages: it aligns the sample illuminated plane on the main platform rotation axis for both transmission and reflection measurements and offers flexibility for the sample framing. But above all, it increases the limit altitude $\theta_{2\text{lim}}$ at which a measurement is still reliable to 85° for most sample configurations. A detailed analysis of the emerging angles obstruction is made in Section 4.2.3.

The maximal sample size that can be handled is $40 \times 40 \text{ cm}^2$. Diaphragms of different circular opening sizes (10, 15, 20, 30 cm diameter) are available to limit the illuminated sample surface to a given area. In case of rather homogeneous optical materials with micro-scale physical structures (clear or opalescent glass e.g.), small diameter diaphragms should be used; in case of materials with larger physical structures (solar blinds, louvers, etc.), larger diaphragms must be chosen. This principle applies to any kind of goniophotometric equipment, whatever the measurements.

To avoid edge effects, the diaphragm diameter should be chosen smaller than the sample's dimensions, but significantly larger than its thickness (typically by a factor of 10). Besides, placing

the diaphragm on the external (incident) interface of the sample allows a better control of the possible divergence of incoming rays. Finally, it can be noted that to avoid a direct vision of the light source through transparent or on mirrored samples, the source diameter needs to be larger or equal to the sample surface, which is verified for both sources used for BT(R)DF characterization (see Section 3.4.1).

3.2.5 Diffusing projection screen

As mentioned in Section 3.1, the function of the triangular projection screen is to allow the CCD camera to view the distribution of light emerging from the characterized sample in one of the six hemisphere portions on a single image (each represents a solid angle of $\frac{2\pi}{6}$ steradian). Its geometrical, material and coating properties are described in this section.

Material and geometry

Figure 3.10 illustrates the light detection system. The projection screen consists of a 1 cm thick triangular panel made of FOREX[®] (manufactured by Alcan Airex AG), that is mounted on a 0.9 cm mounting support (honeycomb structure sandwiched between two carbon fiber layers) and covered with a diffusing paint (LMT photometer paint, see below).

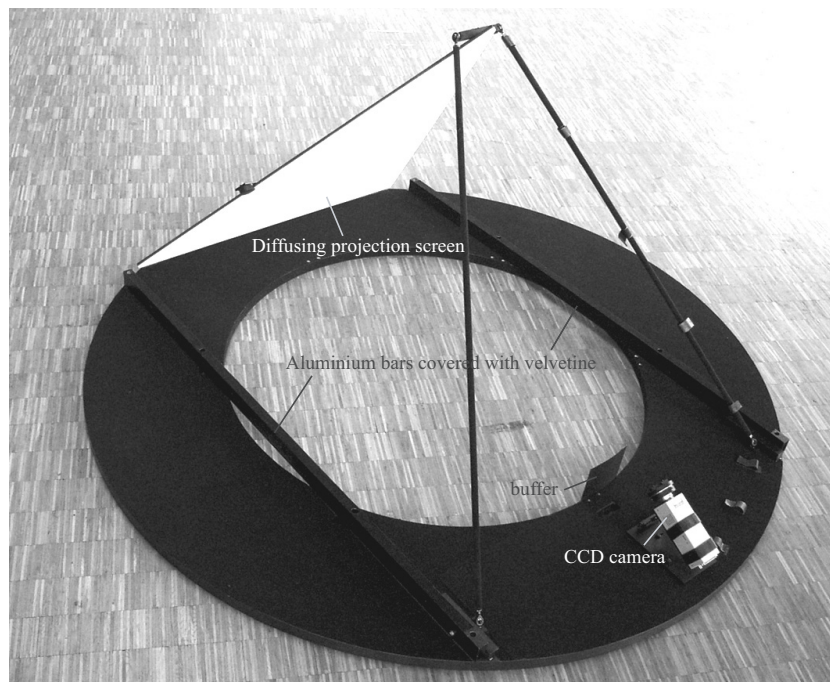


Figure 3.10: Screen and camera facing each other on the rotating ring.

The screen is fixed on the rotating ring opposite to the camera at an inclination angle Θ_0 from the ring plane equal to $\arctan \frac{2}{\sqrt{3}} \cong 49.1^\circ$ by the way of adjustable carbon fiber rods. Its orthogonal projection on the sample plane thus determines an equilateral triangle, as schematized in Figure 3.1(a). To ensure an accurate positioning and tilt angle, tests with a laser beam were conducted as well as plumbline checks to adjust the position of the summit.

The screen itself is an isosceles triangle of dimensions 117.7 cm (base) and 155.6 cm (perpendicular height). It is thus slightly larger than the effective detection area (see Figure 3.11); the latter presents a 115 cm base (= equilateral triangle's edges) and a 152.1 cm perpendicular height, so that the difference in level H between the detection area base and its apex is equal to $152.1 \times \sin \Theta_0 = 115$ cm as well.

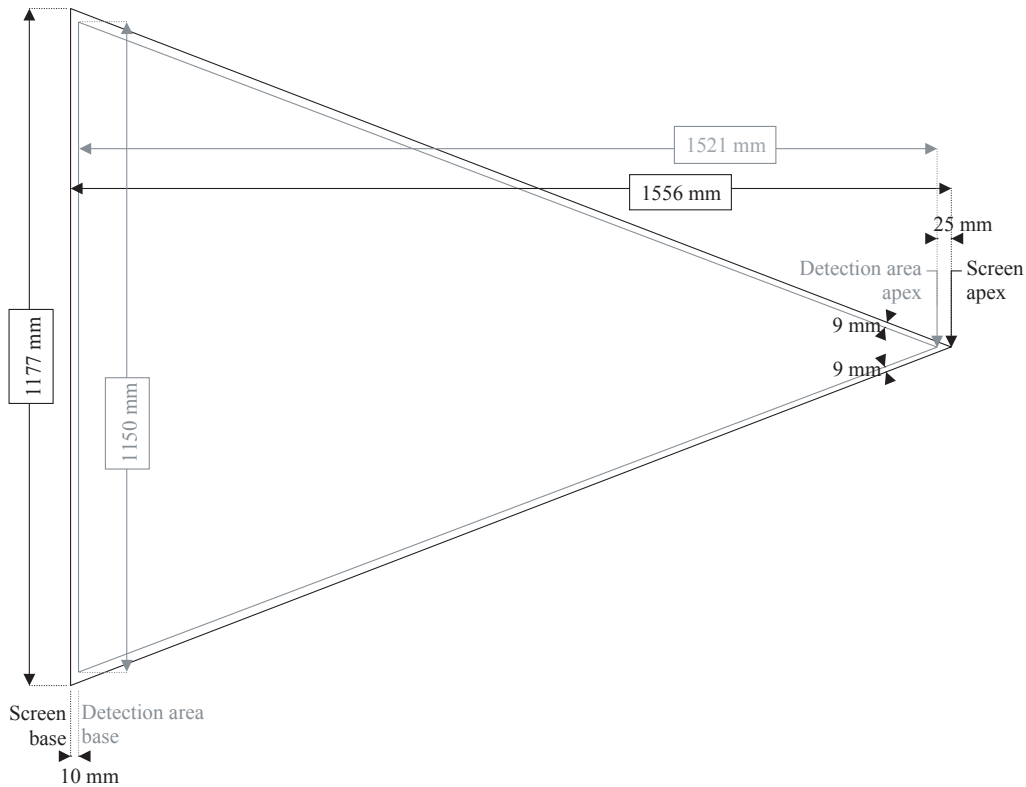


Figure 3.11: Projection screen dimensions vs. detection area.

Coating

The projection screen is covered with a diffusing white paint (LMT Photometer paint PHP 80), made of a mixture of barium sulphate (BaSO_4) and of water-soluble binder; a selected black pigment is added to achieve a spectrally neutral reflectance over the visible range, presenting variations lower than 1.5% as shown on Figure 3.12). The black pigment also reduces the reflectance to between 75% and 85% (depending on the mixture properties), which is consistent with the Commission Internationale de l'Eclairage (1989) recommendations concerning integrating spheres. LMT photometer paints with higher values (e.g. 92%) are also available, but show poorer spectral constancy; the Kodak White Reflectance Coating, considered as well for its high reflection coefficient, was rejected for the same reason; as far as the Spectralon[®] reflectance material from labsphere[®] is concerned, it was unfortunately too expensive to be used for a 1 m^2 triangular panel.

A Minolta CR-200b surface chromameter was used to measure the normal/diffuse reflection factor at different places on the screen: it led to a mean value of 0.749, with relative fluctuations of only 0.2%.

Thereafter, luminance values on the screen surface were measured with a Minolta LS-110 luminance-meter (opening angle $\frac{1}{3}^\circ$) at different emerging angular directions and for several impinging angles α . This allowed to assess the diffusion characteristics of the screen paint, and more specifically to compare them with a Lambertian model (perfect diffusion i.e. constant luminance emitted at all emerging angles for a given incident direction). Figure 3.13 shows the measured luminance distribution compared to the ideal Lambertian model; the observed average and maximal relative discrepancies for usual angles were of 2.6% and 10.6% respectively.

It can be noted that poorer results were obtained for grazing impinging angles (i.e. large values of angle α), where a specular component appeared; this has however no impact on the goniophotometer's performances, as possible impinging angles α on the triangular panel always remain lower than 50° because of the light detection system configuration (see Figure 3.4(b)).

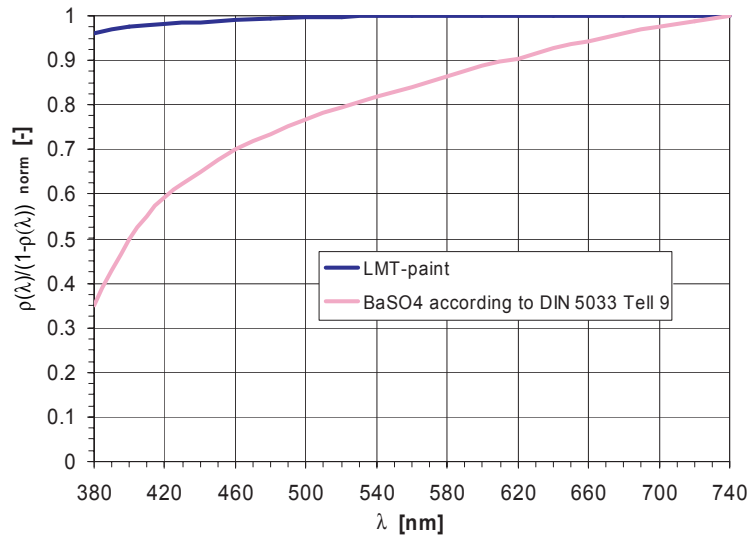
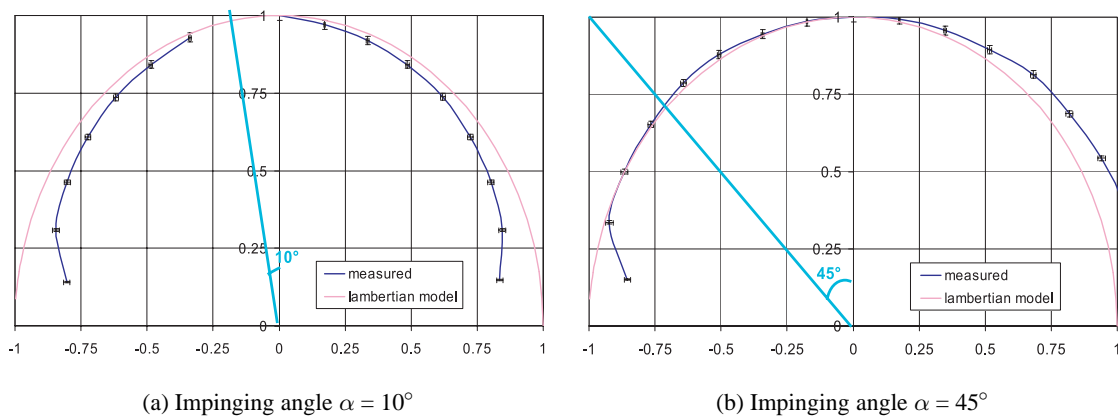


Figure 3.12: Normalized spectral response for the LMT photometer paint PHP 80 compared to a pure BaSO₄ powder (source: LMT Lichtmesstechnik GmbH Berlin (1998)).



(a) Impinging angle $\alpha = 10^\circ$

(b) Impinging angle $\alpha = 45^\circ$

Figure 3.13: Measured luminance distribution due to a reflected light beam on LMT photometer paint vs. theoretical model (perfect diffusion).

As the screen properties can reasonably be considered lambertian, the normal/diffuse and directional/diffuse reflection factors will be equal; they will simply be denominated β_{screen} .

To confirm these observations, a second experiment allowing to assess the screen coating diffusion quality was realized, keeping the luminance-meter at a fixed position and varying the impinging angle α . As the illuminance of the screen decreases according to a cosine law for an increasing α angle, the luminance re-emitted towards the luminance-meter is expected to undergo the same effect if the surface is Lambertian (see Equation (5.5)). The results are reported on Figure 3.14 and show relative discrepancies lower than 1% between the observed and predicted values.

Furthermore, achieving a high diffusion quality allows to avoid problems caused by the sensitivity of the detection device to the polarization state, pointed out by Breitenbach and Rosenfeld (2000) for goniophotometric measurements: as the light emerging from the sample undergoes a diffuse reflection on the projection screen, it is depolarized before reaching the CCD camera (Hecht, 1987).

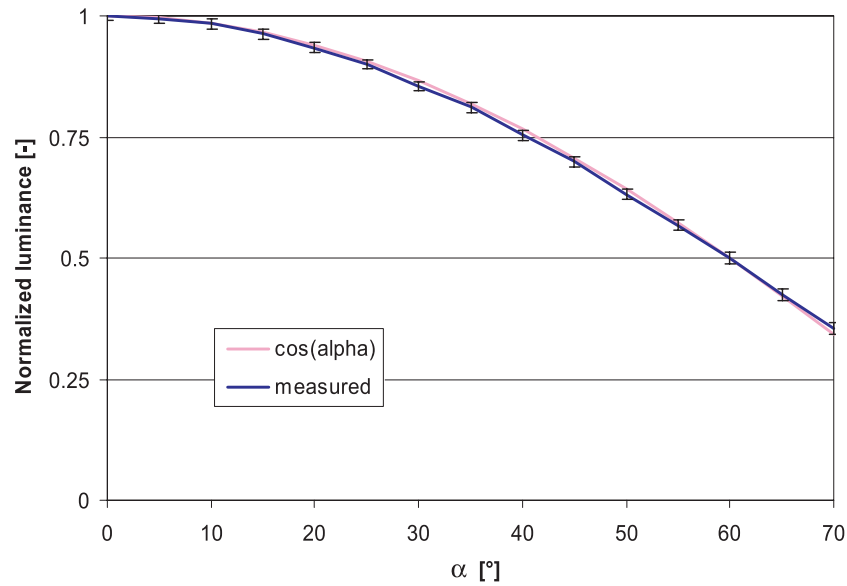


Figure 3.14: Luminance on the screen surface as a function of impinging angle α compared to the expected $\cos \alpha$ law.

3.2.6 CCD video camera

The video camera based on a Charge-Coupled Device (CCD) detector (Kappa CF 8/1 DXCair, 752 x 582 pixels, with Peltier cooling system) is computer-controlled through an ad hoc digital image acquisition and handling software (Image-Pro Plus^{®1}). The latter offers integration intervals comprised between $100\mu\text{s}$ and several hours, a customized adjustment of the signal converter (see Andersen (1998)) and a choice between two gamma values (Ramanath, 2000): 1 (linear response) and 0.45 (the response is a 2.2 power function). As detailed in Section 4.1.2, the latter value for gamma was chosen for resolution optimization reasons.

The camera's optical system is made of a wide-angle lens (6 mm / 1.2, type H0612FI) fixed on a C-mount. The focal length cannot be varied, but the diaphragm aperture can be set manually. Using a variable polarizer to assess the camera's response to the state of polarization showed only a slight sensitivity (pixels greyscale levels only affected by 2% in relative terms), which strengthens the hypothesis that BT(R)DFs are undisturbed by polarization effects.

A special mounting support was designed for the camera and fixed on the rotating ring; to allow a full view of the screen, the camera was inclined 23° regarding the sample plane, as shown on Figure 3.10. A square buffer was placed in front of the camera: it prevents rays entering through the sample aperture from reaching the camera directly and producing glare effects. It was thus positioned in order to limit the camera's view exactly at the detection area's base.

The camera's electric wires are tightened to the carbon fiber rods and exit the light-proof cap through a special slot at its summit (see Figure 3.15). This prevents the rotation of the ring to create problematic unrolling of the wires. As explained in Section 3.4.3, a more complex wiring system will be needed for reflection measurements.

The different calibration procedures necessary to convert this CCD camera into a reliable multiple-points luminance-meter are explained in details in Chapter 4. The additional corrections required to ensure a stable response of the video system and avoid any sensitivity to the room temperature are described in Andersen (1998).

¹Image-Pro Plus[®] The Proven Solution[™], v. 4.1.1.2, Media Cybernetics, L.P.



(a) Camera wires tightened along screen's carbon fiber rods

(b) Exit from conic cap

Figure 3.15: CCD camera's wiring system for transmission measurements.

3.3 Design of the transmission / reflection device

To be converted into a double purpose device, allowing reflection as well as transmission measurements, simply turning over the measurement space is unfortunately not a possible option. On one hand, the incident beam needs to penetrate the light-proof structure in a controlled way to prevent parasitic reflections around the sample. On the other hand, there will be several configurations where the projection screen itself obstructs its path. This section presents the different designs that were considered to overcome these difficulties, and gives a detailed description of the chosen approach.

3.3.1 Physical constraints

As far as possible, the functioning principle on which bidirectional transmission measurements are based is to be maintained for BRDF assessment, including a detection system consisting of a flat diffusing screen towards which a calibrated CCD camera is aiming. The light source is to remain fixed, the incident direction being determined by an appropriate inclination and orientation of the sample through a platform tilt and a sample holder rotation; the sample external interface (on incident side) must stay coplanar with the main platform rotation axis.

A practical and rapid conversion from one mode to the other is necessary. At the same time, the range of possible incident directions is to remain consistent with international standards for bidirectional measurements (see Section B.1), and therefore not be too restrictive as far as angular couples (θ_1, ϕ_1) are concerned. Finally, sample illuminated areas must be appropriate for fenestration systems characterization, i.e. of about 10 cm diameter or more.

To achieve reflection measurements while keeping this particular light detection principle, the incident beam penetration into the measurement space must be carefully controlled, as incoming and emerging light are now on the same side of the sample. As illustrated on Figure 3.16, the illuminated surface must be restricted to the characterized sample area to minimize parasitic light detection; in addition to this, openings in the screen are required to leave the path of the incident beam free, that have to be minimized because they create blind regions where reflected light cannot be analyzed.

3.3.2 Pre-design concepts

Different concepts were considered and their feasibility analyzed before a final concept was determined and constructed. This section briefly describes former designs for the measurement space envelope and for the projection screen, together with the reasons for their rejection.

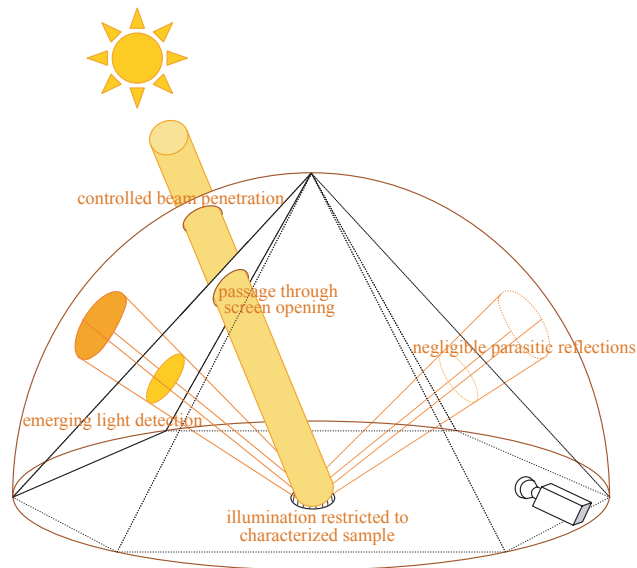


Figure 3.16: Schematic representation of the constraints imposed for bidirectional reflection measurements.

Measurement space envelope

To adapt the measurement space envelope for a controlled incident beam penetration, several designs were first considered:

- A hemispherical cap made of highly absorbing interior surface, consisting of two half hemispheres joint to the main platform. The gap between them supports a non-rigid opaque band (see Figure 3.17); this band presents an aperture remaining fixed in front of the light source for any tilt angle thanks to a system with motorized indented wheels. Using a hemispherical cap allows keeping a constant aperture area, but induces important parasitic reflections for non-normal incident directions as the apparent sample area decreases; furthermore, this system adds up several mechanical difficulties in transmission mode, as the sample is no longer in a clear environment.

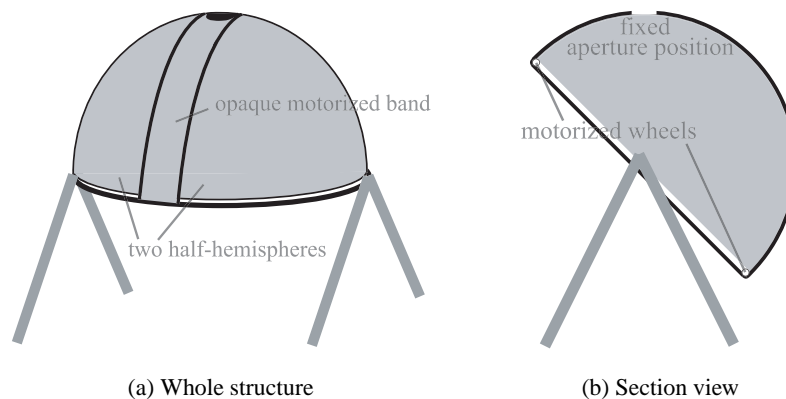


Figure 3.17: Concept with hemispherical cap and revolving band.

- An adaptation of the original conic cap by removing a band along one of the cone's generatrices and adding a tilting panel for the incident light control (see Figure 3.18). This cumbersome system needs both the missing band to be filled in and the tilting panel to be removed for transmission measurements; besides that, parasitic light remains difficult to handle.

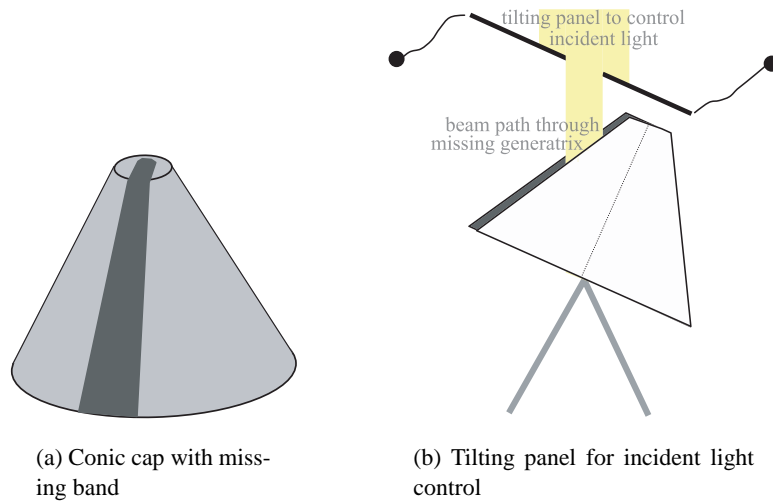


Figure 3.18: Concept with modified conic cap.

- A hemispherical cap with a missing band on a quarter circle (Figure 3.19(a)), fixed on the main platform. This cap is combined to a strip secured to the goniophotometer's support (therefore fixed in space) that restricts the incident light penetration to its unique circular hole, placed in front of the source. Protection against parasitic light between the strip and the cap is ensured by a rail equipped with brushes. The motionless strip can either be fixed on a horizontal ring that surrounds the goniophotometer (Figure 3.19(b)), stand on the floor

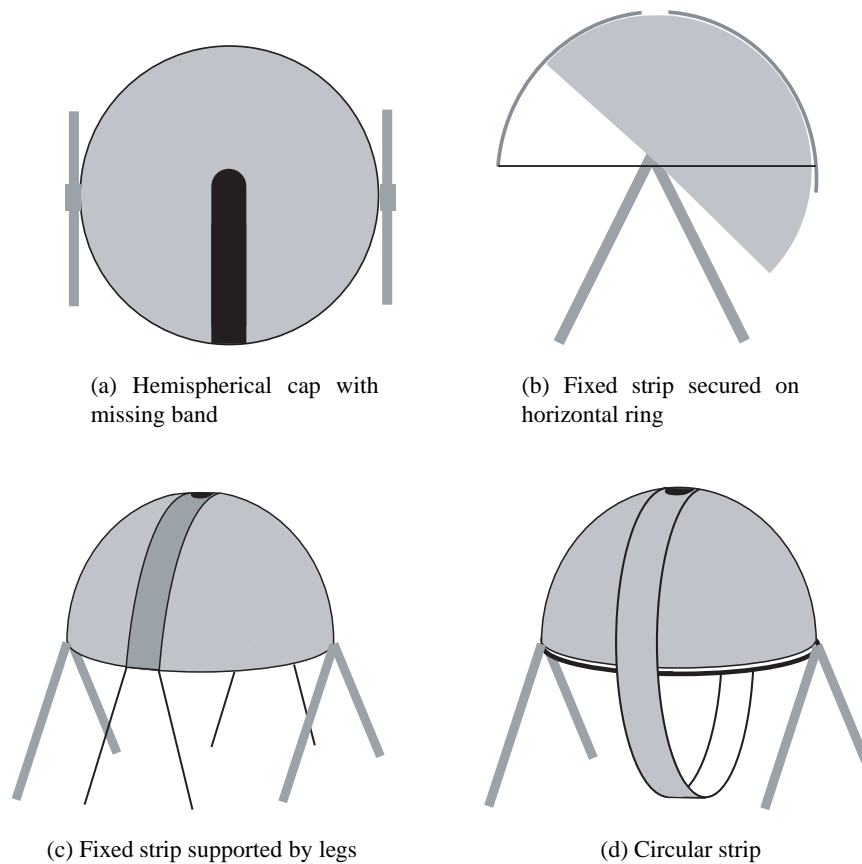
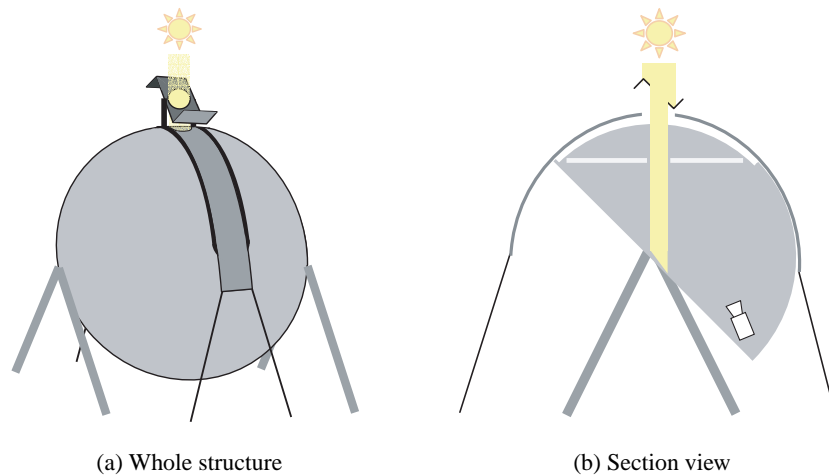


Figure 3.19: Concept with hemispherical cap and (hemi)-circular fixed strip.

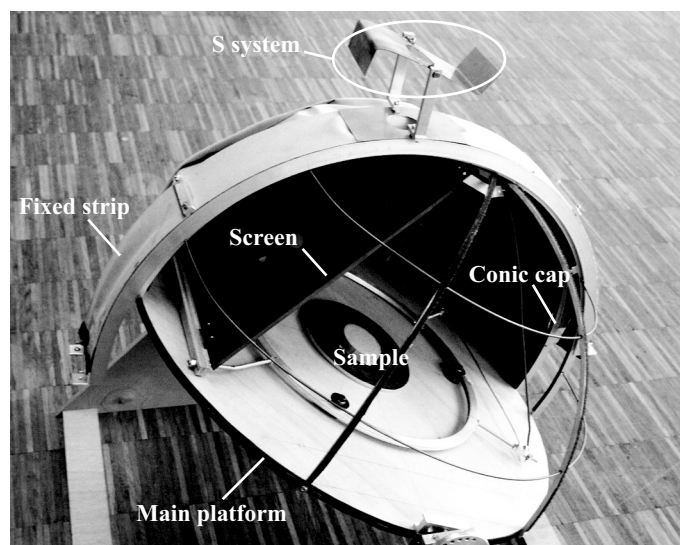
thanks to supporting legs (Figure 3.19(c)) or make up a complete circle (Figure 3.19(d)) to avoid any parasitic light penetration for grazing angles. This option, like the previous ones, unfortunately induces increasing parasitic reflections around the sample for larger θ angles, the penetration aperture being of fixed dimensions; besides, it requires the strip to be removed for transmission measurements in order not to restrict possible sample dimensions, which makes it impractical.

- A concept similar to the one of Figures 3.19(a) and 3.19(c), yet with a fixed strip surmounted by a tilting “S” system (see Figure 3.20(a)). This system allows to restrict the impinging beam to the apparent surface of the sample exactly (Figure 3.20(b)): the circular aperture, of same diameter as the sample, remains always parallel to the main platform (i.e. the sample plane), allowing to obstruct any light out of the sample’s apparent surface. A scale model of this design, shown on Figure 3.20, was realized for a more detailed feasibility analysis in combination with the projection screen concept. Unfortunately, the handling of the fixed strip, that still needs to be removed in transmission mode, remains impractical. Besides, the simultaneous orientation of the “S” system would require an additional robotic device, as a purely mechanical structure (e.g. relying on jointed rods) was unworkable in practice.



(a) Whole structure

(b) Section view



(c) Mock-up

Figure 3.20: Concept with hemispherical cap, fixed strip and “S” system.

Projection screen

The main objective for the design of the projection screen was to avoid any obstruction of the impinging light beam (for all screen positions and tilt angles), while minimizing the blind zone created for the camera by the removed part of the screen. As a consequence, the following solutions were considered:

- A first concept, illustrated in Figure 3.21(a), consisted of a screen transparent to incident light but diffusing on its other face; it had to be put aside for lack of an adequate material, despite its unique advantages of avoiding a blind zone while allowing continuous incident altitudes θ_1 (except for a necessary step after normal incidence, see Figure 3.21(b)).

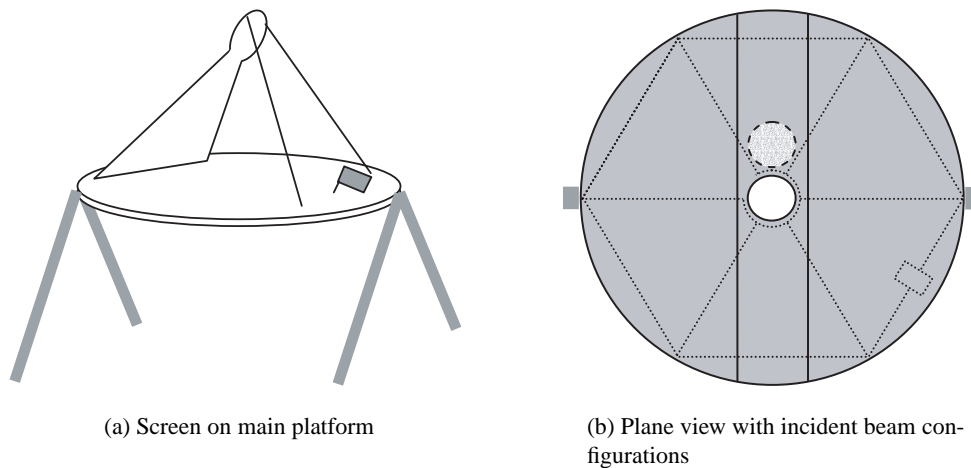


Figure 3.21: Transparent-diffuse screen option with elliptic piece at the summit.

- A screen with flipping parts was considered, creating a path for the impinging beam along the edge between two adjacent screen positions (Figure 3.22(a)). Such flipping movements are, however, difficult to realize from a mechanical point of view; furthermore, unless many small flipping panels are used (which increases the number of flipping components and joints), it induces an important loss of information (blind zone). Another variant would be to have a screen where the missing central part consists of a set of small retractable strips that can be arranged to create an opening of approximate dimensions (Figure 3.22(b)); at the same time, the numerous joints inevitably induce a loss in diffusion quality.

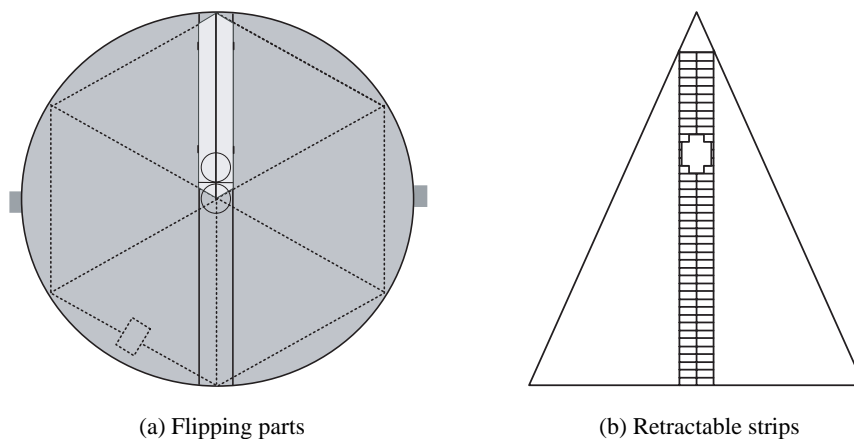


Figure 3.22: Screen parts flipped over or retracted for incident light passage.

- A third option consisted of a screen supporting a perforated band, movable over the central screen area thanks to an unrolling system fixed on either side of the screen (Figure 3.23). A quasi-continuity in altitude angles is in consequence possible (except around normal incidence because of the obstruction created by the band's stretch), but as the opening is of fixed size, it must be dimensioned according to the largest required path for incident light, which induces an important blind zone. Another problem was the diffusion quality difference between the screen surface and the unrolling band.

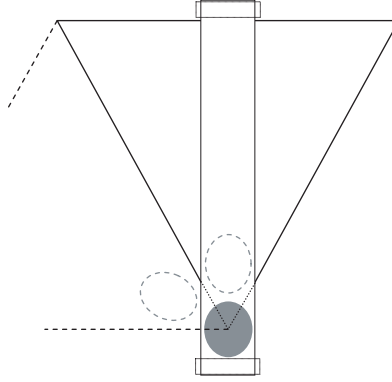


Figure 3.23: Screen with unrolling perforated band.

3.3.3 Final concept

The final design of the envelope is similar to the concept illustrated in Figure 3.17, except that a motorized unrolling system, as shown on Figure 3.23, was preferred to a revolving strip. This allows to limit the strip's arc to a quarter circle only, a rolling mechanism being placed at each end; the main platform is therefore free of any element requiring laborious handling when switching to transmission mode. The unrolling of the synthetic strip determines the position of the circular aperture, of diameter equal to the sample's and facing the light source for any θ_1 angle.

As a hemispherical geometry of the envelope is in fact only necessary to support the strip's arc (i.e. on a quarter circle), it was decided for cost savings reasons to adapt the existing conic cap instead of constructing a whole new hemispherical envelope. Practically, as detailed in Section 3.4.2, additional carbon fiber parts were added on the existing envelope, strengthened with a supporting frame used as the structural base for the beam control device.

In order to control precisely the illuminated sample area and thus minimize the parasitic reflections and blind zone, a metal sheet was fixed on the supporting frame underneath the moving strip. It was perforated with a set of elliptic openings of dimensions given by the apparent sample surface (accounting for tilt angle θ_1) and of corresponding positions on the quarter circle arc. It serves as well as a gliding support for the motorized strip as for the final "shaping" of the beam impinging on the sample surface.

Such a system unfortunately restricts the possible altitude angles θ_1 . Yet, as none of the former projection screen concepts could be retained, a principle based on individually removable screen parts was developed, that also asks for a discretization of possible incident altitudes. It became therefore irrelevant to keep the flexibility in θ_1 a priority for the light beam penetration system.

The projection screen concept relies on the removal of elliptic covers by a robotic mechanism (this system is described in more details in Section 3.4.4). The ellipses' dimensions were again determined by the apparent sample area accounting for angle θ_1 , yet this time projected on a surface oblique to the sample plane with tilt angle $\Theta_0 \cong 49.1^\circ$.

The main advantage offered by this option compared to the former ideas is that the induced blind spot can be exactly reduced to the light beam's area, which allows a minimal loss of information on the emerging light distribution. Of course, a blind spot only appears for one of the six screen positions, except for normal incidence where the tip needs to be removed for all of them.

As an overlap of two successive light beam openings is to be ruled out for the metal sheet as well as for the projection screen, the sample size needs to be limited. As a matter of fact, the optimal combination of altitude step $\Delta\theta_1$ and sample diameter D are determined on one hand by the device's geometry itself, and on the other hand by the minimal illuminated area required for advanced fenestration systems or coating materials characterizations. Obviously, as a larger diameter D calls for a coarser resolution in θ_1 , a compromise was necessary.

The distance from the ellipse at normal incidence ($\theta_1 = 0^\circ$) and the next one ($\theta_1 = \Delta\theta_1$) on the projection screen (closer to the sample than the metal sheet) being the most critical, it is the one chosen for determining the minimal step in altitude $\Delta\theta_1$ and the maximal diameter D for reflection measurements. In this case, their relation can be deduced from trigonometric considerations, leading to Equation (3.1) where d_\perp is the minimal distance between the sample center and the screen plane:

$$D = 2d_\perp \cdot \frac{\tan \Theta_0 - \tan(\Theta_0 - \Delta\theta_1)}{\frac{1}{\cos \Theta_0} + \frac{1}{\cos(\Theta_0 - \Delta\theta_1)}} \quad (3.1)$$

Considering different intervals $\Delta\theta_1$ (1° , 5° , 10° , 12° , 15° , etc.) and calculating the corresponding values for D , it appeared that to allow sample diameters of at least 10 cm, the step in altitude had to be greater than 6° to ensure a (minimal) 1 cm margin around the theoretical elliptic shape. For practical applications, the more standard step in θ_1 of 10° was chosen, associated to a 15 cm diameter for the sample. It was verified that for such conditions, the first elliptic cover after the tip ($\theta_1 = 10^\circ$) would be entirely comprised inside the physical screen (the panel would consist of totally separate pieces for a larger one).

The functioning principle is illustrated by the sequence of images given in Figure 3.24. Once its applicability in practice was verified, the new components were designed and constructed.

3.4 Modification of components

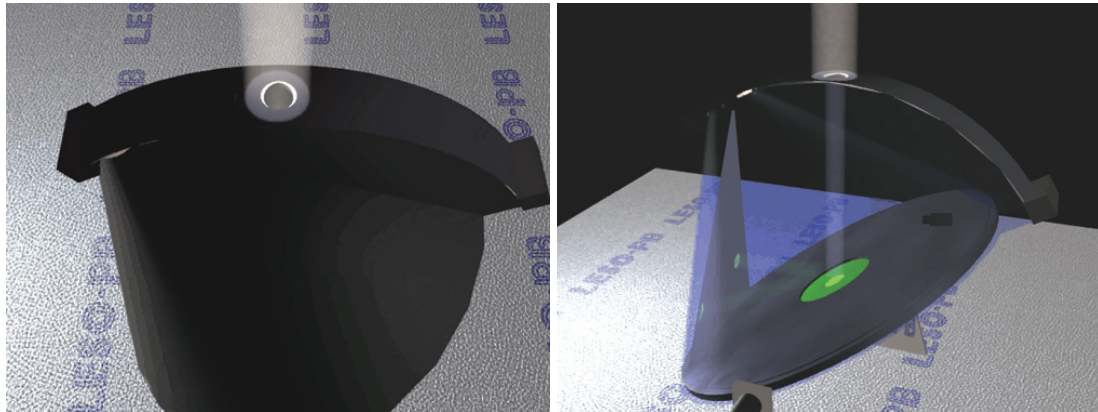
Although the CCD camera and the basic mechanical structure are identical for BTDF and BRDF assessments, several components had to be altered or replaced; this section presents these modifications as well as the design of the new elements.

3.4.1 Light source

As mentioned in Section 3.2.3, the HMI 2.5 kW spotlight projector used during the first phase of the goniophotometer's development had to be replaced by a more efficient light source for the novel device.

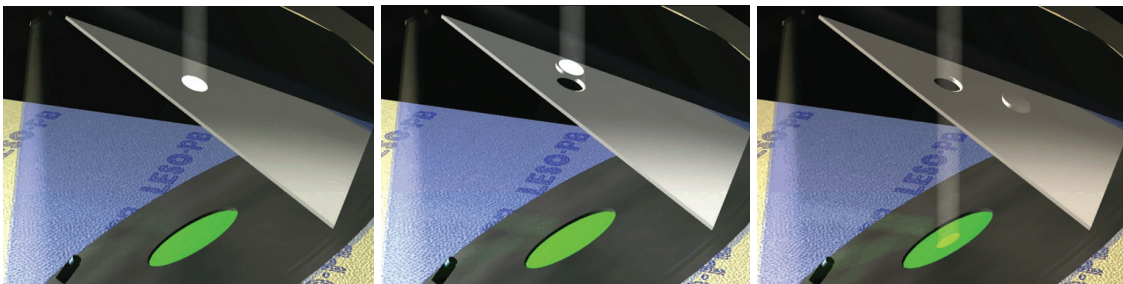
The main factors influencing the choice of the new source were of three kinds:

- a high illuminance uniformity over the sample area had to be reached;
- the blurredness around the sample (due to the impinging beam's control by elliptic apertures) had to be minimized;
- the sample illuminance had to be maximized in order to increase the signal to noise ratio.



(a) Mobile strip hole over adequate elliptic opening

(b) Controlled illumination of sample surface



(c) Obstruction by screen

(d) Lifting of screen cover

(e) Removal from beam path

Figure 3.24: Control of incident beam penetration and path through obstructing screen.

Source model selection

Before opting for a wholly new light source, a conversion of the existing one to verify the above criteria was attempted.

Although showing a good illuminance uniformity over the sample area for transmission measurements (1.8% standard deviation), a strong blurredness was observed around the sample when adding an elliptic aperture at 1.5 m from the sample to control the impinging beam (the 1.5 m distance was determined by the device's geometry, see Section 3.4.2). This effect was caused by the fact that the distance from sample to hole (1.5 m) was too large compared to the hole to source distance (5 m).

To quantify blurredness, the relative difference between uniform area and full spot size was used, illustrated in Figure 3.25(a). To delimit the full spot, the group of all pixels brighter than the minimal greyscale level for which they were still adjacent was considered. Within the blurred region, illuminance values grow from zero to the value at which a sufficient uniformity is achieved (detailed on page 45); it is thus responsible for parasitic reflections around the sample area.

Unfortunately, when placing the goniophotometer further away from the source in order to reduce blurredness, the illuminance measured on the sample plane decreased in a dramatic way, as shown by Figure 3.25(b). Keeping the existing light source was therefore excluded.

To proceed to an optimal choice of the light source, an in-depth study of the relation between the beam properties and the required accuracy for the quantities implicated in a BT(R)DF assessment was achieved.

The illuminance reached on the sample plane has a direct impact on two parameters: on one hand, it affects the relative error on the lowest detectable screen luminance (limited by the cal-

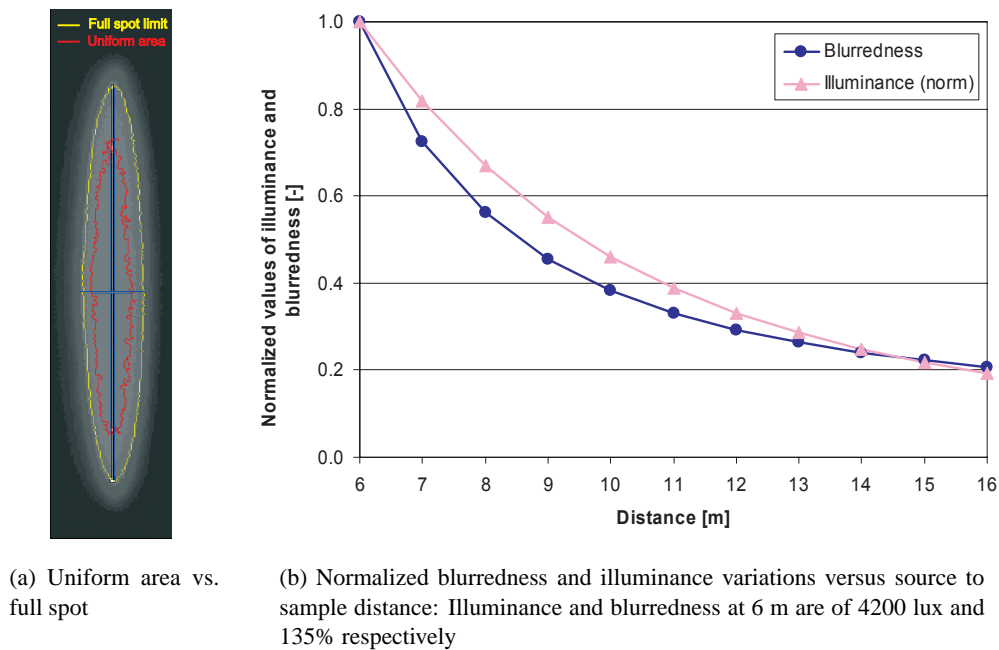


Figure 3.25: Sample plane illumination study for the HMI 2.5 kW spotlight.

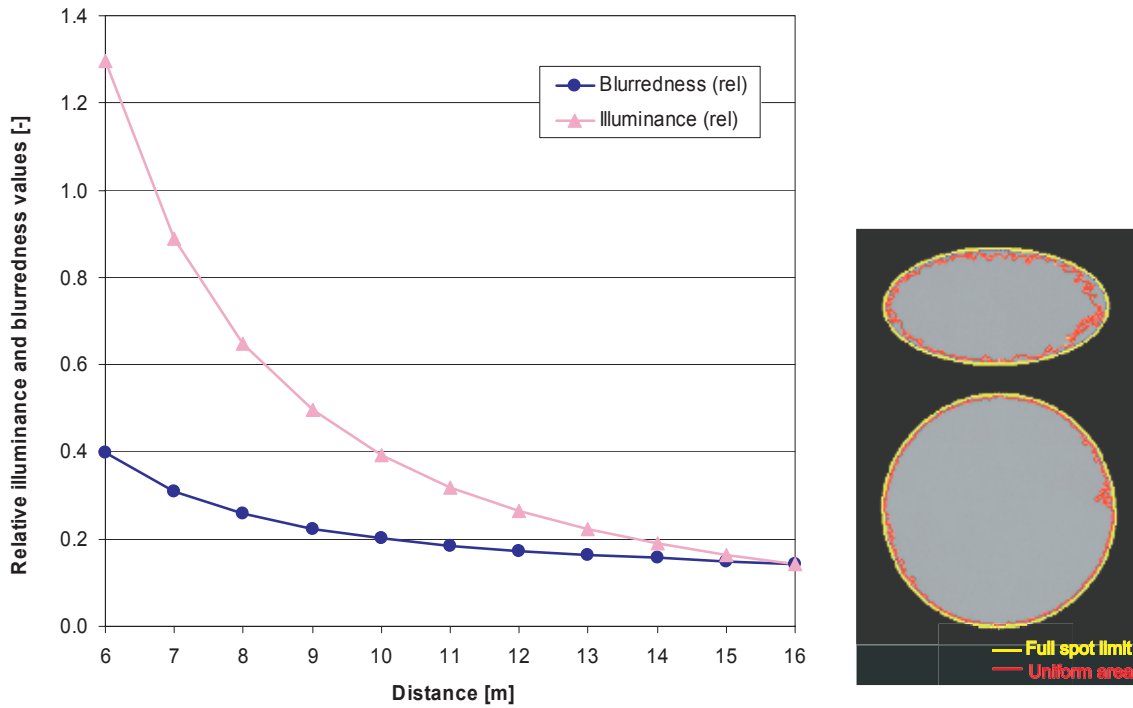
ibration instrument itself, see Section 4.1.2); on the other hand, it determines the threshold of observable BT(R)DF values. At the same time, it is itself determined by the source intensity and by its distance to the sample, primarily responsible for the blurred region around the sample.

Several types of light sources placed at various distances from the sample were thus analyzed; their performances were assessed against these different criteria. Amongst them, two stage followspots were retained because of their improved performances compared to the HMI 2.5 kW spotlight:

- The model “Canto 1200msr” (1.2 kW) comprises a discharge lamp combined to a glass reflector and twin condenser lenses, a zoom optical system and a dimming unit. It produces a uniformity in illuminance similar to the HMI 2.5 kW spotlight, a significantly lower blurredness (factor 2.5) and only slightly higher sample illuminance values (Figure 3.26(a)), still insufficient for accurate BT(R)DF assessment.
- The model “Aramis 1013” (HMI 2.5 kW, 4.5/8° zoom) is equipped with an OSRAM discharge lamp (5600 K, 240 kLumens) combined to a quartz condenser and a full dimmer. It produces more than sufficient illuminance values and a reasonably low blurredness (see Figure 3.26(b)); it was unfortunately too expensive to be retained.

A third stage followspot was therefore considered, fulfilling the expectations in a satisfactory way: the model “Korrigan 1011+” (HMI 1.2 kW, 5/9° zoom) illustrated in Figure 3.27(a). It shows characteristics close to the “Aramis” model (optical system, dimmer, color temperature) while providing a more focused beam, thus reaching sufficient illuminances even though twice less powerful; its characteristics are explained below.

The optimal distance, lens aperture and iris opening were determined by an extensive study of the blurredness and illuminance level variations; an analysis result example is shown on Figure 3.27(b). This study led to the following settings: distance 10.3 m, lens aperture $\phi 10'$, fully open iris, 100% dimmer.



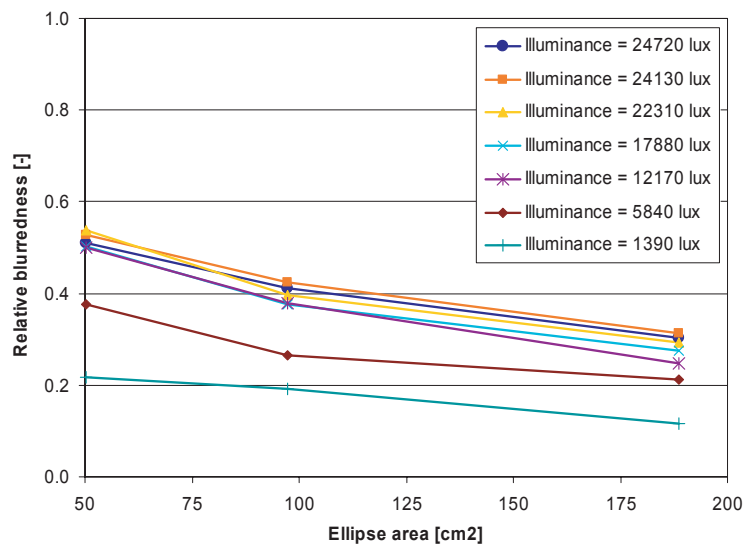
(a) Relative blurriness and illuminance variations for “Canto” 1.2 kW followspot, compared to HMI 2.5 kW spotlight data (Figure 3.25(b)): Illuminance and blurriness at 6 m are respectively equal to 5500 lux and 54%

(b) Uniform area vs. full light for “Aramis” 2.5 kW followspot

Figure 3.26: Sample plane illumination study for two followspot models.



(a) “Korrigan” 1.2 kW followspot



(b) Blurriness as a function of the elliptic opening’s area, for different illuminance values (relative to HMI 2.5 kW spotlight data: blurriness varies between 15% and 70%)

Figure 3.27: Light source chosen for the BT&RDF goniophotometer.

Incident beam properties

The incident light spectrum is quite close to the HMI 2.5 kW spotlight, as both lamps are of discharge type: it is given in Figure 3.28. The achieved illuminance uniformity over the sample area was checked with the same experiment as for the former source. Average variations of 1.4% were observed in relative terms; they remained below 2% for grazing angles.

As far as light beam collimation is concerned, its important influence on BT(R)DF values asked for a detailed analysis, presented in Section 4.3.1.

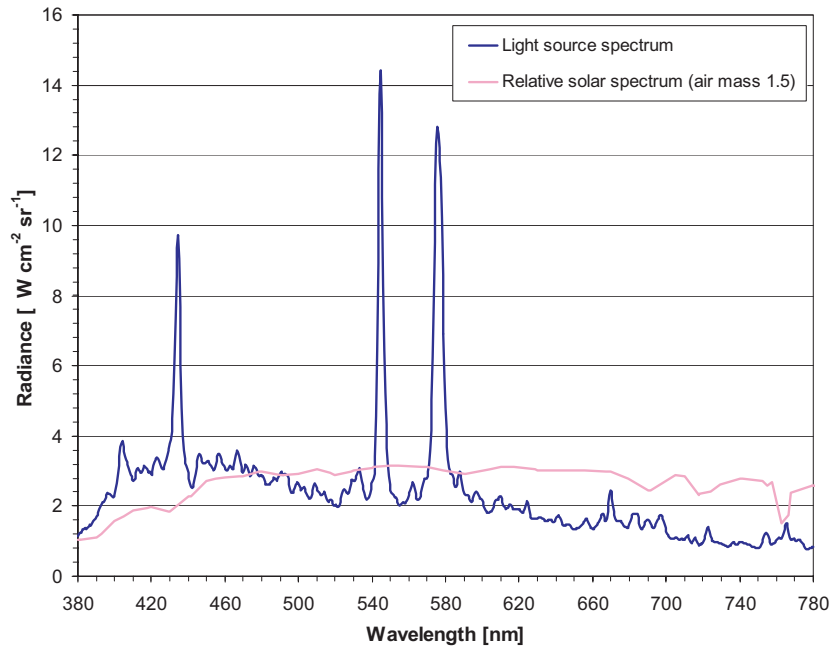


Figure 3.28: Spectral characteristics of the HMI 1.2 kW “Korrigan” light source and comparison to the solar spectral distribution (air mass 1.5, divided by a factor $3.5 \cdot 10^{-5}$ for better display).

Sample illuminance measurement

During a BT(R)DF characterization, the sample illuminance is measured simultaneously with each image capture to associate an accurate value of $E_1(\theta_1)$ to it. This is achieved thanks to an external luxmeter (LMT, Pocket-Lux 2B, illuminance range from 0 to 20,000 lux, converted in a voltage from 0 to 10 V), connected to a data acquisition card (NI-DAQ, PCI 1200).

By ensuring an optimal simultaneity between image exposure period (integration interval) and sampling of illuminance data (averaged into a single value), a high accuracy in the $E_1(\theta_1)$ value corresponding to a given image can be reached. It also allows to account for the slight temporal light source fluctuations, lower than 1%.

In the former design of the goniophotometer (transmission only), the luxmeter was placed on the edge of the sample holder, as can be spotted on the left-hand side of Figure 3.9(a). It was therefore almost coplanar to the sample but shifted from its centre, the shifting effect being corrected.

For reflection measurements, however, keeping the sensor next to the sample requires to move it at each characterization mode change (or to have a second one on the other side), which is highly impractical. On the other hand, it asks for an enlargement of the illuminated area beyond the actual sample surface to light up the sensor properly; this creates unwanted parasitic reflections and induces an avoidable loss of information due to the larger blind spot (screen hole).

In consequence, it was decided to mount it on a static vertical rod fixed on the goniophotometer's structure, as shown on Figure 3.29. This unique luxmeter can be used for both transmission or reflection measurements equivalently; one only needs to determine the correction factor to apply for compensating the luxmeter's position (both closer to the source and shifted from the central beam axis) and the sample plane inclination.

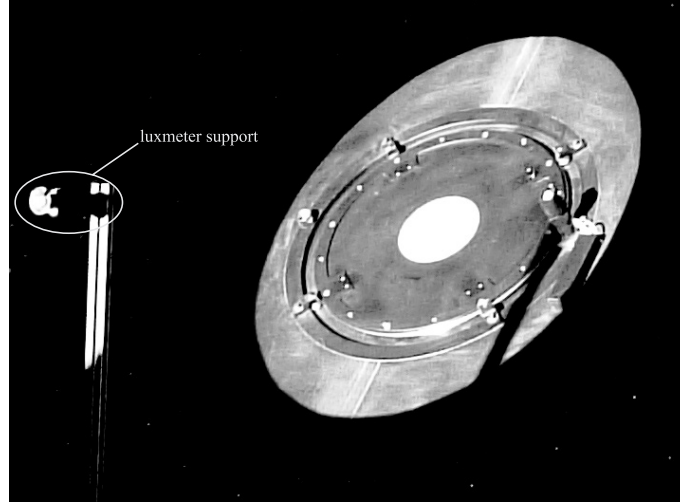


Figure 3.29: Independent luxmeter support for simultaneous illuminance measurement.

Illuminance correction

To establish the relation between the illuminance measured at the theoretical (sample centre) and practical (luxmeter support) locations, a second calibrated LMT luxmeter was positioned right at the sample centre; illuminance values for varying θ_1 angles were then measured with both instruments simultaneously. Their ratio determined the appropriate correction factor, equal to $0.81 \cos \theta_1$.

This experiment also allows to verify the luxmeter's accuracy by comparing the experimentally assessed variation of $E_1(\theta_1)$ to the (ideal) cosine law. The agreement between the two is found to be excellent (average relative difference lower than 1%).

3.4.2 Measurement space envelope

The measurement space envelope for BT(R)DF measurements, shown on Figure 3.30, consists of a carbon fiber cap strengthened by a structural metallic frame; this frame also supports a static stainless-steel perforated sheet, on which a moving synthetic strip can glide.

As mentioned in Section 3.3.3, the incident beam is controlled through one of the cut-out ellipses of the metal sheet, selected by unrolling the synthetic strip to position its circular aperture adequately.

Carbon fiber cap

The carbon fiber conic cap was modified to host the light beam control system. More specifically, as it had to present a hemispherical geometry along slightly more than a quarter circle, the cone was split in two halves separated by a 28 cm gap; vertical parts also made of carbon fiber were added along two of the cone's edges (see Figure 3.31(a)), the gap on the other side of the cone being closed by a flat carbon fiber piece. An access door for servicing was designed as well.

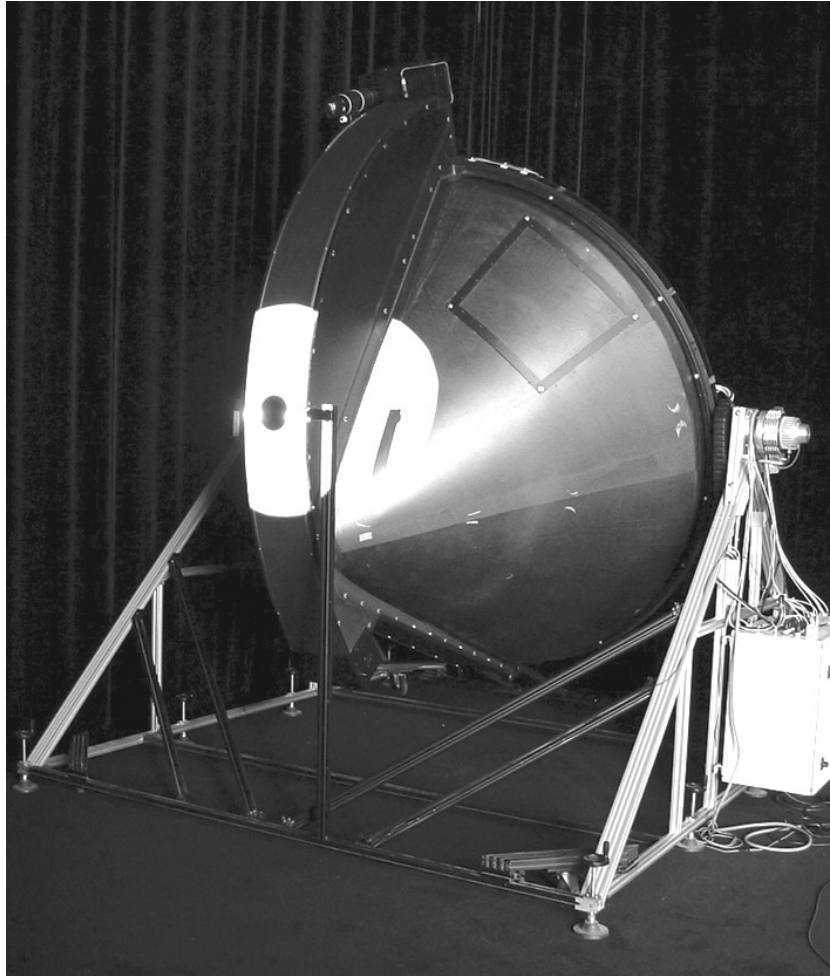


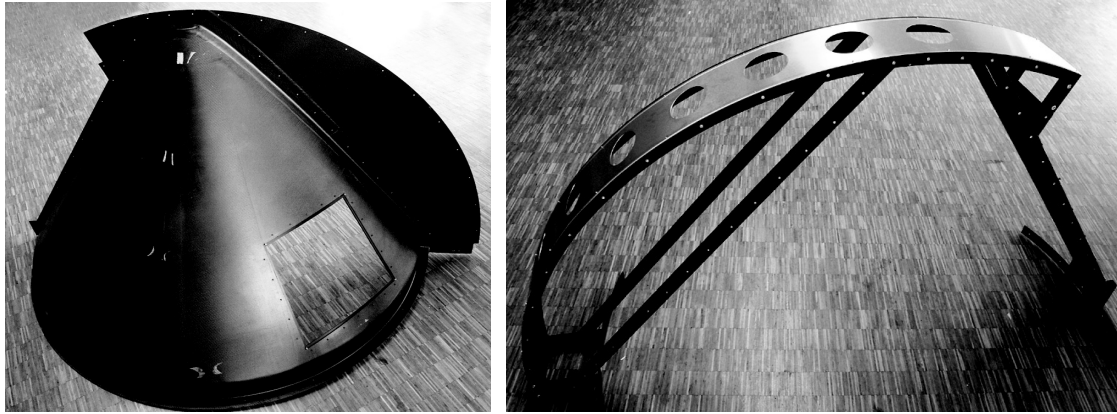
Figure 3.30: Goniophotometer in reflection mode (BRDF assessment).

Quarter-circular support frame

The metallic frame supporting the light control system and joint to the carbon fiber cap was fixed on the main platform itself. It consists of an arrangement of 0.15 cm thick stainless-steel tubes presenting a 4×4 cm square section and painted in black; they make up a curved rail consisting of a pair of structurally stable quarter circle arcs of 154 cm radius, shown in Figure 3.31(b) (details about the frame's geometry can be found in Appendix A). The rail's radius was actually limited by both the rotating ring's dimensions, defining its minimal value (128 cm), and the device's structure height, limiting it to 158 cm.

As the frame is used as structural support for the perforated sheet responsible for an accurate incident beam control, its exact geometry has to be precisely determined after mounting on the goniophotometer platform. This was done by measuring the distance between the sample centre and the external face of the curved tubes every 10° with the aid of a plumbline for exact alignment; the radius was found equal to 154.4 ± 0.1 cm.

However, an experiment conducted with a fixed laser beam pointing at either one of the rails while rotating the structure around the main platform horizontal axis stressed out the fact the rails were also slightly curved sideways, and could make up ± 0.4 cm shifts with a strict vertical plane. As this could not be corrected on the frame itself, it was compensated when fixing the perforated metal sheet, as explained below.



(a) Adapted carbon fiber cap

(b) Metal sheet with cut-out ellipses on support frame

Figure 3.31: Structural components of modified measurement space envelope.

Static stainless steel sheet

The determination of the actual position and dimensions of the cut out ellipses required a multiple stages process for an optimal incident light control:

- First, the theoretical geometric properties of the ellipses were determined based on trigonometric considerations, assuming a perfectly parallel beam reaching an elliptic surface of apparent horizontal axis 15 cm and vertical axis $15 \cdot \cos \theta_1$.
- Then, the ellipses dimensions were adjusted to the real incident beam, of imperfect collimation and thus producing blurred regions around the uniformly illuminated area (see Section 3.4.1), responsible for parasitic reflections. Once the optimal source distance was determined, different elliptic shapes were tried out to compare the achieved sample surface illumination. The most efficient compromise was established between optimal uniformity over the whole sample area and lower parasitic light flux; this was done for each ellipse individually, as more relative blurredness appeared for smaller ellipses. The determined shapes, cut out of cardboard sheets, were tested successfully; they led to only few percent of non-uniformly illuminated sample area while guaranteeing an average relative blurredness area lower than 10%. It can be noted that these remaining parasitic reflections were reduced to a negligible level by adding a ring of highly absorbing material (“velvetine”) around the sample.
- Finally, the positions of the ellipses on the metal sheet had to account for the frame manufacturing imperfections (see above). The metal sheet was thus mounted temporarily on the frame, allowing to centre the ellipses thanks to a plumbline course driven by a progressive platform inclination. Their positioning was thereafter verified by pointing a fixed laser on the central axis and tilting the device to get each ellipse’s centre coincident with the laser spot; this test showed that an appropriate accuracy was achieved (± 0.05 cm deviation). Before sending the metal sheet for cutting out, these positions were adjusted to a flat configuration of the sheet (i.e. to its neutral fiber), to avoid slight shifts due to the sheet’s thickness.

The final positions and dimensions are given on Figure 3.32. The resulting perforated metal sheet is shown on Figure 3.31(b); its inside surface is covered with “velvetine” (reflection factor lower than 1%).

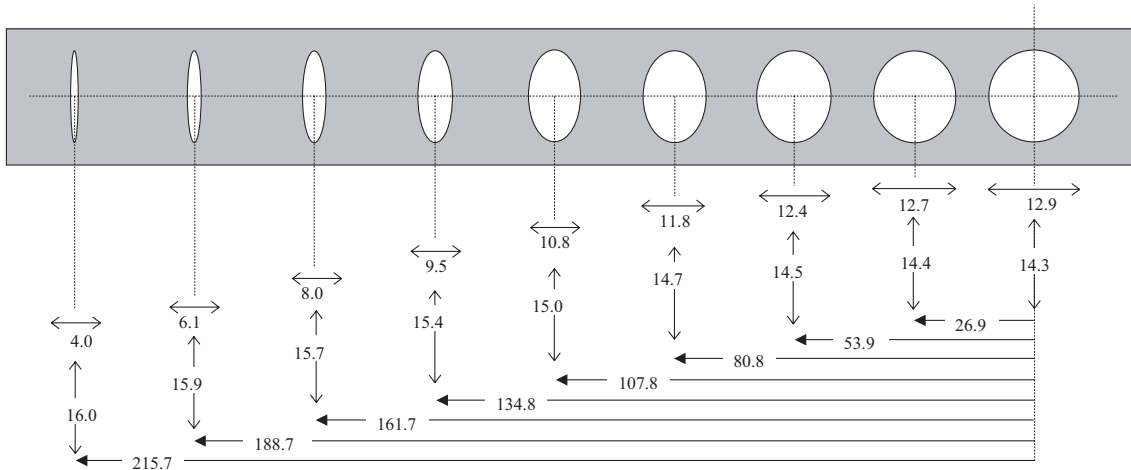


Figure 3.32: Dimensions and positions (in cm) of the elliptic shapes cut out from the metal sheet.

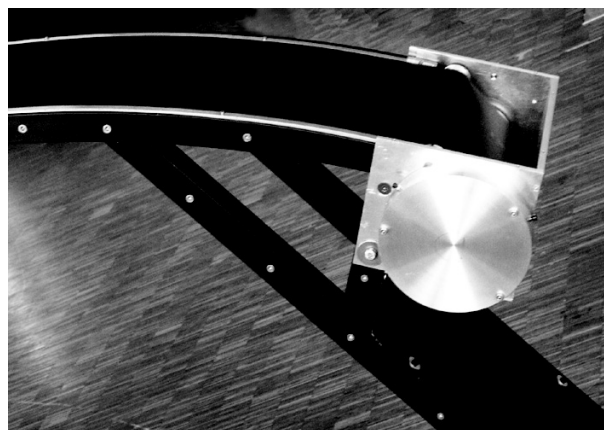
Moving synthetic strip

The role of the synthetic strip is to select the elliptic hole through which the incident light's path will be adequately controlled (according to altitude θ_1); at the same time, it prevents light from entering the measurement space through any other opening. Its unique aperture is therefore circular, slightly larger than the largest ellipse (i.e. the one associated to normal incidence); the chosen 10° step in altitude ensures that a 15 cm diameter hole never overlaps two consecutive entrances.

To automate the positioning of this circular aperture, the strip's gliding movements on its metal sheet support are driven by a motorized winder at one end (Figure 3.33(a)), combined to a spring system at the other (Figure 3.33(b)). Once the spring features ensuring a reliable and smooth unrolling of the strip were defined, the return torque necessary to compensate the induced tension could be measured. The spring and motorized winder cases, shown on Figure 3.33, were designed and fixed to the support frame outside the incident beam path.



(a) Motorized strip winding with opto-sensor for home positioning



(b) Spring system to ensure strip tension

Figure 3.33: Motorized unrolling of the synthetic strip for its adequate positioning on the metal sheet.

This axis is controlled by the external Creonics card already used for the sample holder (second axis in Section 3.2.1). The DC motor drives a non-reversing reduction gear to avoid off-power rewinding. An opto-sensor home switch detects the hole position in the strip (Figure 3.33(a)) and ensures proper positioning of the aperture. Velocity, gains and acceleration parameters are adjusted for efficient but smooth movements of the strip. The relation between motor units and strip movements varies with the strip winding, and thus depends on its thickness; it was determined experimentally for each aperture position and converted into θ_1 degrees for an easier command.

3.4.3 Main platform and rotating ring

The main platform and rotating ring did not require important modifications, their mechanical structure and rotation system being viable for the reconfigured device as well. However, some adjustments of their movements and balance were required, as well as a redesign of the camera's wiring system exit (to which the screen motor cables were added); these modifications are explained below.

Besides, the sample fixation system had to be adapted to reflection measurements too, where the characterized surface (still coplanar to the main platform) is on the other side of the diaphragm. Therefore, special clipping elements were designed for the sample holder's ring, tightened on the four pairs of screw holes visible on Figure 3.9(a). As far as the sample's rotation is concerned, it must be executed in opposite directions whether in transmission or reflection mode, as the referential is inverted (see Section 5.4.3 and Appendix B).

Rigidity, balance and movements

As the ceiling of the dark chamber is not high enough to allow the new source to be positioned at the proper distance (10.3 m) above the sample, it was set up on a large tripod on the floor, at the goniophotometer's horizontal rotation axis height.

The movements of the main platform were adapted accordingly: they were shifted 90° and adjusted to a 180° rotation from one vertical to the other.

The additional weight caused by the support frame and the synthetic strip system requested a mechanical compensation of the strong imbalance sustained by the main platform rotation axle. Counterweights were designed for that purpose, that compensate the torque created by the different massive elements. This torque was first assessed with the help of dynamometers and the necessary compensating weights calculated from these measurements. A pair of 80 cm long, $2\mathcal{F}$ tilted rods capable of supporting lead pieces up to 10×5 kg were constructed and fixed on the edges of the main platform (on its horizontal rotation axis). The achieved balance was confirmed by the very low current necessary to keep the device in place (inferior to 1 A), that was checked at different inclinations.

However, as the exact alignment of all components is crucial for the the incident beam control, the remaining slight weight effect on the main platform positioning asked for a software compensation for optimal adjustment; the correction factors (lower than 0.3°) were determined experimentally using a protractor and a spirit level; they were thereafter checked by observing the light beam centering on the sample surface.

To leave the incident beam passage free of any obstruction for grazing angles, the rotating ring rigidification bars had to be rotated 90° from their configuration in Figure 3.10; however, the projection screen being a lot heavier than for the transmission version (see Section 3.4.4 below), they were no longer capable of avoiding a non-negligible flexing. An aluminium arc was therefore added behind the screen, fixed on the pair of bars. Minimizing the ring's bending is indeed critical because the image of the screen will be shifted if its relative position to the camera is modified.

To ensure a reliable localization of the detection area on the digital images, a screen location procedure was developed, detailed in Section 4.2.1.

For both the main platform and the rotating ring motors, the velocity, gains and acceleration parameters were adapted to the larger inertia (measurement space envelope, counterweights, heavier screen).

Winding cables system

The wiring system shown on Figure 3.15 could not be kept for reflection measurements, because the cables were obstructing the impinging beam path. It was in consequence wholly re-designed to prevent any disturbance of incoming (and emerging) light for all possible tilt angles and screen positions.

The main difficulty is that one end of the cables is static (the one out of the measurement space), while the other rotates with the ring on which the camera and the screen are mounted (both the camera's and screen wagon's wiring systems need to be driven out).

It was therefore decided to exploit the unused space underneath the ring, with one strong constraint induced by its indented belt winding (Figure 3.5(a)) that forbids any movement or additional element in that area.

A first concept comprising a fixed exit from the ring and a rotating entry was considered: an elastic band was used to ensure a controlled course of the protective chain gathering the various cables, steered by curved guiding rails. A simplified model of it was constructed for feasibility study (Figure 3.34(a)).

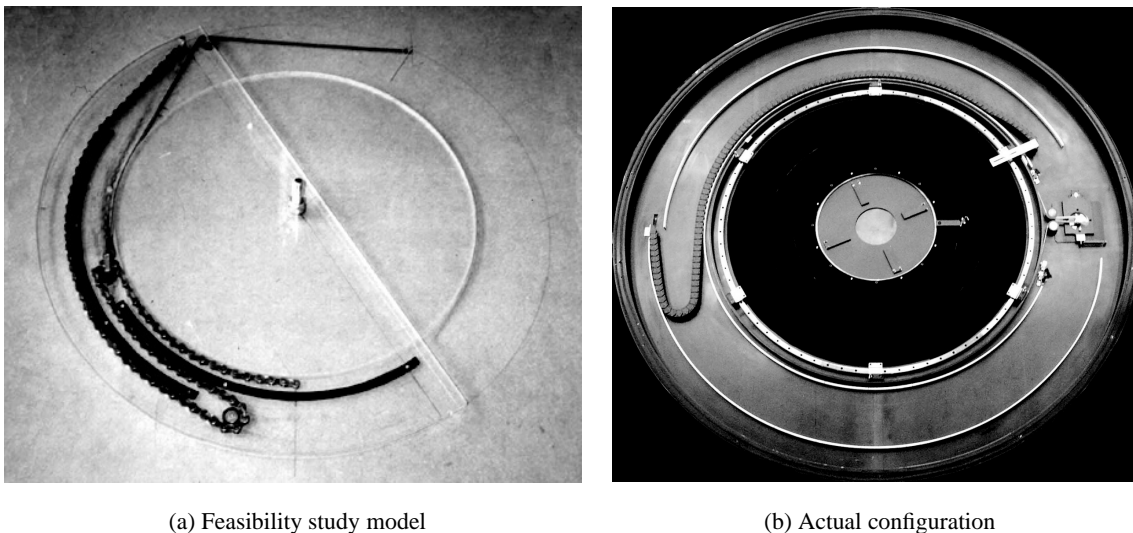


Figure 3.34: Protective chain winding underneath the rotating ring to get the camera and screen cables out of the measurement space.

The final wiring system, shown on Figure 3.34(b), is based a similar principle, but uses an improved chain design to get rid of the many mechanical, wearing and security problems that occur when using an elastic band. The chosen chain only bends on one side (slightly on the other), which allows a good control of its course. To guarantee its free unrolling for any device tilt and prevent it to rub against itself in extreme cases, guiding rails were added, fixed directly on the main platform.

3.4.4 Diffusing projection screen

The dimensions, placement and coating characteristics are the only properties of the projection screen that were kept identical for this new configuration. The modifications concerning the screen materials and its removable covers system are explained below.

Materials and fixing

The screen's lateral parts are composed of a 1 cm thick core in PVC foam (manufactured by Alcan Airex AG), sandwiched between two 0.1 cm aluminium foils.

In a 22.4 cm wide band on the central axis, where the elliptic holes are cut out, aluminium was chosen as the core material, to allow for accurate mechanical processing. This rigid support hosts the various inserts needed for the robotic system and the covers positioning.

The covers themselves consist of a 1 cm thick core of Uniform[®] (POM) (manufactured by BASF Plastics), sandwiched between two 0.1 cm aluminium layers.

The screen side facing the sample is covered with the same diffusing LMT paint as the one used for the FOREX[®] panel for transmission measurements; its detailed reflection characteristics, once the paint applied, were found to be identical as well.

In order to hold the screen in a stable tilted position (of tilt angle $\Theta_1 = 49.1^\circ$), the pair of carbon fiber rods shown on Figure 3.10 could not be kept as they were. Even if fixed elsewhere on the screen edges, the tests realized with the device mock-up (Figure 3.20(c)) revealed that there was always a configuration where they were in the incident beam's path.

Therefore, a special fixing piece of hexagonal shape was designed, shown on Figure 3.35(a). Choosing a polygon instead of a circle allows to keep a flat surface for fixing the motorized wagon rails and is easier to rigidify. At the same time, it avoids any obstruction to the incident beam, as well for normal incidence as for $\theta_1 = 10^\circ$ for all six screen positions. Its shape is however not the one of a regular hexagon: although for mechanical reasons it had to be fixed to the physical screen, its edges had to be based on the (smaller) detection surface dimensions (see Figure 3.11) for the six positions, and were thus adjusted accordingly.

In order to ensure an open sight of the whole screen area from the camera's point of view (see Figure 3.35(b)), one of the hexagon edges was modified for an apex to be added.

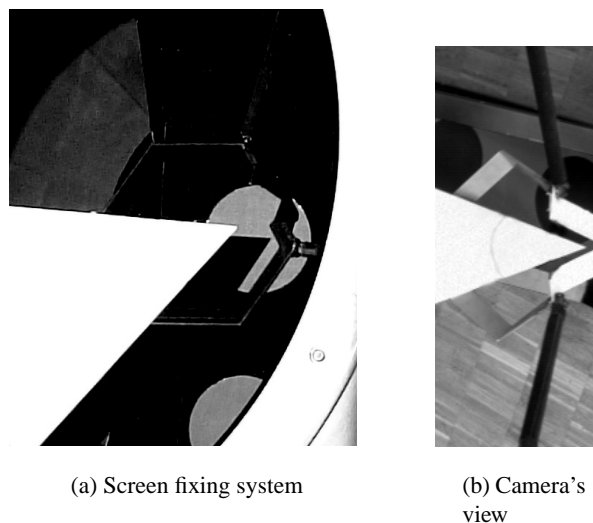


Figure 3.35: Hexagonal screen fixing piece to ensure incident beam path, with added apex to avoid screen image obstruction.

The carbon fiber rods were then fixed to the hexagonal piece so as to follow the edges of the virtual screen opposite the physical one, thus out of the beam path.

Three light-emitting diodes (LED's) were added around the screen to ensure a fine (pixel level) localization of the screen detection area on the images (see Section 4.2.1). Their respective positions were chosen as close as possible to its three summits for better accuracy; constraints due to the incident beam path had yet to be accounted for, particularly critical around the normal and next to normal (10°) incident directions. They were placed slightly backwards from the screen surface to prevent parasitic reflections, at an illumination level just sufficient to allow their precise pinpointing on the digital image. They are represented on Figure 4.6.

Elliptic covers geometry

As mentioned above, the removal of screen covers only aims at leaving the incident beam path free, the controlling of its shape being taken care of by the ellipses cut out from the metal sheet.

To minimize the blind zones, these screen covers must present elliptic shapes as well. Their exact geometry was determined following a similar procedure as for the metal sheet:

- First, their theoretical dimensions and positions were deduced by trigonometry on the basis of the intersection of a perfectly parallel beam (reaching the sample at different θ_1 angles) with the tilted detection surface (accounting for the shift between sample and detection screen base planes, see Section 4.2).
- Then, using on the results provided by the sample illumination analysis with the actual light source and on the metal sheet ellipses dimensions, adjusted horizontal and vertical axes for the screen ellipses were estimated, to which a 2 mm margin was added to avoid edge effects.
- After that, to determine the actual dimensions of the cut out covers, the thickness of the screen had to be taken into account; on the other hand, the covers insertion required a slant between the upper (external) and lower (internal) sides of the screen, chosen unique and equal to 20° to ease the screen manufacturing. To leave the beam's passage free through a screen of significant thickness, larger upper ellipses are required when the angle between the incoming beam and the screen plane increases (i.e. when $|\theta_1 - \Theta_0|$ increases). The ellipses were thus adjusted accordingly, depending on each one's incident tilt angle.
- Finally, as the above adjustment was only necessary for the ellipses half farthest from the $\theta_1 = \Theta_0$ direction, their vertical axes (and thus the blind zones) were reduced by re-centering them to open a passage for the actual beam only, still accounting for the screen thickness and a constant 20° slant.

The resulting dimensions are given in Table 3.1. A screen prototype was realized to check the concept, shown on Figure 3.36(a); it confirmed the adequacy of the metal sheet and screen ellipses combination, and backed up their calculated dimensions and positions.

Automatic system for covers removal

The elliptic covers are held in place by small and strong permanent magnets inserted in the screen central piece. To achieve their removal and repositioning, a "permanent electro-magnet" (PEM) is used, i.e. a permanent magnet that can be deactivated by powering the surrounding coil. This PEM is mounted on a small wagon running on two rails parallel to the main axis of the screen thanks to an indented belt forming a closed loop. An additional on-board mechanism allows it to move up and down from approximately 3 cm, in order to extract and replace the covers.

Theta ($^{\circ}$)	Ellipse center position (cm)	Vertical axis, upper side (cm)	Horizontal axis, upper side (cm)	Vertical axis, lower side (cm)	Horizontal axis, lower side (cm)
0	152.1	21.6	15.3	20.7	14.4
10	125.0	18.8	15.5	18.0	14.6
20	104.3	16.1	15.6	15.3	14.7
30	87.3	13.9	15.7	13.0	14.8
40	72.4	12.1	15.9	11.2	15.0
50	58.3	10.4	16.3	9.5	15.4
60	44.1	9.0	16.6	8.1	15.7
70	28.9	7.4	16.8	6.6	15.9
80	11.4	5.8	16.9	4.9	16.0

Table 3.1: Positions (distances from detection area base) and dimensions of elliptic screen covers.

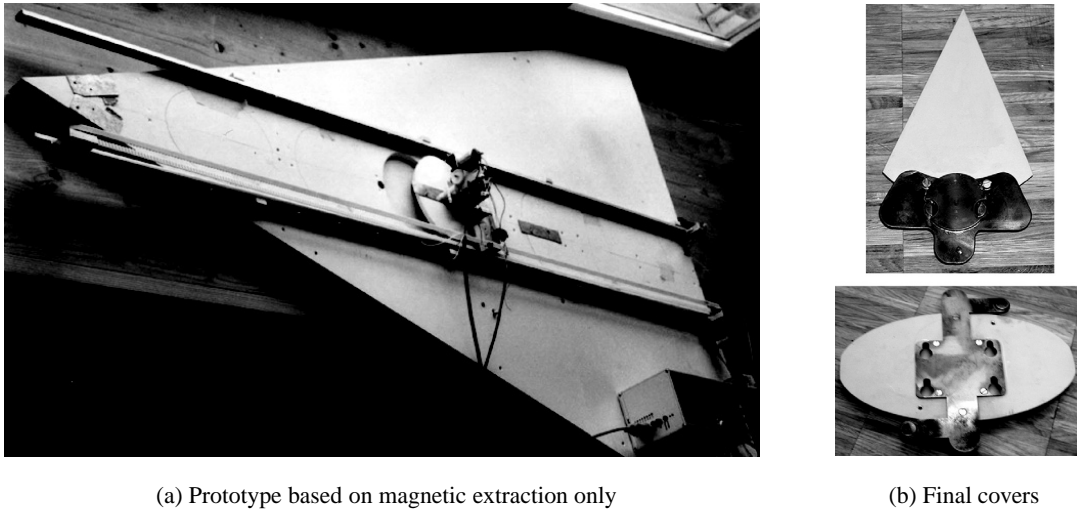


Figure 3.36: Former and actual screen covers extraction systems.

To allow the handling of all covers (and of the tip cover in particular), the rails must stand out of the screen itself, as can be observed on Figure 3.36(a). Their placement was strongly restricted by spatial constraints due to the beam path, critical for the normal and $\theta_i = 10^{\circ}$ incident directions.

The wagon is driven by a stepping motor, controlled by a specific ISEL micro-controller with a RS-232 interface. A typical cycle of extraction, removal and replacement of a cover is sequenced as follows:

- Wagon moved above the appropriate cover, PEM deactivated and lowered, then activated again to retrieve the cover by lifting it up;
- Wagon positioned out of the beam path and kept in place as long as needed to complete the image acquisition and processing phase;
- Wagon moved back above the open hole, PEM lowered, deactivated then lifted up empty, the cover being back in place.

The choice of a PEM instead of a simple EM was based on safety reasons: in case of an unexpected power-off while a cover is removed, the PEM will still hold it whereas an EM would drop it and therefore cause possible damage.

This concept was successfully tested with the screen prototype realized according to the initial design, shown on Figure 3.36(a): it consisted of a 1 cm FOREX[®] panel sandwiched between two 1 mm carbon fiber layers for rigidity and lightness. However, for cost and delay reasons, the carbon

fiber had to be replaced by aluminium, which induced much heavier elements to be removed and put back in place.

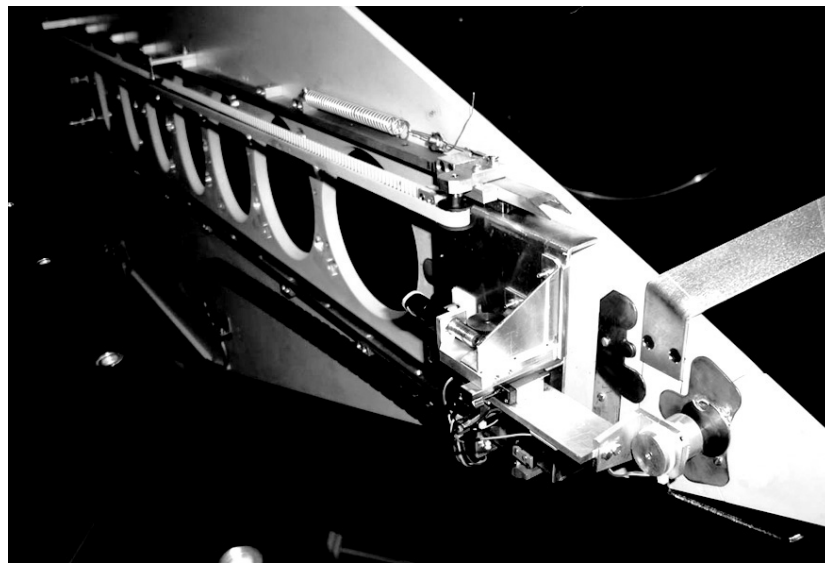
As stronger permanent magnets had to be used, the extraction system based on a PEM only was no longer reliable enough. A mechanical “extractor” was therefore added, using four screw-like pins that get inserted in four slots carved in each cover, shown on Figure 3.36(b); centering pins were added as well on protruding fingers to ensure a reliable positioning. An extra shift was implemented for the wagon movements to allow the extraction system to have a secure grip on the covers.

The limitations in the rails length made it impossible for this extractor to reach the tip cover. Its handling thus required an additional PEM device, together with some extra commands.

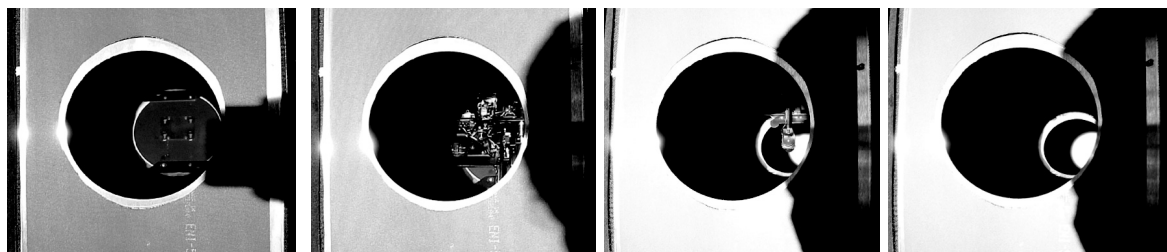
Once the wagon movements were adequately calibrated to position it right above each cover, this new design was tested successfully with hundreds of random extractions at different screen inclinations.

The definitive screen panel is shown on Figure 3.37(a), where the wagon is in position to remove the tip cover and where all other covers are missing; to avoid the residual inter-reflections on the screen slants, the latter were painted in black (and the hexagonal piece was covered with “velvetine”, see Figure 3.35(a)).

Figures 3.37(b) to 3.37(e) illustrate the sequence of events taking place when the projection screen obstructs the incident beam path.



(a) Motorized wagon and steering rails for covers extraction



(b) Obstructing cover

(c) Motorized extraction

(d) Removal

(e) Sample illumination

Figure 3.37: Motorized screen with removable covers for incident beam path.

Chapter 4

Calibration procedures

“I find that a great part of the information I have was acquired by looking up something and finding something else on the way.” (Franklin P. Adams)

4.1 CCD camera

The CCD camera must be converted into a reliable multiple-points luminance-meter. Hence, its spectral sensitivity has to be consistent with the human eye’s spectral response; on the other hand, the digital images have to be converted into accurate luminance maps, expressed in $\text{Cd}\cdot\text{m}^2$.

This section presents the experimental procedures that were necessary to achieve these two calibrations, respectively named spectral and photometric calibrations. An overview of these experiments were published within two articles describing the early stages of the goniophotometer’s development, Andersen et al. (2000) and Andersen et al. (2001).

4.1.1 Spectral calibration

To adapt the CCD camera’s spectral sensitivity to the human eye’s (given by the photopic function $V(\lambda)$ (Commission Internationale de l’Eclairage, 1932) on Figure 4.2), its spectral response must be determined. Then, once an adequate combination of correcting filters is chosen, their optimal respective thickness can be calculated by minimizing the differences with the $V(\lambda)$ function.

As detailed in Andersen (1998), the camera was in fact already equipped with a filter placed in front of the CCD sensor; although this filter restricts the signal mainly to the visible range, it unfortunately does not correct it photopically, which called for the following calibration procedures.

Spectral sensitivity assessment

Two experiments were carried out, both using the set-up represented in Figure 4.1.

A halogen source was placed in front of the input port of a monochromator, which selects specific radiations restricted to a 5 nm spectral range. The produced quasi-monochromatic beam was then reflected on an achromatic diffusing screen (of constant reflectance factor over the whole visible spectrum) and redirected towards the CCD camera and a calibrated detector (spectrophotometer ORIEL MultispecTM 1/8M Spectrograph). Both sensors simultaneously analysed the emitted radiance, the spectrophotometer by assessing its value in $\mu\text{W}\cdot\text{m}^2\cdot\text{sr}^{-1}$ and the camera by providing the associated pixels’ greyscale levels (0 to 255), the integration interval being fixed. Radiance was preferred to a photometric quantity (integrated over $V(\lambda)$), to ensure an appropriate resolution in the blue and red spectral ranges.

A set of measurements was achieved by decreasing the light beam intensity until the detected signal reached the same order of magnitude as their own error. The relation between pixel greyscale values and their associated radiance, checked spectrally-independent by repeating the experiment with other wavelengths, was therefore determined.

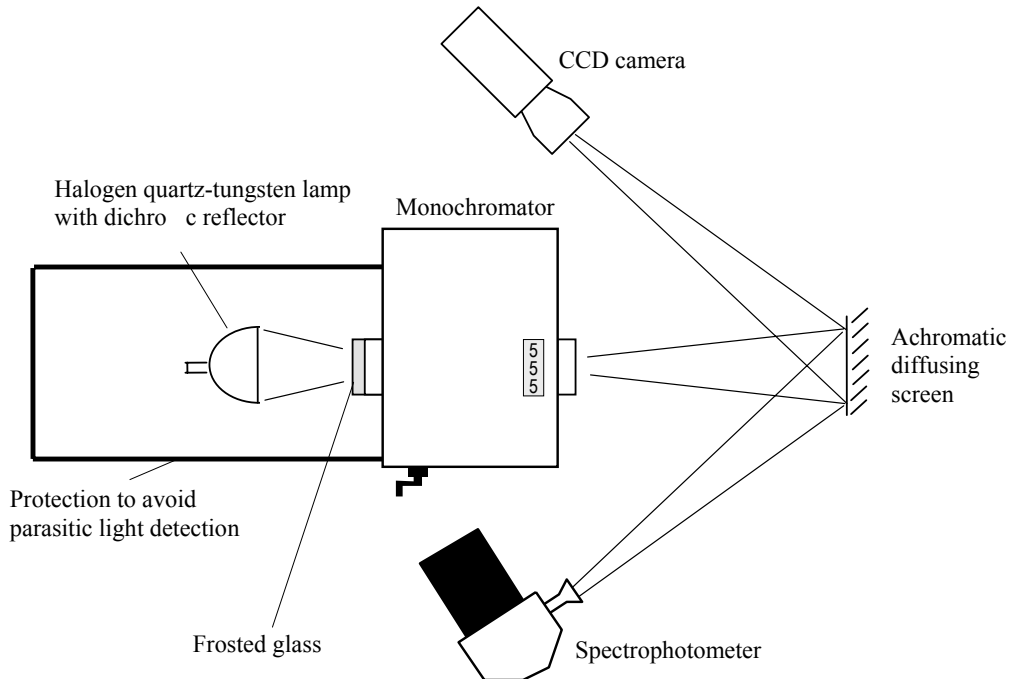


Figure 4.1: Experimental disposal for spectral calibration.

The second experiment was almost identical, except that the wavelength of the emerging radiation was modified instead of the beam intensity, that remained constant. Pixels greyscale values were converted into the corresponding radiances using the previous experiment, and compared to the values simultaneously measured by the spectrophotometer. Their ratio led to the raw spectral sensitivity curve of the CCD camera $S_{\text{raw}}(\lambda)$, normalized at 555 nm and shown in Figure 4.2; this ratio was checked to be independent from the position of the analyzed pixels on the digital image. It was observed that the camera was much too sensitive in the blue and the red parts of the spectrum compared to the human eye: photopic filters were therefore needed to fit its response to the $V(\lambda)$ photopic curve.

Determination of optimal photopic filters combination

Based on a filters selection by Berrutto (1996) for the same kind of correction, three filters of uniform bulk composition (colored glass) were chosen, two manufactured by Kopp (Nb. 3384 and 3307) to reduce the excessive sensitivity in the low wavelengths range (long pass filters) and a Schott filter (type BG39) gradually cutting off wavelengths between 560 and 680 nm (short pass filter).

Once a sample of each was acquired, their transmission properties (for thickness 3.01, 3.14 and 2.04 mm for the Kopp 3384, 3307 and Schott BG39 respectively) were assessed experimentally with the spectrophotometer. Thereafter, each one's optimal thickness had to be determined, in order that their combined transmission brings the camera's normalized spectral response $S(\lambda)$ as close as possible to the photopic function $V(\lambda)$. This leads to minimizing the difference $|V(\lambda) - S(\lambda)|$ at each wavelength λ .

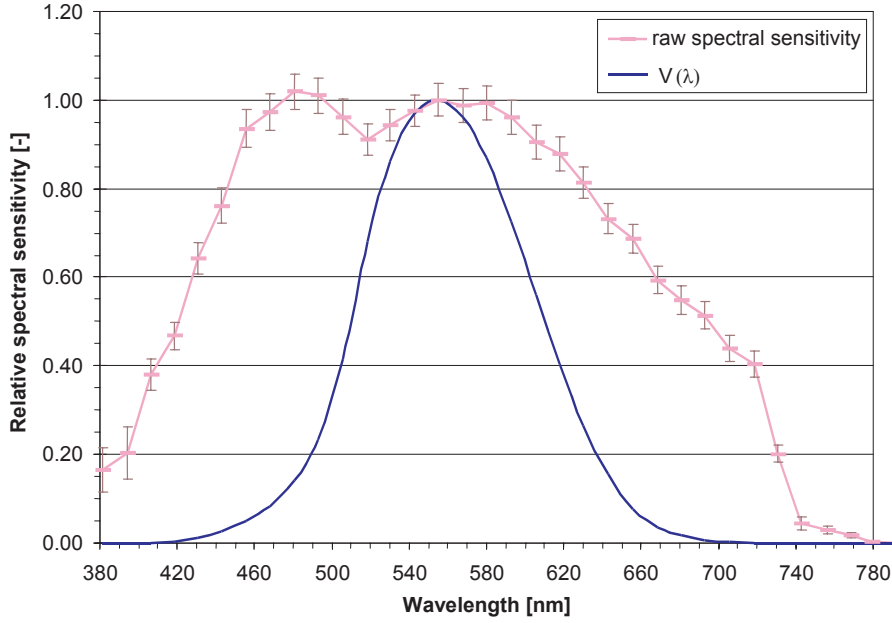


Figure 4.2: Raw spectral sensitivity of the CCD camera and comparison with photopic curve $V(\lambda)$.

A least-square method was therefore applied. $S(\lambda)$ can be expressed as the normalized product of the raw spectral response $S_{\text{raw}}(\lambda)$ and the transmission factor $T_{\text{comb}}(\lambda)$ resulting from the combination of the three correcting filters. In consequence, the function F_{min} that had to be minimized is given by Equation (4.1); it was deduced from Wright et al. (1969) and adapted to reduce the impact of low sensitivity points (Berrutto, 1996; Andersen, 1998):

$$F_{\text{min}} = \sum_{n=1}^{N_{\lambda}} \frac{1}{V(\lambda_n) + 0.01} \cdot \left(V(\lambda_n) - \kappa \cdot S_{\text{raw}}(\lambda_n) \cdot T_{\text{comb}}(\lambda_n) \right)^2 \quad (4.1)$$

where N_{λ} (-) is the total number of considered wavelengths and κ the normalization factor, given by Equation (4.2):

$$\kappa = \frac{1}{\max_{n=1}^{N_{\lambda}} S_{\text{raw}}(\lambda_n) \cdot T_{\text{comb}}(\lambda_n)} \quad (4.2)$$

Beer-Lambert's law (Ryer, 1997) states a logarithmic relation between a filter's internal transmittance τ_i at a given wavelength (i.e. after surface reflection losses are accounted for) and its thickness e . It is given by Equation (4.3), where the internal transmittance τ_{i_0} at thickness e_0 is known:

$$\frac{\log \tau_i}{e} = \frac{\log \tau_{i_0}}{e_0} \quad (4.3)$$

This relation is equivalent to Equation (4.4) for external (total) transmittance, R_l being the reflection loss factor for the filter, typically equal to 0.911 for the kind of considered filters (ORIEL Instruments, 2003):

$$\frac{\log \frac{T}{R_l}}{e} = \frac{\log \frac{T_0}{R_l}}{e_0} \quad (4.4)$$

We can therefore express $T_{\text{comb}}(\lambda_n)$ according to Equation (4.5) as the product of the three individual filters transmission ($k = 1, 2$ and 3 for the Kopp 3384, 3307 and Schott BG39 filters respectively):

$$T_{\text{comb}}(\lambda_n) = R_l^3 \cdot \prod_{k=1}^3 \tau_{i_{0k}}(\lambda_n)^{\frac{e_k}{e_0k}} = R_l^{(3 - \sum_{k=1}^3 \frac{e_k}{e_0k})} \cdot \prod_{k=1}^3 T_{0k}(\lambda_n)^{\frac{e_k}{e_0k}} \quad (4.5)$$

This leads to the final expression of F_{\min} :

$$F_{\min} = \sum_{n=1}^{N_\lambda} \frac{1}{V(\lambda_n) + 0.01} \cdot \left(V(\lambda_n) - \kappa \cdot S_{\text{raw}}(\lambda_n) \cdot R_l^{(3 - \sum_{k=1}^3 \frac{e_k}{e_{0k}})} \cdot \prod_{k=1}^3 T_{0k}(\lambda_n)^{\frac{e_k}{e_{0k}}} \right)^2 \quad (4.6)$$

The optimal thickness e_k for the three filters, determined using Microsoft[®] Excel's Solver, are:

- 0.47 mm for the Kopp 3384
- 3.09 mm for the Kopp 3307
- 1.20 mm for the Schott BG39.

Once each filter's thickness was adjusted by grounding it down to the above values, its transmittance over the visible spectrum could be measured: the resulting curves are shown on Figure 4.3, together with the combined transmission function T_{comb} .

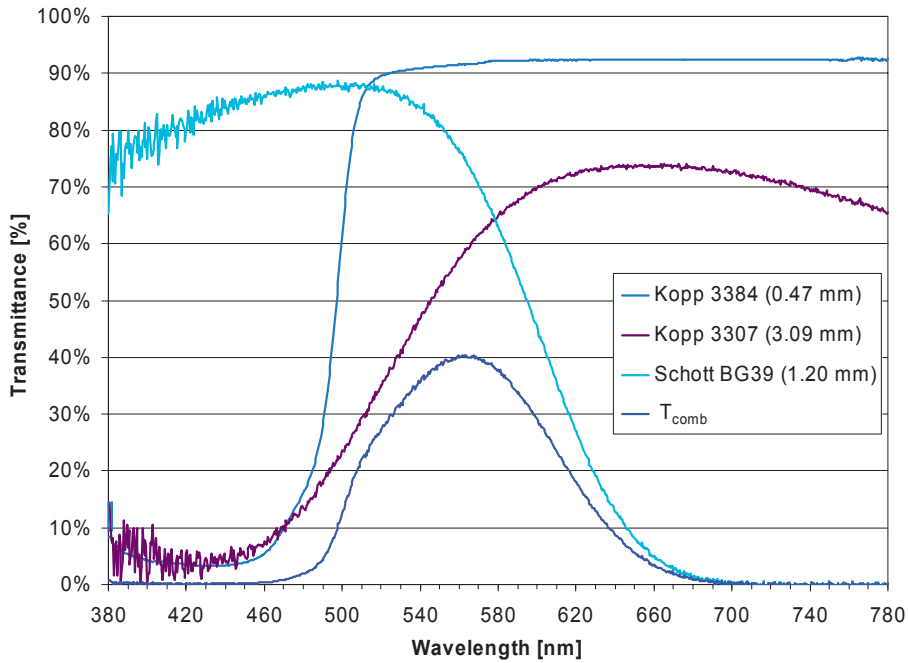


Figure 4.3: Individual and combined filter transmission functions, at optimal thickness.

Corrected spectral sensitivity

The filters were set in front of the camera's lenses thanks to a specially designed filter holder. The spectral sensitivity could then be experimentally assessed, using the same method as before. The corrected response $S(\lambda)$ is given on Figure 4.4 (distinguished by the suffix "meas").

As shown on that figure, the corrected spectral sensitivity of the camera matches the photopic curve $V(\lambda)$ properly. To quantify their agreement, the function f'_1 was used; it is defined in Commission Internationale de l'Éclairage (1987) as "the degree to which the relative spectral sensitivity $S(\lambda)$ matches the spectral luminous efficiency $V(\lambda)$ of the human eye for photopic vision" and is given by Equation (4.7):

$$f'_1 = 0.0093584 \cdot \sum_{n=1}^{N_\lambda} |S(\lambda_n) - V(\lambda_n)| \cdot \Delta\lambda_n \quad (4.7)$$

The constant 0.0093584 in Equation (4.7) is only valid if wavelengths are expressed in (nm); $\Delta\lambda_n$ represents the interval between consecutive wavelengths λ_{n-1} and λ_n .

f'_1 was found to be equal to 10.2%. The mathematical prediction based on expected transmittance T_k at calculated thickness e_k is plotted on Figure 4.4 as well (“predicted $S(\lambda)$ (F_{\min} calc)”); the calculation of f'_1 for this theoretical curve led to 8.3%, which shows that the optimization methodology proved accurate, despite the exponential impact of the measurement errors for T_{0_k} on the final transmittance T_k ; this impact is even more critical when ϵ_{0_k} and e_k are very different, as is typically the case for the Kopp 3384 filter.

As detailed in Section 6.1, the 10.2% value is not to be taken as a relative uncertainty on achieved BT(R)DF data: it only appears as a second order error thanks to the photometric calibration, which reduces its impact to less than 1%.

The f'_1 function could actually have been used as minimization function instead of F_{\min} . As a matter of fact, the expected corrected sensitivity according to a filters thickness optimization based on f'_1 's minimization led to very similar results, as shown on Figure 4.4 (“predicted $S(\lambda)$ (f'_1 calc)”) : the average relative difference were lower than 3% for the three $S(\lambda)$ curves.

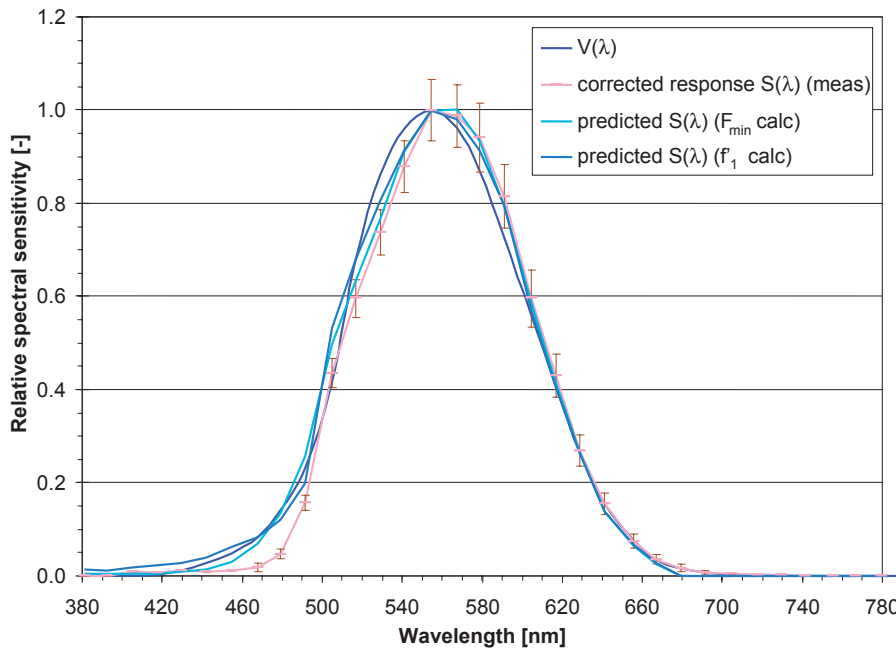


Figure 4.4: Spectral sensitivity of the CCD camera equipped with ad hoc filters: measured response and mathematical predictions compared to human eye's photopic response $V(\lambda)$.

4.1.2 Photometric calibration

The photometric calibration determines the relations between pixels greyscale values (0 to 255) and the corresponding luminances L_{screen} ; these relations depend on the CCD camera integration interval.

To achieve this, an experimental disposal was set up. It consisted of a light source illuminating a diffusing white surface towards which both the CCD camera and a Minolta LS-110 luminance-meter were pointed. Their respective measurement results (greyscale level image and luminance value) could this way be compared for several situations, and their relation be established.

To minimize the impact of the difference between the camera's spectral sensitivity $S(\lambda)$ and the photopic function $V(\lambda)$ (see Section 6.1.1), the BT(R)DF assessment source itself was used

for the photometric calibration. A large range of luminance values, necessary to achieve a high accuracy, could thus be produced thanks to its full dimming capability. This was not possible for the former source (HMI 2.5 kW spotlight with Fresnel lens) that was moreover fixed on the ceiling; hence, another calibration source was then used (Halogen spot with reflector, 500 W), placed at different distances from the reflecting surface to vary the luminance observed on the screen.

For each illumination situation (i.e. each re-emitted luminance value), pictures were taken at all possible integration intervals used for sample characterizations, in order to be compared with the (single) luminance monitored by the luminance-meter for this particular situation.

The lowest integration interval was chosen to be 40 ms, to avoid beating effects with the light source's own frequency (50 Hz AC supply). On the other hand, as the longest integration interval is used for every screen position whatever the luminance range (to ensure the finest resolution for background light), it has to remain reasonably short for the characterization process efficiency, while still offering a sufficiently low threshold for usual transmission (reflection) figures. Therefore, a longest exposure of 2.56 s was chosen as a standard, which limits the observed luminances to $0.3 \text{ Cd}\cdot\text{m}^{-2}$. The possible integration intervals thus range from 40 ms to 2.56 s, with a doubling at each step. The camera was actually also calibrated at 5.12 s (i.e. luminance assessment until $0.15 \text{ Cd}\cdot\text{m}^{-2}$), that can easily be included in a BT(R)DF characterization process if necessary.

In case particularly low luminances need to be detected, the integration interval can be increased further (about a minute is required to detect luminances as low as $0.01 \text{ Cd}\cdot\text{m}^{-2}$). However, the measurements accuracy remains limited by the luminance-meter used for calibration, as $0.01 \text{ Cd}\cdot\text{m}^{-2}$ is the lowest measurable value.

Once the set of possible integration intervals was determined, the number of diaphragm stops was set so that no pixel saturation occurred at 40 ms, even on the projection screen area closest to the sample (i.e. at distance d_{\perp}) for perfectly transparent (reflecting) materials. This maximal luminance is equal to about $2500 \text{ Cd}\cdot\text{m}^{-2}$ with the HMI 1.2 kW "Korrigan" followspot (it reached $850 \text{ Cd}\cdot\text{m}^{-2}$ with the former source); the diaphragm was thus set (and blocked) in order to achieve a greyscale level of about 220 for this luminance value, which prevents non-linear effects occurring at greyscale levels close to 255.

The calibration process could then be started: luminances were gradually decreased from $3500 \text{ Cd}\cdot\text{m}^{-2}$ to $0.02 \text{ Cd}\cdot\text{m}^{-2}$, until the associated pixels became under-exposed even for the longest integration interval (5.12 s). The relative experimental error generally remained lower than 1%.

The conversion polynomial functions deduced from the measured data are given in Figure 4.5 for all considered integration intervals (because of the low relative experimental error (1%), error bars were too short to be displayed); they were implemented in the image acquisition and handling software Image-Pro Plus[®] to automate the image conversion (see Section 5.3.1).

The non-linear property of the response curves was deliberately chosen to achieve a good resolution for low luminances by selecting a gamma value of 0.45: a linear relation (i.e. $\gamma = 1$) did not offer large enough greyscale level dynamics for small luminance differences in dark regions. Over the whole luminance range, a same relative error on the luminances could this way be kept for a given absolute error on the greyscale levels.

Another important feature to be noted on Figure 4.5 is that all calibration curves start at the greyscale level 49. This is due to the fact that the camera hardware needs a small positive signal associated to absolute darkness to avoid noise clipping. Indeed, the output of an a/d converter being null for an input that can be slightly negative, a small positive value becomes necessary to avoid the drifting margin. Besides, the camera hardware is obviously optimized for a linear response ($\gamma = 1$), where only 5 LSB (Least Significant Bits i.e. complete darkness at greyscale level = 5) are required, whereas 48 are lost for $\gamma = 0.45$.

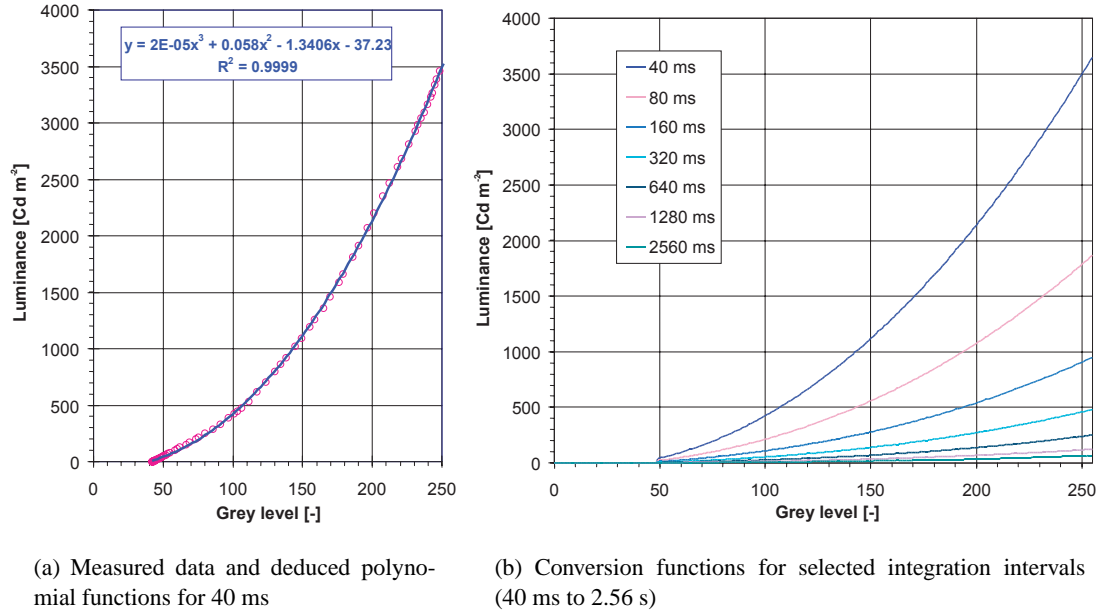


Figure 4.5: Photometric calibration of the CCD camera: conversion functions from pixel greyscale value to luminance.

4.2 Spatial calibration

The aim of the spatial calibration is to determine the relationship between the spherical coordinates (θ_2, ϕ_2) defined around the sample (see Figure 2.1) and the pixel co-ordinates (X, Y) on the captured image. It can be considered in three steps:

- first ensure a fixed position of the screen area on the digital image;
- then relate the screen's pixels to their corresponding emerging polar angles $(\theta_{\text{Ref}}, \psi_2)$ for a reference situation and an arbitrary screen position;
- finally, determine the hemispherical polar angles (θ_2, ϕ_2) accounting for the current screen position, the sample thickness e_s and the incident azimuth ϕ_1 .

These different calibration phases are described in the subsequent sections, followed by a study of the partial obstruction of emerging light, mentioned in Section 3.2.4.

The sample being non-punctual implies that a same point on the screen will possibly be reached by rays emitted along different directions over the sample area, with a divergence proportional to the latter. Practically, outgoing directions (θ_2, ϕ_2) will be launched from the sample's center and the spatial calibration based on this assumption, considering the possible divergence of rays as a measurement error (see Section 6.1.2); as detailed in Section B.1.3, this divergence is in fact compensated in the way that BT(R)DFs are averaged inside sectors of greater angular interval.

4.2.1 Screen image position adjustment

As explained in Section 3.4.4, three light-emitting diodes (LED's) (light green for a better perception by the spectrally corrected CCD camera) were installed close to the projection screen summits in order to be localized on the image, as shown on Figure 4.6; they determine the pixels corresponding to the actual screen detection area with a high accuracy.

The idea is to adjust a triangular Area Of Interest (AOI) according to these pixels and duplicate the image to produce a slightly smaller one that circumscribes the detection area exactly. As the

(X, Y) pixel coordinates on this duplicated image will in consequence always be associated to the same positions on the screen, all geometric calibrations or processing on digital images will be based on the latter.

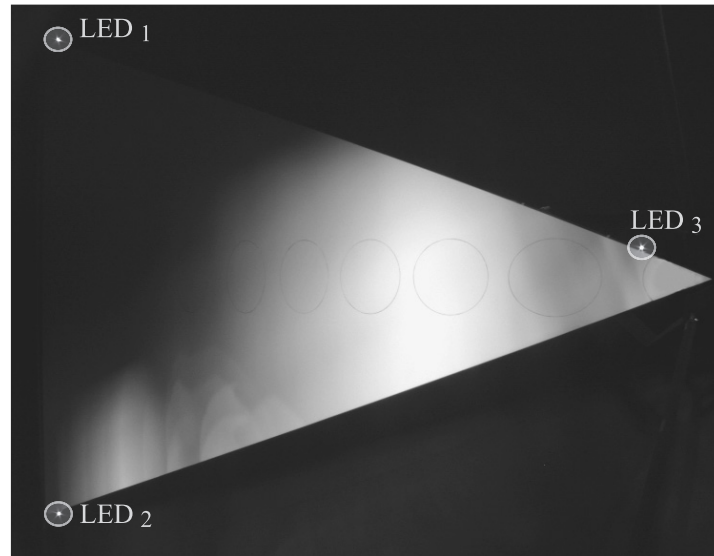


Figure 4.6: Adjustment of the image pixels corresponding to the screen detection area thanks to three LED's localized on the image.

Practically, such an AOI is stored for a particular position relative to the LED's and shifted (horizontally and/or vertically) according to their actual position on the full image. The latter is given by the maximal pixel value within their respectively produced bright spots.

As the detection area only moves slightly on the image during a characterization session (up to a few pixels at most along X and/or Y), the pixel groups where the diodes are expected to appear remain restricted: it is possible to keep the search area as small as 18×18 pixels still being sure not to miss the LED's position. This allows to keep the search areas out of the screen image, reducing the risk of mistaking a nearby transmitted (reflected) light spot for a LED.

However, as larger shifts can occur between two characterization sessions realized at very distant moments, a broader - although as reliable - search has to be conducted at the beginning of a session. This was done by extending the three investigated pixel groups to 50×50 regions around usual LED's positions and localizing maxima within these regions in the absence of light. The significant shifts between two time spaced out sessions required a real-time adjustment; it hence prevented from using a predetermined XY shift dataset, that was first created for all six screen positions at every device tilt configuration (with 10° steps).

The following sequence of events takes place at the beginning of a characterization session, which fulfills the above requirements:

- When the light proof cap faces the light source and no metal sheet ellipse is uncovered (i.e. when no light penetrates the measurement space), the switched on LED's are localized at the longest integration time; their respective positions (bright spots maxima) on the captured image are stored and used as centers of the future smaller search areas;
- Before each image capture, the three 18×18 search areas are positioned accordingly and the LED's are localized on the current image; the necessary AOI shift in X and Y is deduced from their respective positions and applied to all images taken at this particular screen position.

4.2.2 Reference situation

Before considering spatial variations, a reference case was chosen to compare possible modifications to it. An arbitrary screen position was therefore analyzed; the relation between a position on the real screen area, given by its cartesian coordinates (x, y) , and the corresponding polar coordinates $(\theta_{2\text{Ref}}, \psi_2)$ could thus be determined.

As illustrated by Figure 4.7, the base plane chosen to define the polar coordinates referential was the plane parallel to the sample and comprising the detection area base; on the figure, only the actual detection area and not the full screen is represented for simplification. x and y are measured according to Figure 4.7 along the detection area base and its central axis, .

Altitude $\theta_{2\text{Ref}}$ is the angle between the considered direction and the normal to the sample plane; ψ_2 is its azimuth angle, projected on the same plane and comprised between -30° and $+30^\circ$ (null along the central axis of the screen).

As the detection area base is shifted 7.5 cm from the external (incident) sample plane for mechanical reasons (rotating ring structure and movements, main platform), this reference situation actually corresponds to a sample thickness $e_s = 7.5$ cm for transmission measurements; such a thickness indeed shifts the internal (emerging) sample interface plane down to the detection area's base level.

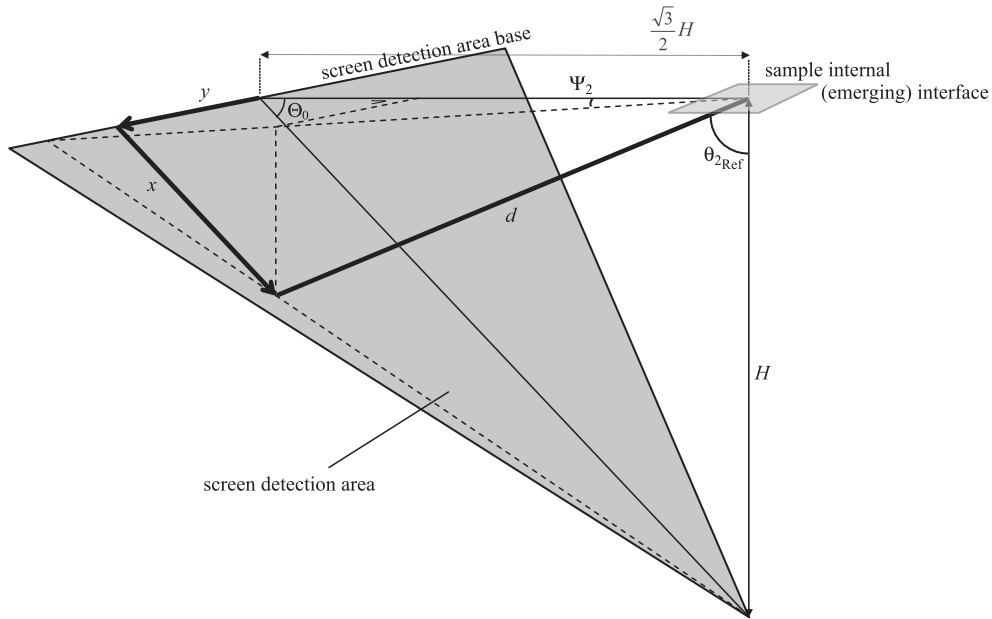


Figure 4.7: Relation between reference polar coordinates $(\theta_{2\text{Ref}}, \psi_2)$ and cartesian screen coordinates (x, y) .

The cartesian coordinates (x, y) on the screen detection area can be expressed as functions of their associated polar angles $(\theta_{2\text{Ref}}, \psi_2)$ through Equations (4.8), deduced from trigonometric considerations:

$$\begin{aligned}
 x &= \frac{H}{\sin \Theta_0} \cdot \frac{1}{\frac{2}{\sqrt{3}} \cdot \tan \theta_{2\text{Ref}} \cdot \cos \psi_2 + 1} \\
 y &= H \frac{\sin \psi_2}{\frac{2}{\sqrt{3}} \cdot \cos \psi_2 + \cot \theta_{2\text{Ref}}}
 \end{aligned} \tag{4.8}$$

where H is the “vertical” distance from the detection area apex to the base plane ($H = 115$ cm, see Section 3.2.5).

In order to incorporate image aberrations directly, thus avoiding an independent correction of the image distortions, a map of 901 points of polar coordinates $(\theta_{2\text{Ref}}, \psi_2)$ taken every 2.5° in altitude and azimuth over a 60° interval was drawn on a replica of the projection screen. This calibration panel was positioned on the carbon fiber support (see Figure 3.10); its image captured by the camera is shown on Figure 4.8. Each of the 901 points was then manually located and associated to the corresponding pixel's coordinates (X, Y) .

This dataset is thereafter used to determine the $(X, Y) \leftrightarrow (\theta_{2\text{Ref}}, \psi_2)$ relations for the whole detection area on the CCD image, thanks to a two-dimensional interpolation procedure applied for the other pixels using MATLAB^{®1}.

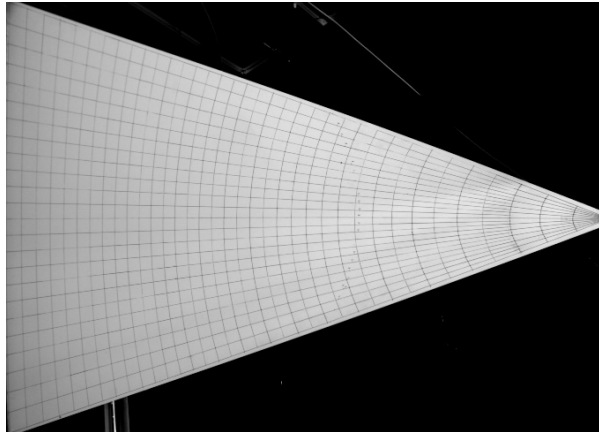


Figure 4.8: Calibration grid of resolution 2.5° in altitude and azimuth for the reference situation.

Based on these relations, a pair of 685×488 matrices $M_{\theta_{2\text{Ref}}}$ and M_{ψ_2} was created, of dimensions equal to the duplicated image size and represented on a pixel greyscale on Figures 4.9(a) and 4.9(b). Their coefficients are respectively equal to the $\theta_{2\text{Ref}}$ and ψ_2 angles associated to the corresponding (duplicated) image pixels. Out of the screen detection area, the matrix coefficients are set to *NaN* (Not A Number).

A third quantity revealed itself essential for the spatial calibration: the distance d_{Ref} between the referential origin and the screen plane along direction $(\theta_{2\text{Ref}}, \psi_2)$. It is given by Equation (4.9):

$$d_{\text{Ref}} = \frac{H}{\frac{2}{\sqrt{3}} \cdot \sin \theta_{2\text{Ref}} \cdot \cos \psi_2 + \cos \theta_{2\text{Ref}}} \quad (4.9)$$

Once both reference matrices $M_{\theta_{2\text{Ref}}}$ and M_{ψ_2} were completed, a similar one for d_{Ref} could be calculated based on Equation (4.9), named $M_{d_{\text{Ref}}}$ and represented on Figure 4.9(c).

These three matrices were used as a calculation basis for referential variations (see Section 4.2.3); for a better visual display on Figure 4.9, the 0 to 255 greyscale was fitted to each parameter's angular or metric range individually. Their respective values vary from 0° to 90° for $\theta_{2\text{Ref}}$, -30° to 30° for ψ_2 , and 753 cm to 115 cm for d_{Ref} . Pixels out of the screen area (*NaN* in the matrices) were arbitrarily set to 0.

On the image of the reconfigured screen, shown in Figure 4.10(a), pixels corresponding to the elliptic covers borders appear darker and thus needed to be removed from the procedure. For this, a mask putting all concerned pixels to zero (for the duplicated screen image) was created, illustrated in Figure 4.10(b). This mask is unique as the covers positions do not depend on the spatial referential.

¹MATLAB[®], v. 6.1.0.450, The MathWorks, Inc.

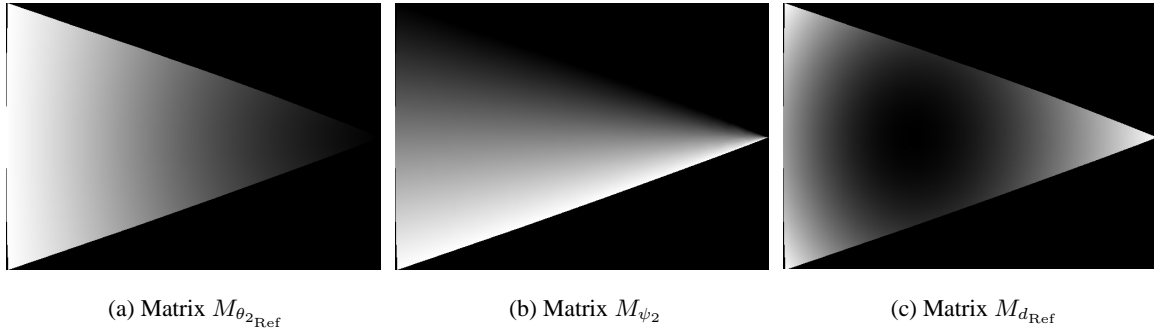


Figure 4.9: Digital representation of reference matrices.

When creating the appropriate averaging grid (Section 5.2), the mask (converted into a binary matrix with 0 on the covers borders and 1 elsewhere) was used to exclude the altered pixels from the BT(R)DF assessment. Of course, for the critical (obstructing) screen position in the reflection mode, the pixels inside the current θ_1 cover border had to be excluded too (see Section 5.2.2); for that purpose, nine similar binary matrices were prepared with null coefficients inside ellipses $\theta_1 = 0$ to $\theta_1 = 80$ and on all ellipses borders.

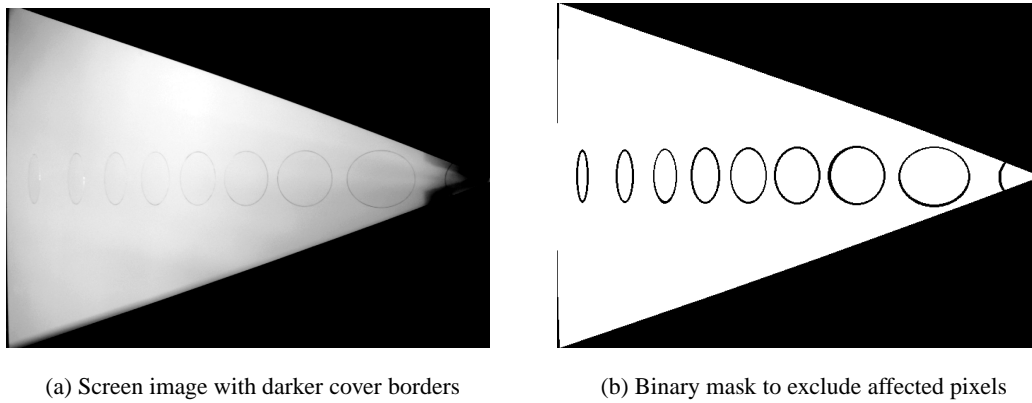


Figure 4.10: Localization and removal of elliptic covers borders on acquired images for unaltered BT(R)DF assessment.

4.2.3 Spatial referential variations

As the referential is linked to the sample itself, the emerging polar angles (θ_2, ϕ_2) had to be adapted to two sample parameters:

- in transmission mode, to the sample thickness e_s , as the emerging interface determines the referential base plane (in reflection mode, the single configuration corresponds to a null thickness, as incident and emerging interfaces are coplanar); a given point on the screen (or a same pixel on the image) thus corresponds to varying θ_2 angles, depending on e_s ;
- in both modes, to the incident azimuth ϕ_1 ; indeed, as the sample's tilt and orientation determine the incident direction, the azimuth origin axis is rotated around the normal to the sample according to angle ϕ_1 ; hence, a given point on the screen (a same pixel) can also correspond to different ϕ_2 values.

Practically, angles (θ_2, ϕ_2) were adapted in “real-time” to the current situation thanks to a flexible, pixel-level approach explained below (and in more details in Section 5.2); it included an interaction with MATLAB®.

The determination of the actual θ_2 and ϕ_2 angles for the current sample configuration took place in two steps: first, the geometric parameters and their analytic relations were studied; then, as the direction (θ_2, ϕ_2) is in the end associated to emerging hemisphere areas defined by the BT(R)DF averaging grid, a calculation method was developed for creating the referential adapted matrices on which the averaging grid is based. These procedures are explained below.

At a prior stage of development, BT(R)DF measurements were carried out with a fixed referential (Andersen et al., 2000, 2001). Instead of associating polar coordinates (θ_2, ϕ_2) to each pixel (X, Y) individually, the gravity centers of the $(\Delta\theta_2, \Delta\phi_2)$ sectors were taken as directional references and matrices M_{θ_2} and M_{ψ_2} were only used to define grids of given averaging intervals. However, the important restrictions in flexibility (averaging grid intervals, ϕ_1) and accuracy (average distance d per sector, sample thickness parameter neglected) called for the development of the detailed and adaptable spatial calibration presented here.

Analytical variations

As illustrated by Figure 4.11, the correspondence between $(\theta_{2\text{Ref}}, \psi_2)$ and (θ_2, ψ_2) depends on different fixed quantities (gap $g = 7.5\text{cm}$, distance H , angle Θ_0) and on the variable sample thickness e_s , that can induce significant differences in the altitude θ_2 to which a given pixel corresponds (e.g. up to 2° between a null thickness and a situation where $e_s = 3\text{ cm}$).

In fact, only θ_2 varies with e_s , whereas ψ_2 remains unchanged. Defining it as a function of $\theta_{2\text{Ref}}$, ψ_2 and d_{Ref} using Equations (4.8) and (4.9), Equation (4.10) can be written:

$$\theta_2 = \arcsin \frac{d_{\text{Ref}} \cdot \sin \theta_{2\text{Ref}}}{\sqrt{(d_{\text{Ref}} \cdot \cos \theta_{2\text{Ref}} + (g - e_s))^2 + (d_{\text{Ref}} \cdot \sin \theta_{2\text{Ref}})^2}} \quad (4.10)$$

The distance d between the sample center (in the emerging interface) and the screen is actually equal to the denominator in Equation (4.10); it can also be written as a function of θ_2 through Equation (4.11), the generalized equivalent of Equation (4.9):

$$d = \frac{H + g - e_s}{\frac{2}{\sqrt{3}} \cdot \sin \theta_2 \cdot \cos \psi_2 + \cos \theta_2} \quad (4.11)$$

Matrices M_{θ_2} and M_d were created according to the sample thickness e_s using matrices $M_{\theta_{2\text{Ref}}}$, M_{ψ_2} and $M_{d_{\text{Ref}}}$ and Equations (4.10) and (4.11) (the arithmetic operations being applied to each of their coefficients individually). The accuracy of the M_{θ_2} matrices was checked experimentally for the $e_s = 0$ situations with a laser beam. Both M_{θ_2} and M_d are unique for all six screen positions, for a given sample configuration. Together with M_{ψ_2} , they provide the essential parameters for the creation of the averaging grid (see Section 5.2) as well as for compensating distance and light tilt effects on acquired images (creation of a correction factor matrix, see Section 5.4.1), to achieve pixel-level accurate BT(R)DF data.

The azimuth angle ϕ_2 defined for the whole hemisphere is independent from the incident azimuth ϕ_1 ; it depends, however, on the screen position considered, which requires a different approach when relating ϕ_2 to ψ_2 , presented here.

Each screen position has to be considered as being part of a global combination that “rebuilds” the emerging hemisphere according to six complementary projections, on which ϕ_2 (or ψ_2) values follow radial lines from triangle apex to base, as shown on Figure 4.11. As illustrated in Figure 4.12, changing the incident azimuth ϕ_1 is materialized by a rotation of the sample, to which the output referential is linked. It is therefore essential to determine the exact position of the azimuth origin axis, and first of all the screen position number p_0 on which it is projected, fully determined by the ϕ_1 parameter.

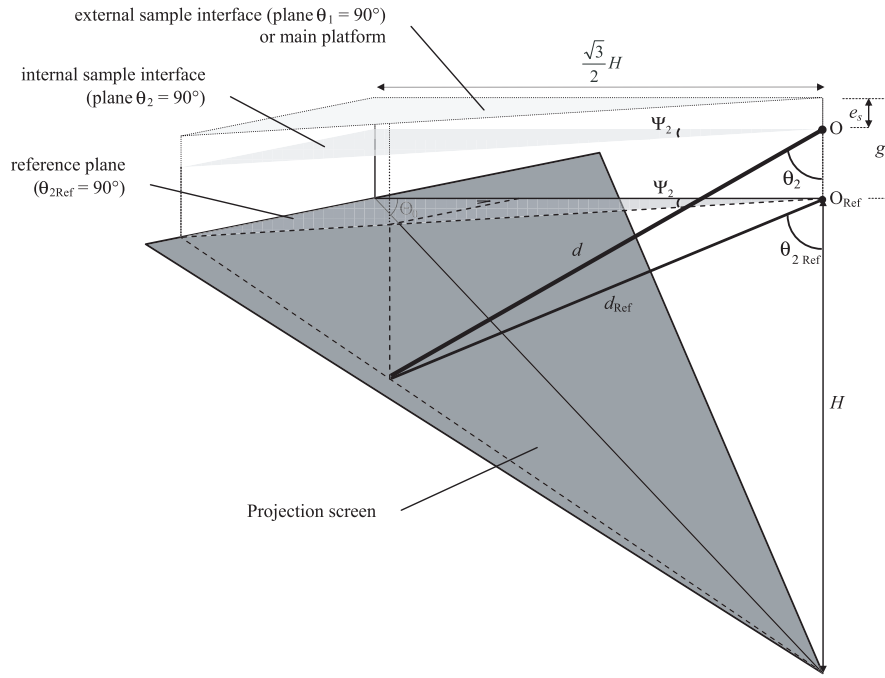


Figure 4.11: Relation between polar co-ordinates (θ_2, ψ_2) and reference coordinates (θ_{2Ref}, ψ_2) .

p_0 is defined as the screen position comprising the origin axis for ϕ_2 . The exact position of this axis is given by $\psi_{20}(\phi_1, \Delta\phi_2)$, equal to the ψ_2 value on screen position p_0 at which it is projected. $\psi_{20}(\phi_1, \Delta\phi_2)$ is comprised between -30° and $+30^\circ$ and equals zero only if $\phi_1 = N \cdot 60^\circ$.

The relation between ϕ_2 and ψ_2 can therefore be expressed as follows in transmission mode:

$$\phi_{2T} = (\Delta p_0 \cdot 60^\circ + \psi_2 - \psi_{20} + 360^\circ) \bmod 360^\circ \quad (4.12)$$

where Δp_0 is the number of screen positions separating p_0 from the current position p , according to the screen numbering order of Figure 4.12.

In reflection mode, the ϕ_2 referential is characterized by a reverted screen position numbering: the six positions' chronology remains unchanged but the device is turned over towards the incident light source, as illustrated by Figures 3.2(a) and 3.3(a). Hence, Equation (4.12) becomes:

$$\phi_{2R} = (2\phi_1 - \Delta p_0 \cdot 60^\circ - \psi_2 + \psi_{20}) \bmod 360^\circ \quad (4.13)$$

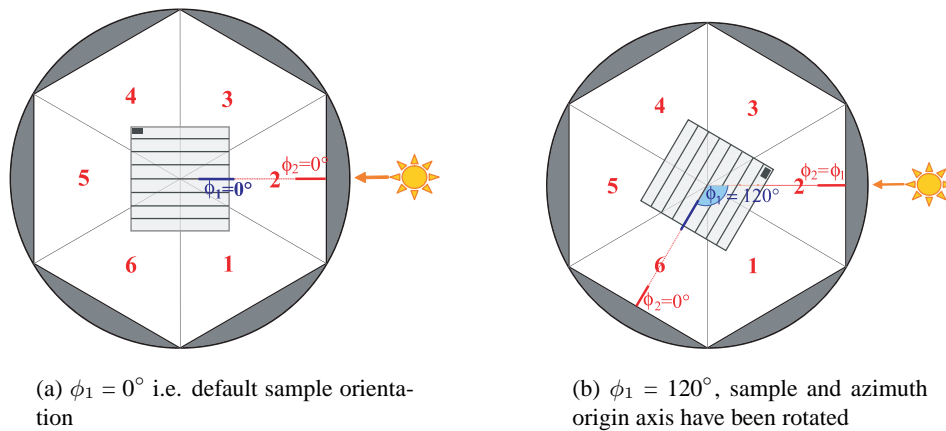


Figure 4.12: Orthogonal projection view of the sample orientation superimposed on the six screen positions.

Averaging grid adaptations

As mentioned above and detailed in Section 5.2, matrices M_{θ_2} and M_{ψ_2} served as a basis for creating BT(R)DF averaging grids according to the chosen angular intervals $(\Delta\theta_2, \Delta\phi_2)$.

$\Delta\theta_2$ can be chosen in-between 0.5° and 90° (with a minimal step of 0.1°); $\Delta\phi_2$ must be a divisor of 60° , with a minimal step of 0.5° . Such constraints avoid problems inherent to resolutions going down to the image pixellisation itself and allow an analysis of the six screen images according to the same individual grid.

As θ_2 values only depend on the sample thickness e_s , the different fringes delimited by $N \cdot \Delta\theta_2 - \frac{1}{2}\Delta\theta_2$ and $N \cdot \Delta\theta_2 + \frac{1}{2}\Delta\theta_2$ ($N = 0 \dots \frac{90}{\Delta\theta_2}$) can be easily calculated from M_{θ_2} and $\Delta\theta_2$.

Figure 4.13 shows the superposition of an averaging grid corresponding to $e_s = g = 7.5$ cm (reference situation, grid sectors delimited by drawn boundaries) over the pattern of sectors associated to $e_s = 0$ (greyscale level pattern). In both cases, the output resolution $(\Delta\theta_2, \Delta\phi_2)$ is equal to $(10^\circ, 15^\circ)$. This figure also outlines the effect of increasing sample thickness on the $(X, Y) \leftrightarrow (\theta_2, \psi_2)$ relation, stronger for growing values of θ_2 .

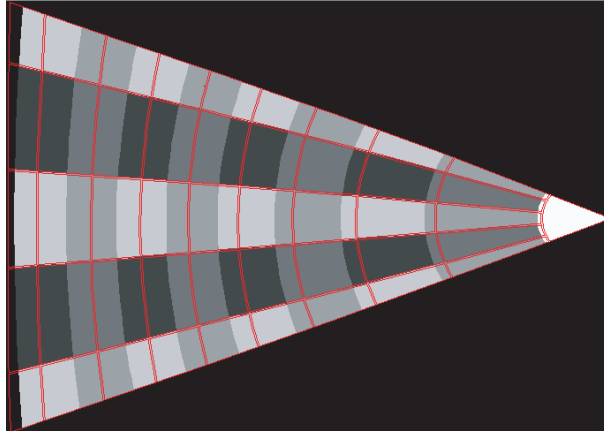


Figure 4.13: Superimposed averaging grids with $(\Delta\theta_2, \Delta\phi_2) = (10^\circ, 15^\circ)$ for $e_s = 7.5$ cm (sectors borders) and $e_s = 0$ (greyscale level pattern).

As far as ϕ_2 and $\Delta\phi_2$ values are concerned, the averaging grid has to be understood as a splitting of the whole emerging hemisphere, probably presenting several sectors that overlap two screen positions. All six being invariants, the ϕ_1 rotation of the sample (Figure 4.12) induces a simultaneous revolution of the averaging grid, illustrated by Figure 4.14(a). Generally speaking, any sector is delimited in azimuth by intervals $[N\Delta\phi_2 - \frac{1}{2}\Delta\phi_2; N\Delta\phi_2 + \frac{1}{2}\Delta\phi_2]$ ($N = 0 \dots \frac{360}{\Delta\phi_2}$), wherever ϕ_2 finds its origin axis.

From the averaging grid's configuration point of view, two types of situations must be distinguished: either ϕ_1 is a multiple of $\Delta\phi_2$, or not.

In the first case, the averaging sectors arrangement remains unchanged from the default grid applied when $\phi_1 = 0^\circ$, although the azimuth angles ϕ_2 to which they correspond will depend on the exact value of ϕ_1 (see Figure 4.14(a)).

In the case ϕ_1 is not a multiple of $\Delta\phi_2$, the shift in azimuth does not correspond to entire grid steps anymore, which induces the general grid to be completely different from the default one: sectors ϕ_2 and ψ_2 do not match, as shown on Figure 4.14(b). A new individual grid must therefore be built to subdivide the screen into appropriate averaging sectors. Thanks to the mentioned conditions imposed on $\Delta\phi_2$, it can be kept unique for the six screen positions, with analytical adaptations to be established for the corresponding sectors coordinates (Section 5.4.3).

As illustrated on Figure 4.15, the gathering of pixels on the screen image undergoes a rotation according to the general grid shift. In practice, a $\phi_1 \bmod \Delta\phi_2$ term (equal to 5° for the case displayed on the figure) is added to the M_{ψ_2} matrix and the pixels gathering takes place based on the resulting “shifted” matrix.

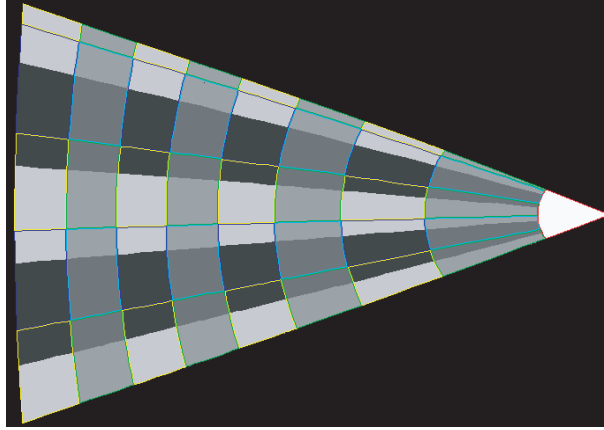


Figure 4.15: Superimposed averaging grids with $(\Delta\theta_2, \Delta\phi_2) = (10^\circ, 15^\circ)$ for $\phi_1 = 50^\circ$ (sectors borders) and $\phi_1 = 0^\circ$ (greyscale level pattern), displaying a 5° shift in azimuth.

4.2.4 Obstruction of emerging light

As mentioned in Section 3.2.4, mechanical constraints induce a gap g between the external sample interface and the detection area base (see Figure 4.16); this gap causes a small fraction of the emerging light not to be detected properly (a few degrees at grazing altitudes). The emerging light path to the projection screen is indeed partially obstructed by either the rotating ring rim or the main platform’s edge (see Figure 4.16), depending on the sample diameter and thickness.

A larger sample diaphragm aperture increases the obstructed part of the hemisphere, as it induces a more important projection screen area only partially illuminated. An increasing sample thickness, on the other hand, lowers the obstruction, as emerging rays are then emitted from a plane closer to the screen detection area base. This only applies for transmission measurements; in reflection mode, a null thickness must be considered to evaluate obstruction for any sample.

As illustrated by Figure 4.17, angle $\theta_{2,\text{lim}}$ is defined as the limit emerging altitude angle for which no light obstruction occurs, i.e. the highest θ_2 angle for which rays starting at the edge of the emitting area (point E) can still reach the projection screen without hindrance. Accounting for illuminated area diameter and sample thickness, its value is determined by the distance d_{bst} and height h_{obst} of the first obstacle to the emerging light path. As can be observed on Figure 4.16, light obstruction is totally avoided as soon as e_s exceeds 6.7 cm.

To take a possible divergence of rays within the characterized sample into account, the diameter D_{out} , larger than D , was considered for estimating obstruction. To assess D_{out} , the difference $\Delta D_{\text{diff}} = \frac{1}{2}(D_{\text{out,meas}} - D_{\text{meas}})$ was first measured with a very diffusing element of thickness $e_{s_{\text{meas}}}$, thus for the most pessimistic situation as far as obstruction is concerned. Then, the following linear extrapolation was applied to determine ΔD for any thickness e_s :

$$D_{\text{out,diff}} = D + \Delta D_{\text{diff}} = D + \frac{e_s}{e_{s_{\text{meas}}}} \Delta D_{\text{meas}} \quad (4.14)$$

where $\Delta D_{\text{meas}} = 0.25$ cm and $e_{s_{\text{meas}}} = 0.6$ cm. For usual sample thickness and diameter, the $\frac{D_{\text{out,diff}}}{D}$ ratio is inferior to 1.1.

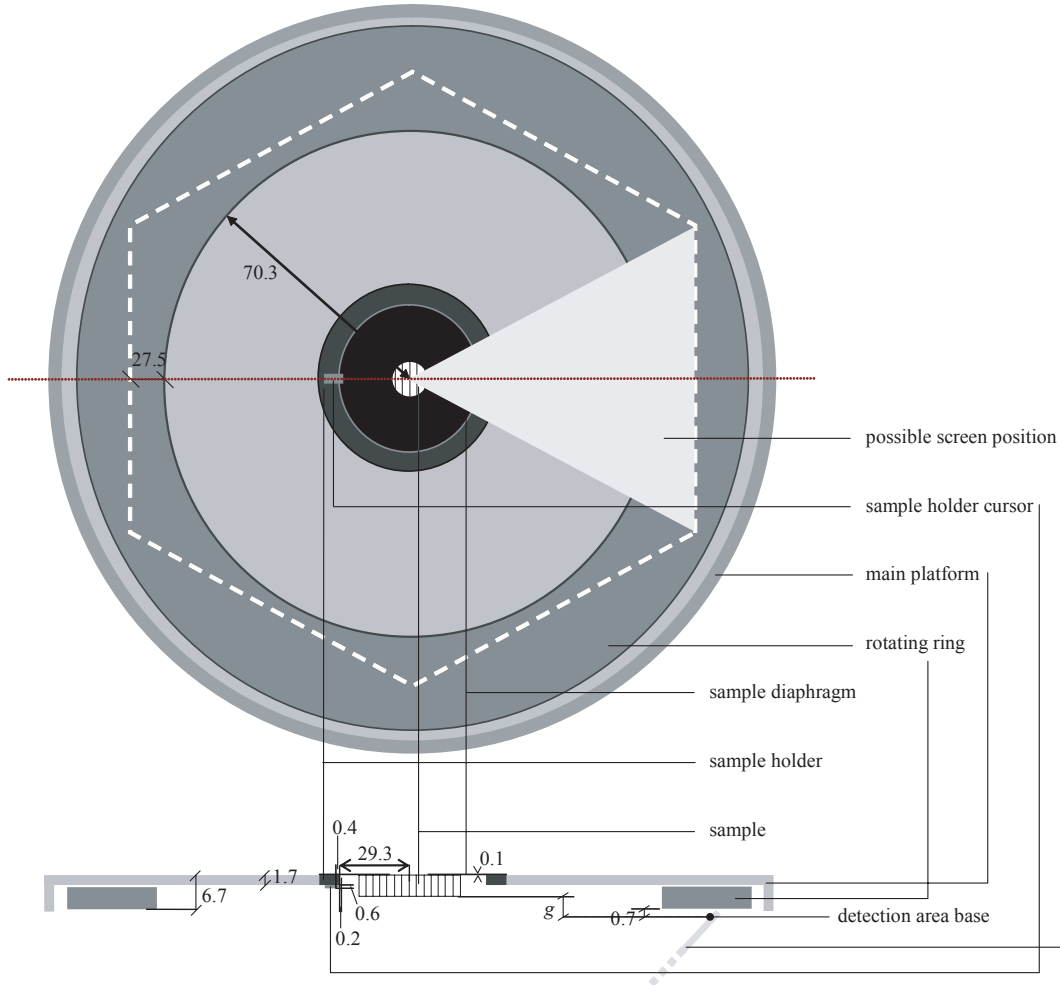


Figure 4.16: Schematic representation of the goniophotometer's mechanical components geometry: plane and section views (all dimensions are given in cm; more detailed views are provided in Appendix A)

Basically, two situations occur: either grazing rays are stopped by the rotating ring rim (i.e. E is under line \overline{AB} in Figure 4.17 and $d_{\text{obst}} = 70.3$ cm, $h_{\text{obst}} = 6.7$ cm) or by the main platform edge. This second case should be considered in its most restrictive configuration, i.e. when the screen is opposite the position appearing on Figure 4.16. This leads the sample holder cursor to be first in the way and means E is above the line \overline{AB} but under \overline{BC} ($d_{\text{obst}} = 29.7$ cm, $h_{\text{obst}} = 2.3$ cm). The configuration E above \overline{BC} never happens in practice because the illuminated diameter D is limited to 30 cm.

Based on this dependence of d_{obst} and h_{obst} on e_s and D , Equation (4.15) can be written, based on trigonometric considerations in the $ABCE$ plane:

$$\theta_{2\text{lim}} = 90^\circ - \arctan \frac{\sin \zeta}{\cos \zeta + \frac{D_{\text{out}} \cdot \sin(\Theta_0 + \zeta)}{2 \cdot \sin \Theta_0 \cdot (\frac{\sqrt{3}}{2} \cdot (H+g) - \frac{D_{\text{out}}}{2} - \frac{e_s}{\tan \Theta_0})}} \quad (4.15)$$

with

$$\zeta = \arctan \frac{h_{\text{obst}} - e_s}{d_{\text{obst}} - \frac{D_{\text{out}}}{2}}$$

To exclude non-representative BT(R)DF data, $\Delta\theta_2$ fringes are only kept if at least half of the associated averaging sectors' area is unobstructed. $\theta_{2\text{max}}$ defines the maximal averaging sector's altitude, i.e. the maximal value of $N \cdot \Delta\theta_2$ for which sectors around emerging directions ($N \cdot \Delta\theta_2, \phi_2$) are maintained; sectors are eliminated if $\theta_{2\text{lim}} \leq \theta_{2\text{max}}$.

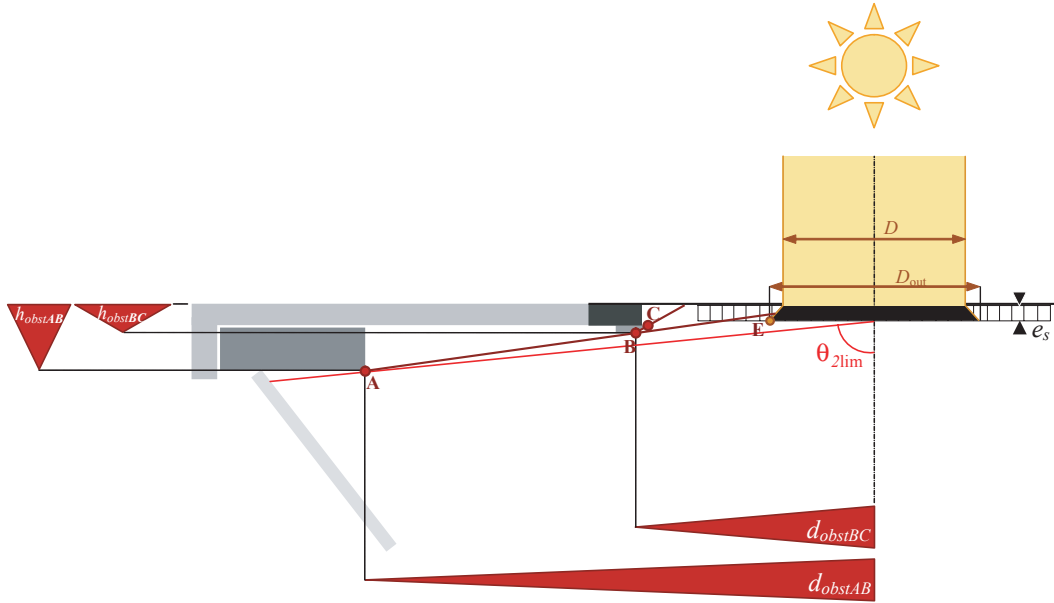


Figure 4.17: Analysis of the different configurations causing an obstruction to emerging light.

Typical $\theta_{2\text{lim}}$ values are given in Table 4.1 for different sample thickness and diameter combinations. It can be observed that even in the worst case of obstruction (large diameter, thin sample), the lost fraction of the emerging hemisphere is lower than 10% ($(90^\circ - \theta_{2\text{lim}}) < 6^\circ$), leading to a low loss of emerging directions, moreover associated to the emerging hemisphere region of least interest (grazing outgoing angles).

e_s (cm)	$\theta_{2\text{lim}D=10\text{cm}}$	$\theta_{2\text{lim}D=20\text{cm}}$	$\theta_{2\text{lim}D=30\text{cm}}$
0.0	84.6°	84.5°	84.4°
1.5	85.8°	85.7°	85.6°
3.0	87.0°	87.0°	86.9°
4.5	88.3°	88.2°	88.2°
6.0	89.5°	89.5°	89.5°
7.5	90.0°	90.0°	90.0°

Table 4.1: Limit altitude $\theta_{2\text{lim}}$ still detectable without obstruction of emerging rays for different sample thickness and diameters.

It must be noted that for grazing incident altitudes θ_1 in reflection mode, an obstruction of the incoming beam can occur due to the presence of the CCD camera in the way. Actually, as θ_1 values are discretized according to 10° steps, this actually only occurs at $\theta_1 = 80^\circ$. To handle this problem, special routines were added in the piloting software, as explained in Section 5.1.2.

4.3 Additional corrections

Other possible sources of experimental error had to be checked to avoid losses of accuracy in the BT(R)DF assessment. Whenever possible, they were compensated or corrected analytically. This section presents the experimental assessment of three critical physical parameters: the incident beam collimation, the uniformity of the pixels response and the parasitic light, mainly due to the incident beam penetration in BRDF mode. A correction procedure was developed for each of them, as detailed below.

4.3.1 Incident beam collimation

The collimation of the incident beam has a strong impact on assessed BT(R)DF values. Indeed, an increasing spread of impinging rays will directly affect the emerging rays' opening angles and induce larger illuminated areas on the projection screen. Therefore, assuming the illuminated sample area to be of diameter D and the beam to be perfectly collimated leads to an underestimation of the projected light emergence areas, influencing monitored BT(R)DF data.

In order to account for the light source spread and proceed to the required correction, the collimation of the incident beam reaching the illuminated area was evaluated experimentally, a correction factor being deduced from the results.

Experimental determination of incident rays collimation

To determine the angular divergence η of the rays reaching the characterized region of the sample, a comparison of the measured (real source) and theoretically expected (perfectly parallel beam) diameters of illuminated areas on the projection screen was realized for different diaphragm apertures in the absence of any sample.

As illustrated in Figure 4.18(a) and expressed in Equation (4.16), the theoretical diameter D_p was calculated from geometrical considerations, based on the projection of a perfectly collimated beam passing through a circular hole of diameter D on a screen tilted by an angle Θ_0 for varying θ_1 angles between the hole plane and the beam axis.

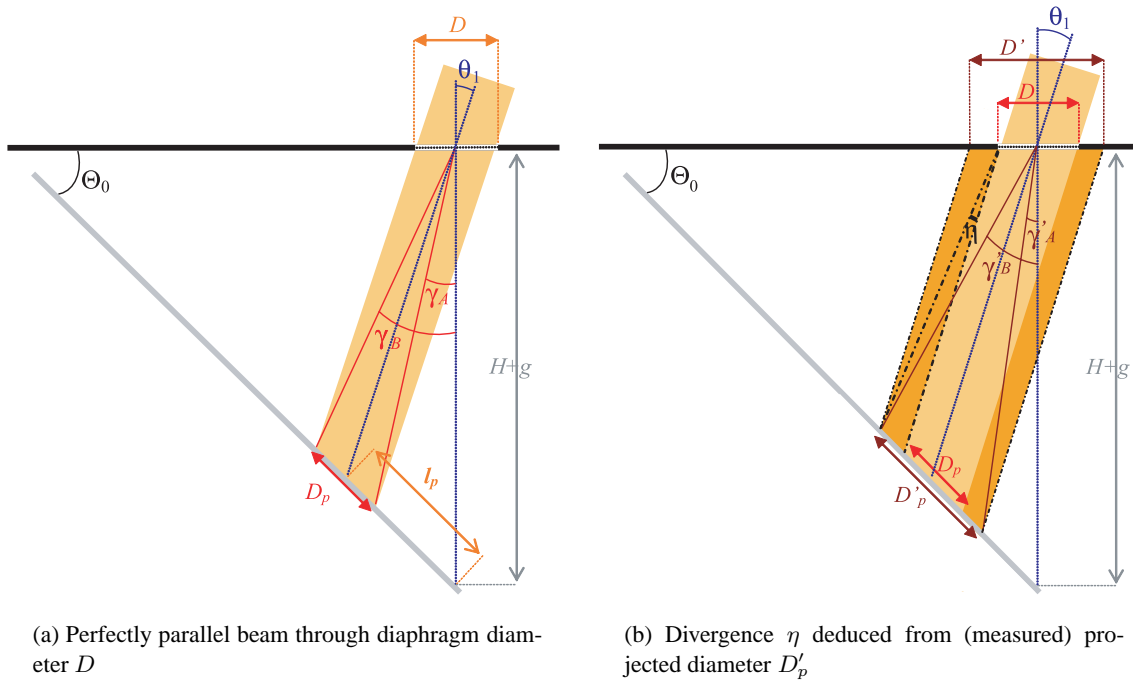


Figure 4.18: Geometric quantities used to evaluate the divergence η of the incident rays reaching the characterized sample area.

Naming l_p the distance between the center of D_p and the screen detection area apex (Equation (4.17)), one can calculate the angles γ_a and γ_b that determine D_p 's edges through Equations (4.18) and (4.19), based on a trigonometric study of Figure 4.18(a):

$$D_p = \frac{D \cdot \cos \theta_1}{\cos(\theta_1 - \Theta_0)} \quad (4.16)$$

$$l_p = \frac{(H + g) \cdot \sin \theta_1}{\cos(\Theta_0 - \theta_1)} \quad (4.17)$$

$$\gamma_a = \arctan \frac{(l_p - \frac{D_p}{2}) \cos \Theta_0}{H + g - (l_p - \frac{D_p}{2}) \cdot \sin \Theta_0} \quad (4.18)$$

$$\gamma_b = \arctan \frac{(l_p + \frac{D_p}{2}) \cos \Theta_0}{H + g - (l_p + \frac{D_p}{2}) \cdot \sin \Theta_0} \quad (4.19)$$

Matrix M_{θ_2} was then used to select the X coordinates of the image pixels associated to angles γ_a and γ_b on the screen central axis (see Figure 4.18(a)), for different D and θ_1 values. This allowed to convert the theoretical diameters $D_p = D_p(D, \theta_1)$ into pixel units.

To compare these results to the actual spot sizes $D'_p(D, \theta_1)$ observed on the projection screen (see Figure 4.18(b)), the greyscale level variations along the central screen axis of images corresponding to the same parameters D and θ_1 were studied.

These line profiles were then normalized and compared to theoretical step functions from light to darkness, based on the D_p values expressed in pixels. Integrating both functions, one can evaluate to what extent they differ from each other.

Figure 4.19 provides two examples of such profiles that were obtained for a diameter $D = 10$ cm for the former (Section 3.2.3) and present (Section 3.4.1) light sources. As can be observed on these figures - and was confirmed by the quantitative analysis of integrated values -, the collimation of the second source is significantly better, the difference with the theoretical step being about 3 times smaller on average.

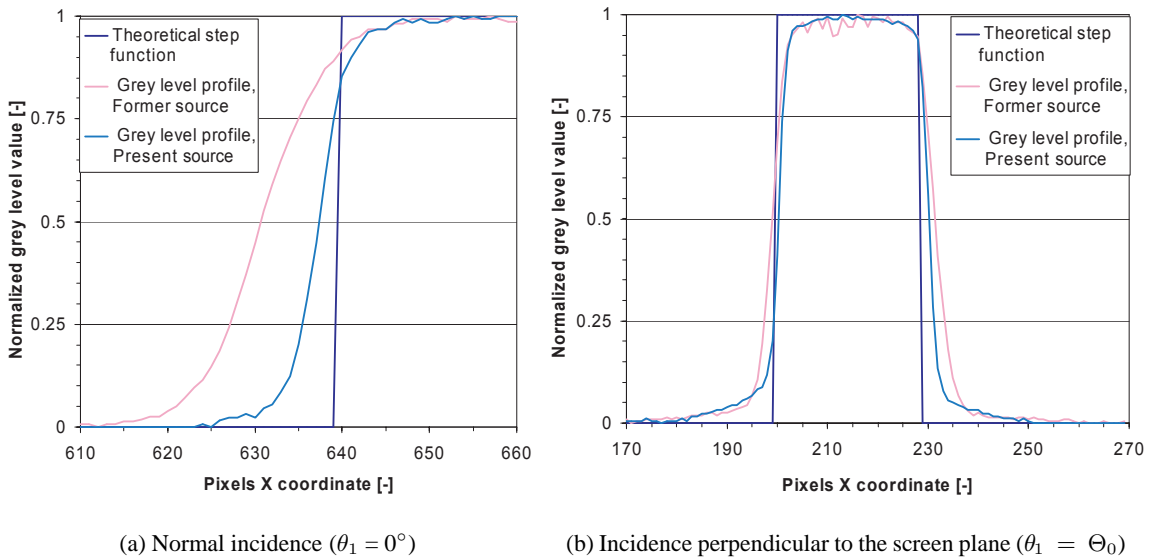


Figure 4.19: Greyscale level profiles observed on the screen projection image compared to the theoretical step function expected with perfectly parallel rays (10 cm diameter diaphragm, single aperture).

For each (D, θ_1) configuration, a value for η was determined in three steps:

- First, the γ'_a and γ'_b angles that would produce projected diameters equal to the measured $D'_p(D, \theta_1)$ (see Figure 4.18(b)) were calculated using matrix M_{θ_2} to convert D'_p values expressed in pixels into polar angles;
- Then, the diameter D' that would be required to achieve such projected diameters D'_p with perfectly parallel rays was deduced from the obtained values for γ'_a and γ'_b through Equa-

tion (4.20), using similar trigonometric considerations as for Equations (4.16) to (4.19) but based on Figure 4.18(b):

$$D' = \frac{(H + g) \cdot \cos(\Theta_0 - \theta_1)}{\cos \theta_1} \cdot \left(\frac{\sin \gamma'_b}{\cos(\Theta_0 - \gamma'_b)} - \frac{\sin \gamma'_a}{\cos(\Theta_0 - \gamma'_a)} \right) \quad (4.20)$$

- Finally, divergence angles $\eta(D, \theta_1)$ were calculated from Equation (4.21):

$$\eta = \arctan \frac{\frac{1}{2}(D' - D)}{H + g - \frac{D'}{2} \cdot \tan \Theta_0} \quad (4.21)$$

The obtained values for η vary from 0.4° to 1.1° for the former source and from 0.1° to 0.3° for the actual one, for increasing apparent diameters $D \cdot \cos \theta_1$ with $10 \text{ cm} \leq D \leq 30 \text{ cm}$ and $0^\circ \leq \theta_1 \leq 70^\circ$.

Diameter correction factor

Although very low for the actual source thanks to the great distance from source to sample, such η values proved of significant influence for the BTDF assessment with the former source. Indeed, as BT(R)DFs are deduced from quantities directly dependent on the sample illuminated area, even small corrections on its diameter can have a significant impact on the final BT(R)DF data ($A = \pi \frac{D^2}{4} \Rightarrow \frac{\Delta A}{A} = \sqrt{2} \frac{\Delta D}{D}$).

Based on the measured $D'(D, \theta_1)$ values, ratios $\frac{D'}{D}$ were deduced and averaged according to similar apparent diameters $D \cdot \cos \theta_1$. A set of correction factors was thus determined and applied to the sample area parameter each time it was called during the characterization process, detailed in Chapter 5.

The resulting correction factors range from 1.04 to 1.02 for the former source and remain very close to 1.01 for the present one. The correction was thus significant in the first case, where the BTDF results showed an improved accuracy once it was applied. The procedure was kept for the actual source as well, even though the impact on BT(R)DFs was generally lower than 2% in relative terms.

4.3.2 Image uniformity

Because of the CCD camera's optical system (CCD component sensitivity and lens aberrations), a slight darkening of the image towards its borders was observed. As even small variations in the pixels greyscale values can induce significant changes in their associated luminances (especially for short integration intervals), it was important to quantify this effect and if possible correct it.

The uniformity of the captured images was thus assessed in details and a correction figure created, as explained below. The compensation must take place on the pixels greyscale values directly (non-calibrated, 8 bits images), as it does not depend on the object aimed at by the camera; of course, it still impacts directly on the corresponding luminances, deduced from the pixels response.

Experimental assessment of image uniformity

This procedure aims at controlling whether a uniform luminance distribution produces an image of equal greyscale levels, and if not at quantifying the difference between the actual and expected pixels response.

For this purpose, a calibrated light source was used and a small diffusing element placed in front of it to get an object emitting a constant luminance from a defined surface. Several images

of this object were captured by the CCD camera at different integration intervals and for varying relative positions of the latter, moved from one position to another in a same vertical plane; this allowed to have the bright spot of constant luminance appear in various places of the image. Integration times were varied from 40 ms to 640 ms, beyond which pixels were saturated: such a range of exposures offered a stronger statistical set of data and provided a way to verify that darkening was indeed independent from the exposure.

After covering the screen image area with an extensive set of measured regions, storing the (X, Y) coordinates and the greyscale values of the corresponding pixels, an analysis of their response was made in regard to the maximal level obtained over the whole image.

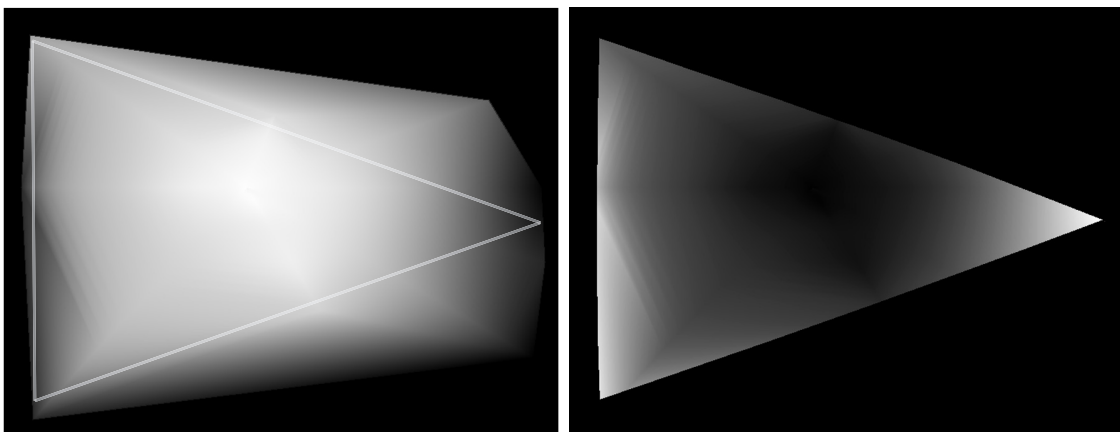
The obtained results confirmed that the inhomogeneity of the greyscale values was not dependent on the integration interval, the variations from one exposure to another being very low ($\sim 0.2\%$) and showing no systematic relation. The darkening effects induced relative errors of up to 5.6%, but remained generally lower.

Creation of correction figure

Based on the measured greyscale level variations, a correction mask was created. First, a surface interpolation between the experimentally determined greyscale level differences at pixels coordinates (X, Y) had to be achieved; this was done for all other coordinates inside the screen image area to produce a matrix reproducing the now quantified darkening effect.

The obtained matrix coefficients are represented on a grey level scale in Figure 4.20(a), where the 0 to 255 dynamic fits the 5.6% maximal difference and thus enhances greatly the actual pixels darkening effects; screen edges are added on the figure for easier comparison with Figure 4.20(b).

Then, a correction figure was created based on this matrix, providing the factors by which each (X, Y) pixel will be multiplied to compensate the darkening effect, comprised between 1 and 1.056. The obtained figure is shown on Figure 4.20(b) with, again, a greyscale level dynamic adapted to the correction factors range.



(a) Darkening effect over the investigated image area

(b) Correction factors over the screen area

Figure 4.20: Representation of the image darkening effect and the correction figure based on a surface interpolation of monitored data.

4.3.3 Parasitic light

Whether in transmission or in reflection mode, parasitic light due to internal reflections of light fluxes emerging from the sample is unavoidable; these reflections occur either after the light flux is re-diffused by the projection screen, or directly, if it is emitted in directions out of the currently collected $\frac{2\pi}{6}$ steradian portion of hemisphere. They can however be minimized and made negligible by choosing highly absorbing materials for the goniophotometer's inner surfaces that were therefore covered with "velvetine", as mentioned in Section 3.2.2. This precaution proved to be successful, as explained below.

Of course, light penetrations through the joints of the measurement space envelope components were first carefully checked and filled in to make the device tight to any external light flux.

In reflection mode, an additional source of parasitic light is caused by the reflection of the incoming beam around the sample, necessary to achieve a sufficiently uniform sample illuminance (see Section 3.4.1). To reduce it to a minimum, a 10 cm large ring of "velvetine" was added around the sample diaphragms apertures, which brought these reflections below the camera's detection threshold, as explained below.

Quantifying "black"

First, an analysis was carried out with a fully opaque sample to determine the pixel greyscale and luminance values that were to be associated with "black". Pictures were taken at all used integration intervals. The maximal greyscale level observed on the images was 48 independently of the exposure, with a mean value of 42.5. By extrapolating the photometric curve to 48 (see Figure 4.5) for the longest integration interval (2.56 s), a luminance of $0.26 \text{ Cd}\cdot\text{m}^{-2}$ was found.

It was then verified whether for a highly transmitting (or similarly reflecting) element, internal reflections would not affect the BT(R)DF assessment. For this purpose, new pictures were taken in the absence of any sample (100% transmission) and converted into luminance maps without putting values below greyscale level 49 to zero, but using instead extrapolated photometric curves.

The luminances obtained out of the illuminated screen area were analyzed for all six screen positions: it was observed that the "background" value was of about $0.28 \text{ Cd}\cdot\text{m}^{-2}$ in average, which was therefore extremely close to the $0.26 \text{ Cd}\cdot\text{m}^{-2}$ found for the "black" definition. Hence, this value could be considered negligible.

This allowed to show that setting the photometric calibration curves to 0 for grey levels below 49 was sufficient to avoid any significant influence of internal reflection. This method implicates that screen luminance values inferior to $0.3 \text{ Cd}\cdot\text{m}^{-2}$ are not detected for the standard set of integration intervals; however, such a limit is more than reasonable considering that it represents only 0.01% of the detectable screen luminance range.

Parasitic light caused by beam penetration

When the incident beam passes through the controlling elliptic opening, reflections on the edges of the metal sheet ellipse cannot be prevented. As the CCD camera is obviously not aligned with the pair of sheet and screen ellipses, this effect can be viewed directly on the images, because the sheet ellipses appear shifted behind the screen openings.

To assess its impact on a BRDF assessment as well as the extent to which reflections around the sample could possibly affect the monitored data, pictures of the screen were taken at the longest integration interval and for a highly absorbing sample ("velvetine" sheet) for the six screen positions, with θ_1 varying from 0° to 80° with 10° steps.

As can be observed on Figure 4.21, the reflections on the metal sheet ellipse edges produced a fine but bright luminous crescent to be removed from the measurements. Fortunately, the brightest pixels of this crescent were in fact inside the screen's elliptic cover area, thus automatically excluded from the BRDF assessment (see Sections 4.2.2 and 5.2.2); the few bright pixels out of these ellipses were eliminated by extending the screen covers borders accordingly (see Figure 4.10(b)).

However, a part of this reflected light undergoes a second reflection on the screen opening edges this time, producing some remaining parasitic light around the latter (of course only detectable at the longest integration interval). For characterized systems presenting very low reflective properties, this small effect can nevertheless be significant, and a software procedure was therefore developed to compensate it.

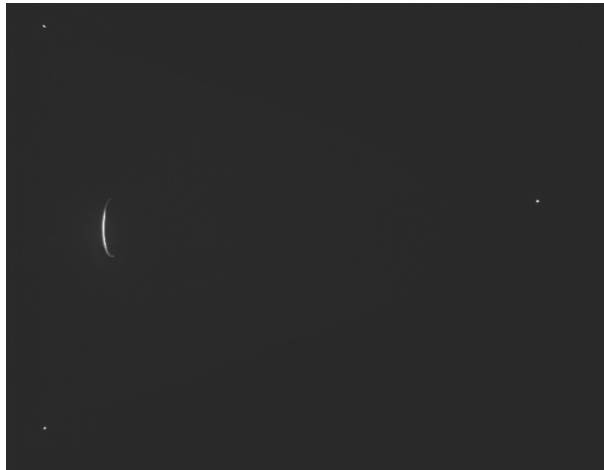


Figure 4.21: Reflection of penetrating beam on the controlling ellipse edges for an incidence $\theta_1 = 70^\circ$.

Based on the captured images with the “velvetine” sheet, an analysis of the maximum greyscale levels reached by all non-eliminated pixels was made to determine the screen positions and θ angles where a compensation was required.

At all altitudes θ_1 , only the obstructing screen position proved to be critical, i.e. a single position for all θ_1 angles in-between 10° and 80° and all six for normal incidence. This result allowed two important statements:

- the reflection effects on the edges of the screen openings were indeed the ones responsible for the remaining parasitic light observed on long exposed images;
- the addition of a “velvetine” ring around the sample to absorb the non-uniform excess of incident light was sufficient to prevent any significant parasitic reflections from this area, as a fully illuminated “velvetine” sample already presented undetectable, thus negligible, reflective properties.

During a BRDF characterization and only for the critical screen positions, the created luminance maps (corresponding to situations that should be completely dark) are subtracted from the once calibrated screen images, as explained in Section 5.3.2.

Chapter 5

Command and processing

“If you torture the data long enough, Nature will confess.” (Ronald Coase)

5.1 Characterization process for bidirectional measurements

The BT(R)DF characterization aims to produce three kinds of deliverables:

- a BT(R)DF data file for each incident direction (θ_1, ϕ_1) , providing monitored values for every emerging direction (θ_2, ϕ_2) ;
- an image-based recombination of the emerging hemisphere that gathers the six screen views captured by the CCD camera;
- a 3D synthetic representation of the data, to provide an intuitive and efficient visualization of the monitored results.

An outline of the command interface developed for this purpose is given below (more details can be found in Appendix B), as well as an overview of the sequence of events taking place during a monitoring procedure. The major processing phases appearing in this overview are explained further in this chapter. The last section presents the different graphical representations developed for BT(R)DF data, as well as some application examples.

5.1.1 Command interface

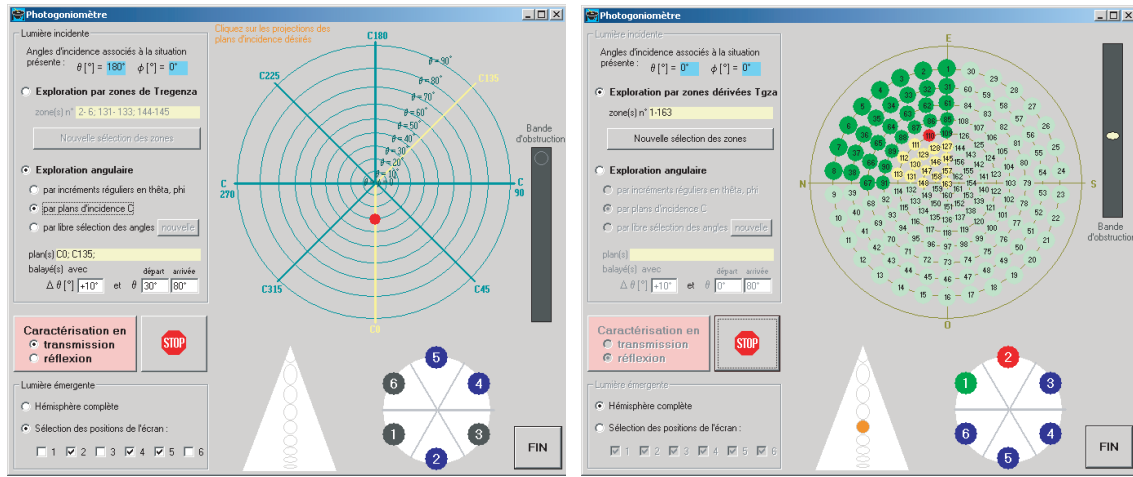
A full automation of the BT(R)DF assessment procedure is of course essential to make the measurement device powerful. A special effort was put in designing a user-friendly interface, that provides a graphical information during the characterization process and allows as much freedom as possible on the incidence and emergence monitoring parameters. At the same time, it must of course efficiently control the driving of the goniophotometer as well as the image acquisition and final processing.

The driving software was developed in Microsoft Visual Basic^{®1}, allowing the implementation of Image-Pro Plus[®] commands with specific dll files, as well as an efficient data exchange with Matlab[®] via a DDE (Dynamic Data Exchange) protocol.

The main user interface is shown on Figure 5.1, when defining the characterization parameters in transmission mode (Figure 5.1(a)) and during a monitoring process in reflection mode (Figure 5.1(b)). The mode selection is simply chosen by the appropriate option on the main command button, and all necessary referential and parametric adaptations are applied instantaneously.

¹Microsoft Visual Basic[®] 6.0 for 32-bit Windows Development, Microsoft Corp.

As can be observed on these figures, graphics are paired with a textual window as well for the incidence parameters (set of incident directions (θ_1, ϕ_1) and moving strip status for beam penetration) as for the selection of screen positions and the covers configuration. This allows an easy follow-up of the monitoring procedure and provides the user with appreciable flexibility during both calibration and real BT(R)DF measurement phases.



(a) Selection of BTDF monitoring parameters

(b) Display of BRDF monitoring status

Figure 5.1: Driving software interface for BT(R)DF assessment.

As shown on Figure B.1, side windows specifically designed for the goniophotometer's operations (hidden in Figure 5.1) are included in the interface as well, and allow a status control and individual movements of the main platform, the rotating ring, the sample, the moving strip or the motorized wagon for screen covers extraction. Choosing to run only certain monitoring phases is also possible (averaging grid creation, image capture, image processing, recombined visualization, final data file), which is particularly useful for testing operations.

The reader is referred to Appendix B for more details about the interface's features. The possible options for the set of incident directions and emergence parameters are explained, and a more extensive description of a monitoring process from the user's point of view is given, together with the final BT(R)DF data file format.

5.1.2 Program structure

Figure 5.2 outlines the general program structure developed to achieve a BT(R)DF assessment for an arbitrary set of incident directions $(\theta_{1_i}, \phi_{1_i})$ for $i = 1 \dots N_i$, N_i being the total number of incident directions; the selection of screen positions p is defined by arbitrary first and last positions p_{\min} and p_{\max} , generally equal to 1 and 6.

As can be observed on this flow-chart, the different procedures necessary to extract BT(R)DF data from raw (8 bits) digital images for defined incidence configurations are executed as follows:

- After initializing the motor command parameters, a homing of all axes is executed before being moved to their respective zero positions. Thereafter, an image is captured by the CCD camera to locate the three screen positioning LED's (see Section 4.2.1).
- The incidence and exploration parameters are selected using either graphical or textual functionalities of the interface: exploration type and investigation steps in incidence, screen positions in emergence (see Section B.1 for details).

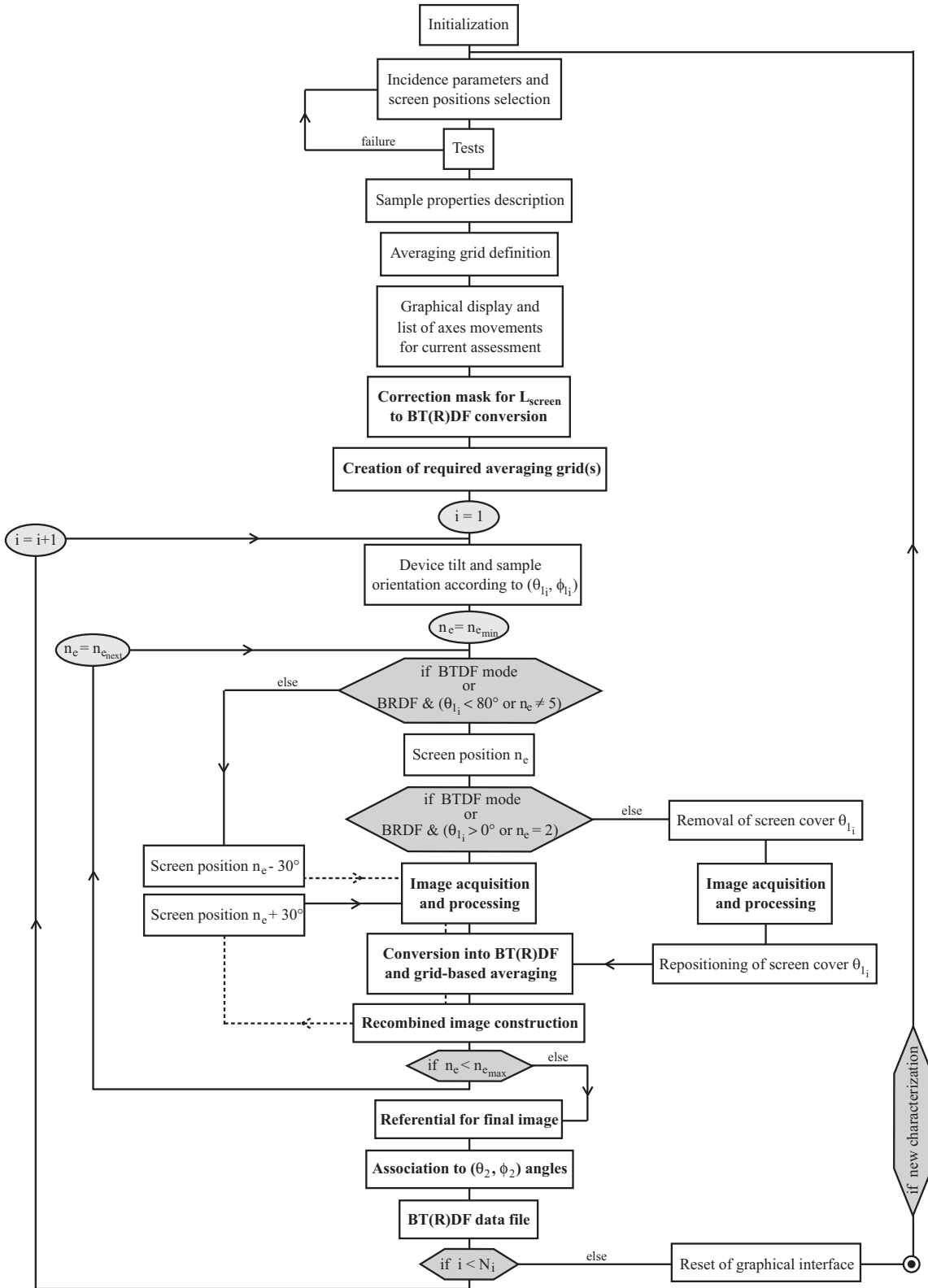


Figure 5.2: Synoptic flow-chart of major phases for BT(R)DF assessment.

- After the chosen parameters are tested successfully (see Section B.2), a new window appears, shown on Figure B.8(a), used to describe the sample's properties. If applicable, symmetries are accounted for to reduce the set of incident directions (see Section B.1.1).

- Based on the sample diameter D , angular intervals $\Delta\theta_2$ and $\Delta\phi_2$ are recommended in order to apply an optimal averaging grid on the digital BT(R)DF maps (see Section B.1.3).
- As explained in details in Section 5.2, matrices corresponding to the new averaging grid configurations are created via a DDE protocol with Matlab[®], accounting for parameters e_s , D , θ_1 (only in reflection mode), ϕ_1 , $\Delta\theta_2$, $\Delta\phi_2$, $\theta_{2_{\text{lim}}}$ and $\theta_{2_{\text{max}}}$.
- At the same time, a correction mask for the L_{screen} to $BT(R)DF$ conversion is calculated based on Equation (5.7) and using matrices M_{θ_2} , M_{ψ_2} and M_d .
- When this unique preparatory phase is completed, a double-loop procedure is initiated: at each new incident direction (θ_1, ϕ_1) , the main platform and the sample holder axes are first positioned properly, and the graphical interface is actualized. The following sequence is then achieved:
 - If $\theta_1 = 80^\circ$ and $p = 5$ in reflection mode, the camera is in the way of the incoming beam. A third loop is then required (cf. Figure 5.2) as two screen positions will be necessary to make up p , respectively shifted by $+30^\circ$ and -30° (or by $\pm \text{Int}(\frac{30}{\Delta\phi_2})$ if $\Delta\phi_2$ is not a divisor of 30).
 - At each screen position p , a set of images is captured by the CCD camera, at all integration times necessary to cover the current luminance dynamic; they are then processed to achieve a complete $\frac{L_{\text{screen}}}{E_1(\theta_1)}$ mapping of the projection screen, as detailed in Sections 5.3.1 and 5.3.2. If the screen is in a critical position (obstruction of the incident beam path in reflection mode), these procedures are preceded and followed by the removal and repositioning of the appropriate screen cover.
 - A correction factor is applied at the pixel level to compensate distance and light tilt effects by multiplying the resulting image with the associated correction mask created beforehand, leading to a BT(R)DF image map of screen position p (see Section 5.4.1). Then, applying the adequate averaging grid, the calibrated pixels are gathered in $(\Delta\theta_2, \Delta\phi_2)$ angular sectors (see Section 5.4.3).
 - The BT(R)DF image map is thereafter processed to be included in a full visualization of the emerging hemisphere, combining all selected screen positions into one global image (see Section 5.3.3).
- When all screen positions have been investigated, the recombined image is adapted to fit a unique default referential to allow reliable comparisons.
- The weighted averages of the different angular sectors are calculated and associated with their respective direction (θ_2, ϕ_2) .
- Finally, a complete BT(R)DF data file of consistent format is created for the current incident direction (θ_1, ϕ_1) (cf. Section B.2.1).
- The graphical interface is then reset to its initial configuration; all exploration parameters are re-initialized for the program to be ready for a new characterization process.

The following sections describe in further detail some of the major procedures taking place in this assessment process and that appear in bold characters in Figure 5.2. They are organized slightly differently from their strict chronology for a more coherent structure.

5.2 Averaging grid for BT(R)DF data

The assessment method of the bidirectional goniophotometer differs from conventional ones in the way that it splits the emerging hemisphere into a regular grid of averaging sectors ($\Delta\theta_2$, $\Delta\phi_2$), as illustrated in Figure 5.3(a). Any risk of missing a discontinuity in the emerging luminance figure is thus prevented. This method allows to produce a finite set of BT(R)DF data, each associated to a foursome $(\theta_1, \phi_1, \theta_2, \phi_2)$ where the apparent gaps $\Delta\theta_2$ and $\Delta\phi_2$ between two data do not determine their resolution (as would be the case in a conventional scanning process where interpolation is implicit): they just provide the angular distance between two averaging sectors centers (θ, ϕ_2) and $(\theta_2, \phi_2 \pm \Delta\phi_2)$ or $(\theta_2 \pm \Delta\theta_2, \phi_2)$, that all truly represent adjacent hemisphere portions.

$\Delta\theta_2$ and $\Delta\phi_2$ are only limited by the angular dimensions of the digital image's pixels, of about 0.1° and 0.3° in altitude and azimuth respectively (mean values over the screen area). However, such extreme definitions are very rarely required for fenestration systems assessment, especially as the illuminated sample area is likely to be of 10 or 15 cm diameter. Indeed, to remain consistent with the possible divergence of rays reaching a given point, the chosen angular resolution must remain coherent with the illuminated sample area (see Section B.1.3), requiring the definition of $\Delta\theta_2$ and $\Delta\phi_2$ to be flexible. As BT(R)DF applications can vary greatly (industry, architecture, daylighting simulation tools), such a flexibility is also preferable to respond to different requests in spatial definition.

The assessment of BT(R)DF data being based on the assessment of the luminance distribution $L_{\text{screen}}(\theta_2, \phi_2)$ on a triangular projection surface, the latter must be divided into a grid of averaging sectors corresponding to angular intervals $\Delta\theta_2$ and $\Delta\phi_2$; these sectors are thus limited by $[\theta_2 - \frac{1}{2}\Delta\theta_2; \theta_2 + \frac{1}{2}\Delta\theta_2[$ in altitude and by $[\phi_2 - \frac{1}{2}\Delta\phi_2; \phi_2 + \frac{1}{2}\Delta\phi_2[$ in azimuth for each direction (θ_2, ϕ_2) . Their size (i.e. the number of comprised pixels) is hence inversely proportional to the number of outgoing directions. Two examples of such grids are illustrated by greyscale level patterns on Figures 5.3(b) and 5.3(c) for $(\Delta\theta_2, \Delta\phi_2)$ equal to $(5^\circ, 5^\circ)$ and $(10^\circ, 15^\circ)$ respectively.

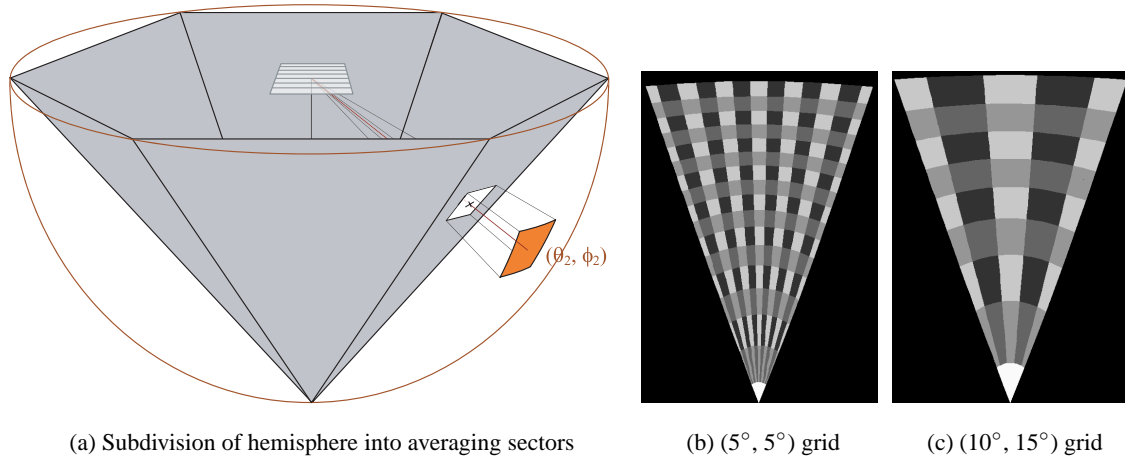


Figure 5.3: Averaging grid for BT(R)DF data according to angular intervals $(\Delta\theta_2, \Delta\phi_2)$.

To optimize averaging grids regarding spatial accuracy, a flexible and accurate matrix-based method was developed and is explained below. Its major phases were outlined in Andersen (2001) and described more extensively in Andersen (In Press). It was experimented successfully for usual and critical situations: coherent results were provided in the determination of averaging sectors and showed no restrictions on sample properties or grid definitions. As these calculation procedures take place before the iterative measurement sequence (and are re-used for further characterizations), they induce no lengthening in a BT(R)DF assessment.

5.2.1 Pixel gathering according to angular grid

A new screen averaging grid has to be defined for every new combination of the five variables: e_s , D , $\Delta\theta_2$, $\Delta\phi_2$ and S_ψ , where S_ψ defines the minimal azimuth shift, equal to $\phi_1 \bmod \Delta\phi_2$ (see Section 4.2.3). A sixth variable providing altitude θ_1 needs to be added for BRDF measurements, to account for eliminated pixels (blind spot) when a screen cover is removed.

To minimize the grid construction procedure, several checks are first applied to partially or fully re-use existing grids stored during previous characterizations. A DDE protocol is then launched with Matlab[®] for the construction of the N_G new averaging grids, associated to the different S_ψ shifts defined in Section 4.2.3.

Before creating individual $(\Delta\theta_2, \Delta\phi_2)$ clusters of matrix coefficients, the latter are gathered in $\Delta\theta_2$ and $\Delta\phi_2$ groups: using matrices M_{θ_2} and M_{ψ_2} , two sets of binary matrices are created:

- $M_{\{\theta\}}$ for the gathering of altitude coefficients within $\Delta\theta_2$ intervals;
- $M_{\{\psi\}}$ for the gathering of azimuth coefficients within $\Delta\phi_2$ intervals.

For a given $\Delta\theta_2$, a different $M_{\{\theta\}}$ matrix is associated to every discrete θ_2 value between 0 and $\theta_{2\max}$ (according to a $\Delta\theta_2$ step), leading to $\frac{\theta_{2\max}}{\Delta\theta_2} + 1$ binary altitude matrices in total; the “+1” includes the screen apex sector (corresponding to $\theta_2 = 0^\circ$).

These matrices are calculated from M_{θ_2} and thus depend on e_s ; their coefficients are equal to 1 when related to coefficients in M_{θ_2} comprised within a same $\Delta\theta_2$ interval, otherwise equal to 0. For each discrete θ_2 value, $M_{\{\theta\}}(\theta_2)$ thus presents non-zero coefficients only at coordinates corresponding to M_{θ_2} coefficients within the $\theta_2 \pm \frac{1}{2}\Delta\theta_2$ interval.

To account for the limit altitude angle $\theta_{2\lim}$ defined in Section 4.2.4, all coefficients with θ_2 values either superior to $\theta_{2\lim}$ or to $(\theta_{2\max} + \frac{1}{2}\Delta\theta_2)$ are put to zero; the matrices $M_{\{\theta\}}(\theta_2)$ therefore depend on D as well.

Binary matrices $M_{\{\psi\}}$ also represent groups of azimuth values within a same $\Delta\phi_2$ interval, but need to account for the azimuth shift parameter S_ψ too.

For each shift S_ψ (in total N_G shifts), a different $M_{\psi'_2}$ matrix is calculated by adding S_ψ to M_{ψ_2} . The resulting ψ'_2 coefficients can then be gathered for each $M_{\psi'_2}$ matrix (in total N_G matrices) according to $\Delta\phi_2$ intervals:

- as the number and configuration of ψ'_2 intervals on the screen depend on both $\Delta\phi_2$ and S_ψ , a function of these parameters is needed to delimit the values of the discrete steps $0, \pm\Delta\phi_2, \pm 2 \cdot \Delta\phi_2 \dots$ around which ψ'_2 values are gathered; this function is named $L_{\psi'_2\pm}$ (index “-” for the lower limit on the screen, “+” for the upper limit);
- for a given $\Delta\phi_2$ and for each shift S_ψ , a different $M_{\{\psi\}}$ matrix is associated to every discrete ψ'_2 value between $L_{\psi'_2-}$ and $L_{\psi'_2+}$; this leads to $N_G \cdot \left(\frac{L_{\psi'_2+} - L_{\psi'_2-}}{\Delta\phi_2} + 1 \right)$ binary azimuth matrices in total; the “+1” term takes into account that a single sector overlapping two screen positions has to be counted twice;
- these matrices present coefficients equal to 1 when related to coefficients in $M_{\psi'_2}$ comprised within a same $\Delta\phi_2$ interval, otherwise equal to 0. For each discrete ψ'_2 value and each S_ψ , $M_{\{\psi\}}(\psi'_2, S_\psi)$ thus presents non-zero coefficients only at coordinates corresponding to $M_{\psi'_2}$ coefficients within the $\psi'_2 \pm \frac{1}{2}\Delta\phi_2$ interval.

Once all the matrices $M_{\{\theta\}}(\theta_2)$ and $M_{\{\psi\}}(\psi'_2, S_\psi)$ are available, their element-per-element multiplications according to pairs of values θ_2 and ψ'_2 are used to determine the different averaging sectors $(\Delta\theta_2, \Delta\phi_2)$ around directions (θ_2, ψ'_2) for each shift situation S_ψ .

The resulting groups of non-zero coefficients can in principle be applied almost directly during a characterization process: once the image pixels are fully calibrated into BT(R)DFs, the image is imported as a matrix into Matlab[®] and the coefficients averaged according to intervals $(\Delta\theta_2, \Delta\phi_2)$. This method was tested successfully; however, as this loop sequence takes place at every screen position, the processing time is increased significantly, especially for fine averaging grids (small $\Delta\theta_2$ and/or $\Delta\phi_2$ values): 20 more seconds were necessary at each screen position for a $(5^\circ, 5^\circ)$ grid).

As Image-Pro Plus[®] proposes a very efficient method for analyzing an image within defined groups of pixels, this method was adapted to take advantage of it, adding several operations on the $M_{\{\theta\}}(\theta_2)$ and $M_{\{\psi\}}(\psi'_2, S_\psi)$ matrices to create greyscale level patterns out of them. The latter are used by Image-Pro Plus[®] as supports for outlining the pixels groups properly. Examples are shown on Figures 5.3(b) and 5.3(c); their construction is explained below.

5.2.2 Grid assembling

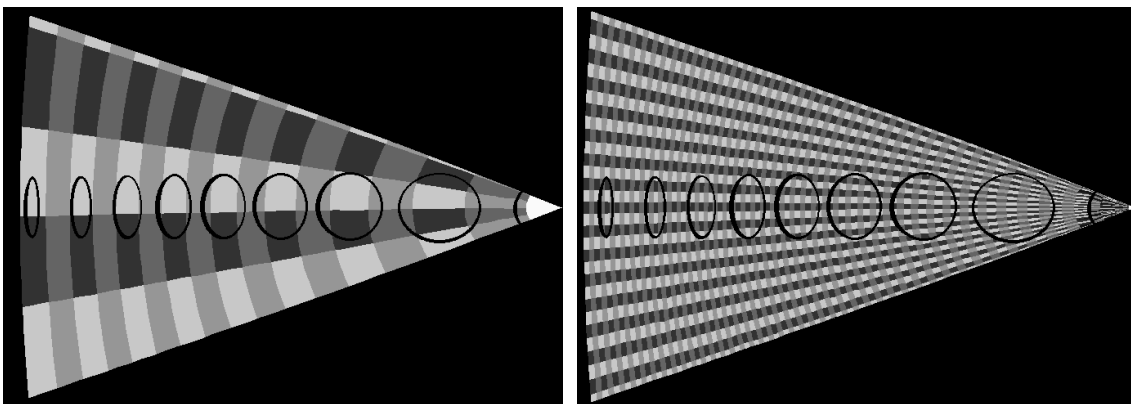
The averaging grid sectors can either be delimited by a network of lines or by a greyscale level pattern. In order not to loose boundary pixels, the second option was chosen.

This pattern must consist of 8-connected clusters of pixels (i.e. with a shared edge or adjoining corner) presenting different greyscale values if they are associated to different adjacent sectors.

In consequence, the set of matrices resulting from the $M_{\{\theta\}}(\theta_2)$ by $M_{\{\psi\}}(\psi'_2, S_\psi)$ multiplications for each combination of θ_2 , ψ'_2 and S_ψ parameters are first assembled within binary matrices in a way that no cluster of non-zero coefficients is 8-connected to another. Before being gathered into one complete matrix, a greyscale level class is associated to each one of them. The number of such classes is limited to 16 because of Image-Pro Plus[®] constraints imposed on the range of usable greyscale levels for outlining pixels groups; however, five classes (equal to 50, 100, 150, 200 and 250) are generally sufficient to delimit all coefficients clusters properly, as in Figures 5.3(b) and 5.3(c) for instance.

Finally, the coefficients corresponding to the borders of the screen covers are removed (put to *NaN*), which often creates distinct sub-sectors associated to a same averaging sector (θ_2, ψ'_2) .

The N_G resulting matrices are then converted into 8 bits images of corresponding greyscale level patterns. Two examples are illustrated in Figure 5.4 for different grid configurations, alternating from one class to the other to ensure that the averaging sectors are fully determined.



(a) $(\Delta\theta_2, \Delta\phi_2) = (5^\circ, 5^\circ)$, $S_\psi = 4$: five classes

(b) $(\Delta\theta_2, \Delta\phi_2) = (1^\circ, 2^\circ)$, $S_\psi = 0$: six classes

Figure 5.4: Grey level patterns for averaging grid outlining.

For each sub-sector, a set of five parameters are determined:

- $N_{\theta\psi'}$ specifies its cipher according to a numbering based on an angular logic: θ_2 decreasing from $\theta_{2\max}$ to 0, with ψ'_2 increasing from $L_{\psi'_2-}(S_\psi)$ to $L_{\psi'_2+}(S_\psi)$ at each θ_2 ;
- N_{IP+} defines what number, amongst the total list of outlines that Image-Pro Plus[®] will produce, this particular sub-sector will be associated to: N_{IP+} thus follows the Image-Pro Plus[®] numbering logic, illustrated in Figure 5.5, and sorts the outlines per class (from the highest grey value to the lowest) according to the minimal coordinates X and Y of the comprised pixels, from the lowest Y then X to the largest (X and Y finding their origin in the top left-hand corner of the image).
- Variable N_{subZ} is superior to 1 if the averaging sector to which the sub-sector belongs contains more than one of them;
- Sometimes, an averaging sector doesn't find associated pixels (typically for small $\Delta\phi_2$ values and low θ_2 , like on Figure 5.4(b) close to the screen summit); in this case, it will be twinned with the closest existing one. All sub-sectors belonging to the latter will then get their parameter $N_{\text{non}\exists}$ superior to one. This does not concern the possibly eliminated sectors due to the blind spot induced by a removed cover (as in Figure 5.5), treated with the last parameter N_{blind} ;
- N_{blind} is a variable set to θ_1 if the sub-sector is eliminated when the elliptic cover around θ_1 is removed in reflection mode; it is set to -1 if never affected. This parameter thus allows to predict the new Image-Pro Plus[®] count taking place when a blind zone appears.

A matrix containing variables $N_{\theta\psi'}$, N_{IP+} , N_{subZ} , $N_{\text{non}\exists}$ and N_{blind} for all sub-sectors is finally sent back to Visual Basic via DDE.

Based on the N_G greyscale level patterns imported into Image-Pro Plus[®], the corresponding grids of outlines can be created according to a number of classes equal to the number of different greyscale levels, as illustrated in Figure 5.5. 8-connected groups of pixels will therefore be differentiated in the same way as for the equivalent Matlab[®] matrix, which ensures a correct numbering management.

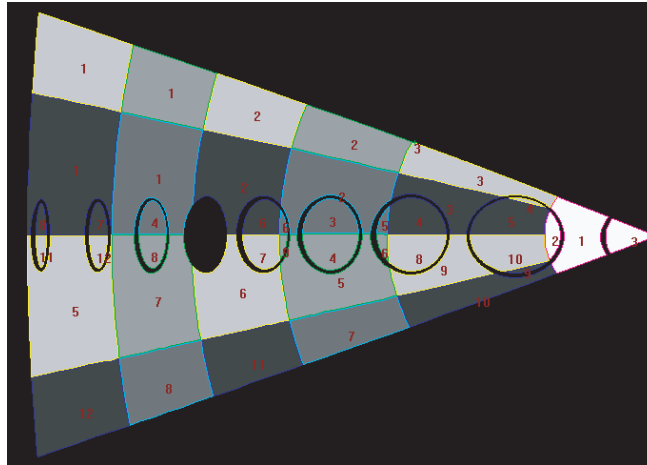


Figure 5.5: Image-Pro Plus[®] outlines for BT(R)DF averaging inside angular sectors $(\Delta\theta_2, \Delta\phi_2) = (15^\circ, 20^\circ)$ (azimuth shift $S_\psi = 10^\circ$, blind zone around $\theta_2 = 50^\circ$).

These grids of outlines will then be applied on each of the calibrated BT(R)DF maps, depending on the current S_ψ azimuth shift, for mean BT(R)DFs inside each sub-sector to be assessed as well as the number of comprised pixels.

5.3 Image acquisition and processing

The general image acquisition and processing procedure is the following: at each screen position, digital images are captured at several integration intervals and greyscale levels are transformed into corresponding luminances; as illustrated by Figure 5.6, the superposition of different integration intervals for the same luminous situation improves the accuracy of luminance measurements (32 bits values) and avoids over-exposure (saturation) and/or under-exposure in presence of high luminance dynamics.

This section provides an overview of the different procedures applied on the captured images. Amongst them, the acquisition method, partial masking (according to the optimal luminance calibration range) and combination into a calibrated floating-point image was largely adapted from Michel (1999). The last part describes how the six final BT(R)DF screen maps are handled to visualize the light flux emerging from the sample as an integral view .

5.3.1 Image capture and illuminance measurement

Depending on the luminance dynamic, assessed with a short integration interval (80 ms) to reduce saturation risks, the N_{im} optimal integration intervals are selected amongst the calibrated ones ($1 \leq N_{\text{im}} \leq 7$, see Section 4.1.2) and applied from the longest to the shortest of the N_{im} images taken at the screen's current position. After the last image is acquired, it is checked that no pixels are still saturated.

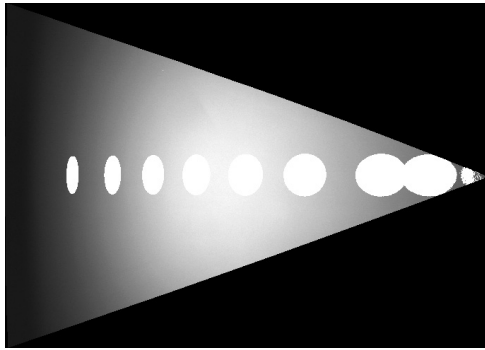
Simultaneously with each image capture, the illuminance $E_{\perp}(t)$ on a plane perpendicular to the incident beam is measured by a luxmeter connected to the computer (see Section 3.4.1); the illuminance values $E_{\perp}(t)$ acquired over a period corresponding to the image integration interval are then averaged to have a unique value E_{\perp} for each image, accounting for the small light source fluctuations; this value is then corrected into the corresponding sample plane illuminance \bar{E}_{\perp} (see Section 3.4.1). This sequence of operations is summarized in the upper part of the flow-chart of Figure 5.7.

5.3.2 Image correction and composition

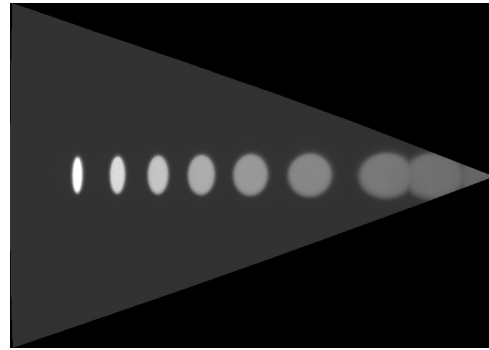
Before the N_{im} captured images are converted into luminance maps, three corrections must be applied on the greyscale levels directly:

- One pixel inside the screen area is dysfunctional and leads to aberrant values. Although its impact on BT(R)DF data is negligible as long as the averaging grid intervals remain reasonably large, it can become perceptible for fine grids or narrow luminance peaks. Thus, a small calculation routine was implemented to remove it from the image analysis by assigning it the mean value of its neighbors.
- As explained in Section 4.1.2, all pixels of grey level below 49 have to be put to zero.
- The compensation of the darkening effect on the image borders (see Section 4.3.2) requires a floating-point format (32 bits instead of 8 bits) for both the the correction figure and the captured images. In practice, the latter are first converted into floating-points, multiplied by the (32 bits) correction figure minus 1, the resulting figure being converted back in grey levels (8 bits) before its addition to the initial image.

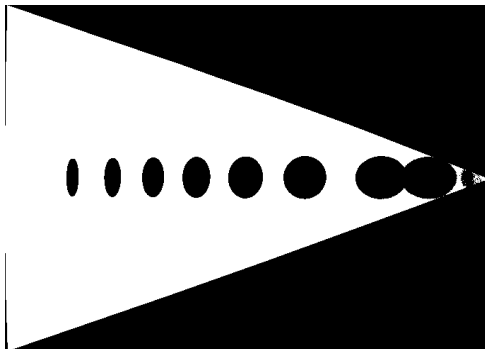
According to a loop sequence treating the N_{im} corrected 8 bits images one by one, from the longest to the shortest integration intervals, different operations are applied; they are described below and summarized in the flow-chart of Figure 5.7.



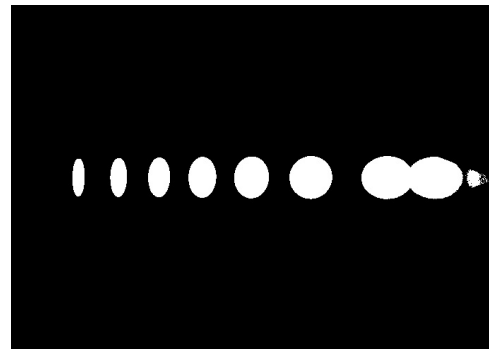
(a) Long exposure, adapted to background



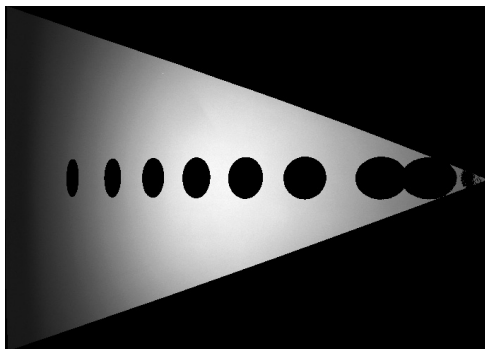
(b) Short exposure, adapted to bright spots



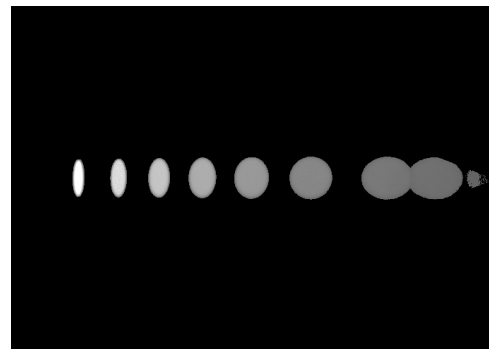
(c) Binary mask for long exposure image



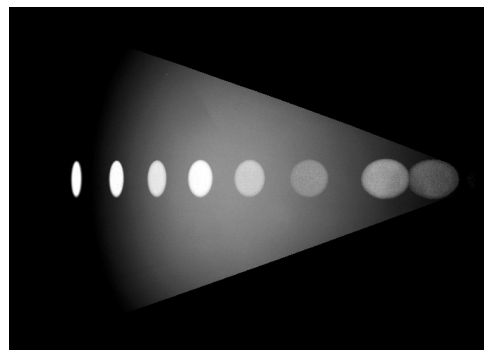
(d) Binary mask for short exposure image



(e) Saturated pixels eliminated (masked)



(f) Under-exposed pixels eliminated



(g) Combination into full digital image

Figure 5.6: General image acquisition and processing principle: saturation and/or under-exposure avoided by superposing partially masked images captured at different integration intervals.

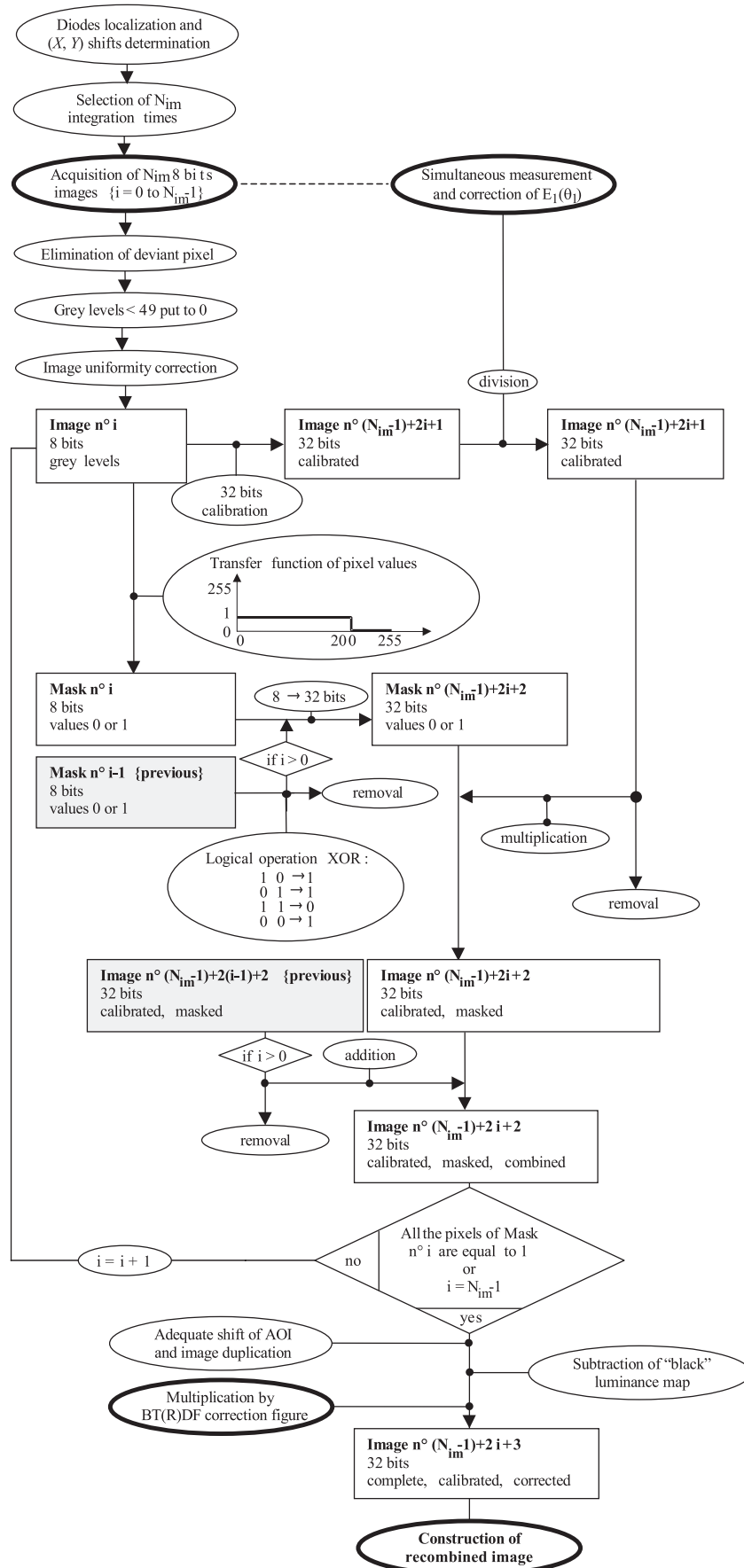


Figure 5.7: Flow-chart of image calibration and combination procedures.

- On one hand, each 8 bits image is transformed into a 32 bits (floating point) luminance (L_{screen}) map via the appropriate calibration (see Section 4.1.2); the latter is then divided by the corresponding illuminance value $E_1(\theta_1)$, which makes up an image composed of pixels equal to $\frac{L_{\text{screen}}(\theta_1, \phi_1, \theta_2, \psi_2)}{E_1(\theta_1)}$ ratios.
- On the other hand, each 8 bits image is processed so that all its saturated (> 200) or already treated (at a longer integration interval) pixels are set to nil, the remaining ones being set to 1; this makes up a binary 8 bits mask, thereafter converted into a binary floating-point image.
- The resulting mask is multiplied by the 32 bits calibrated image it corresponds to, producing a partially masked floating-point map of $\frac{L_{\text{screen}}}{E_1}$ ratios.
- The current partially masked map is then combined with the previous one, which, at the end of the loop sequence (i.e. when all N_{im} images have been treated), ends up with a fully calibrated and complete 32 bits map of the $\frac{L_{\text{screen}}}{E_1}$ ratios.

The screen detection area is then isolated by applying the adequate (X, Y) shift to the triangular Area Of Interest and duplicating the circumscribed image (see Section 4.2.1). In case of a BRDF characterization with the screen in its obstructing position, the appropriate “black” luminance map (see Section 4.3.3) is subtracted from it.

5.3.3 Global visualization through recombined screen images

Although the set of BT(R)DF data represents the most important deliverable of a sample characterization, the large amount of information contained in the screen maps is worth converting into a synthetic representation, to benefit in a different way from the image-based assessment method (continuous investigation of the emerging light flux with a pixel-level resolution).

After being converted into BT(R)DF maps accounting for distance and light inclination effects (see Section 5.4.1), a progressive composition of the six screen images is performed.

Each screen map, represented in white on Figure 5.8, is first resized to produce an equilateral triangle, then rotated according to the considered screen position p ($p=4$ in the shown example) and appropriately positioned on an integral view to build up a superposition of the six screen maps in a hexagon, as for the orthogonal projection schematized in Figure 3.1(a). To be sure that the brightest pixels on the final image correspond to the highest BT(R)DF values for the whole six screen maps, grey levels are processed at each new screen position to fit the global BT(R)DF dynamic.

The final view thus offers a direct information about the directional transmission (reflection) properties of the considered sample, as well as details otherwise lost in the averaging process.

Although the individual screen images are composed of 488×685 pixels, the global visualization is much smaller (400×400 pixels for the final image), in order to reduce the required storage memory; this, however, remains widely sufficient for representing BT(R)DF figures properly.

In case $\theta_1 = 80^\circ$ in reflection mode and $p = 5$, the camera obstructs part of the incoming light beam, which asks for a splitting of p into two positions (see Section 5.1.2).

A special routine was used for the global visualization construction: the proper screen image halves for each new position are first selected, then inverted, rotated and processed with an adaptation of their respective pixel greyscale values; they are finally combined to make up a full screen image again, added to the progressive hexagonal superposition.

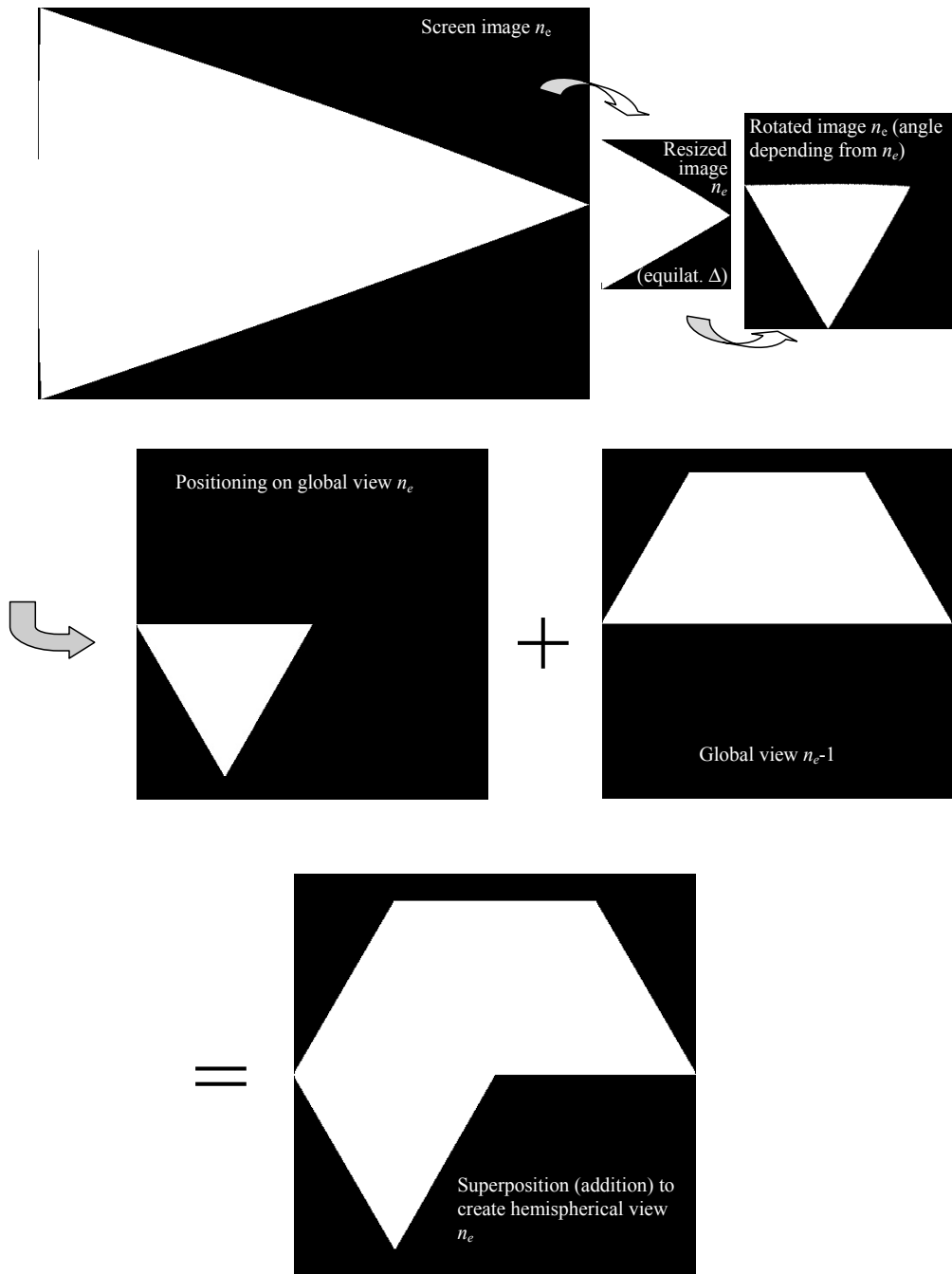


Figure 5.8: Sequence of operations applied to each BT(R)DF screen map to produce an integral view of all screen positions.

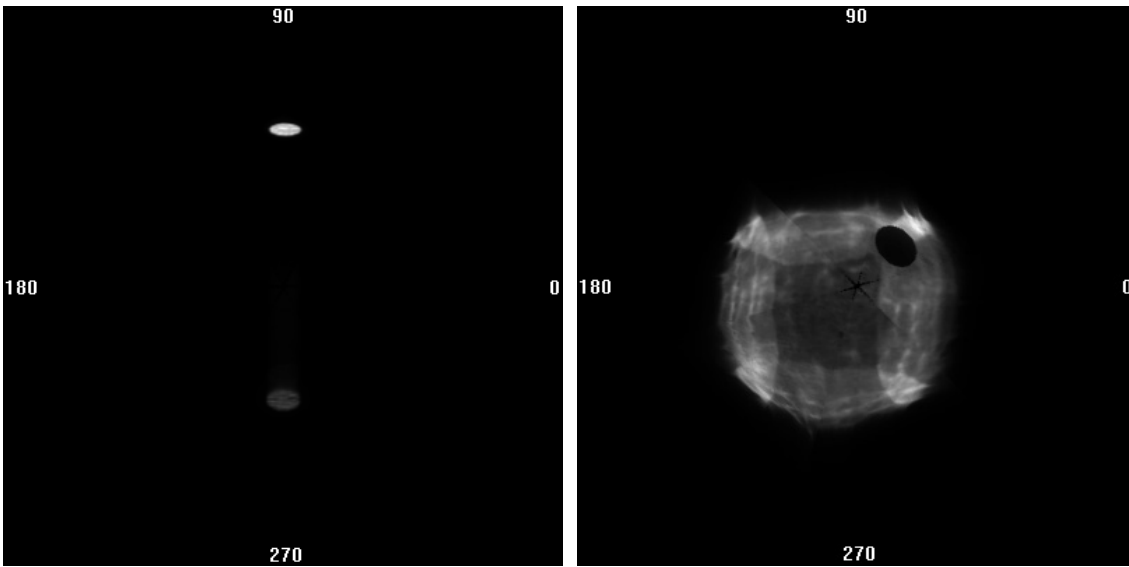
When p is the last selected screen position, the recombined image is processed to make it fit a default referential for emerging light distribution, identical for any incident direction and characterization mode for an easier comparison and reading: all images represent a view from the $\theta_1 = 0^\circ$ direction in Figure 2.1; this means that the virtual observer is always supposed to be on the light source side of the sample with the $\phi_i = 0$ axis appearing on the right-hand side, ϕ_i values increasing counterclockwise.

Appropriate ϕ_1 -dependent rotations, that differ whether in transmission or reflection mode, are thus applied on the recombined image; landmarks for ϕ_i coordinates 0° , 90° , 180° and 270° are added to facilitate the reading.

Two representations are shown in Figure 5.9 for:

- a prismatic panel with $42^\circ/5^\circ$ gratings (see Section C.3.1) for incidence ($20^\circ, 270^\circ$) in transmission mode (Figure 5.9(a));
- curved mirror squares (see Section C.2.4) for incidence ($10^\circ, 45^\circ$) in reflection mode (Figure 5.9(b)), where the blind spot induced by the removed screen cover can be observed.

These figures show that the prismatic film presents sharp transmission features, with two main peaks of unequal luminance (brightness), whereas the particular geometry of the mirrored surface induces the emerging rays to converge within diamond-shaped fringes.



(a) BTDF ($20^\circ, 270^\circ$) for prismatic panel

(b) BRDF ($10^\circ, 45^\circ$) for curved mirror squares

Figure 5.9: BT(R)DF (θ_1, ϕ_1) visualization for the whole hemisphere (2π steradian solid angle), based on a recombination of the six screen digital maps.

5.4 BT(R)DF data extraction

The floating-point image consisting of a pixel-level map of $\frac{L_{\text{screen}}(\theta_1, \phi_1, \theta_2, \psi_2)}{E_1(\theta_1)}$ ratios for a given screen position must be processed further to become a BT(R)DF map, by an adequate conversion established in Section 5.4.1.

As the chosen assessment method does not separate specular from diffuse transmission (reflection) although these two components are defined differently, a study of how this impacts on the measurement adequacy is presented in Section 5.4.2.

Finally, the averaging procedure to extract usable BT(R)DF values from the continuous digital maps is described (Section 5.4.3), that allows to produce a finite set of data according to a predetermined grid of regular angular intervals ($\Delta\theta_2, \Delta\phi_2$).

5.4.1 Conversion from screen luminance to BT(R)DF

To establish the relation between $\frac{L_{\text{screen}}}{E_1}$ ratios and the corresponding BT(R)DF data, some geometrical considerations are required, illustrated by Figure 5.10, together with an analysis of the different photometric quantities.

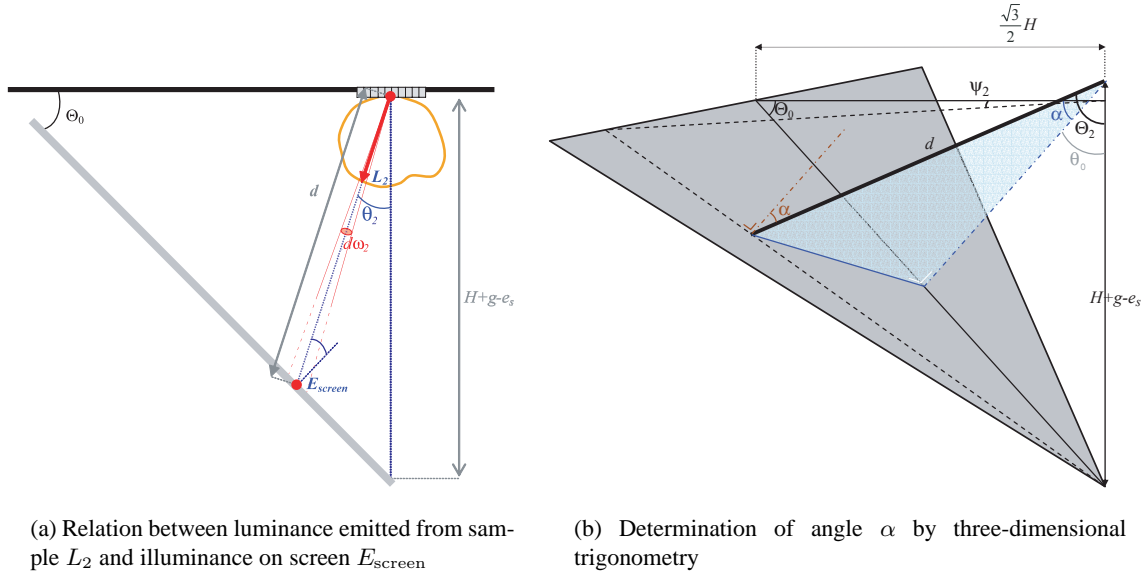


Figure 5.10: Geometric and photometric quantities determinant in a BT(R)DF assessment.

For an arbitrary screen position p , the luminance $L_2(\theta_2, \psi_2)$ emitted towards the screen by an area element dA of the sample within a solid angle element $d\omega_2$ along direction (θ_2, ϕ_2) is given by Equation (5.1) (Association Française de l'Éclairage, 1991), where $d\Phi_2$ is the element of light flux emitted within $d\omega_2$:

$$L_2 = \lim_{dA, d\omega_2 \rightarrow 0} \frac{d^2\Phi_2}{d\omega_2 \cdot dA \cdot \cos \theta_2} \quad (\text{Cd} \cdot \text{m}^{-2}) \quad (5.1)$$

On the other hand, the illuminance $E_{\text{screen}}(\theta_2, \psi_2)$ on a screen surface element dS , due to the intensity I_2 emitted from the sample within a solid angle element $d\omega_2$ along direction (θ_2, ϕ_2) , can be deduced from Bouguer's law through Equation (5.2) (Commission Internationale de l'Éclairage, 1983a):

$$E_{\text{screen}} = \lim_{dS \rightarrow 0} \frac{d\Phi_2}{dS} = \lim_{d\omega_2 \rightarrow 0} \frac{d\Phi_2 \cdot \cos \alpha}{d\omega_2 \cdot d^2} \quad (\text{lux}) \quad (5.2)$$

where α is the angle between direction (θ_2, ψ_2) and the normal to the screen plane, illustrated by Figure 5.10(a) for $\psi_2 = 0$ (Equation (5.3)) and by Figure 5.10(b) in the general case (Equation (5.4) derived from (4.11)):

$$\alpha(\theta_2, 0) = |\Theta_0 - \theta_2| \quad (5.3)$$

$$\alpha(\theta_2, \psi_2) = \arccos \left(\cos \Theta_0 \cdot \left(\frac{2}{\sqrt{3}} \cdot \sin \theta_2 \cdot \cos \psi_2 + \cos \theta_2 \right) \right) \quad (5.4)$$

As the screen surface can be considered as lambertian (perfectly diffusing, see Section 3.2.5), the luminance L_{screen} re-emitted from the screen in any direction is constant for a given E_{screen} . We can thus calculate E_{screen} as a function of L_{screen} and ρ_{screen} (-), the screen's reflection coefficient:

$$\rho_{\text{screen}} E_{\text{screen}} = \int_0^{\frac{\pi}{2}} d\theta \int_0^{2\pi} L_{\text{screen}} \cdot \cos \theta \cdot \sin \theta \, d\phi = 2\pi \cdot L_{\text{screen}} \cdot \left[\frac{1}{2} \sin^2 \theta \right]_0^{\frac{\pi}{2}} = \pi \cdot L_{\text{screen}} \quad (5.5)$$

This leads to the following relation between L_2 and L_{screen} , where A is the sample area:

$$L_2 = \frac{\pi \cdot d^2}{\rho_{\text{screen}} \cdot A \cdot \cos \alpha \cdot \cos \theta_2} \cdot L_{\text{screen}} \quad (\text{Cd} \cdot \text{m}^{-2}) \quad (5.6)$$

The Bidirectional Transmission (Reflection) Distribution Function $BT(R)DF$ being defined as the ratio between the emerging luminance L_2 and the illuminance on the sample plane E_1 (thus expressed in $\text{Cd} \cdot \text{m}^{-2} \cdot \text{lux}^{-1}$ or sr^{-1} , see Section 2.1), it can be written as a function of the polar angles $\theta_1, \phi_1, \theta_2$ and ϕ_2 according to Equation (5.7), deduced from (5.6):

$$BT(R)DF(\theta_1, \phi_1, \theta_2, \phi_2) = \frac{\pi}{\rho_{\text{screen}}} \cdot \frac{d^2(\theta_2, \psi_2)}{A \cdot \cos \alpha \cdot \cos \theta_2} \cdot \frac{L_{\text{screen}}(\theta_1, \phi_1, \theta_2, \phi_2)}{E_1(\theta_1)} \quad (5.7)$$

Equation (5.7) allows to deduce the $BT(R)DF$ data of each pixel once its calibrated L_{screen} value is determined. It indeed compensates:

- the reflection coefficient of the diffusing screen ρ_{screen} ;
- the distance d from the sample center to a particular point on the screen along direction (θ_2, ψ_2) , i.e. the average distance from the sample area to this point, represented by pixel (X, Y) on the image;
- the sample area A ;
- the emerging angle θ_2 (that affects the apparent emitting (sample) surface);
- the angle α from which the emerging light reaches the screen;
- and of course the illuminance E_1 received by the sample directly from the light source.

Thanks to the matrix-based method described in Section 4.2, Equation (5.7) can be applied at the pixel level. For this purpose, a correction matrix $M_{C_{BT(R)DF}}$ is created, based on the proportionality factor between $BT(R)DF$ s and the $\frac{L_{\text{screen}}}{E_1}$ ratios provided by the calibrated pixels. This matrix is given by Equation (5.8), where the operations are applied on each coefficient individually and where matrix M_α is calculated from Equation (5.4) replacing θ_2 and ψ_2 by M_{θ_2} and M_{ψ_2} respectively:

$$M_{C_{BT(R)DF}} = \frac{\pi}{\rho_{\text{screen}}} \cdot \frac{M_d^2}{A \cdot \cos M_\alpha \cdot \cos M_{\theta_2}} \quad (5.8)$$

Based on matrix $M_{C_{BT(R)DF}}$, a floating-point correction figure can be created. A different $M_{C_{BT(R)DF}}$ figure is needed for every new combination of parameters e_s and D : indeed, e_s determines the M_d, M_{θ_2} and M_α coefficients while D defines area A .

An approximate digital representation of matrix $M_{C_{BT(R)DF}}$ is given on Figure 5.11(a), the correction factors range being far too important to be adequately represented by 256 grey levels (they vary from about 37,000 to $1.4 \cdot 10^{21}$ [-] for an arbitrary area $A = 1 \text{ cm}^2$).

To illustrate its effect, the raw screen image obtained with a perfectly diffusing material is shown on Figure 5.11(b), which, after correction, should become a map of similar pixel values. As can be observed on these figures, the impact of the squared distance factor d^2 is preponderant. When comparing Figure 5.11(a) with Figure 4.9(c), it can also be noticed that the other factors induce a shift of the minimum of $M_{C_{BT(R)DF}}$ towards lower θ_2 : M_d and $M_{C_{BT(R)DF}}$ are indeed respectively minimal for $\theta_2 = \Theta_0$ and 35.6° .

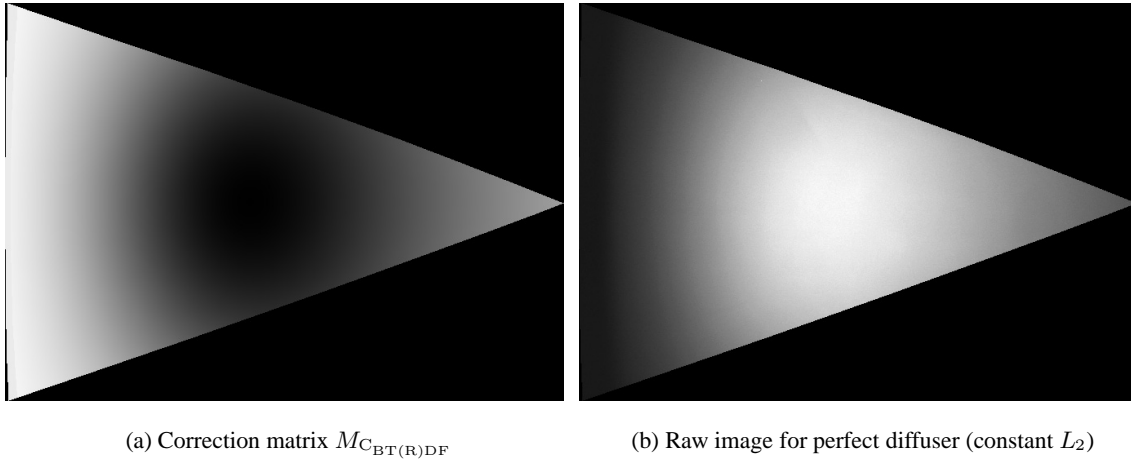


Figure 5.11: Digital representation of the compensation of distance and light tilting effects to convert $\frac{L_{screen}}{E_1}$ ratios into $BT(R)DF$ values with a pixel-level spatial accuracy.

5.4.2 Simultaneous assessment of specular and diffuse components

As mentioned in Section 2.1, the Commission Internationale de l’Eclairage (1977) defines a BT(R)DF only in reference to scattered light. Indeed, as literally expressed by the term “directional”, BT(R)DFs are formally defined for differential quantities, i.e. over infinitesimal elements of sample area dA and solid angles $d\omega_1$ and $d\omega_2$. Hence, regular transmittance (or specular reflectance²) leads to a Dirac function (δ -function) in the direct transmitting (reflecting) direction $(\theta_2, \phi_2) = (\theta_1, \phi_1 + 180^\circ)$.

However, as physical measurements are always made over finite intervals (neither infinite nor infinitesimal) and as the incident beam is never perfectly collimated (not even for the sun, showing rays presenting a 0.25° spread), any measurement becomes an average value over these intervals (Nicodemus et al., 1977; Apian-Bennewitz and von der Hardt, 1998). This also applies to BT(R)DF measurements, the strict directional formalism becoming irrelevant and having to be considered in a broader sense.

As pointed out by Nicodemus et al. (1977), when emerging light distributions vary rapidly, which is typically the case around regular (specular) or quasi-regular (quasi-specular) “peaks”, goniophotometric measurement data are very sensitive to the angular-resolution of the instrument, which makes the figures averaged over the resolution interval of little significance. Integrated or average values for BT(R)DFs over a certain detection area, of appropriate size and configuration, then become more useful than the concept of BT(R)DFs approximating δ -functions.

The bi-conical formalism answers these constraints by resorting to bi-conical distribution functions instead of BT(R)DFs, integrating the latter over the involved incoming and outgoing solid angles ω_1 and ω_2 (Nicodemus et al., 1977; McCluney, 1994).

Yet, to avoid using a different formalism whether the emerging light distribution is diffuse or presents high luminance gradients (the bi-conical one being very heavy to handle in practice), a study of the most appropriate detection areas appears as a resourceful approach.

This study is presented below, followed by an investigation of how this influences the assessed BT(R)DF data in the case of complex glazing with strongly specular transmission features like prismatic panels. An overview of this analysis for the former source only was published in Andersen and Scartezzini (2003) and as an appendix in Andersen et al. (2003b).

²Terminology according to American Society for Testing and Materials (1997a).

Regular (specular) and diffuse components of emerging light flux

From the produced screen luminance maps $L_{\text{screen}}(\theta_1, \phi_1, \theta_2, \phi_2)$, two different types of information can be extracted:

- In the case of scattered light, the $L_{\text{screen,diff}}$ values allow to determine the luminance distribution $L_2(\theta_1, \phi_1, \theta_2, \psi_2)$ emitted by the sample.
- In the case of direct transmittance (resp. reflectance), i.e. regular (resp. specular) light flux, $L_{\text{screen,spec}}$ values allow to deduce the direct transmission (resp. reflection) factor $\tau_{\text{dir}}(\theta_1, \phi_1)$ (resp. $\rho_{\text{dir}}(\theta_1, \phi_1)$), accounting for the source intensity (provided by the simultaneously measured illuminance $E_1(\theta_1)$).

To keep a single conversion factor matrix $M_{\text{C}_{\text{BT(R)DF}}}$ for both types of luminances and assess them using the same method, equivalent expressions must be verified. This will define conditions to be fulfilled when analyzing L_{screen} maps.

Figure 5.12(a) illustrates the separation of emerging light into diffuse and regular (specular) components.

The only distance to be considered in the first case is d , the distance between the detector surface and the sample, as the sample truly becomes a secondary light source; in the second, it is distance $h + d$ from the source to the detection surface that drives the screen illuminance E_{screen} (and thus L_{screen}).

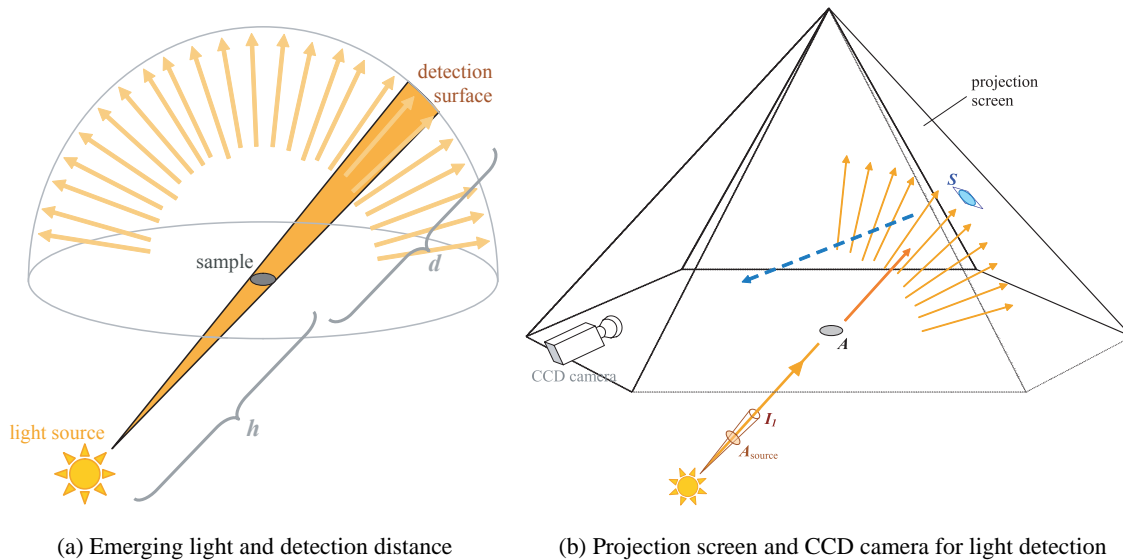


Figure 5.12: Regular (specular) and diffuse components in the goniophotometric assessment of emerging light.

As a matter of fact, the value to consider for h is not the physical distance from the sample to the source lens or bulb (here equal to 10.3 m), but its virtual distance to an equivalent point source.

Indeed, as the illuminance measured perpendicularly to the incident beam follows Bouguer's law with a correlation of 99%, the beam can be considered as issued from a point source situated at a distance $h = \frac{1}{2}D \tan \eta$, where the spread η of the incident rays reaching the sample area $\pi \frac{D^2}{4}$ was determined experimentally (see Section 4.3.1).

From the values observed for η for different sample diameters D , one can deduce an average value for h , equal to 25.9 ± 0.3 m (h was of about 8 m for the former source).

The detection principle specific to the present goniophotometer is illustrated in Figure 5.12(b) for transmission measurements (also valid in reflection mode with the light source on the other side of the sample); S stands for an arbitrary detection area on the projection screen.

To express the screen luminance $L_{\text{screen_diff}}$ due to diffuse emerging light, we can modify Equation (5.7) into Equation (5.9):

$$L_{\text{screen_diff}} = \frac{\rho_{\text{screen}}}{\pi} \cdot \frac{L_2 \cdot A \cdot \cos \theta_2 \cdot \cos \alpha}{d^2} \quad (5.9)$$

On the other hand, in order to express $L_{\text{screen_spec}}$ due to regularly (specularly) transmitted (reflected) light, we can write $E_{\text{screen_spec}}$ (the illuminance received on the projection screen) in terms of the light source intensity I_1 by Equation (5.10):

$$E_{\text{screen_spec}} = \tau_{\text{dir}} | \rho_{\text{dir}} \cdot \frac{I_1 \cdot \cos \alpha}{(h + d)^2} \quad (5.10)$$

where the combined symbol $\tau_{\text{dir}} | \rho_{\text{dir}}$ is used instead of either τ_{dir} or ρ_{dir} for simplification.

The relation between $E_{\text{screen_spec}}$ and $L_{\text{screen_spec}}$ being given by Equation (5.5), and as I_1 can be expressed in terms of E_1 using Bouguer's law:

$$I_1 = h^2 \cdot E_1(\theta_1) \quad (5.11)$$

one obtains Equation (5.12) for $L_{\text{screen_spec}}$:

$$L_{\text{screen_spec}} = \tau_{\text{dir}} | \rho_{\text{dir}} \cdot \frac{\rho_{\text{screen}}}{\pi} \cdot \frac{h^2 \cdot \cos \alpha}{(h + d)^2} \cdot E_1 \quad (5.12)$$

Both Equations (5.9) and (5.12) require the projection screen to be lambertian, which was shown to be a very reasonable assumption (see Section 3.2.5).

Conditions for a simultaneous assessment of specular and diffuse light components

Considering Equations (5.9) and (5.12) to be equivalent asks relation (5.13) to be verified:

$$L_2 \approx \tau_{\text{dir}} | \rho_{\text{dir}} \cdot \frac{d^2 \cdot h^2}{(h + d)^2} \cdot \frac{1}{A \cdot \cos \theta_2} \cdot E_1 \quad (5.13)$$

E_1 is defined as the ratio between the incident light flux Φ_1 and the apparent receiving surface $A \cos \theta_1$. As far as L_2 and $\tau_{\text{dir}} | \rho_{\text{dir}}$ are concerned, they can be expressed in average quantities by Equations (5.14), where Φ_2 is the emerging light flux and Ω_2 the solid angle around direction (θ_2 , ϕ_2):

$$\begin{aligned} L_2 &= \frac{\Phi_2}{A \cdot \cos \theta_2 \cdot \Omega_2} \\ \tau_{\text{dir}} | \rho_{\text{dir}} &= \frac{\Phi_2}{\Phi_1} \end{aligned} \quad (5.14)$$

We can thus rewrite Equation (5.13) into (5.15):

$$\frac{1}{\Omega_2} \approx \frac{d^2 \cdot h^2}{(h + d)^2} \cdot \frac{1}{A \cdot \cos \theta_1} \quad (5.15)$$

According to the solid angle definition for Ω_2 given by Equation (5.16):

$$\Omega_2 = \frac{S \cdot \cos \alpha}{d^2} \quad (5.16)$$

the conditions that have to be fulfilled by the digital imaging-based goniophotometer for assessing both regular (specular) and diffuse light components can be expressed by Equation (5.17):

$$\frac{h^2}{(h+d)^2} \approx \frac{A \cdot \cos \theta_1}{S \cdot \cos \alpha} \quad (5.17)$$

This conclusion fits very well with intuition: to compensate the fact that the sample is not punctual, the detection of the emerging light distribution should be made according to patches that consider luminance peaks as whole entities. Murray-Coleman and Smith (1990) actually made a statement in very good agreement with the above development, by asserting that “when the sample size exactly matches the image of the source in a perfectly [regular or] specular sample, the correct peak B[T]RDF is measured and spatial resolution is maximized”; it can be noted that this statement assumes the regular (specular) component of emerging light flux to be included in a BT(R)DF assessment.

Impact on BT(R)DF assessment accuracy

To evaluate how strongly the fulfillment of Equation (5.17) influences the BT(R)DF data achieved with the goniophotometer, a simulation model of the latter was constructed with the commercial ray-tracing software TracePro^{®3}. Measured BTDFs for prismatic glazing were compared first to simulated values obtained with a faithful copy of the experimental device (see Section 6.5.2), then to simulation results achieved with an ideal set-up model (described in more detail in Section 6.5.3), consisting of optimal components and geometry for a perfect fulfillment of Equation (5.17). As a consequence:

- A virtual sun is chosen as the light source, presenting a beam spectrum as close as possible to the real sun and showing perfectly parallel rays⁴.
- The detection surface is hemispherical and perfectly absorbing to avoid inter-reflections; in addition to this, an optimized diameter is determined for the detector to satisfy Equation (5.17): as the light source is considered infinitely far away, the ratio $\frac{h^2}{(h+d)^2}$ tends towards 1, and therefore, the ratio $\frac{A \cdot \cos \theta_1}{S \cdot \cos \alpha}$ (or rather $\frac{A \cdot \cos \theta_1}{S}$ as the averaging areas S are normal to the rays for a hemispherical detector) has to come as close to 1 as possible.

The experimental conditions impose given values on both the sample area A and the averaging grid resolution ($\Delta\theta_2$, $\Delta\phi_2$); hence, the values of S over the hemisphere will be determined only by the virtual detector's radius. The latter is therefore calculated in order that the average value of the right-hand part of Equation (5.17) equals 1 over the default set of 145 incident directions (θ_1 , ϕ_1) (or more specifically over the set of values for θ_1 weighted by each one's occurrence in the default incident directions set).

By observing the discrepancies between BTDF data obtained for optimal conditions (ideal model) and measured or simulated values under real conditions, one can find out how the fulfillment of Equation (5.17) influences the accuracy of the results, and to what extent an approximation is acceptable. Figure 5.13 provides the comparative results obtained for different incident directions and prism gratings geometries.

³TracePro[®] Expert - 2.3 & 2.4.0 releases, Lambda Research Corp.

⁴To estimate a value for η_{sun} , we can proceed as follows: naming R_{sun} and L_{sun} the sun's radius and distance to the earth respectively, and R_{earth} the earth's radius, η_{sun} can be expressed as $\arctan\left(\frac{\frac{D}{2}}{R_{\text{earth}}} \cdot \frac{R_{\text{sun}} + R_{\text{earth}}}{L_{\text{sun}}}\right) \simeq \arctan\left(\frac{D}{2} \cdot \frac{\tan 0.25^\circ}{R_{\text{earth}}}\right)$; $\eta_{\text{sun}}(^{\circ})$ is found to be of the order of 10^{-9} (Williams, 2003).

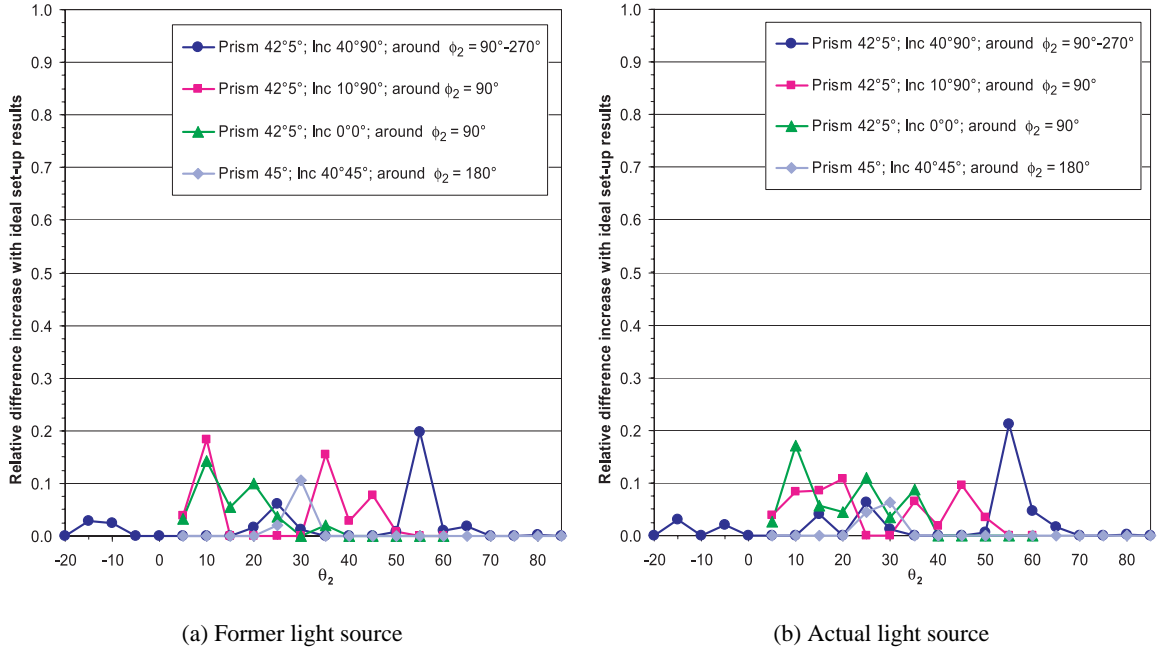


Figure 5.13: Relative discrepancies between BTDFs calculated with the ideal model and measured or simulated data under real conditions.

As h is equal to 25.9 m (resp. 8 m with the former source) and as the average distance d from the sample to the diffusing screen is 0.905 m, the mean distance ratio is equal to 0.93 (resp. 0.79), whereas the average value of the area ratio is 1.01 for the default diameter $D = 10$ cm and averaging grid intervals $(\Delta\theta_2, \Delta\phi_2) = (5^\circ, 5^\circ)$. Besides, as the screen is a flat surface, d is a function of θ_2 and ψ_2 , inducing that the fulfillment of Equation (5.17) will, at best, only be possible on an average and not for all individual directions (θ_2, ψ_2) .

Fortunately, the experimental conditions, that only verify Equation (5.17) within a 10% margin (resp. 22% for the former source), induce lower relative impact on achieved BTDF values: amongst the discrepancies observed on Figure 5.13 for the two sources, more than 9 out of 10 are inferior to 7%, resp. 10%.

This shows that although Equation (5.17) is only approximately fulfilled for the present gonophotometer set-up, BTDF results (and likewise BRDFs) remain coherent and reliable even for the regular light distributions of prismatic panels. On one hand, this statement supports the assumptions made for the building up of the device; on the other hand, it makes the simultaneous measurement of diffuse and regular (specular) components of light acceptable and suggests to revisit in the future the formal CIE definition for BT(R)DFs (Commission Internationale de l'Eclairage, 1977).

Of course, this assessment method leads to BT(R)DF average values not only related to the emerging rays direction, but also to the angular areas where these rays are detected. This has however no significant effect on the monitored data as long as the sample to detector distance is large compared to the sample size, a factor of 10 being accepted as reasonable. This restriction is verified satisfactorily for the most usual sample diameters ($D \leq 15$ cm); as larger D values are chosen only with coarse averaging grid intervals, it becomes less critical to avoid a small correlation with the distance parameter.

5.4.3 Weighted averaging and association to polar angles

Once all screen positions have been investigated, their corresponding sub-sectors files can be gathered into one. Sub-sectors associated to a same angular sector (θ_2, ϕ_2) are averaged, applying a weighting factor proportional to their respective area; angular sectors can be split either because of eliminated pixels on the covers borders, or because they overlap adjacent screen positions (generally two, six for the $(\theta_2, \phi_2) = (0^\circ, 0^\circ)$ sector); they can also be split if consisting of pixels that are not all 8-connected. Although the image pixels represent unequal portions of the full screen area because of perspective and image distortion effects, it was checked that no perceptible modification in BT(R)DF datas was observed when associating graded weights to each of them; thus, a sub-sector's area is simply given by the number of comprised pixels.

In reflection mode, the blind spot (removed screen cover) may induce one or several missing angular sector(s); a *NaN* value is assigned to such sectors, as well as to any one not sufficiently represented, i.e. whose area was withdrawn by more than 25%. *NaN* values are also assigned to missing angular sectors due to an unselected screen position.

Finally, all angular sectors are related to their specific (θ_2, ϕ_2) angles, using both the N_{IP+} to $N_{\theta\psi'}$ numbering conversion and Equations (4.12) or (4.13); in reflection mode and for $\theta_1 = 80^\circ$, a special data processing is needed on top of this for the fifth screen position, that has to be separated in two (see Section 5.1.2).

After the full BT(R)DF data set is determined for all emerging directions (θ_2, ϕ_2) for the current incident direction (θ_1, ϕ_1) , an ASCII file is created, of format described in Section B.2.1, containing the following data:

- the sample characteristics;
- the measurement parameters;
- the directional-hemispherical light transmittance or reflectance $\bar{\tau}_{dh}$ or $\bar{\rho}_{dh}$, based on an integration of the BT(R)DF values (see Section 6.4.1);
- the list of BT(R)DF values for each associated angular direction (θ_2, ϕ_2) .

5.5 Bidirectional data for photometric performances assessment

Several graphical representations were developed to achieve a synthetic and intuitive display of the monitored BT(R)DF data, described below. They allow to get a general idea of the transmission or reflection properties (e.g. rather diffuse, strongly specular) as well as to spot particular features easily (e.g. luminance peaks, privileged emergence planes).

An example is provided for transmission measurements, where two kinds of venetian blind prototypes are compared. This study was published previously in Andersen (2002), together with the graphical representations description for BTDFs only.

An overview of some direct applications for visual comfort assessment is then given, followed by a brief description of how bidirectional functions were integrated in *Radiance*⁵ simulations, based on backwards ray-tracing calculations (Ward Larson and Shakespeare, 1998) and designed to produce photo-realistic images of indoor environments.

⁵*Radiance Lighting Simulation and Rendering System*, ©The Regents of the University of California (<http://hobbes.lbl.gov> (Berkeley, California) and <http://nestor.epfl.ch> (Lausanne, Switzerland)).

5.5.1 Graphical representations

Three types of graphical representations were developed to provide various visualization possibilities of the transmitted or reflected light distribution features:

- the projection of the BT(R)DF values on a virtual hemisphere, allowing a precise analysis of the angular distribution;
- a photometric solid, representing the BT(R)DF data in spherical coordinates with growing radii and lighter colors for higher values;
- several section views of this solid, providing an accurate display of the numerical values distribution.

The referential is adapted from BTDF to BRDF mode, to remain consistent with the coordinates defined on Figure 2.1. Short explanatory titles are added for each of them, as well as the directional-hemispherical light transmittance (reflectance) τ_{dh} (ρ_{dh}) deduced from Equation (6.12) in Section 6.4.1.

Two very different systems, whose pictures are shown on Figure 5.14, were chosen to illustrate these geometric figures: a laser cut panel (Edmonds, 1993), characterized in transmission for incidence $(\theta_1, \phi_1) = (40^\circ, 90^\circ)$, and a fabric blind, characterized in reflection for incidence $(60^\circ, 90^\circ)$ and presenting a reflective grey coating on its external face, and a red one on the inside. Both systems are described in more detail in Appendix C, where the extensive set of BT(R)DF data is listed.

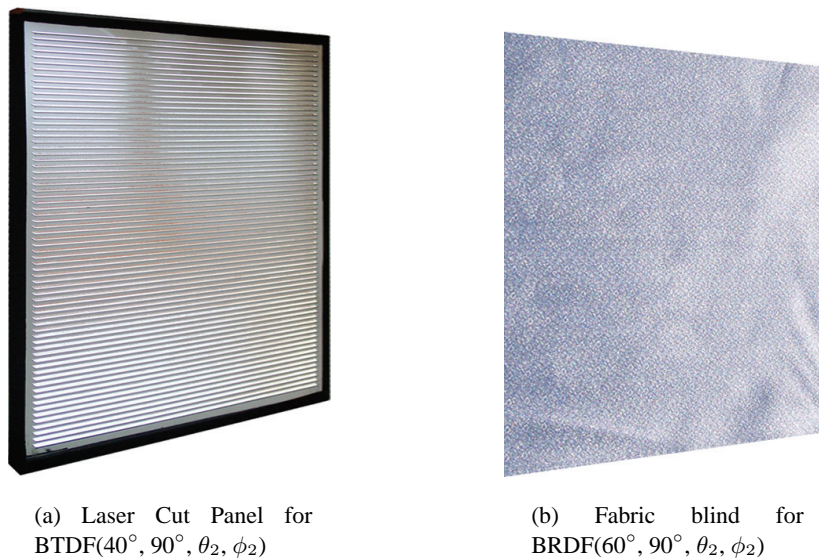


Figure 5.14: Fenestration systems illustrating the three developed graphical representations of BT(R)DFs.

Projection on virtual hemisphere

The projection of the transmission features on a virtual hemisphere is based on the following principle: each BT(R)DF value, measured inside a given angular averaging sector, is represented by the corresponding patch standing on the hemisphere vault. A color scale reproduces the BT(R)DF dynamic range for a given incident direction and allows to visualize the numerical data. The point of view from which the hemisphere is seen can be freely chosen.

Figure 5.15 shows this projection for the two mentioned samples, with different output grid intervals. This representation leads to a clear understanding of the angular distribution of the transmitted (reflected) light flux, as the values of θ_2 and ϕ_2 are easily read on such a projection. It completes very well the visualization proposed by the integral calibrated image (see Figure 5.9) when the viewing direction is vertical: the recomposed image provides finer details about transmission or reflection features, whereas the hemispherical projection allows a quantitative evaluation of BT(R)DFs and a more accurate angular and spatial display.

In both cases, the $\phi_2 = 0$ axis is kept on the right-hand side and the emerging light distribution is viewed from the positive $\theta_1 = 0$ axis (source side). This induces that the hemisphere is bulging towards the observer in reflection mode and appears as a cavity in transmission mode.

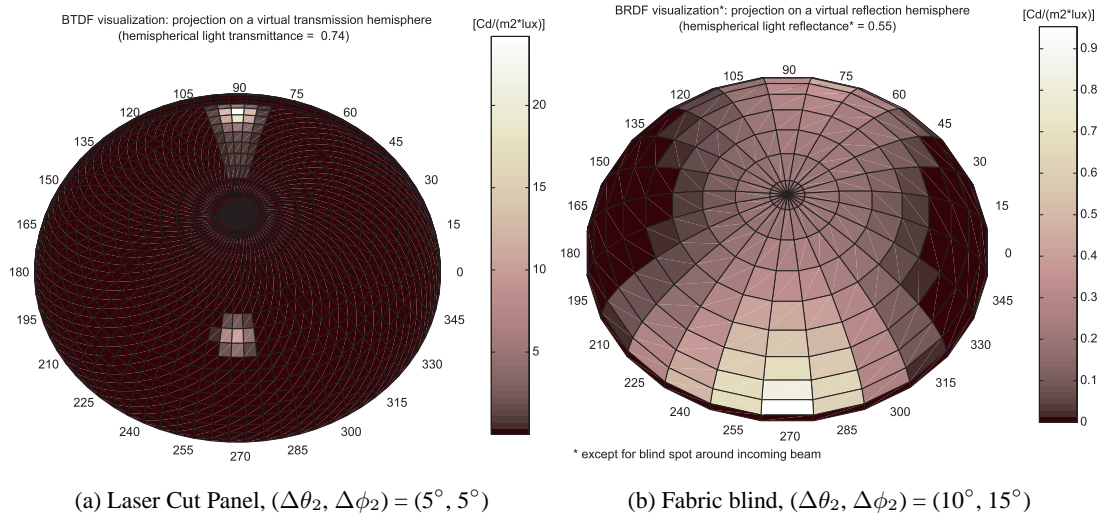


Figure 5.15: Hemispherical projections of BT(R)DF data.

Photometric solid

The photometric solid (Ashdown, 2000) can be defined as a three-dimensional representation of the luminous intensity characteristics; it is commonly provided for artificial lighting fixtures (luminaires) according to section planes where the incident direction parameter is eliminated, which makes the functions only two dimensional (θ_2 and ϕ_2) instead of four ($\theta_1, \phi_1, \theta_2$ and ϕ_2).

When creating a photometric solid, a grid based on a spherical referential is built, each point being represented by a triplet $(BT(R)DF, \theta_2, \phi_2)$, where the numerical value of the BT(R)DFs are used as the radial distances. The point of view is again chosen freely. This graphical representation, therefore, gives a synthetic and intuitive view of the angular distribution of emerging light: luminance peaks will appear like sharp emerging shapes, whereas a diffuse transmission will produce a "smooth solid", presenting only small shade differences. An instantaneous understanding of a material's photometric performances is thus achieved.

As can be observed on Figure 5.16, the incident direction (θ_1, ϕ_1) is represented on these graphs for a clearer visualization; the azimuth variation ϕ_2 is also made explicit by the polar grid added on the sample plane. The color scale is proportional to the BT(R)DF range for a given incident direction, as well as the radial distance to the referential origin. On the displayed examples, one can easily observe a splitting of the incident beam into two distinct outgoing directions for the laser cut panel (Figure 5.16(a)) and a rather diffuse reflection for the fabric blind (Figure 5.16(b)), separated in two different space portions, one around the specular direction and the other around the retro-reflected one.

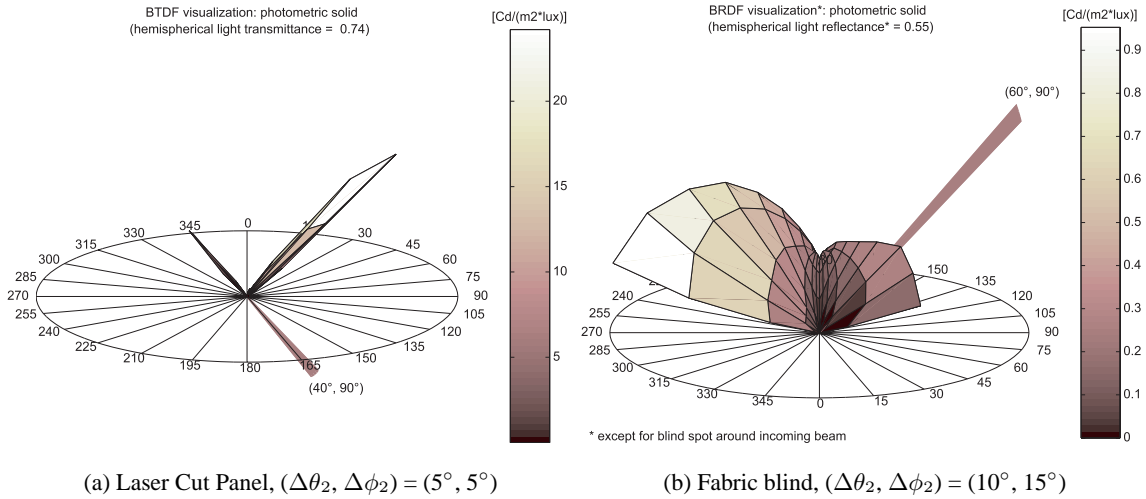


Figure 5.16: Photometric solids for BT(R)DF data representation.

Section views

The third possible representation consists of several section views of the photometric solid along vertical planes (C planes perpendicular to the sample).

Only the most significant section planes $C\phi_2$ are chosen for display, i.e. where at least one of the BT(R)DF values for all θ_2 along the plane $C\phi_2$ is greater or equal to 10% of the global BT(R)DF maximum, the preference being given to the highest BT(R)DFs (only twelve figures can be displayed at most).

As mentioned before, these curves are similar to the luminous intensity distributions found in artificial lighting catalogues, even though the latter only provide one or two sections in general. As can be observed on Figure 5.17, each curve is shown in polar coordinates giving the azimuth value ϕ_2 of the associated $C\phi_2$ section planes, the BT(R)DF scale and the altitude angles θ_2 . This representation yields a clear quantitative analysis of BT(R)DFs, focusing on an efficient display of the numerical data themselves.

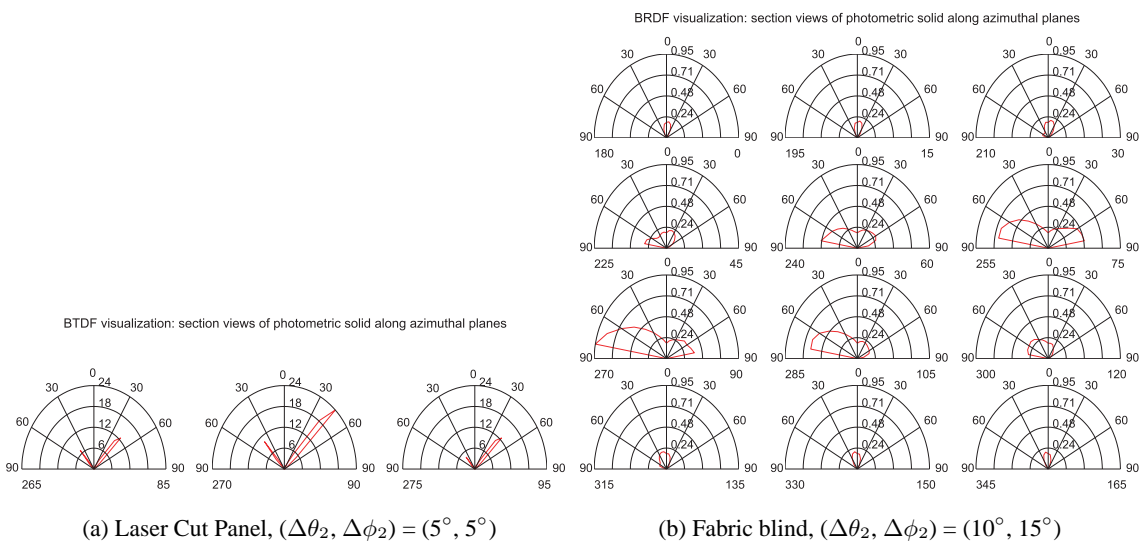
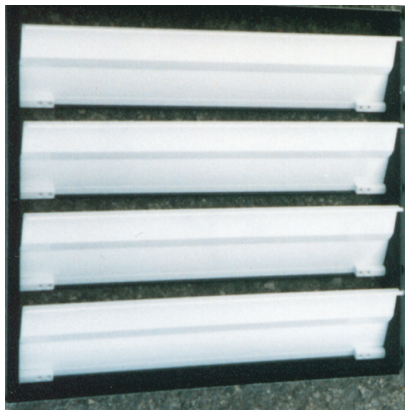


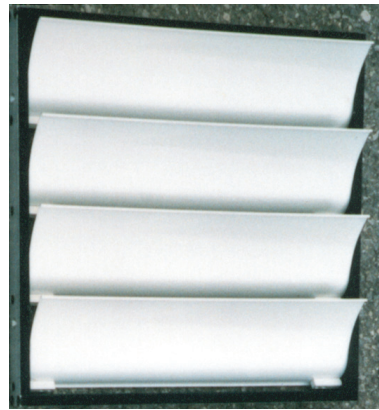
Figure 5.17: Section views along azimuth planes $C\phi_2$ of the BT(R)DF photometric solids.

5.5.2 Application of photometric solids

To illustrate how to use the above described graphical representations, transmission features of a conventional venetian blind with white metallic slats (Figure 5.18(a)) are compared to those of an optimized prototype (named “Shine”), presenting a pearl grey quartz coating used in car body manufacturing and of spoon-like profile shape (Figure 5.18(b)). Both are manufactured by Baumann-Hüppe AG and were characterized with the present goniophotometer according to the same set of incident directions (every 30° in altitude along the $C0$, $C90$ and $C270$ azimuth planes). The slats are of equal dimensions (profile 10 cm, length 34 cm, distance between slats 8 cm) and their tilt angle is fixed to 30° in regard to the window plane.



(a) Conventional white slats



(b) Optimized prototype “Shine”

Figure 5.18: Two venetian blind prototypes for BTDF comparison.

Figure 5.19 compares the transmission figures of the conventional white blind and the “Shine” prototype for normal incidence, showing important discrepancies. The first one mainly presents a regular transmission through the slats (peak along the incident direction, see Figure 5.19(c)), with a small reflection on the coating; this leads to a little increase of BTDF values in the direction $(\theta_2, \phi_2) = (60^\circ, 90^\circ)$, observable on the hemispherical projection provided by Figure 5.19(a). The second one shows no regular component and presents a quasi-diffuse transmittance (with only a slight deformation of the photometric solid in favor of normal transmittance, see Figure 5.19(d)), except along a particular direction where an important fraction of reflected light on the slats can be observed (see Figures 5.19(b) and 5.19(d)).

Even though of same global design, the two venetian blinds thus present very different light-transmission properties due to their slats coating and profile. Under this incidence, the “Shine” prototype induces an important diffuse transmittance and redirects light out of the original ray direction, whereas the conventional blind only slightly affects the incident light path and shows a quasi-negligible effect of diffuseness. It can be added that the observed BTDF extrema are seven times lower for the optimized blind than the conventional slats, leading to a diffusion reducing glare risks under clear sky conditions.

The same features appear for larger incidence angles θ_1 (Figure 5.20): a regular transmission can be observed for the white slats, with small effects of reflection shifted towards higher azimuths (clockwise on projection 5.20(a)). For the “Shine” prototype, the light transmission is quite diffuse, yet with a clearer deformation along the direct transmission direction, as shown by Figure 5.20(d); this direction indeed gets closer to the reflected direction, which generates a superposition of effects.

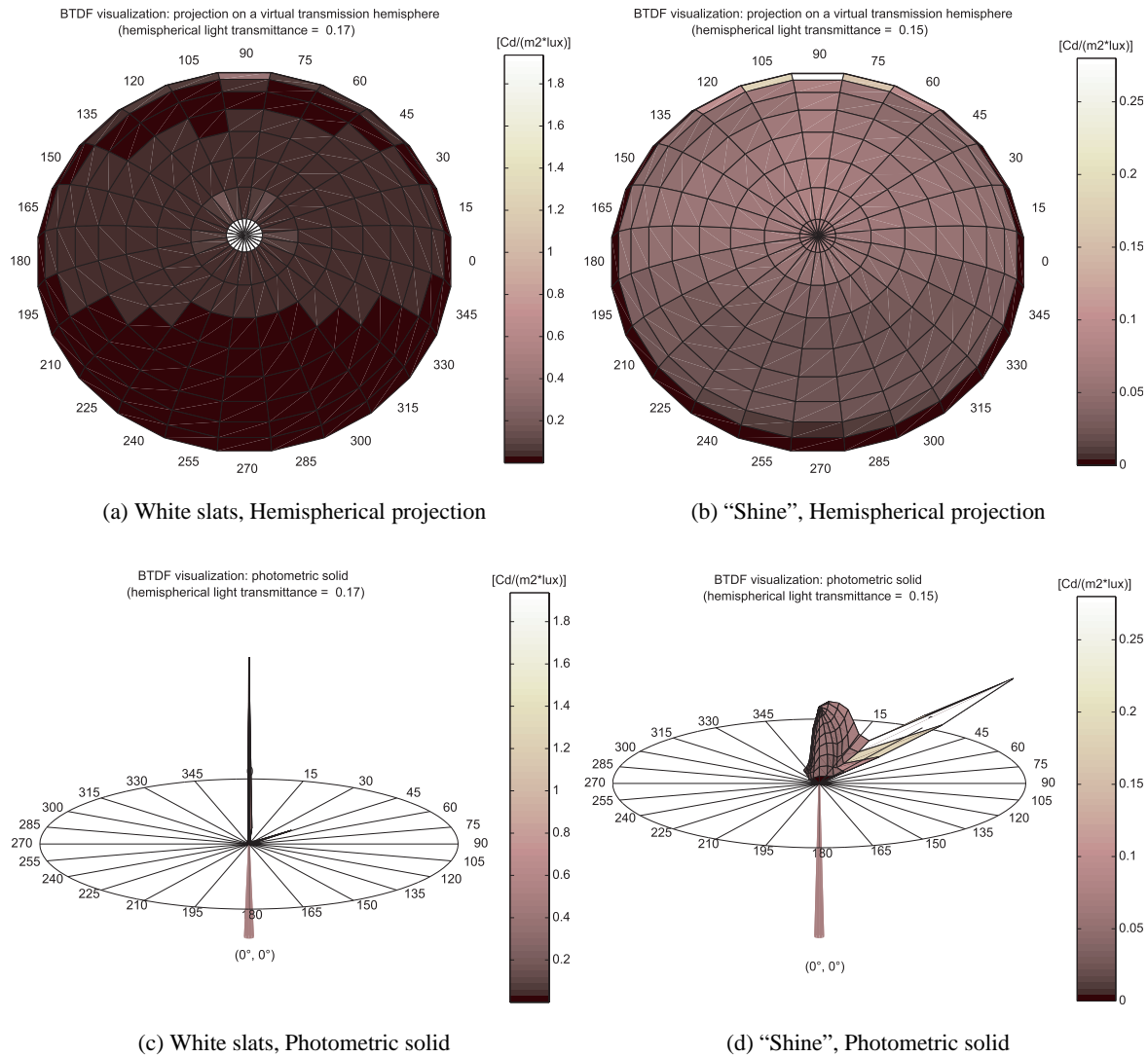


Figure 5.19: Graphical representations of BTDF data for two solar blinds for incidence $(\theta_1, \phi_1) = (0^\circ, 0^\circ)$.

For other incidences along the azimuth plane $C90$ (i.e. where $\phi_1 = 90^\circ$), the transmission features of both blinds are quite similar, as can be observed on Figure 5.21: the major part of the incoming light is reflected on the slats and redirected along a coplanar direction (transmission peaks around $\phi_2 = 90^\circ$, see Figures 5.21(a) and 5.21(b)); a minor part is slightly diffused, more significantly for the white slats (Figures C.25(a) and C.25(b)), which also presents a more extended region for the reflection peak.

Finally, along the azimuth plane $C270$, the incoming light flux is almost not perturbed when passing through the blinds. Figure 5.22 shows similar transmission features and BTDF ranges (Figures 5.22(c) and 5.22(d)) and even identical striped luminous spots (Figures 5.22(a) and 5.22(b)).

These figures outline strong glare occurrences at such incident angles; fortunately, for lateral windows, they can never be part of any actual sun course. They are in consequence only applicable for light flux that would be reflected by ground, which of course reduces drastically the risk of glare.

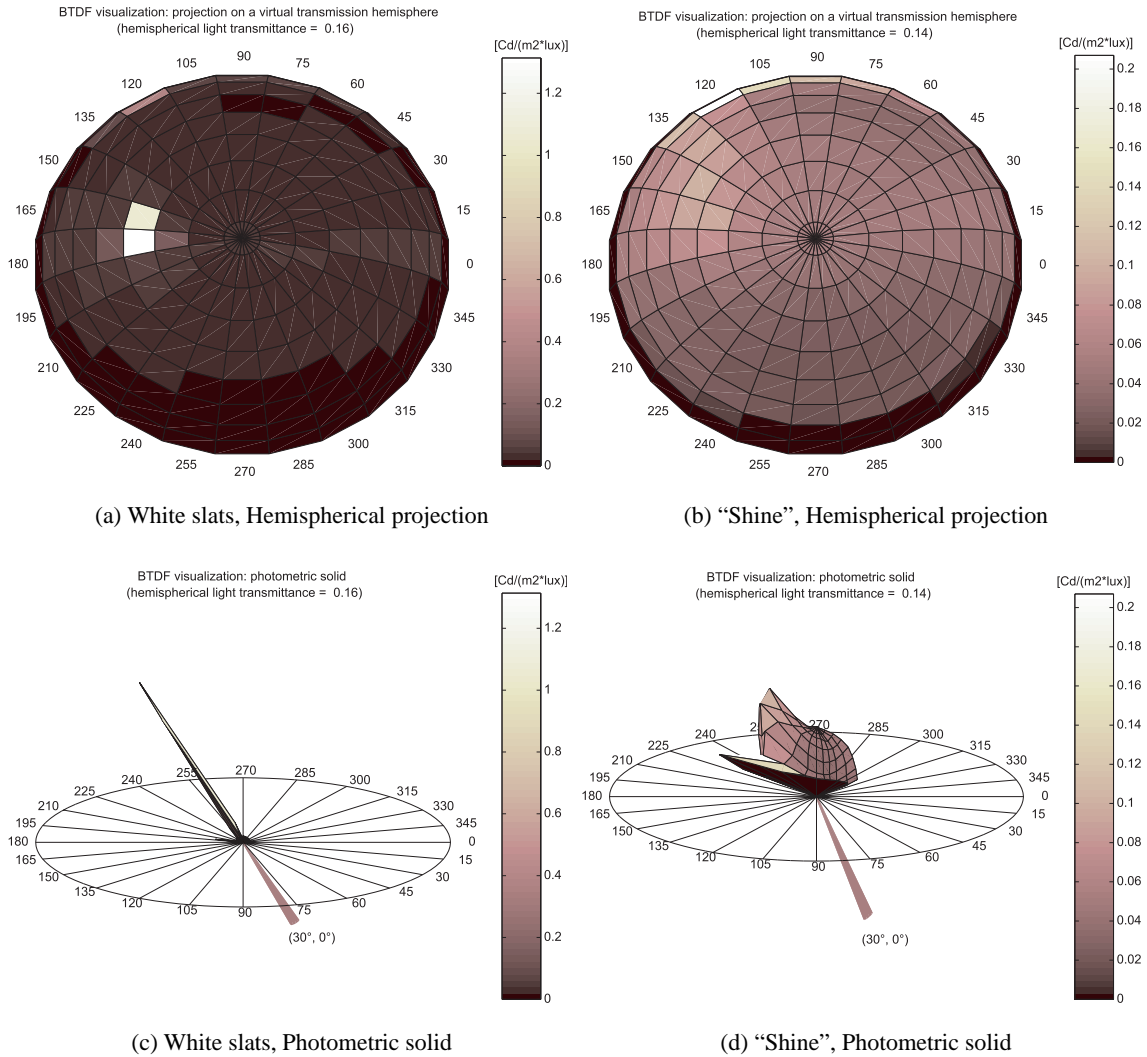


Figure 5.20: Graphical representations of BTDF data for two solar blinds for incidence $(\theta_1, \phi_1) = (30^\circ, 0^\circ)$.

The analysis of these different representations led a good understanding of the transmission features of the two products: the "Shine" prototype can take advantage of its diffusing properties to reduce glare risks; moreover, its significant redirecting (reflecting) capability can be used for many incident positions to illuminate the ceiling, which therefore becomes a secondary natural light source.

5.5.3 Visual comfort assessment based on bidirectional data

Using the same two blind prototypes, a simplified evaluation and comparison of visual comfort performances (Scartezzini et al., 1997a; van Dijk, 2001) is proposed, based on BTDF data; unique impinging and emerging directions were chosen for simplicity.

As the BT(R)DF is defined as the ratio of the luminance L_2 emitted along direction (θ_2, ϕ_2) and the illuminance $E_1(\theta_1)$ on the sample plane (see Equation (2.1)), a quantitative study of the luminance distribution after transmission (or reflection) through (on) a system can be realized easily by assuming $E_1(\theta_1)$ values corresponding to certain outdoor conditions (e.g. illuminance on a vertical plane under clear sky for a particular sun position).

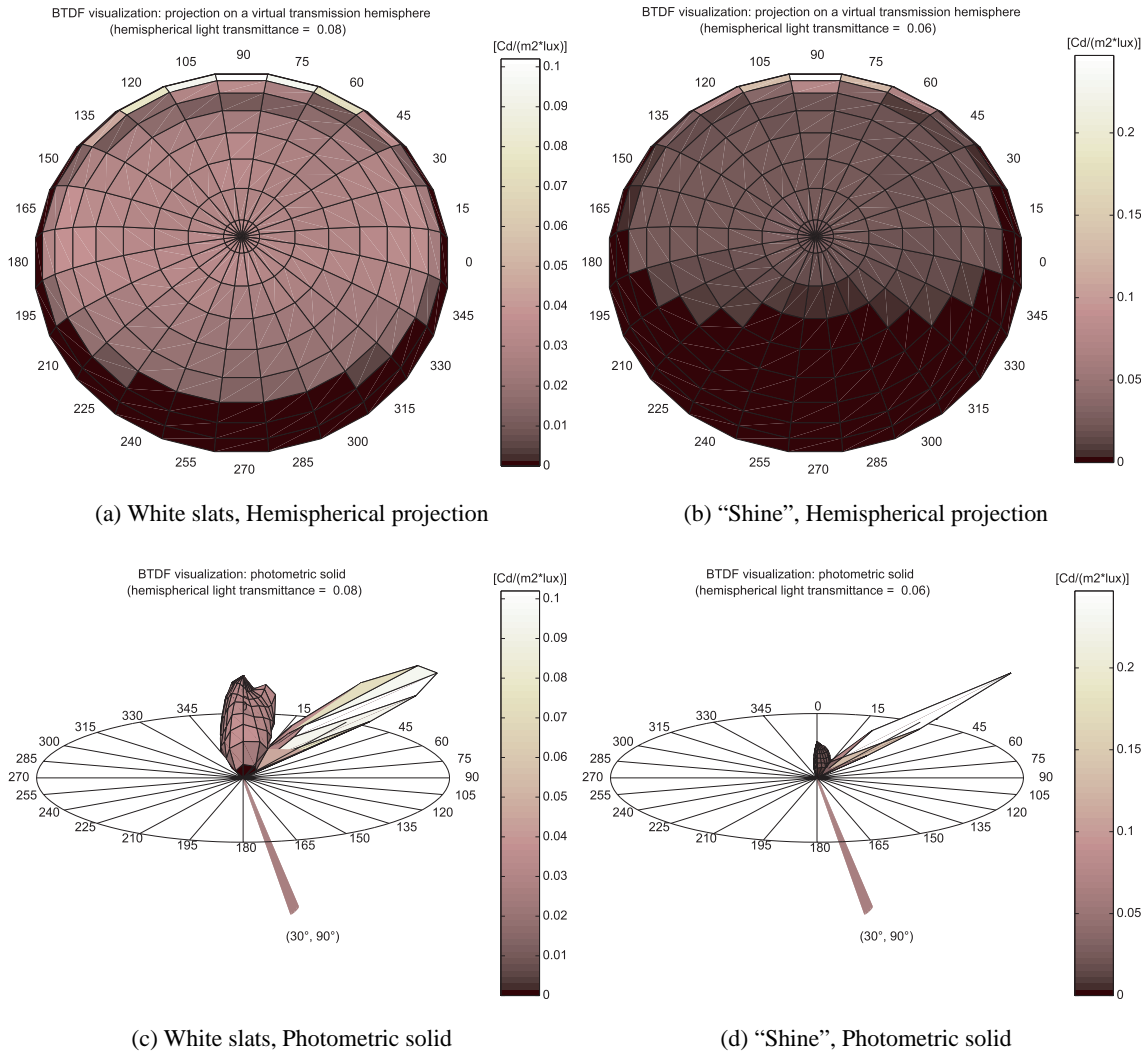


Figure 5.21: Graphical representations of BTDF data for two solar blinds for incidence $(\theta_1, \phi_1) = (30^\circ, 90^\circ)$.

Hence, based on the BT(R)DF data set of a given fenestration system, it is possible to deduce whether the emerging luminances will potentially induce glare effects (Commission Internationale de l’Eclairage, 1983b), and whether illuminance is sufficient for a specific task (computer work, writing).

The lighting recommendations in the Office Fédéral des Questions Conjonctuelles (1994) state that a situation can be considered comfortable for the human eye if the luminance contrasts do not exceed the ratio 1:3 in the ergorama and 1:10 in the panorama, respectively limited by 30° and 60° angular opening, as shown on Figure 5.23(a) (Illuminating Engineering Society of North America, 1984).

Figure 5.23(b) illustrates a basic situation for the evaluation of luminance contrasts; the panorama was extended to a 180° opening angle for sake of simplicity: a computer workplace is oriented perpendicularly to a nearby window, on which a solar blind is installed; the window is placed at a height corresponding to the worker’s eyes.

As a consequence, the examined BTDF values will be associated to the direction $(\theta_2, \phi_2) = (0^\circ, 0^\circ)$, for a fictitious sunlight incident direction $(\theta_1, \phi_1) = (0^\circ, 0^\circ)$.

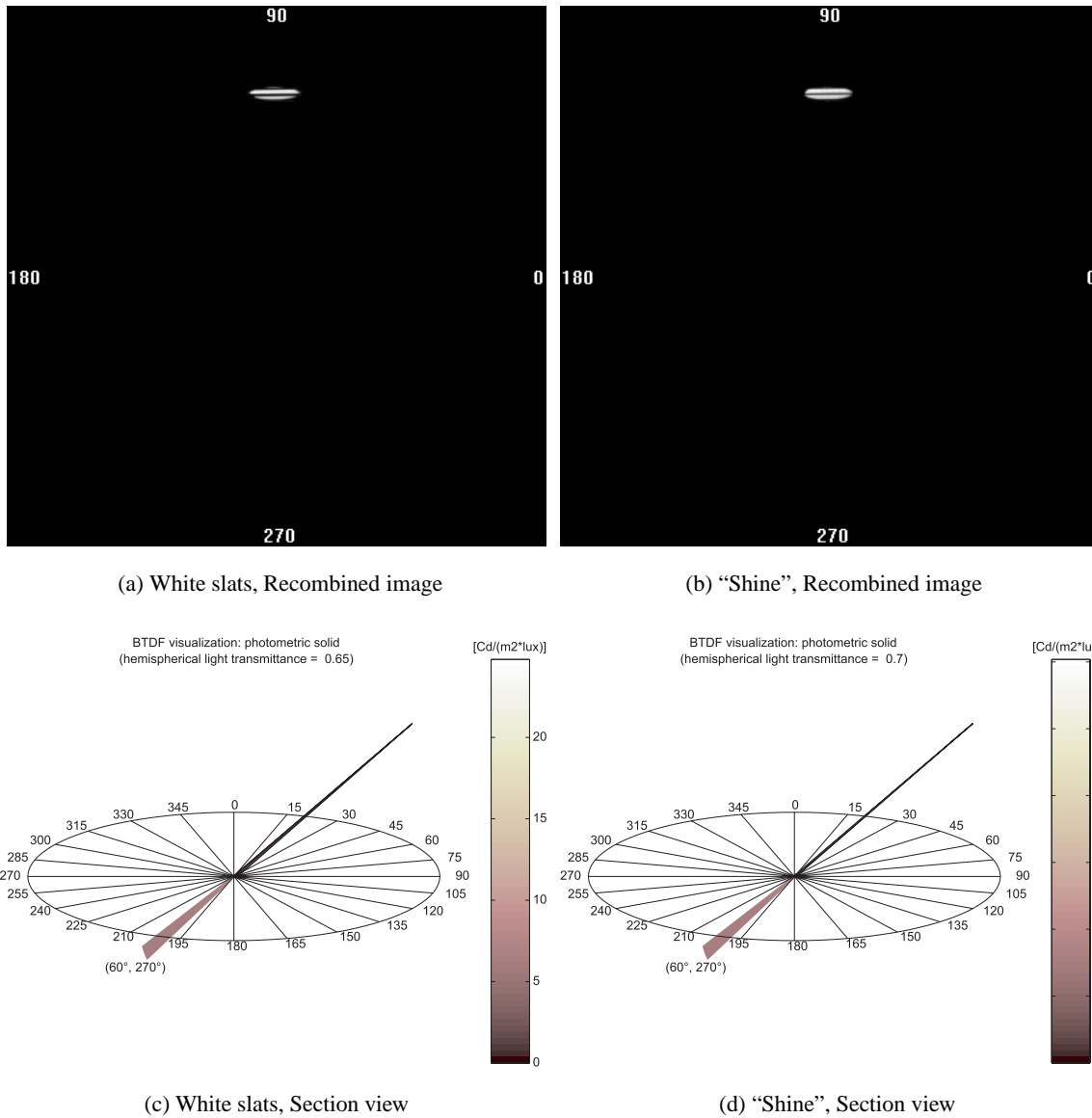


Figure 5.22: Graphical representations of BTDF data for two solar blinds for incidence $(\theta_1, \phi_1) = (60^\circ, 270^\circ)$.

Picking up the corresponding BTDF values for the conventional and optimized blinds, we obtain respective $BTDF(0^\circ, 0^\circ, 0^\circ, 0^\circ)$ values of 1.937 and $0.070 \text{ Cd}\cdot\text{m}^{-2}\cdot\text{lux}^{-1}$.

To account for the reduction of the daylight flux by the window glazing (situated behind the blinds), each BTDF value is multiplied by an approximate transmission factor 0.85 (double glazing), which leads to respective values of 1.646 and 0.060 for the two blinds.

Choosing a representative illuminance E_1 equal to 40,000 lux for clear sky conditions, the emerging luminances L_2 can be calculated according to Equation (2.1) and are found to be of 65,858 and $2,380 \text{ Cd}\cdot\text{m}^{-2}$ for the white slats and optimized blind respectively.

As the luminance produced by a computer screen is in general comprised between 100 and $200 \text{ Cd}\cdot\text{m}^{-2}$, one can deduce that emerging luminances higher than $2,000 \text{ Cd}\cdot\text{m}^{-2}$ will probably induce glare effects (luminance contrast larger than 10).

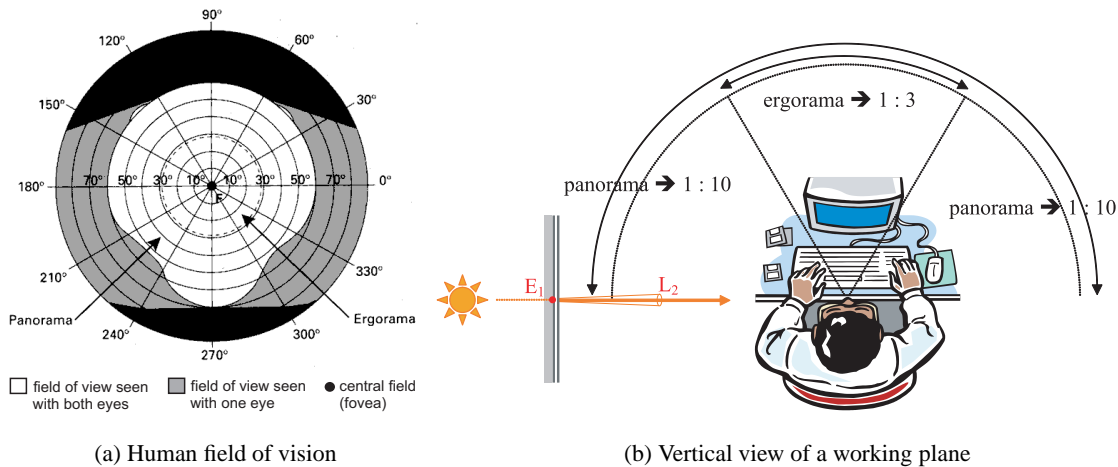


Figure 5.23: Ergorama and panorama for the study of luminance constraints.

In our case study, one immediately sees that the “Shine” prototype will induce a far more comfortable situation than the conventional white slats, where direct transmission is very important (Figure 5.19(c)). The graphical representations illustrated in Figures 5.19 to 5.21 also show that the major part of a beam reaching the “Shine” prototype is transmitted along a grazing direction (around $\theta_2 = 70^\circ$) thanks to the reflection on the slats, which shows that glare will probably not occur at a reasonable distance from the window.

A generalization of this example to other directions (θ_1, ϕ_1) and (θ_2, ϕ_2) and to other sample orientations, slats inclinations, relative positions of worker and window would be necessary for assessing real situations. The purpose of this simple study was only to show a way to extract information from BTDF data sets, and to point out the complementarity and usefulness of both graphical and numerical forms.

The use of computational methods becomes necessary in practical cases, as the assessment of daylight performances inside a room (e.g. illuminance at a given position) requires a lot of factors to be taken into account (dimensions, position, reflection factor of components, etc.).

5.5.4 Description of complex glazings in building simulations

Integrating BT(R)DF data in daylight simulation tools is an important issue to achieve an accurate rendering of light propagation for complex fenestration systems. An example of such an integration is here given with the lighting simulation tool *Radiance* (Ward Larson and Shakespeare, 1998).

Different fenestration materials presenting strong regular features were considered: a holographic film (see Section C.2.3), a 3M prismatic film (see Section C.3.2) and the laser cut panel (see Section C.2.1) whose transmission properties were shown in Figures 5.15(a) to 5.17(a). Only for the laser cut panel, however, has an substantial set of images been created.

This work, conducted in parallel to the measurement device development, is described in (Kaempf, 2003); the main achieved results are presented here.

Because of the strong specular transmission features of these types of glazing, the prismatic type material “prism2”, considered as a direct light component redirecting material, was chosen to be adapted amongst the available ones in *Radiance*. From this material, the two output directions of defined transmission coefficients produced from a given light direction can be calculated.

As the calculation process requires the light distribution function to be determined solely by the direction and transmission coefficient of the two main redirected components, the measured BTDF values were first processed:

- after being converted into their corresponding transmission factors τ_{dir} in (%), the two main peaks were isolated;
- their respective geometric centers were then located;
- finally, the averaging sectors contributing to each peak were gathered by summing up their associated transmission factors.

Once the the BTDF data were formatted for a proper integration into *Radiance*, the global transmission figure resulting from the combination of several weighted incident flux was deduced to re-create a realistic sky luminance distribution. For this combination, the sky vault discretization proposed by Tregenza (1987) within the IDMP international programme was used (see Section B.1.1), together with the all-weather model from Perez et al. (1993).

A sequence of the resulting images is shown on Figure 5.24 at different (solar) times of the day for the laser cut panel mounted on the upper part of a window in an arbitrary south-facing window. The chosen day is March 21st (equinox), the calculations being performed for a clear sky at latitude 47°N.

On these figures, one can observe the transmission characteristics noticed on Figures 5.15(a) to 5.17(a), and illustrated in Figure 1.2(a): only a small part of the impinging flux is transmitted regularly for most incident directions, whereas the major part is redirected upwards (towards the ceiling for a lateral window, which thus becomes a secondary natural light source). This effect is particularly visible in Figures 5.24(c), 5.24(e) and 5.24(g) where it can be compared to the nearby regular transmission of the clear glass (lower window pane).

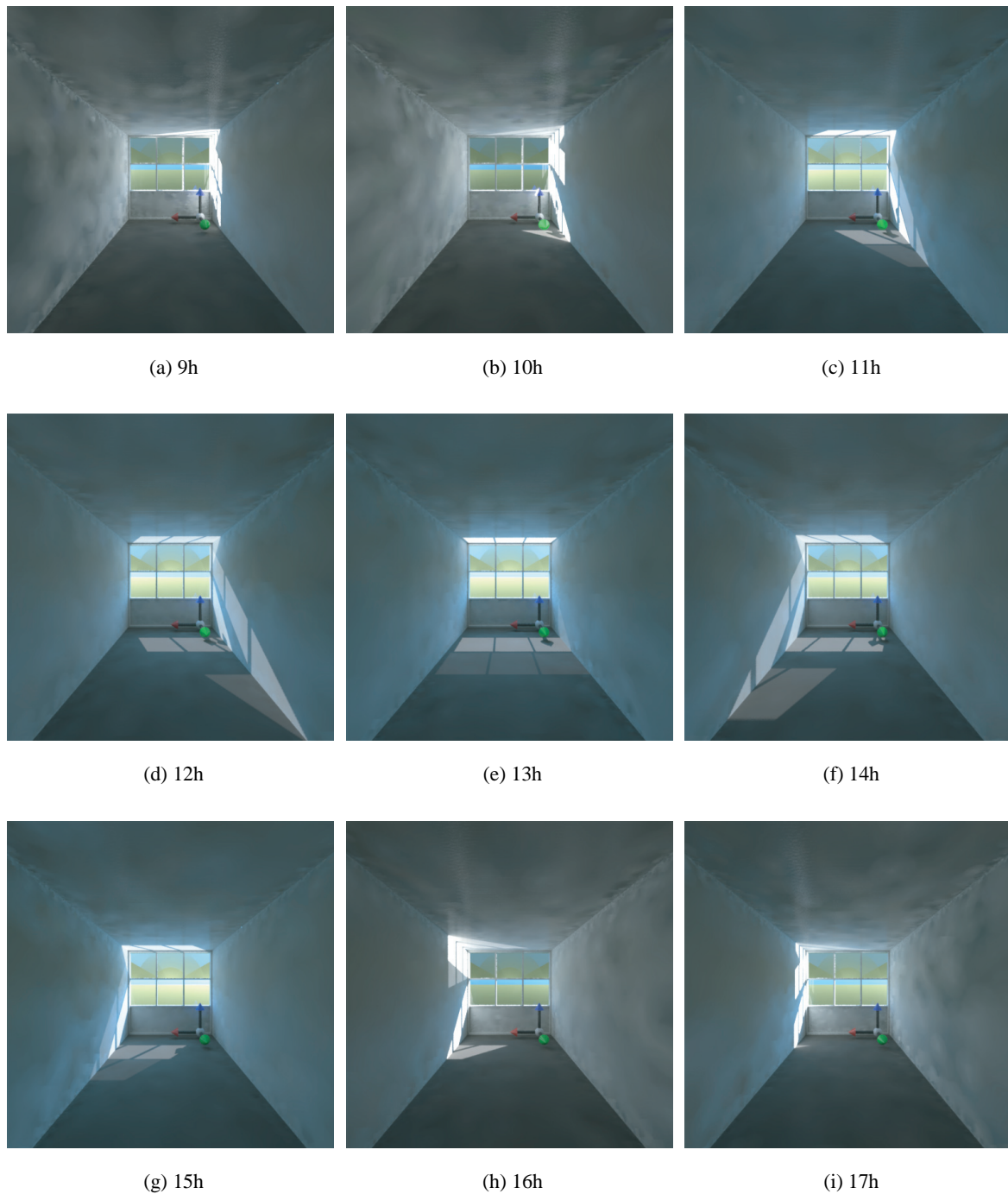


Figure 5.24: *Radiance* simulation results at different solar times for a side window consisting of a laser cut panel (upper portion) and a clear glass (lower portion). The laser cut panel transmission features are based on monitored BTDF data.

Chapter 6

Validation

“No amount of experimentation can ever prove me right; a single experiment can prove me wrong.” (Albert Einstein)

6.1 Experimental error

As for any new measurement device, validation of results is a crucial issue. The state of the art in complex glazings assessment being unfortunately too incipient, there are no standard procedures for validating goniophotometric data yet. As a consequence, different approaches were chosen:

- assessment of error at each intermediate stage of calibration and processing, a final error being deduced (Section 6.1);
- bidirectional measurements of systems presenting a known symmetry and verification against standard luminance-meter data or analytical calculations (Section 6.2);
- empirical validation based on bidirectional measurements comparisons between different devices (Section 6.3); in case of disagreement, however, no conclusion can be established;
- assessment of hemispherical optical properties by integrating BT(R)DF data over the whole hemisphere and comparison to Ulbricht sphere measurements (Commission Internationale de l’Eclairage, 1998) (Section 6.4);
- comparison of monitored data with ray-tracing simulations (Section 6.5) to achieve a higher level of details in the BT(R)DF behaviour assessment.

As mentioned in Section 2.2, at least one of the first four methods has been applied for other existing goniophotometers. In this chapter, the validation results obtained with all five approaches are presented.

6.1.1 Calibration error sources

The multiple calibrations necessary to assess BT(R)DF data in an appropriate way imply several possible sources of error. It is therefore important to evaluate inaccuracies induced at each calibration step and deduce the global impact on BT(R)DFs of such an assessment method: spectral and photometric calibrations of the CCD camera (Section 4.1); spatial calibration based on an interpolated grid of localized pixels (Section 4.2); sample illuminance measurement and adjustment (Section 3.4.1), correction of the sample diameter (compensation of incident beam spread) and of the image pixel levels (achievement of a uniform luminance mapping exempted from parasitic light) (Section 4.3).

Error due to CCD camera calibration

Spectral calibration

The relative error f'_1 , introduced in Section 4.1.1, determines how well the achieved relative spectral sensitivity $S(\lambda)$ of the CCD camera matches the spectral luminous sensitivity $V(\lambda)$ of the human eye for photopic vision (Commission Internationale de l'Éclairage, 1987). Its expression is given by Equation (6.1), which can be approximated by Equation (4.7):

$$f'_1(-) = \frac{\int_0^\infty |S(\lambda) - V(\lambda)| d\lambda}{\int_0^\infty V(\lambda) d\lambda} \quad (6.1)$$

f'_1 is found to be equal to 10.2%. Its actual impact on the BT(R)DF measurements is however by far lower than 10%, as it only applies as a secondary error source.

Indeed, as the photometric calibration determines the pixel greyscale value to luminance relation accounting for the camera's sensitivity $S(\lambda)$, results will be affected only if the sources used for calibration and characterization present different spectra: the closer $S(\lambda)$ is to $V(\lambda)$, the less these spectrum differences will matter.

To quantify the extent to which these differences will influence the results, the photometric error ϵ is used (Commission Internationale de l'Éclairage, 1987), given by Equation (6.2):

$$\epsilon(\%) = \frac{\left(\sum_{n=1}^{N_\lambda} S(\lambda_n) \cdot \Gamma_{\text{meas}}(\lambda_n) \cdot \Delta\lambda_n \right) \cdot \left(\sum_{n=1}^{N_\lambda} V(\lambda_n) \cdot \Gamma_{\text{calib}}(\lambda_n) \cdot \Delta\lambda_n \right)}{\left(\sum_{n=1}^{N_\lambda} V(\lambda_n) \cdot \Gamma_{\text{meas}}(\lambda_n) \cdot \Delta\lambda_n \right) \cdot \left(\sum_{n=1}^{N_\lambda} S(\lambda_n) \cdot \Gamma_{\text{calib}}(\lambda_n) \cdot \Delta\lambda_n \right)} \quad (6.2)$$

where $\Gamma_{\text{meas}}(\lambda)$ and $\Gamma_{\text{calib}}(\lambda)$ are the spectral radiances of the light source used respectively for BT(R)DF assessment and photometric calibration, expressed in ($\mu\text{W} \cdot \text{cm}^{-2} \cdot \text{sr}^{-1}$).

As the measurement source itself was used for calibration, ϵ can be neglected, as it thus only depends on the source's own fluctuations in spectrum of about 0.6%; when assessed against the solar spectrum, the photometric error does not go beyond 0.6% either. For the former source, however, ϵ reached 2% (3% when assessed against the solar spectrum), as a different calibration source had to be used (see Section 4.1.2).

One important restriction of the achieved BT(R)DF data's appositeness should be outlined, due to their photometric nature: a spectrally selective sample (colored or coated glass, film, screen) will not be differentiable from a neutral but less transmissive (reflective) one if the total loss in emerging luminance is the same. This typically induces that no conclusion can be made on the BT(R)DF resulting from a superposition of possibly selective layers if these were only assessed individually (thus requiring them to be characterized again in their superposed configuration).

Photometric calibration

Experimental errors during photometric calibration directly influence the luminances deduced from the raw digital images, and therefore the BT(R)DF themselves.

The luminances measured by the reference luminance-meter showed certain variations, yet very low: for usual luminances, an average relative fluctuation of 0.3% was observed, that remained below 2% for the lowest measured values. As far as the analyzed area on the diffusing surface is concerned, the standard deviation in greyscale level of the comprised pixels was inferior to 1% in relative terms, which means they differed on average by less than 1 absolute level.

Error due to spatial calibration

Amongst the different procedures necessary to achieve spatial calibration (see Section 4.2), only two can induce experimental errors, as all others are based on pure geometrical and analytical

relations: the screen positioning based on the LED's localization and the creation of the reference coordinates matrices $M_{\theta_{2\text{Ref}}}$ and M_{ψ_2} .

The accuracy of the screen position localization, determined by the bright spots maxima on the digital image, was assessed by observing how consistent the observed (X, Y) shifts are from one photodiode to another for different incident angles θ_1 and screen positions p . They were found either equal in both X and Y or disagreeing by at most one pixel in a given direction. As far as the $(\theta_{2\text{Ref}}, \psi_2)$ reference grid is concerned, the distances were reported with 0.5 mm inaccuracies, imperceptible on the digital image. The exact inclination of the screen, supposedly equal to Θ , is treated in Section 6.1.3. As a consequence, no significant impact on BT(R)DF data due to spatial calibration can be established.

Measurement conditions and correction factors

Sample illuminance assessment

As explained in Section 3.4.1, the illuminance uniformity showed 1.4% relative variations over the sample area (2% for grazing angles $\theta_1 > 70^\circ$); the simultaneous luxmeter measurements for E_1 , as well as their distance and position correction factor, showed less than 1% relative inaccuracy.

Incident beam spread correction

Thanks to the procedure described in Section 4.3.1, correction factors are applied to the diameter D to compensate the spread of rays reaching the considered sample area; these factors showed a relative error of 1.4%, which therefore affects the area with a 2% relative error $\left(\frac{\Delta A}{A} = \sqrt{2} \frac{\Delta D}{D}\right)$.

Impact of image non-uniformity

The image non-uniformity (darkening of pixels towards the edges) is corrected by an adequate factor applied to the pixel levels (see Section 4.3.2), determined with a 0.6% relative error.

Parasitic light detection

As detailed in Section 4.3.3, no influence of internal reflections could be observed, whereas some detectable parasitic light was caused by the light rays penetrating in case of obstructing screen positions in reflection mode. This excess of light flux being compensated in any case by a subtraction of the background image, no significant impact remains, leading to a negligible source of error.

6.1.2 Inaccuracies due to processing or mechanical constraints

The captured digital images are treated as maps of luminances to be converted into BT(R)DF data. Several parameters influence the quality of the achieved maps: resolution, handling of eliminated pixels (screen covers borders, blind spot, obstruction for grazing angles), correspondence between pixel coordinates and emerging direction, screen diffusion quality.

Resolution and removal of image pixels

Pixels size and weighted average

The level of details that can be reached in the BT(R)DF map remains limited by the digital image resolution. The duplicated image circumscribing the detection area is of dimension 685×488 pixels; based on the $(X, Y) \leftrightarrow (\theta_2, \psi_2)$ conversions, the pixels extent was calculated: in altitude, they were comprised between 0.05° and 0.2° , with a slight dependence on the sample thickness; in azimuth, they were found within a range of 0.1° to 30° (for the very last pixels on the triangle apex), leading to an average value of 0.25° .

Such limit resolutions would actually only be suitable for extremely small sample diaphragm diameters ($D < 0.5$ cm), where edge effects of course become significant in regard to the accuracy

of BT(R)DF data. A minimal value is actually imposed on intervals $\Delta\theta_2$ and $\Delta\phi_2$, of 0.5° and 1° respectively. Fortunately, these limit intervals are by far finer than the ones suitable for the fenestration systems assessment, usually ranging between $(5^\circ, 5^\circ)$ and $(10^\circ, 15^\circ)$, which reduces the pixellisation effect to only about 0.5%. This value was assessed using ray-tracing calculations, as in Section 6.1.3; in this case, BT(R)DF data based on a faithful model of the averaging grid are compared to values obtained with a shifted one (by the equivalent in degrees of half a pixel in altitude and azimuth). More details about the ray-tracing model set-up are given in Section 6.5.2.

As far as the averaging process is concerned, basing it on a unique pixel weight over the whole screen area was confirmed to have an imperceptible impact on BT(R)DF data, affected by less than 0.1% in relative terms.

Impact of blinded pixels

The blind zone induced in reflection mode by the passage of the incident beam through one of the screen positions must not be considered as an error source in itself but as a missing information, that doesn't influence the quality of the monitored BT(R)DF data.

Eliminating the pixels corresponding to the borders of the screen covers, however, does affect BT(R)DFs as it requires an implicit interpolation of neighboring pixels. To estimate the degree to which it influences the final data, bidirectional transmission measurements achieved with the former projection screen (presenting no cut-out ellipses) were compared with those obtained for the same sample and incident directions using the motorized screen. This was done for various glazings presenting very different transmission features and characterized according to various averaging grid intervals $(\Delta\theta_2, \Delta\phi_2)$ (see Appendix C): a diffusing white opalescent plexiglas (described in Section C.1.1), an acrylic prismatic panel (Section C.3.1), a holographic film (Section C.2.3) and a fabric blind (Section C.4.2). The relative differences were calculated for these four materials for several incident directions (four for the plexiglas, five for the prismatic and HOE panels, three for the fabric blind) and thereafter averaged for each material.

It was found that the missing pixels had less than half of the impact for a diffusing material than for a material with strong regular features. This is coherent with the fact that the implicit interpolation within averaging sectors presenting eliminated pixels will affect less the mean BT(R)DF for close pixel values than with large gradients. Overall, a relative error of 5% was found due to the impact of eliminated pixels.

Obstruction of grazing rays

Averaging sectors where more than half of the emerging rays are obstructed by mechanical components (see Section 4.2.4) are simply removed from the final BT(R)DF data file, thus inducing no additional error.

However, an estimation of their value is still needed for the directional-hemispherical transmittance or reflectance calculation (see Section 6.4.1) to avoid data underestimation, especially for very diffusing optical materials. An extrapolation of BT(R)DFs is thus applied along azimuth planes to include values associated to the grazing hemisphere part in the calculation of $\bar{\tau}_{\text{th}}$ or ρ_{dh} .

Directional range due to non-punctual sample

As mentioned in Section 5.2, each surface element on the detection screen (i.e. each image pixel), although associated to a single (average) emerging direction (θ_2, ψ_2) , can be reached by rays corresponding to a range of directions Υ ($^\circ$) that is proportional to the sample illuminated area.

To get an approximate value for Υ in altitude and azimuth, the maximal difference \mathfrak{Y}_2 between $\theta_{2\text{far}}$ and θ_2 or θ_2 and $\theta_{2\text{close}}$ is evaluated accounting for parameters e_s and D , as well as the maximal difference Υ_{ψ_2} between either $\psi_{2\text{far}}$ and ψ_2 or ψ_2 and $\psi_{2\text{close}}$. These two quantities are defined in Figures 6.1(a) and 6.1(b), where θ_{2M} and ψ_{2M} are expressed by Equations (6.3):

$$\theta_{2M} = 90^\circ - \arctan \frac{H - \frac{D \cdot \cos \psi_2}{\sqrt{3}} + g - e_s}{\frac{D}{2}}$$

$$\psi_{2M} = \arctan \frac{D}{2 \cdot d \cdot \sin \theta_2 \cdot \cos \psi_2} \quad (6.3)$$

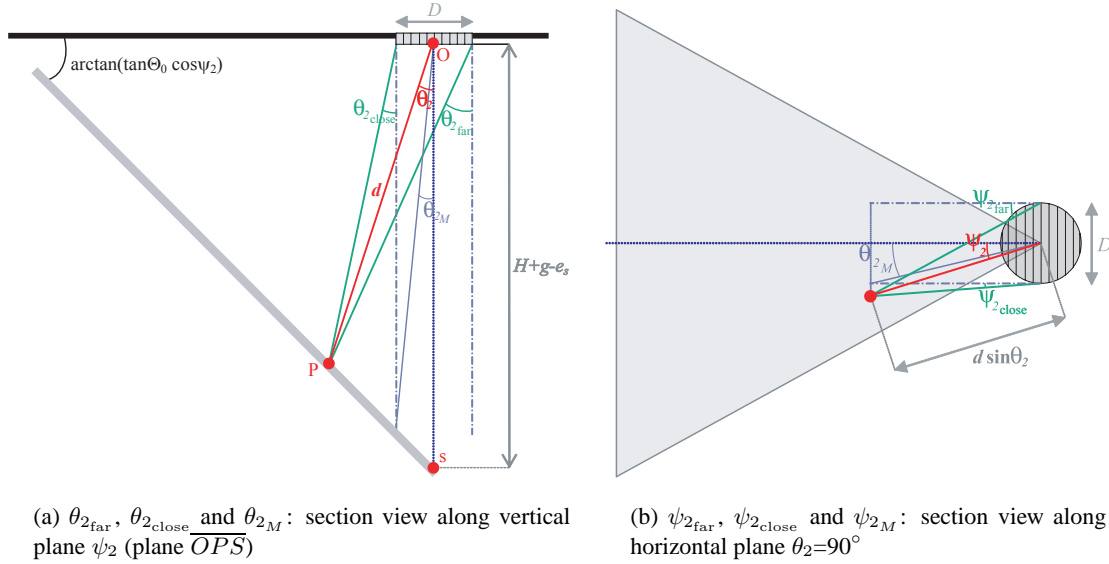


Figure 6.1: Evaluation of the maximal divergence Υ that can be observed for rays emerging from a sample diameter D and reaching a given point on the screen.

The resulting expressions for Υ are given by Equations (6.4), where $\theta_{2\text{close}}$ or $\psi_{2\text{close}}$ are equal to 0 if $\theta_2 \leq \theta_{2M}$ or $\psi_2 \leq \psi_{2M}$ respectively:

$$\begin{aligned} \Upsilon_{\theta_2} &= \max(\theta_{2\text{far}} - \theta_2; \theta_2 - \theta_{2\text{close}}) \\ &= \max\left(\arctan\left(\tan \theta_2 + \frac{D}{2 \cdot d \cdot \cos \theta_2}\right) - \theta_2; \theta_2 - \arctan\left(\tan \theta_2 - \frac{D}{2 \cdot d \cdot \cos \theta_2}\right)\right) \\ \Upsilon_{\psi_2} &= \max(\psi_{2\text{far}} - \psi_2; \psi_2 - \psi_{2\text{close}}) \\ &= \max\left(\arctan(\tan \psi_2 + \tan \psi_{2M}) - \psi_2; \psi_2 - \arctan(\tan \psi_2 - \tan \psi_{2M})\right) \end{aligned} \quad (6.4)$$

As BT(R)DFs are averaged within angular sectors proportional to the sample size (see Section B.1.3 and Equation (5.17)), this possible divergence is compensated as long as $\Delta\theta_2$ and $\Delta\phi_2$ are greater or equal to Υ_{θ_2} and Υ_{ψ_2} respectively. Both Υ_{θ_2} and Υ_{ψ_2} being functions of θ_2 and ϕ_2 and thus varying over the screen area, this compensation needs to be checked for every combination of direction (θ_2, ϕ_2) , thickness e_s (affecting d) and sample diameter D , as D determines the optimal intervals $\Delta\theta_2$ and $\Delta\phi_2$ (typically equal to $(5^\circ, 5^\circ)$, $(10^\circ, 15^\circ)$ and $(15^\circ, 20^\circ)$ for $D = 10, 20$ and 30 cm respectively). Fortunately, the study revealed that such values remained greater than the corresponding Υ_{θ_2} and Υ_{ψ_2} values for almost all of these combinations.

Screen diffusion quality

The screen diffusion variations were assessed experimentally for different impinging and emerging directions and found to be equal to 2.6% (Section 3.2.5). Accounting also for the slight spectral dependence of the reflection coefficient over the visible range (1.5%) and for the 0.2% variation of ρ_{screen} over the surface of the screen, a relative error of 3% ($= \sqrt{0.026^2 + 0.015^2 + 0.002^2}$) was found.

6.1.3 Mechanical components adjustment

As for the pixel resolution impact, ray-tracing simulations were used to get a raw order for the influence of slight imprecisions in alignment and tilt of the goniophotometer's mechanical components.

Incident direction accuracy

The main platform tilting error was estimated between 0.1° to 0.2° ; the sample holder's positioning accuracy was observed to be of $\pm 0.2^\circ$.

Using the experimental set-up model described in Section 6.5.2, two different systems were analyzed: a prism and a venetian blind. Based on forward ray-tracing calculations, their BTDFs were determined respectively for incidences $(\theta_1, \phi_1) = (10^\circ, 90^\circ)$ and $(31^\circ, 30^\circ)$ and for averaging intervals $(\Delta\theta_2, \Delta\phi_2) = (5^\circ, 5^\circ)$ and $(10^\circ, 15^\circ)$. These data were then compared to those obtained for slightly shifted incident directions: $(\theta_1 \pm 0.15^\circ, \phi_1)$ and $(\theta_1, \phi_1 \pm 0.2^\circ)$.

Mean relative BTDF fluctuations of 1.3% and 0.3% were observed for such altitude and azimuth modifications, leading to an error of about 1.3% ($= \sqrt{0.013^2 + 0.003^2}$) due to the incident direction inaccuracy.

Detection screen positioning

The incertitude on the inclination angle Θ_0 of the projection screen was determined with a micrometric protractor and found to be equal to $\pm 0.05^\circ$; the gap g and height H (whose sum makes up the distance from sample plane to detection area apex, see Figure 4.11) showed a less than 1 mm inaccuracy. The six positions of the rotating ring supporting the screen and camera system were verified with both a spirit level and source beam alignments: their inaccuracy was found to be equal to $\pm 0.15^\circ$.

The same method was used to determine how these slight imprecisions could affect the BTDF data for the two mentioned samples and incident directions. The specific relative errors were of 0.3%, 0.2% and 0.7% for the incertitude on Θ_0 , $H + g$ and the screen exact position respectively, leading to a total error due to the detection screen adjustment of 0.8%. As this error is to be associated to the distance d from sample to screen, its effect on BT(R)DFs will be doubled, d being squared in Equation (5.7) (see Section 5.4.1).

6.1.4 Global relative error

Table 6.1 gathers all the significant error sources amongst the above analysis and associates each of them to the affected parameter in Equation (5.7).

Error source	Relative error (%)	Affected parameter
Spectral calibration	0.6	L_{screen}
Photometric calibration	1.0	L_{screen}
Illuminance measurement	1.4	E_1
Beam collimation	2.0	A
Image uniformity	0.6	L_{screen}
Pixel resolution	0.5	(θ_2, ψ_2)
Eliminated pixels	5.0	BT(R)DF
Screen diffusion	3.0	ρ_{screen}
Incident direction	1.3	(θ_1, ϕ_1)
Screen position	1.1	d^2

Table 6.1: Relative errors induced at the different calibration stages and corresponding affected parameter in Equation (5.7).

The global relative error $\varepsilon_{\text{BT(R)DF}}$ on the monitored BT(R)DF data was calculated through Equation (6.5), where f_i and N_f refer to the different individually affected parameters and their number and where $\varepsilon_{\text{elim}}$ refers to the relative error due to eliminated pixels, observed directly on BT(R)DFs and thus added separately:

$$\varepsilon_{\text{BT(R)DF}} = \frac{\Delta \text{BT(R)DF}}{\text{BT(R)DF}} = \sqrt{\sum_{i=1}^{N_f} \left(\frac{\Delta f_i}{f_i}\right)^2} + \varepsilon_{\text{elim}} \quad (6.5)$$

Including the different specific terms of Table 6.1 in Equation (6.5), a global relative error for BT(R)DF data was determined:

$$\varepsilon_{\text{BT(R)DF}} = 4.5\% + 5.0\% \simeq 10\% \quad (6.6)$$

6.2 Analytical verification

For some materials, transmission (reflection) properties can be estimated (sometimes even BT(R)DFs) on the basis of observed symmetries and/or analytical calculations. In this section, several systems were selected for that purpose and compared to theoretical expectations.

6.2.1 Symmetry-based comparisons

Several materials were selected for their known symmetries, checked on the corresponding BT(R)DF data sets:

- a white opalescent plexiglas (Section C.1.1): in transmission, a rotational symmetry is expected; in reflection, a strong specular component of predictable direction $(\theta_2, \phi_2) = (\theta_1, \phi_1 + 180^\circ)$ combined with a diffuse behaviour in all other directions;
- the LMT photometer paint used for the projection screen (Section 3.2.5) with quasi-lambertian reflecting properties;
- a system composed of adjacent curved mirror squares (see Section C.5.2): the mirrored surface geometry induces reflection figures to present diamond-shapes features (quadratic symmetry for normal incidence, axial symmetry along $\phi_2 = \phi_1 + 180^\circ$ for other incident directions).

As shown by Figure 6.2(a), the rotational symmetry for the opalescent plexiglas is apparent on the different section views, which present mean relative differences lower than 1.2% and a lambertian behaviour verified by a 3.1% relative discrepancy for all non-grazing directions.

To study these results at the pixel level (and not restrict the analysis to BTDFs averaged inside angular sectors), calibrated screen images were stored before being converted into BTDFs. Individual $\frac{L_{\text{screen}}}{E_1}$ pixel values obtained on a given θ_2 arc (every 2.5° in altitude and azimuth, see white dots on Figure 6.2(b)) were then corrected in distance and light rays tilt (i.e. multiplied individually by $\frac{d^2}{\cos \alpha}$) and compared to each other.

This detailed investigation showed relative differences lower than 1.3% on average for θ_2 values up to 70° (at most by 7%), which outlines a remarkable agreement between theoretical expectations and experimental results.

The analysis of the same material in reflection (see Figure 6.3(a)) allowed to verify two features: on one hand, the specular reflection was checked to be observed specifically along direction $(\theta_2, \phi_2) = (\theta_1, \phi_1 + 180^\circ)$, which proved perfectly correct for all incident altitudes ($\theta_1 = 0^\circ, 20^\circ, 40^\circ, 60^\circ$ and 80°).

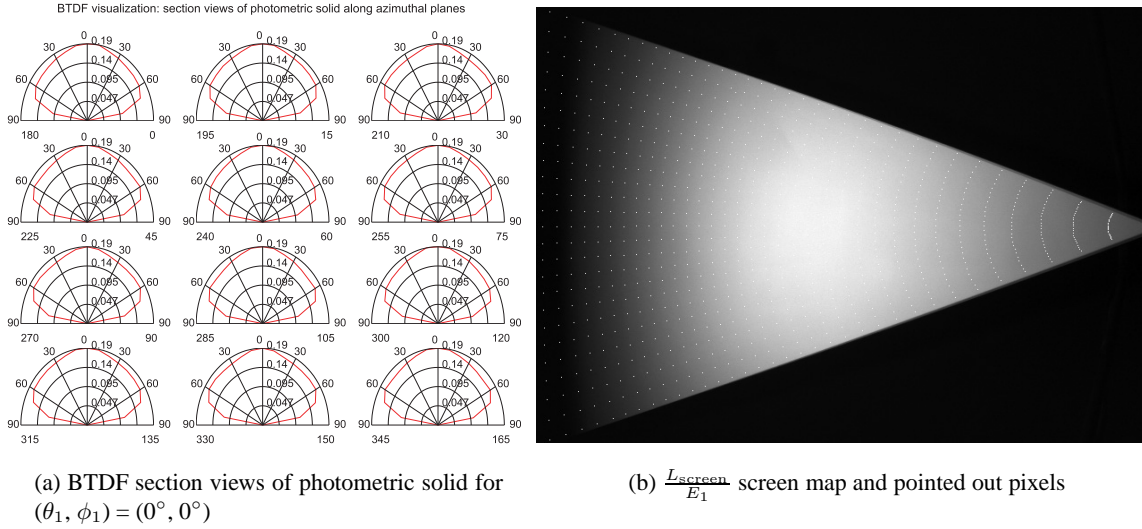


Figure 6.2: Verification of rotational symmetry for a white opalescent plexiglas.

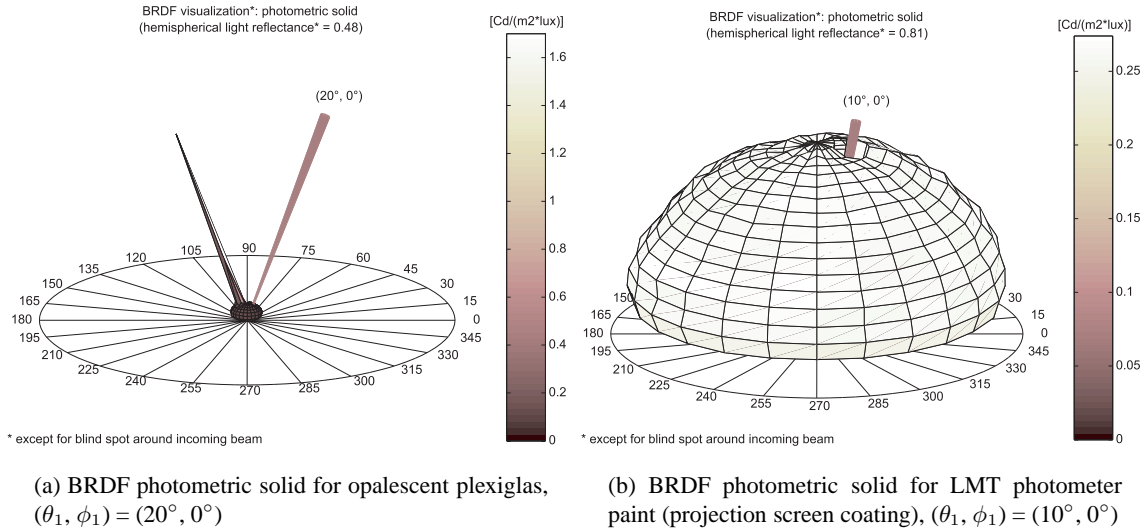


Figure 6.3: Analysis of reflected light distribution for opalescent glass and diffusing paint.

On the other hand, the isotropic diffuse behaviour was checked around normal incidence: it was verified with a 1.5% relative accuracy.

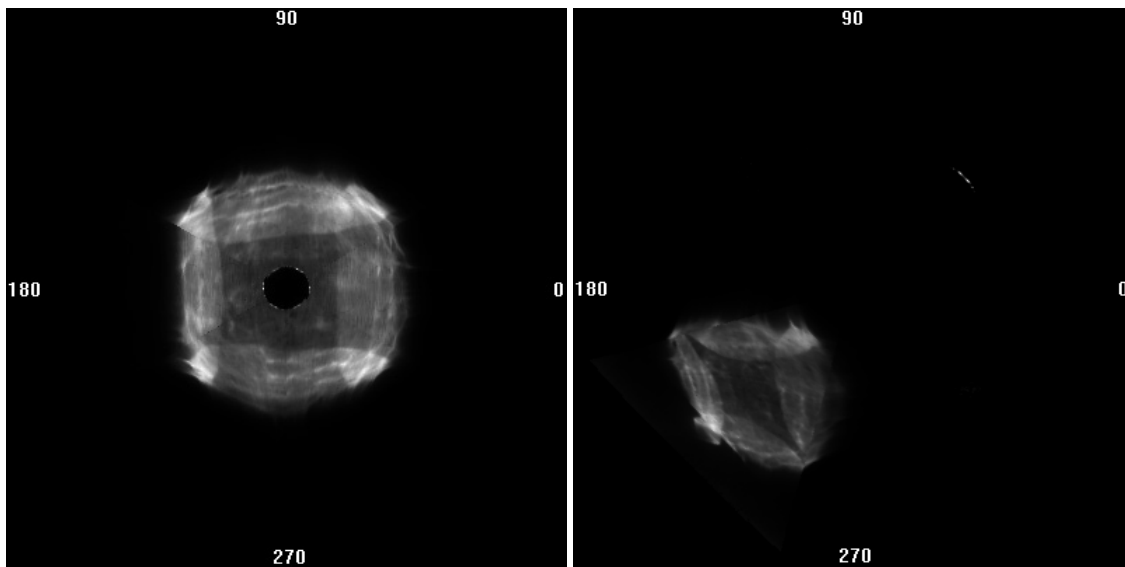
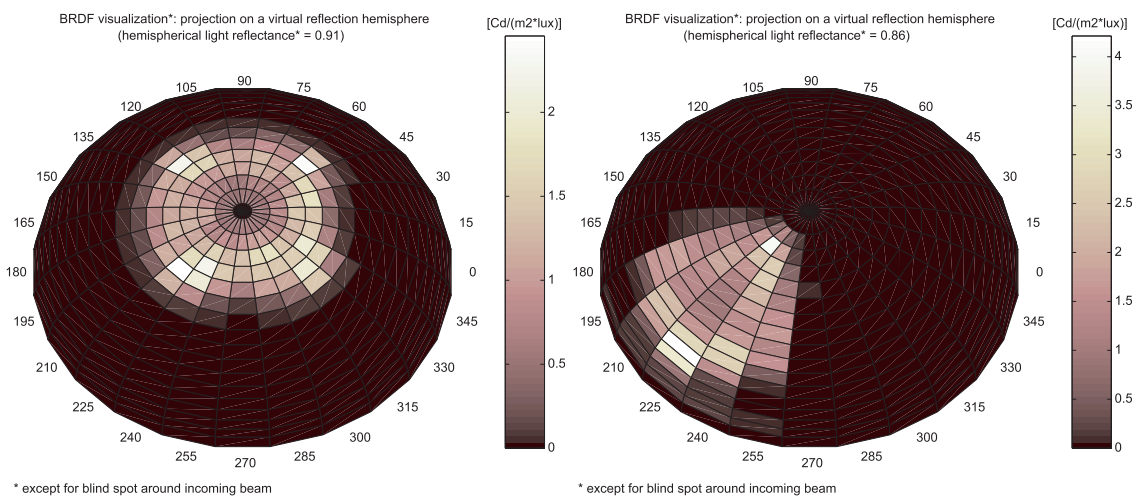
Besides, from the integrated transmittance and reflectance values τ_{dh} and ρ_{dh} for different incident angles $\theta_1 = 0^\circ, 20^\circ, 40^\circ, 60^\circ$ and 80° , the consistency in bidirectional measurements from one mode (BTDF) to the other (BRDF) could be verified, as their sum cannot exceed 100%. In fact, the determined non-absorbed fraction of incident light flux remains around 1% below $\theta_1 = 60^\circ$, and then increases up to 20% for grazing incident altitudes due to a strong decrease in τ_{dh} .

For the LMT diffuse coating, a quasi-lambertian behaviour was verified on the monitored BRDF data: the photometric solid of Figure 6.3(b) is of quasi-hemispherical shape, showing an isotropic distribution of luminances. The observed fluctuations for all θ_2 and ϕ_2 angles remain close to 5.4%: here, not only is a rotational symmetry expected, but also a constant BRDF over the whole emerging hemisphere. This is a very satisfactory result considering the 10% relative error assumed on measured BRDFs and the assessed 2.6% mean variation in diffusion.

The total reflectance ρ_{th} deduced from these BRDF data (see Section 6.4.1) was checked against the $\rho_{\text{screen}} = 0.75$ value assessed with a Minolta CR-200b surface chromameter (see Section 3.2.5): ρ_{th} was found equal to 0.81, leading to a 8% relative discrepancy consistent with the above statement.

Finally, the different integral views and hemispherical projections obtained for the curved mirror squares characterization (see Figure C.5(d)) confirmed the awaited behaviours, as shown by the two examples provided in Figure 6.4: only slight asymmetries can be spotted, imputable to the imperfect execution of the mirror pieces. The fact that neither a sixth order symmetry can be perceived nor a splitting in the reflection figure when passing from one screen position to the other bears out the accuracy and adequacy of the pixels conversion given by Equation (5.7).

Altogether, this whole study led to a remarkable agreement of the monitored data with the theoretical expectations.

(a) Recombined image, $(\theta_1, \phi_1) = (0^\circ, 0^\circ)$ (b) Recombined image, $(\theta_1, \phi_1) = (40^\circ, 45^\circ)$ 

* except for blind spot around incoming beam

* except for blind spot around incoming beam

(c) Hemispherical projection, $(\theta_1, \phi_1) = (0^\circ, 0^\circ)$ (d) Hemispherical projection, $(\theta_1, \phi_1) = (40^\circ, 45^\circ)$

Figure 6.4: Reflection figures for the curved mirror squares for normal and diagonal incident directions.

6.2.2 Theoretical bidirectional functions

For analytic verifications of BT(R)DF data, simple glazing systems are required. Clear glass would provide an excellent example of material presenting well-known transmission properties (e.g. using ISO 9050 (International Organization for Standardization, 2003)), as would a flat mirror of precisely determined ρ_{dir} reflection value; however, the optimal BTDF analytical validation remains the hole (a simple aperture), the luminance distribution being accurately predictable both in direction and value. As explained below, the corresponding analytic equations were established and compared to measured ($\frac{L_{\text{screen}}}{E_1}$) ratios, extracted from the calibrated images.

On the other hand, this basic case provides a very reliable point of comparison for an error estimation of integrated hemispherical transmittance τ_{th} (and thus reflectance ρ_{th}), as discussed in Section 6.4.

Applying Equation (5.12) to a simple aperture ($\tau_{\text{th}} = 1$), one can immediately deduce an expression for ($\frac{L_{\text{screen}}}{E_1}$) within the directly illuminated screen area (unique bright spot); it is given by Equation (6.7):

$$\frac{L_{\text{screen}_{\text{spot}}}}{E_1(\theta_1)} = \frac{\rho_{\text{screen}}}{\pi} \frac{h^2 \cdot \cos \alpha}{(h + d)^2} \quad (6.7)$$

A set of theoretical values were thus established for different θ_1 and D configurations, as well as for shifted screen positions (to vary d and α). They were compared to the ones obtained for the calibrated pixels within the corresponding bright spots, illustrated on Figure 6.5.

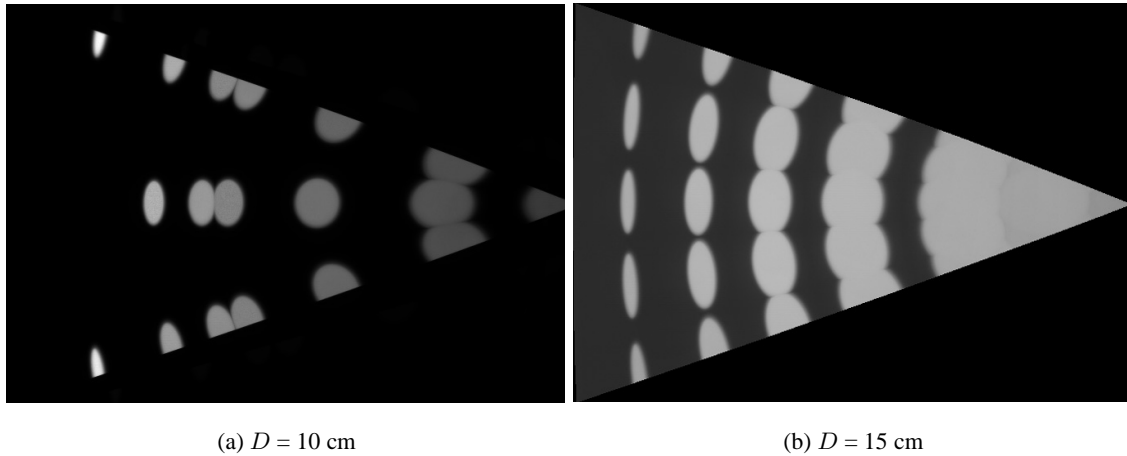


Figure 6.5: Superposition of calibrated images for direct beam (simple aperture), for varying θ_1 and screen positions p , $p \pm 15^\circ$ and $p \pm 30^\circ$.

The comparison led to a very good agreement between theory and measurements: the relative differences were lower than 8.7% with an average of only 2.9% for the considered configurations.

6.3 Empirical validation

Some early stage comparisons of BTDF data monitored with several existing goniophotometers (see Section 2.2) were carried out within the framework of International Energy Agency Task 21 “Daylighting in Buildings” (International Energy Agency, 2000); unfortunately, only a few bidirectional datasets were made available in the end, mainly from the Berlin University of Technology (TUB) in Germany in addition to the EPFL data presented in Appendix C.

In this section, BT(R)DF measurements are compared for three types of glazings to other goniophotometric data. Because of the important differences in the assessment method (mean BT(R)DFs inside adjacent hemisphere parts versus scanning process, see Section 2.2), such comparisons are not applicable for important luminance gradients; systems presenting diffuse components in their emerging light distribution were thus selected.

6.3.1 Inter-laboratory comparison for opalescent glazing

Within the REVIS project conducted by the TNO Building and Construction Research in The Netherlands (van Dijk, 2001), some experimental data could be used for quantitative comparisons, based in particular on bidirectional measurements of a diffuse opalescent material (see Section C.1.2). The comparative results are shown for normal incidence on Figure 6.6 where cosine-corrected ($BTDF \cdot \cos \theta_2$) BTDFs are displayed (American Society for Testing and Materials, 1997b).

A very good agreement between both data can be observed on these section views: the $BTDF \cos \theta_2$ values decrease according to a cosine law for both sets of measurements: the transmission can thus be assumed lambertian, showing constant BRDFs (except for grazing angles) of about 0.063 sr^{-1} for the TNO results and 0.066 for the LESO, i.e. presenting less than 5% difference in relative terms.

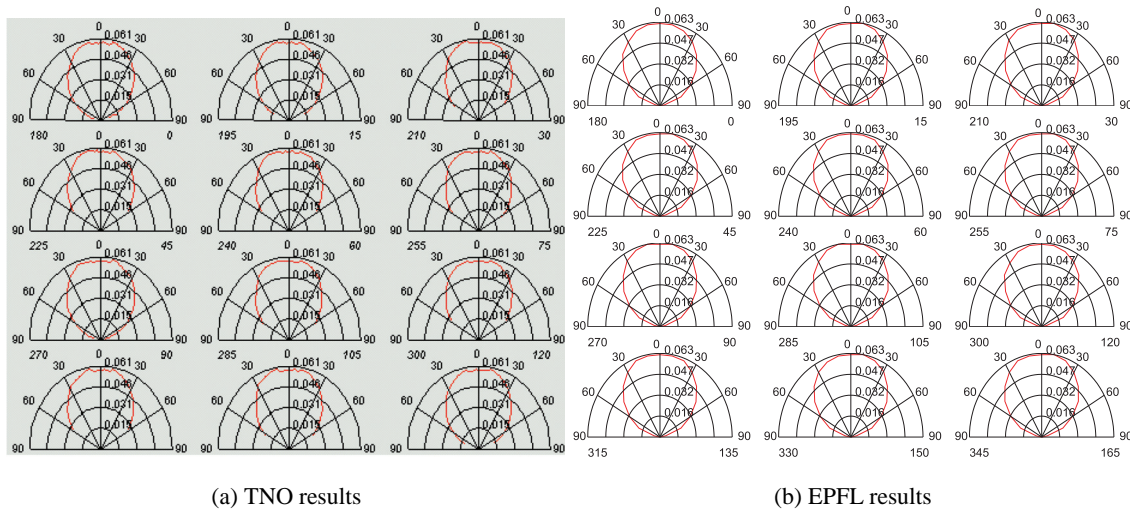


Figure 6.6: $BTDF \cdot \cos \theta_2$ section views for a 2.5 mm thick opalescent material (normal incidence).

Similarly, TUB results for the opalescent plexiglas (see Section C.1.1) were used for a detailed BTDF comparison with EPFL data. For this purpose, all mutually characterized incident angles θ_1 were considered for the white opalescent plexiglas, i.e. $\theta_1 = 0^\circ, 12^\circ, 24^\circ, 36^\circ, 48^\circ, 60^\circ, 72^\circ$. An example of each laboratory's resulting photometric solids is shown on Figure 6.7 for incidence $(\theta_1, \phi_1) = (24^\circ, 0^\circ)$.

After TUB's datasets were averaged inside angular sectors corresponding to the EPFL measurements, the results were compared for all seven incident directions individually. Table 6.2 provides an overview of the observed relative differences.

The results show that both datasets fit within a very reasonable range: for all $(\theta_1, \theta_2, \phi_2)$ configurations, a mean relative difference of 8.1% was found, going down to 6.2% if only non-grazing θ_2 angles are considered ($\theta_2 < 70^\circ$). This proves on one hand the reliability of both devices and on the other hand that the averaging method applied for the EPFL goniophotometer does not alter the measurement's quality.

θ_1 (°)	$\frac{\Delta BTDF}{BTDF}_{\forall \theta_2}$ (%)	$\frac{\Delta BTDF}{BTDF}_{\theta_2 < 70^\circ}$ (%)
0	7.5	6.8
12	8.9	8.2
24	6.3	5.3
36	6.2	5.0
48	8.4	7.1
60	6.7	5.1
72	12.5	6.0

Table 6.2: Mean relative differences between TUB and EPFL measurements for the BTDF characterization of the opalescent plexiglas for different incident altitudes θ_1 .

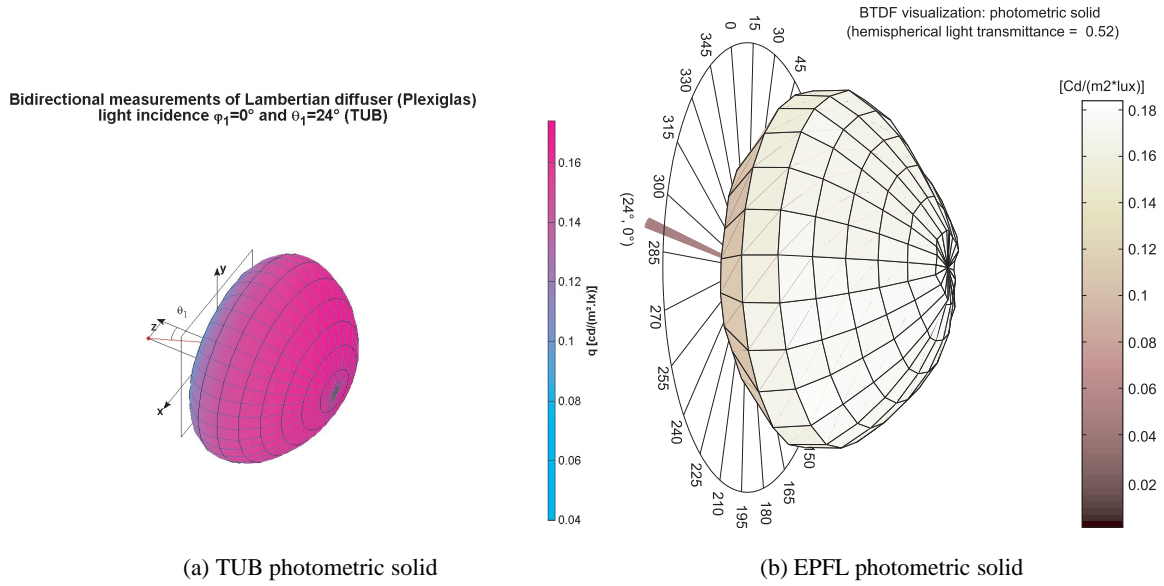


Figure 6.7: BTDF data monitored by TUB and EPFL for the opalescent plexiglas, incidence $(\theta_1, \phi_1) = (24^\circ, 0^\circ)$.

6.3.2 Comparison of diffuse components in a complex BTDF figure

In addition to the above study, the sun-directing glass “LumitopTM” manufactured by Vegla was considered for a BTDF comparison.

Amongst the available set of 145 incident directions, incidence $(\theta_1, \phi_1) = (60^\circ, 285^\circ)$ was selected for the significant scattering features presented by its transmission figure; the latter were spotted out on the hemispherical projection shown on Figure 6.8(a).

The monitored BTDFs are shown on Figures 6.8(b) and 6.8(c) for the two laboratories. The discrete TUB data along directions (θ_2, ϕ_2) were averaged inside angular sectors of intervals $(\Delta\theta_2, \Delta\phi_2) = (5^\circ, 5^\circ)$ according to the EPFL investigation method.

For the selected diffuse space portions, the data were then compared, leading to very satisfying results: although the transmission features were this time not perfectly diffusing, only a 3.5% mean relative difference was found between the two datasets (with a maximal divergence of 8.5%), which strongly reinforces the previous conclusions for perfectly diffusing materials.

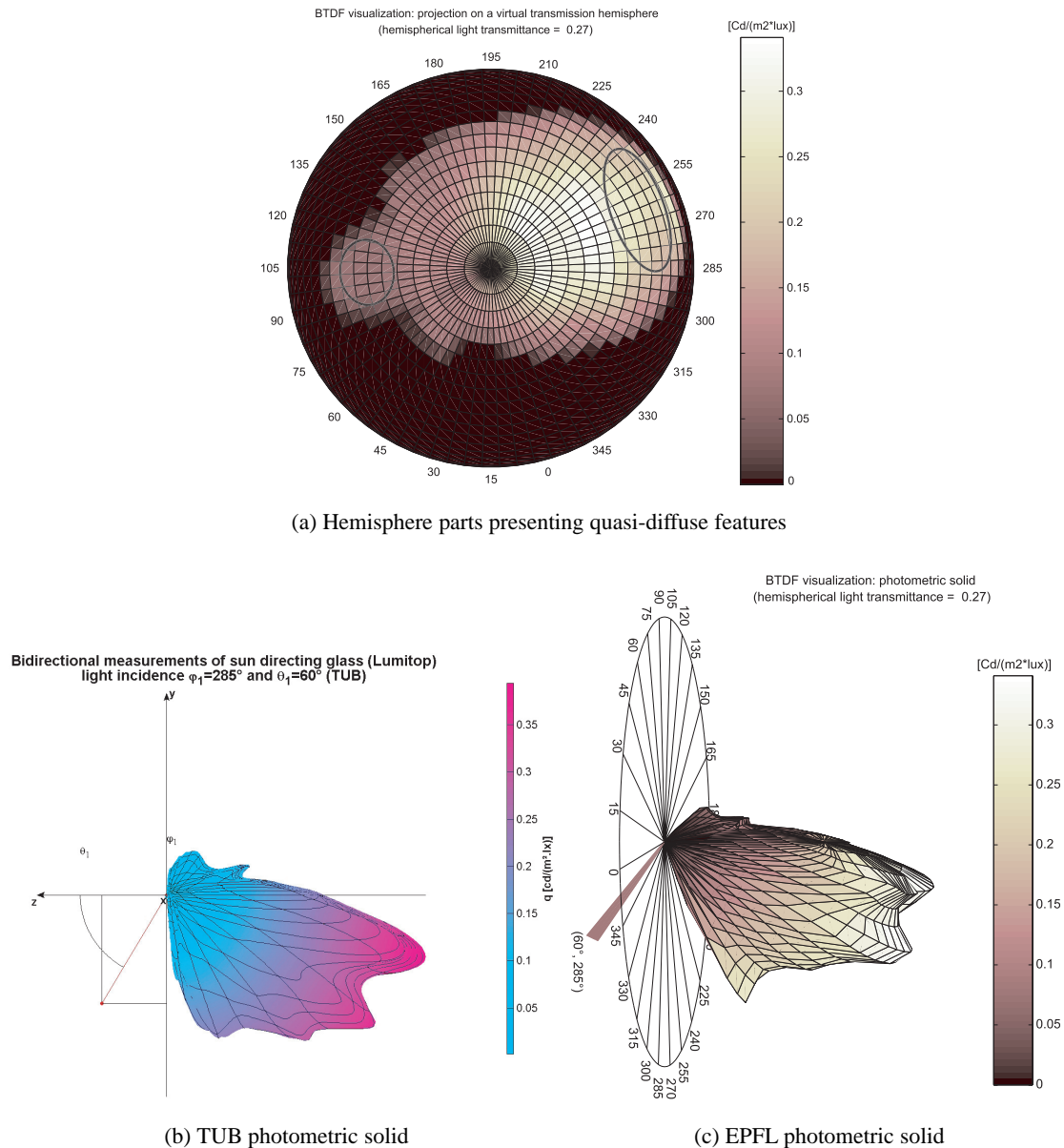


Figure 6.8: BTDF data monitored by TUB and EPFL for the sun directing glass, incidence $(\theta_1, \phi_1) = (60^\circ, 285^\circ)$.

6.4 Directional-hemispherical transmittance (reflectance) comparisons

Considering directional-hemispherical transmittance or reflectance values based on the numerical integration of bidirectional data over the whole emerging hemisphere is one of the most common used methods to validate BT(R)DFs measurements (Murray-Coleman and Smith, 1990; Apian-Bennewitz, 1994; Breitenbach and Rosenfeld, 1998; Andersen et al., 2000; van Dijk, 2001).

From a more general point of view, directional-hemispherical transmittance or reflectance are also widely used to compare different assessment methods for complex fenestration systems performances, as was the case for:

- inter-laboratories comparisons of angle-dependent transmittance or reflectance, either between different types of integrating spheres for translucent films (Chevalier et al., 1998) or between measurements and analytical models for coated glass sheets (Hutchins et al., 2001);

- the development of an angle-dependent Solar Heat Gain Coefficient evaluation procedure, requiring measurements to be compared to matrix layer calculations (Klems et al., 1997) or to analytic model predictions (Breitenbach et al., 1999);
- the comparison of goniophotometric data with results provided by an analytic model (Rosenfeld, 1996; Breitenbach et al., 2001);
- validating either a simple empirical algorithm (Roos, 1997) or detailed structural models (Rubin et al., 1999) against angular-dependent integrating sphere measurements for coated glazings;
- verifying different analytical models against direct-hemispherical transmittance for complex glazings such as solar control films, translucent insulation and venetian blinds (Rosenfeld et al., 2001).

The mathematical development leading from BT(R)DF data to τ_{dh} (or ρ_{dh}) is presented below. The transmittance (or reflectance) deduced from BT(R)DF datasets generated with the goniophotometer were compared to Ulbricht sphere measurements obtained for the same samples by different European laboratories. Finally, τ_{dh} values derived from BTDF data were assessed against ray-tracing calculations for prismatic panels and a mirror-coated venetian blind, using simulation models of these systems.

6.4.1 Integration of BT(R)DF over emerging hemisphere

From a complete BT(R)DF dataset, it is possible to determine the directional-hemispherical visible transmittance $\tau_{\text{dh}}(\theta_1, \phi_1)$ or reflectance $\rho_{\text{dh}}(\theta_1, \phi_1)$, expressed by the combined symbol $\tau_{\text{dh}} | \rho_{\text{dh}}$ for simplification. As mentioned above, this parameter is of great importance in the validation of bidirectional measurements, but also in the assessment of the global photometric behaviour of a fenestration material.

It is calculated at the end of a monitoring process for each incident direction (θ_1, ϕ_1) and appears explicitly in the final BT(R)DF dataset (see Section B.2.1).

Determination of analytical expression

To determine the relation between $\tau_{\text{dh}} | \rho_{\text{dh}}$ and the BT(R)DF data, a hemisphere placed around the sample center and of arbitrary radius R_0 is considered; averaging sectors limited by $[\theta_2 - \frac{1}{2}\Delta\theta_2; \theta_2 + \frac{1}{2}\Delta\theta_2]$ in altitude and by $[\phi_2 - \frac{1}{2}\Delta\phi_2; \phi_2 + \frac{1}{2}\Delta\phi_2]$ in azimuth for each direction (θ_2, ϕ_2) are projected as spherical rectangles, illustrated on Figure 5.3(a).

The area elements ΔS_n , $n = 1 \dots N_{\text{out}}$ resulting from the subdivision of the emerging hemisphere into these N_{out} averaging sectors can be expressed by Equation (6.8):

$$\Delta S_n = R_0^2 \cdot \sin \theta_{2_n} \cdot \Delta\theta_2^{\text{rad}} \cdot \Delta\phi_2^{\text{rad}} \quad (6.8)$$

where $\Delta\theta_2^{\text{rad}}$ and $\Delta\phi_2^{\text{rad}}$ are respectively the altitude and azimuth intervals expressed in radians.

On the other hand, the illuminance $E_{\text{screen}}(\theta_2, \phi_2)$ on the screen surface along direction (θ_2, ϕ_2) (see Equation (5.2)) is related to the illuminance $E_n(\theta_2, \phi_2)$ on the hemispherical surface area ΔS_n by Equation (6.9):

$$E_n = E_{\text{screen}} \frac{d^2}{R_0^2} \cdot \frac{1}{\cos \alpha} \quad (6.9)$$

$\tau_{\text{dh}} | \rho_{\text{dh}}$ being defined as the ratio of the total emerging flux Φ_2 and the incident flux Φ_1 (given by $E_1(\theta_1) \cdot A$), it can be expressed by Equation (6.10):

$$\tau_{\text{dh}} | \rho_{\text{dh}} = \frac{\int_0^{\frac{\pi}{2}} d\theta \int_0^{2\pi} d\phi \Phi_2(\theta_2, \phi_2) d\phi}{E_1 \cdot A} \quad (6.10)$$

The integral over the hemisphere in Equation (6.10) can be approximated by a sum over the N_{out} angular averaging sectors. Using Equations (6.8) and (6.9), as well as Equations (5.5) and (5.7) of Section 5.4.1, $\tau_{\text{dh}}|\rho_{\text{dh}}$ can be expressed in terms of $BT(R)DF$ s by the following equation:

$$\begin{aligned}
\tau_{\text{dh}}|\rho_{\text{dh}} &= \frac{1}{E_1 \cdot A} \cdot \sum_{n=1}^{N_{\text{out}}} \Delta\Phi_{2n} \\
&= \frac{1}{E_1 \cdot A} \cdot \sum_{n=1}^{N_{\text{out}}} E_n \cdot \Delta S_n \\
&= \frac{1}{E_1 \cdot A} \cdot \sum_{n=1}^{N_{\text{out}}} \frac{d^2}{\cos \alpha} \cdot E_{\text{screen}} \cdot \sin \theta_{2n} \cdot \Delta\theta_2^{\text{rad}} \cdot \Delta\phi_2^{\text{rad}} \\
&= \frac{\Delta\theta_2^{\text{rad}} \cdot \Delta\phi_2^{\text{rad}}}{E_1 \cdot A} \cdot \sum_{n=1}^{N_{\text{out}}} \frac{\pi \cdot d^2}{\rho_{\text{screen}} \cdot \cos \alpha} \cdot L_{\text{screen}} \cdot \sin \theta_{2n} \\
&= \Delta\theta_2^{\text{rad}} \cdot \Delta\phi_2^{\text{rad}} \cdot \sum_{n=1}^{N_{\text{out}}} BT(R)DF_n \cdot \sin \theta_{2n} \cdot \cos \theta_{2n} \tag{6.11}
\end{aligned}$$

which leads to the following final equation for $\tau_{\text{dh}}|\rho_{\text{dh}}$, agreeing with the relation provided for instance for τ_{dh} in International Energy Agency (2000):

$$\tau_{\text{dh}}|\rho_{\text{dh}}(\theta_1, \phi_1) = \frac{1}{2} \cdot \Delta\theta_2^{\text{rad}} \cdot \Delta\phi_2^{\text{rad}} \cdot \sum_{\theta_2=0}^{\theta_{2\text{max}}} \sum_{\phi_2=0}^{360^\circ - \Delta\phi_2} BT(R)DF(\theta_1, \phi_1, \theta_2, \phi_2) \cdot \sin(2\theta_2) \tag{6.12}$$

As mentioned in Section 6.1.2, approximate $BT(R)DF$ data are needed in the obstructed grazing hemisphere region to avoid an underestimation of the calculated directional-hemispherical transmittance or reflectance.

As a calculation method purely based on polynomial extrapolation is inappropriate for distributions in transmission or reflection presenting strong gradients in luminance (peaks), a different approach was chosen, based on the behaviour observed for the two last $BT(R)DF$ s ($\theta_{2\text{max}}$ and $\theta_{2\text{max}} - \Delta\theta_2$) for each azimuth ϕ_2 and minimizing the risk of overestimation in obstructed sectors. It was tested for several fictitious cases, usual and extreme, as well as for real data from which certain grazing values were removed; the obtained results were all coherent.

Error on calculated directional-hemispherical transmittance or reflectance

To estimate inaccuracy on determined τ_{dh} or ρ_{dh} values, the calculation of the square root of the summed squared individual errors on $BT(R)DF$ s is a far too pessimistic method, which leads to increasing errors when the averaging grid intervals $\Delta\theta_2$ and $\Delta\phi_2$ decrease: this disagrees with the fact that the sum (6.12) will actually become a better approximation of integral (6.10).

A different approach was in consequence adopted to evaluate these errors, based on comparisons with either calculated or experimentally assessed τ_{dh} or ρ_{dh} values.

For the reasons given in Section 6.2.2, the simple aperture appeared as the most reliable validation case for comparing τ_{dh} (or ρ_{dh}) values based on bidirectional data to theoretical calculations. Thus, for different diaphragm diameters D (10, 15 and 20 cm) and incident altitudes θ_1 (0° to 75°), transmittance τ_{dh} determined through Equation (6.12) were compared to their expected value, equal to 1 (for any diameter D).

About twenty D and θ_1 configurations were considered, showing discrepancies of 5% on average and 15% at most, all but two inferior to 10%. No correlation with either the diameter D or the altitude θ_1 was found, confirming the accuracy of the τ_{dh} (or ρ_{dh}) calculation method.

Based on these results, a range of 10% to 15% was assumed as representative of the error on directional-hemispherical transmittance or reflectance.

To refine this statement and to validate the BT(R)DFs themselves, τ_{dh} and ρ_{dh} values based on goniophotometric data obtained for various systems and incident directions were compared to integrating sphere measurements, as explained in the following section.

This study allowed to determine an error applicable to any system by showing that if a relative error $\varepsilon_{\tau_{\text{dh}}|\rho_{\text{dh}}}$ of 15% was assumed on the $\tau_{\text{dh}} | \rho_{\text{dh}}$ values based on goniophotometric data, the agreement between the two assessment methods was extremely satisfying: their respective error bars were overlapping each other for almost all analyzed configurations (see Figures 6.9 to 6.12). This result was also confirmed by the comparison ray-tracing methods, presented in Section 6.4.3.

6.4.2 Comparisons with Ulbricht sphere measurements

The validation of bidirectional data against integrating sphere measurements was achieved for very different optical materials:

- an opalescent plexiglas panel (see Section C.1.1), presented in Section 6.2.1;
- a laser cut panel (see Section C.2.1), presented in Section 5.5.1;
- a prismatic film, manufactured by 3M and described in Section C.3.2;
- an acrylic prism manufactured by Siemens AG (see Section C.3.1), presenting $42^\circ/5^\circ$ gratings (asymmetric panel) and described in Section 6.5.1;
- two coated fabric blinds out of the four listed in Section C.4.2, one characterized in transmission and one in reflection (whose properties were discussed in Section 5.5.1), in addition to a white opalescent plastic panel (see Section C.1.2) presented in Section 6.3.1.

The directional-hemispherical transmittance (or reflectance for one of the fabric blinds) was assessed with an Ulbricht sphere for each system and for several incident angles. As detailed in Commission Internationale de l'Eclairage (1998), an integrating sphere presents a perfectly diffusing white internal surface, on which the transmitted (reflected) light flux reaches a homogeneous luminance. The ratio between the internal and the incident illuminances measures the directional-hemispherical visible transmittance (reflectance).

The first three optical materials were analyzed within the framework of Task 21 of the International Energy Agency (2000), the Siemens prisms as part of a project on prismatic panels modelling by Compagnon (1994) and the last systems within the REVIS project coordinated by TNO (van Dijk, 2001). These integrating sphere measurements were carried out by different European institutes:

- Berlin University of Technology (TUB), Fraunhofer Institute for Solar Energy Systems (ISE) and Siemens Lighting Division in Germany,
- Bartenbach Lichtlabor (BAL) in Austria,
- Building and Construction Research Organisation (TNO) in The Netherlands,
- Glaceries de Saint-Roch (GSR), Centre de développement du Bâtiment, in France,
- Stazione Sperimentale di Vetro (SSV), Optical Testing Laboratory and Istituto Elettrotecnico Nazionale Galileo Ferraris (IENGF) in Italy,
- the Solar Energy and Building Physics Laboratory (LESO-PB) at EPFL, in Switzerland.

The achieved $\tau_{\text{dh}} | \rho_{\text{dh}}$ values were compared for these different systems with those of the goniophotometer: the results are shown on Figures 6.9 to 6.12.

The relative error on $\tau_{\text{dh}} | \rho_{\text{dh}}$ derived from bidirectional data is estimated to 15% for all fenestration systems, the error bars being displayed accordingly. As far as integrating sphere results are concerned, the values obtained by the different laboratories were averaged, and the considered error deduced from their discrepancies: the error bars shown on Figures 6.9 to 6.12 are thus simply equal to the range of these values, considered separately for each incident direction.

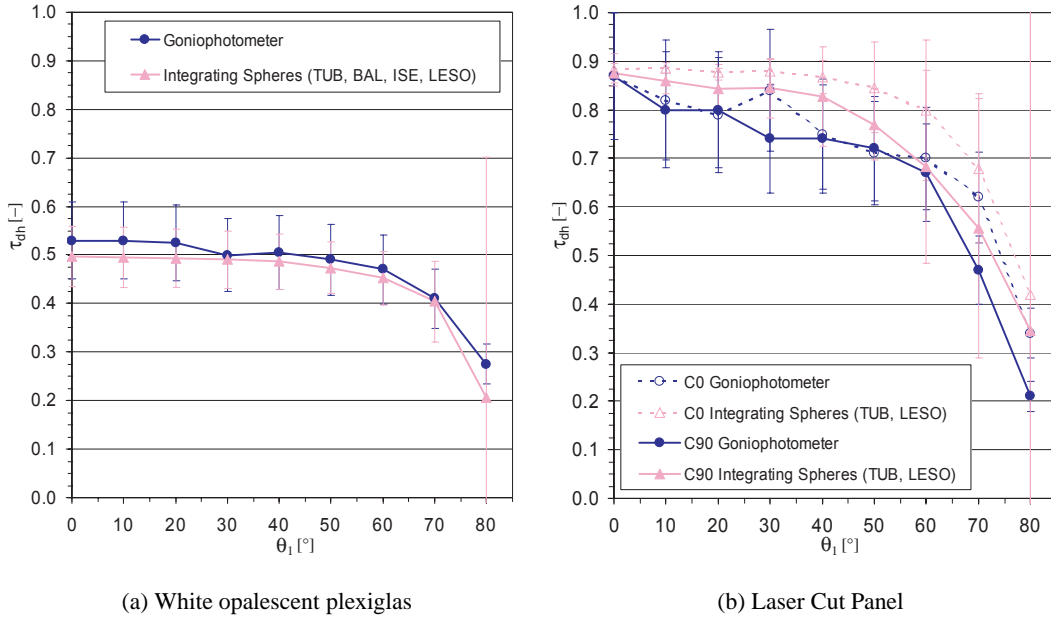


Figure 6.9: Directional-hemispherical light transmittance comparisons for diffusing and redirecting glazings: τ_{dh} values based on BTDF integration validated against Ulbricht sphere measurements.

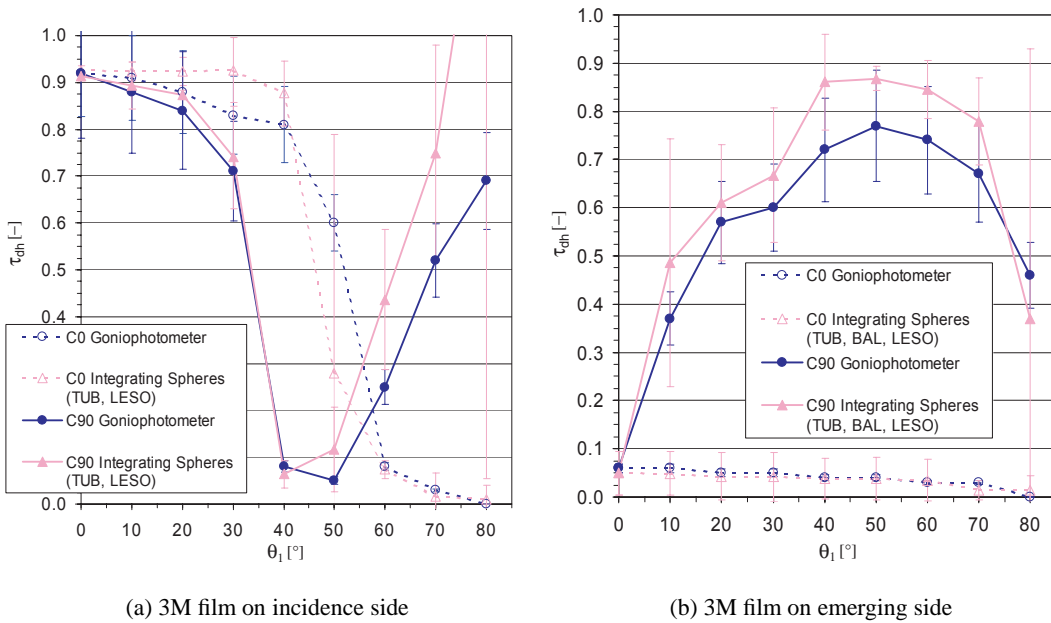


Figure 6.10: Directional-hemispherical light transmittance comparisons for a 3M prismatic film on float glass: τ_{dh} values based on BTDF integration compared to Ulbricht sphere measurements.

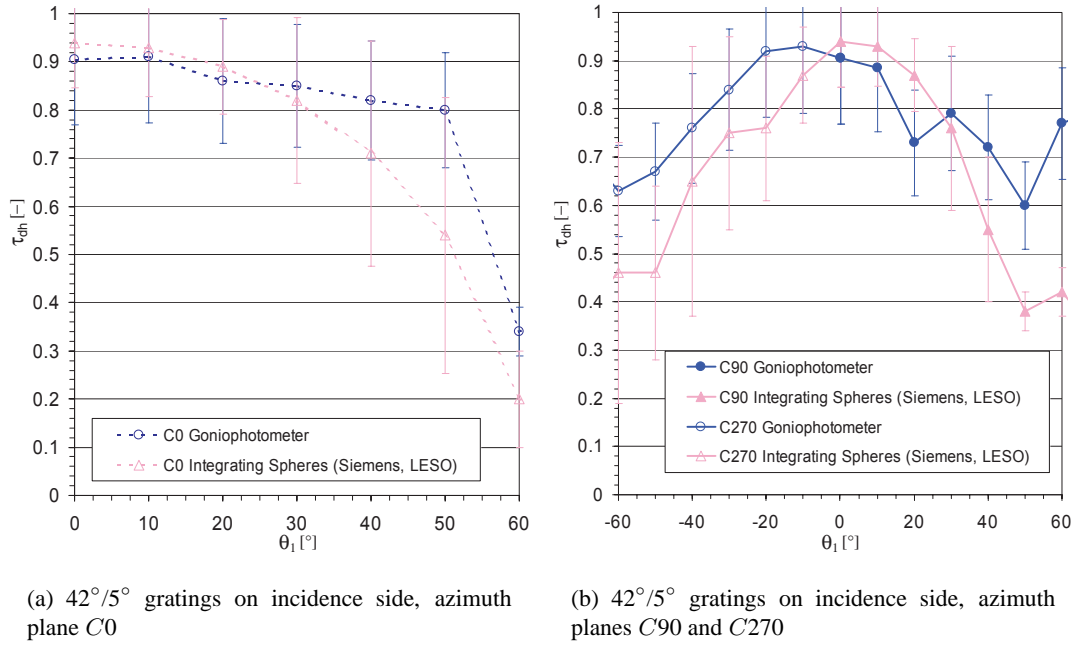


Figure 6.11: Directional-hemispherical light transmittance comparisons for a prismatic panel: τ_{dh} values based on BTDF integration compared to Ulbricht sphere measurements.

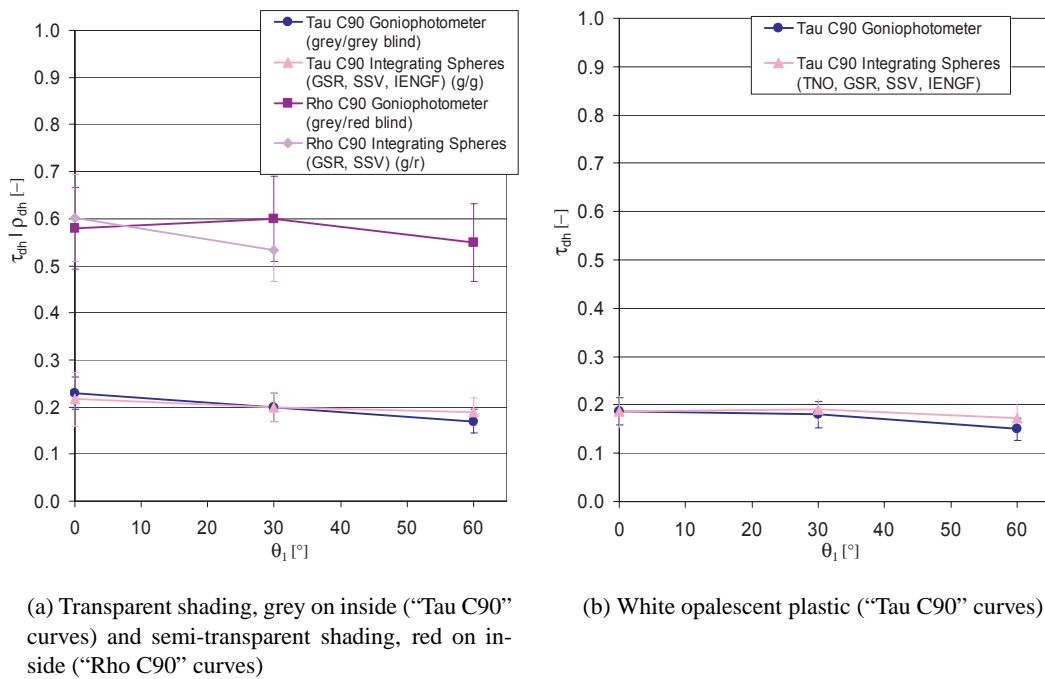


Figure 6.12: Directional-hemispherical light transmittance and reflectance comparisons for fabric blinds with reflective grey coating on the external side, and a diffusing plastic: $\tau_{dh} | \rho_{dh}$ values based on BT(R)DF integration compared to Ulbricht sphere measurements.

Overall, the agreement between the two assessment methods is excellent, as their respective error bars overlap for almost all situations.

If we consider the systems individually, we can observe that for very diffuse materials (Figures 6.9(a) and 6.12(b)), the discrepancies remain generally lower than 6% in relative terms. For strongly specular systems like the laser cut panel or the Siemens prisms (Figures 6.9(b) and 6.11),

as well as the grey/grey fabric blind (Figure 6.12(a), “Tau”), the mean relative difference is of about 14%, which is still very reasonable considering the wide spread in integrating sphere data. Finally, for hybrid systems like the 3M prismatic film (Figure 6.10) or the grey/red fabric blind (Figure 6.12(a), “Rho”) presenting high luminance gradients combined with a smooth light scattering for many incident directions, a mean relative difference of 13% was observed, despite the large differences between integrating sphere data for the 3M prismatic film.

As a consequence, this analysis confirms the accuracy of the BT(R)DF measurements and the adequacy of the $\tau_{\text{dh}}|\rho_{\text{dh}}$ calculation method; it is also shown that the assumed errors of respectively 10% and 15% are applicable for any system type.

6.4.3 Ray-tracing based model

The resort to ray-tracing calculations proved successful as an alternative approach to assess hemispherical transmittance, being compared either to analytical models or to integrating sphere measurements to validate virtual goniophotometers for instance (Mitanchey et al., 1995; De Boer, 2003).

Brunold (2000) shows that good agreement can be achieved between measured and calculated directional-hemispherical transmittance: glasses presenting different optical surface structures were characterized, the discrepancies remaining lower than 10%.

This error margin was confirmed by the study carried out in Section 6.5.4 to test the model’s sensitivity for two types of prismatic panels and a venetian blind prototype (manufactured by Baumann-Hüppe AG). While the relative impact of the model’s accuracy on BT(R)DFs can exceed 20% for the prisms and 40% for the blinds, it was found that $\tau_{\text{dh}}|\rho_{\text{dh}}$ values were only affected by about 10% (resp. 20%), as the directional component is no longer critical.

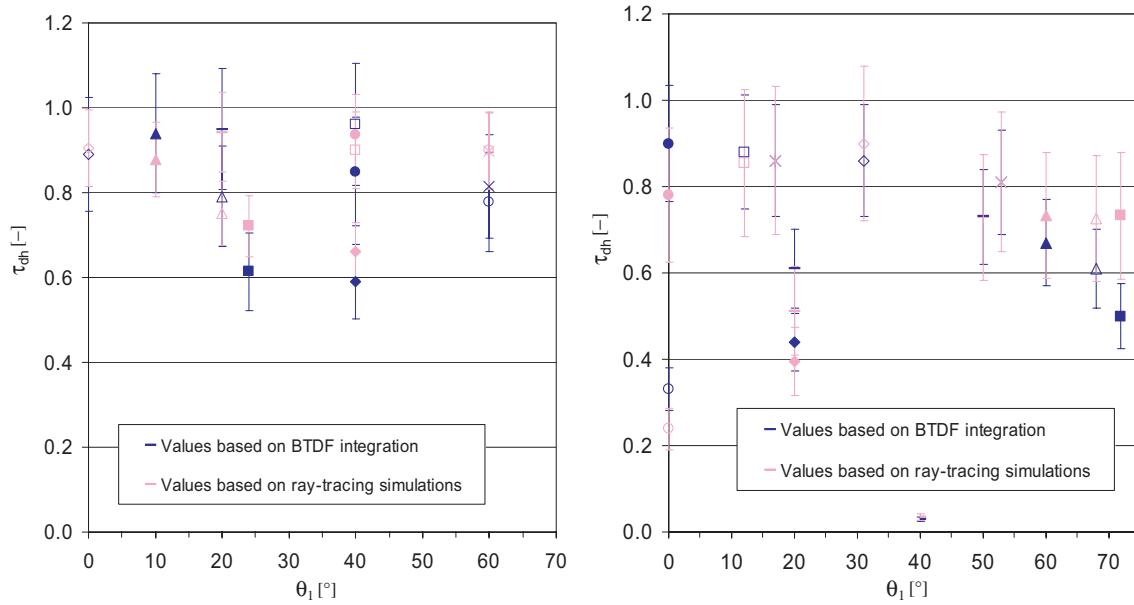
Ray-tracing simulations were in consequence performed for these three systems with the commercial software TracePro®; their modeling is described in Section 6.5.1.

The total transmitted light flux was assessed for several incident directions and different configurations of the prisms and blind, its ratio to the incident flux being compared to the τ_{th} values issued from the integration of BTDF data (Equation (6.12)) for:

- incident directions (40°, 90°), (60°, 90°), (24°, 30°), (40°, 45°) and (60°, 75°) for the symmetric panel (gratings 45°, flat face on incident side);
- incident directions (20°, 0°), (40°, 90°), (0°, 0°), (10°, 90°) and (20°, 270°) for the asymmetric panel, the first two being investigated with the flat face on the incident side, the others with the 42°/5° gratings on the incident side;
- incident directions (0°, 0°), (12°, 90°), (60°, 90°), (20°, 270°), (40°, 270°), (53°, 1°), (31°, 30°), (17°, 45°) and (68°, 45°) for the 0° slats tilt configuration, and (0°, 0°), (20°, 270°) and (50°, 315°) for the 45° slats tilt.

The obtained results were gathered on Figure 6.13, where the values are to be compared in pairs of identical spots, differing only by their color. The error bars associated to each of these spots are respectively of 15%, 10% and 20% for BTDF-based values, the ray-tracing simulations for the prisms and those for the blind.

From the good agreement between the two assessment methods, whose error bars overlap each other whatever system and configuration is analyzed, a confirmation of the τ_{th} values accuracy could be established. This conclusion is of course also valid for ρ_{th} values, the measurement principle being identical.



(a) Siemens prisms, 42°/5° and 45° gratings on either side

(b) Mirror curved slats, at 0° and 45° tilts

Figure 6.13: τ_{dh} values based on BTDF integration compared to ray-tracing simulations based on modeled prisms and venetian blind, for different incident directions (θ_1 , ϕ_1) and system configurations (prism type and orientation, slats tilt): results are to be compared in pairs of identical spots differing only by their color.

6.5 Detailed BT(R)DF comparisons with ray-tracing simulations

The above methods allow a validation of the directional-hemispherical transmittance or reflectance, deduced from BT(R)DF data through Equation (6.12). Detailed comparisons of bidirectional data were carried out on diffusing panels or simple systems for lack of bidirectional measurements from another comparable device. Yet even if such data were available, a disagreement in the results could not lead to definitive conclusions, as neither of the two could be considered as an absolute reference.

The very satisfactory results are of course encouraging for the BT(R)DFs precision; however, these validation methods are not perfectly adapted to assess the individual accuracy of such measurements for each emerging direction.

Ray-tracing simulations provide a useful and objective point of comparison for validating BT(R)DF data in a roundabout approach and evaluating complex systems in full detail.

Many assessment methods for the optical performances of glazing or shading systems resorted to comparisons with ray-tracing simulations:

- to establish a set of quantity and quality criteria for advanced daylight systems and determine their performances with *Radiance* simulations (Moeck, 1998);
- to test a new ray-tracing approach for thermal radiation (Campbell, 1998) or prismatic panel performances (Compagnon, 1994);
- to develop an angle-dependent evaluation procedure of solar heat gain coefficient (g-value) and compare measurements to ray-tracing simulations carried out with the software OptiCAD^{®1} (Kuhn et al., 2001; Platzer, 2002);

¹Opticad Corporation.

- to determine the daylight distribution in a room and compare *Radiance* simulations with office room monitoring (Reinhart and Walkenhorst, 2001).

Yet for all these comparative studies, as well as for the matrix-based or analytical methods developed to evaluate the solar heat gain coefficient of advanced fenestration systems (Klems, 1994; Molina et al., 1995; Rosenfeld, 1996), the considered quantity remained the directional-hemispherical transmittance, overlooking the level of details provided by BT(R)DF data.

In this section, a substantial set of experimental BT(R)DF data for different fenestration systems was compared with ray-tracing simulations: they represent a novel validation methodology for detailed bidirectional properties of a complex system.

The validation method was considered in a roundabout approach, as ray-tracing simulations are by themselves a stochastic thus approximate technique. Such an in-depth study nevertheless allowed both to promote confidence in the BTDF measurement and support the applicability of ray-tracing simulations in the assessment of complex glazings or shadings performances. This work was conducted during a one year stay at the Lawrence Berkeley National Laboratory (LBNL), USA; its results were published in Andersen et al. (2003a) and Andersen et al. (2003b).

As mentioned in Section 2.2, similar comparisons had been attempted for a venetian blind (McCluney and Sung, 1999). Bidirectional measurements achieved at LBNL (Papamichael et al., 1988) were then assessed against ray-tracing calculations performed with the commercial software ASAP^{®2}. Unfortunately, the results did not concur, the discrepancies remaining too significant to allow any conclusion regarding the method's accuracy, even from a qualitative point of view.

The considered systems were of two very different kinds: acrylic prismatic panels on one hand and a mirror coated venetian blind on the other, both having already been used for ray-tracing comparisons in Section 6.4.3.

The prismatic panels were chosen because of their well-known refraction properties and their complex transmission features due to the multiple internal reflections. The venetian blind allowed to increase the model complexity, as it presents geometrical and coating properties more difficult to model than those of an acrylic prism with macroscopic grating.

In practice, the systems were first modeled as faithfully as possible (Section 6.5.1), the experimental conditions for BT(R)DF assessment being reproduced virtually with the commercial forward ray-tracer TracePro[®] (Section 6.5.2) based on the Monte Carlo method (Hammersley and Handscomb, 1964; Glassner, 1995).

Computer simulation results were then compared to BTDF data assessed with the goniophotometer (Section 6.5.5). Calculations were also performed using an ideal model of the detector and the source (of properties as close as possible to the real sun), as explained in Section 6.5.3.

6.5.1 Systems description and modeling

Prismatic glazing

Two acrylic prismatic panels, manufactured by Siemens AG, were selected for this study: one presents symmetric gratings of 45° slope (see Figure 6.14(a)) and the other asymmetric gratings of 42° and 5° slope (Figure 6.14(b)).

The geometrical features of these materials are well defined and can be determined macroscopically. Their physical properties can also be easily described in a simulation program, acrylic being a common material with well-known wavelength-dependent refractive indexes.

²Breault Research Organization, Inc.

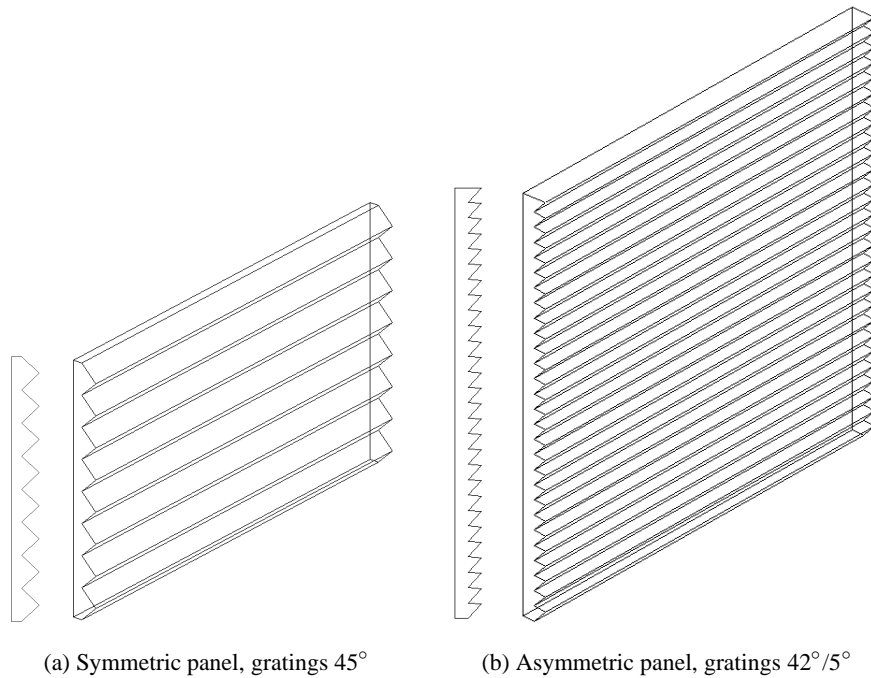


Figure 6.14: Section view and axonometry of the prismatic panels used for BTDF assessment validation.

The dimensions of the two panels are respectively: height (vertical dimension) 90 mm, length (horizontal dimension) 200 mm and thickness 12 mm for the symmetric panel (height of individual grating = 15 mm); height 195 mm, length 200 mm and thickness 12 mm for the asymmetric panel (height of individual grating = 7 mm).

The prismatic elements were modeled as consisting of standard acrylic material, according to the software's database of refractive indices (provided by manufacturers), and according to their real geometrical features, even though ideal because assumed of perfect shape. The simplification hypotheses were those formulated by Compagnon (1994), neglecting light dispersion and absorption inside the prismatic material, edge effects or dust and shape imperfections (like rounded grating edges appearing for any manufactured element). These simplifications were nevertheless taken into account for the simulation model error estimation (see Section 6.5.4).

Venetian blind

The venetian blind considered in this study is shown on Figure 6.15(a). As detailed below, the mirror coating makes the upper slat side a very specular surface (Figure 6.15(b)), whereas the beige paint presents quasi-lambertian diffuse properties (Figure 6.15(c)). These features increase the interest of analyzing such a system, as the numerous inter-reflections undergone by the incident light rays consist of a combination of very different reflection types.

Before modeling a system with a ray-tracing program, its geometrical and coating characteristics have to be precisely and fully known, in order to be implemented properly in the model.

Geometrical properties

The slat's geometrical features were determined with micrometric measurement tools. The measured dimensions are given in Figure 6.15(d); the curvature radius R_{slat} is equal to 96.9 mm, deduced from Equation (6.13) where ξ , l_{slat} and e_{slat} respectively define the slat's thickness, width and curvature amplitude (see Figure 6.15(d)).

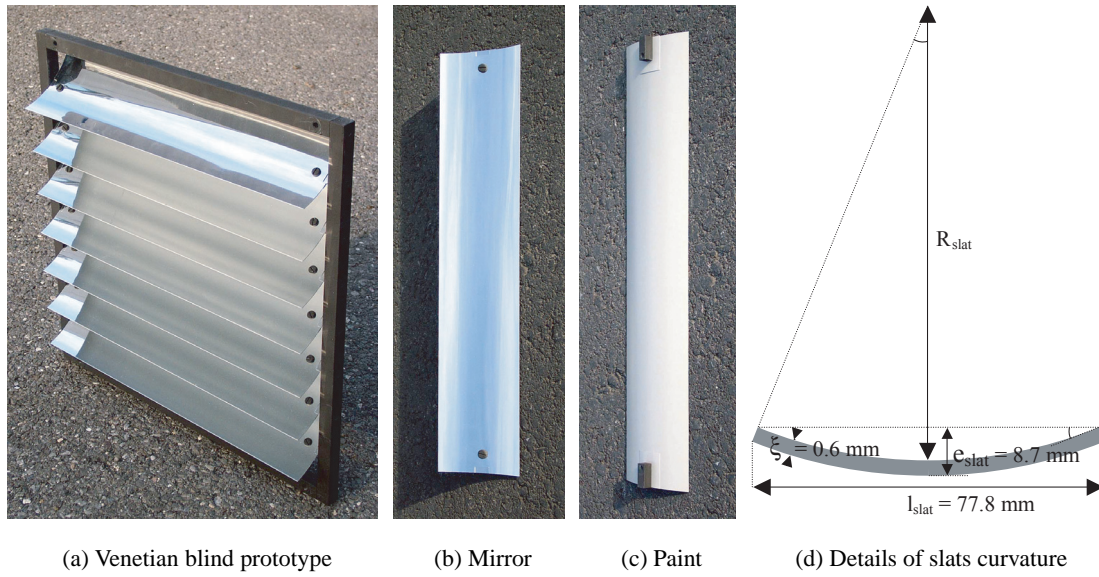


Figure 6.15: Coating and geometrical properties of the venetian blind's slats.

Through a combination of primitive solids (Figure 6.16(a)), a virtual element presenting the same features was created in TracePro[®], its edges being thereafter rounded to avoid aberrant ray paths.

$$R_{\text{slat}} = \frac{(e_{\text{slat}} - \xi)^2 + \frac{1}{4} \cdot \left(l_{\text{slat}} - \frac{\xi \cdot l_{\text{slat}}}{2 \cdot R_{\text{slat}} + \xi} \right)^2}{2 \cdot (e_{\text{slat}} - \xi)} \quad (6.13)$$

An arrangement of seven individual slats was then created according to the positions measured on the sample holder; as far as the modeling of the 45° tilt configuration is concerned, the slats rotation axes were defined taking the dimensions of the mechanical revolving system into account. The obtained venetian blind model is represented on Figure 6.16(b).

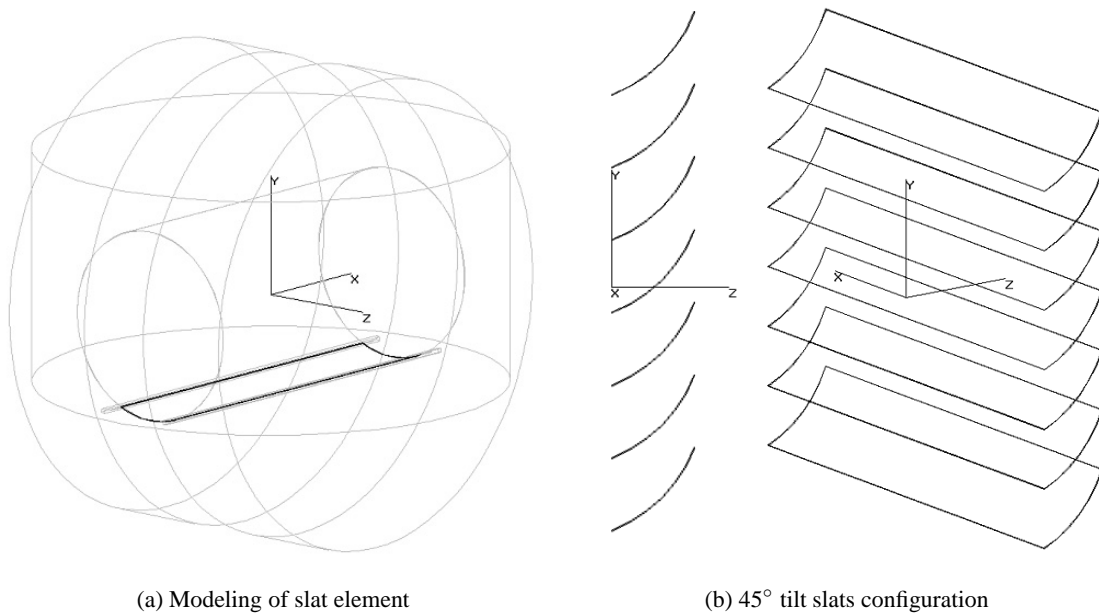


Figure 6.16: Modeling of the venetian blind's geometry.

Mirror and paint coatings

The assessment of the reflective properties of the slats paint and mirror coatings was achieved at LBNL using the Perkin-Elmer Lambda 19 spectrophotometer with an integrating sphere accessory. The reflectance was measured every 5 nm between 300 and 2500 nm on both sides, the spectra being corrected with the reflectance of a calibrated diffuse reflectance standard made of Spectralon. Photopic averages were then taken using the D65 source and CIE 1931 2-degrees observer functions (Commission Internationale de l'Éclairage, 1932); the resulting visible (photopic) total reflectance are equal to 28.6% and 83.7% for the paint and mirror surfaces respectively.

The measured spectra are shown on Figure 6.17 over the complete wavelength interval; their approximation with 50 nm wavelength steps was used for implementing the data into the ray-tracing program.

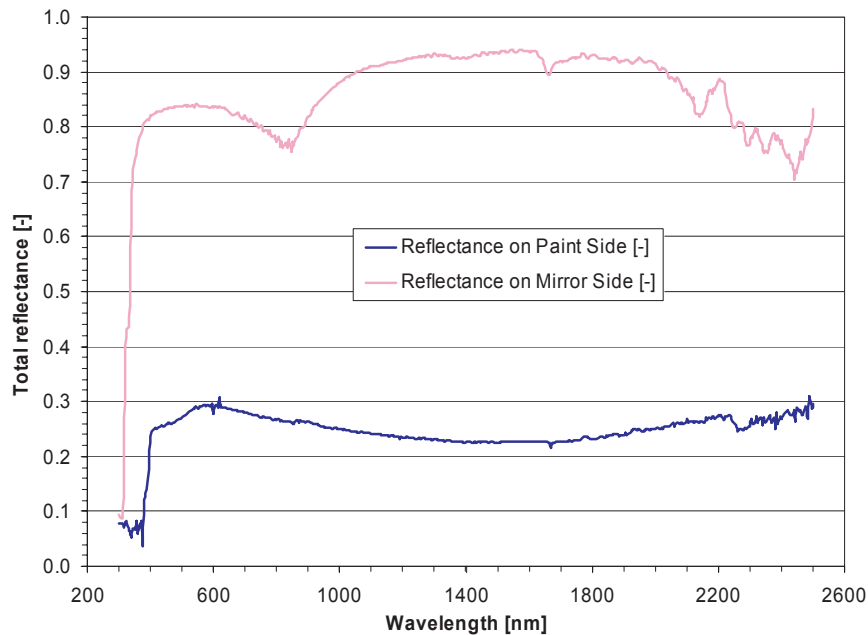


Figure 6.17: Total reflectance, measured every 5 nm, for both mirror and beige mat paint coatings of the curved venetian blinds slats manufactured by Baumann-Hüppe AG.

For both coatings, the reflectance was measured with and without a light trap to collect the specularly reflected beam. For the paint surface, the scans were almost identical, meaning that the reflectance is very diffuse; for the mirror, the scan with light trap was almost nil at all visible wavelengths, showing highly specular properties. In addition to that, the paint surface value was checked with a different apparatus (Colorimeter CR-200b Minolta for assessing the color coordinates and reflectance of diffuse surfaces): the results were found to be very close (difference of 3%).

When creating the coatings files for TracePro[®], a slight specular component of 2% was thus added for the paint surface, and likewise a scattering component for the mirror, otherwise considered respectively perfectly lambertian and specular.

6.5.2 Simulation model of experimental set-up

Both the light source and detection device were simulated with characteristics as close as possible to the reality, although by essence, the model will not take the inevitable imperfections proper to any physical component into account. As for the prism and blind models, these differences were however included in the model error estimation, detailed in Section 6.5.4.

The major constraints for the simulation model were:

- the virtual light source must be of same angular spread as the real one: a set of wavelengths representative of its spectrum were determined and the source positioned in order to reproduce the same incident directions as for the experimental assessment of BTDFs;
- a model of each sample, presenting identical geometrical and physical properties, was constructed, with a sample area exposed to light fitting the experimental illuminated surface;
- a detection screen of same geometry as the one used for the measurement facility had to be modeled, separated into the same pattern of sectors (averaging grid defined in Section 5.2).

For each prismatic panel, five representative incidences were selected: for the symmetric panel (flat face on incident side), $(40^\circ, 90^\circ)$, $(60^\circ, 90^\circ)$, $(24^\circ, 30^\circ)$, $(40^\circ, 45^\circ)$ and $(60^\circ, 75^\circ)$; for the asymmetric panel, $(20^\circ, 0^\circ)$ and $(40^\circ, 90^\circ)$ for the flat face on the incident side, $(0^\circ, 0^\circ)$, $(10^\circ, 90^\circ)$ and $(20^\circ, 270^\circ)$ for the gratings on the incident side.

The venetian blind's BTDF was determined experimentally for a set of 23 different incident directions for two slats arrangements, horizontal (0° tilt) and oblique (45° tilt), amongst which 10 were selected for comparisons to simulations for the 0° slats and 5 for the 45° slats: for the 0° slats tilt configuration, these incident directions were $(0^\circ, 0^\circ)$, $(12^\circ, 90^\circ)$, $(60^\circ, 90^\circ)$, $(20^\circ, 270^\circ)$, $(40^\circ, 270^\circ)$, $(53^\circ, 1^\circ)$, $(31^\circ, 30^\circ)$, $(17^\circ, 45^\circ)$, $(68^\circ, 45^\circ)$ and $(72^\circ, 61^\circ)$; for the 45° slats tilt, the incident directions were $(0^\circ, 0^\circ)$, $(12^\circ, 90^\circ)$, $(20^\circ, 270^\circ)$, $(17^\circ, 45^\circ)$ and $(50^\circ, 315^\circ)$.

Light source

According to the spectrum of the incident source over the visible range (given in Figures 3.7 and 3.28 respectively), a discrete list of wavelengths representative of these spectra was determined; each wavelength was in turn applied to the rays, the different tracing sessions being thereafter combined for the full spectrum analysis.

With the primarily used release of TracePro[®], no adjustable weight could be assigned; each interval determined by a step function that approximates the continuous spectrum, shown on Figure 6.18 for the former source, was thus associated to a certain number of wavelengths considered within each particular interval (displayed on the graph), proportional to its width and the source spectrum amplitude. The weighing option appeared later, and was used for the ideal set-up model described in Section 6.5.3.

As the set of considered wavelengths remained quite large with this method, and involved substantial simulation time, a reduction by a factor four was checked not to affect the results significantly (differences lower than 2%) and used in consequence.

To simulate the rays divergence η defined in Section 4.3.1, a lambertian spread of 0.1F half-angle (0.4° for the former source) was applied to the beam.

Finally, instead of either moving the sample and detector according to the incidence angles (or the source itself), a virtual source was placed against the outside sample interface. Its dimensions were determined to fit the experimental diaphragm aperture (illuminated area), a varying direction vector being associated to the emitted rays depending on the incident direction.

Virtual goniophotometer

To reproduce these assessment conditions virtually, the goniophotometer was faithfully modeled. As explained below, the total photometric flux received by each detection sector was determined and converted into the corresponding BTDF value through Equation (6.14). There was therefore

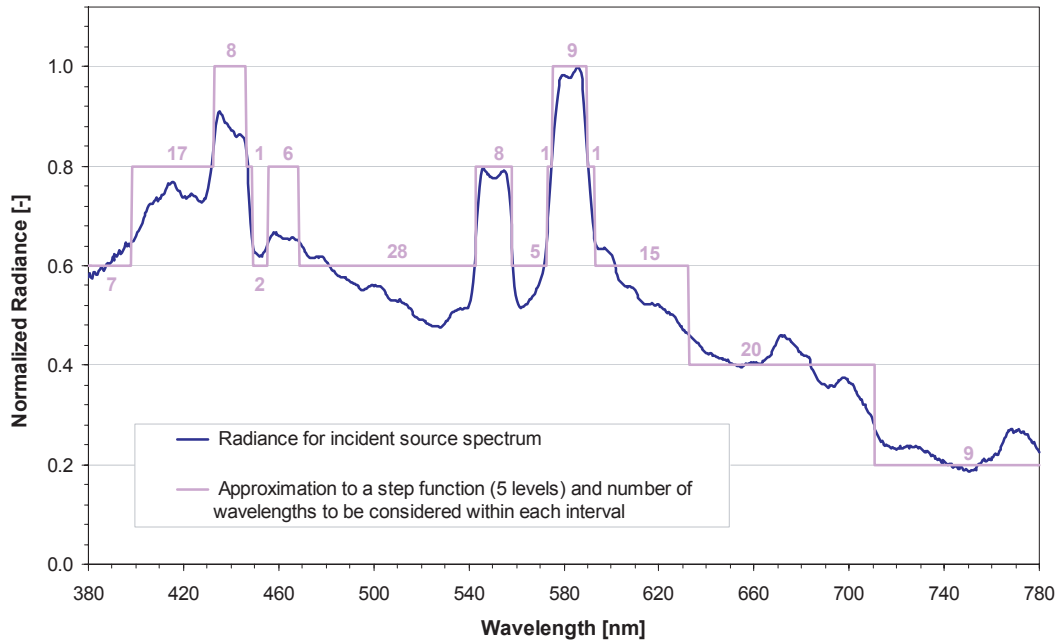


Figure 6.18: Relative spectrum for the real incident source (former HMI 2.5 kW discharge lamp with Fresnel lens) and approximation by step function for a discrete wavelength set.

no need to model the reflection on a diffusing screen and the detection by a virtual CCD camera, the simulation results being already comparable to experimental data.

As the current software features do not allow a spatial investigation of an object according to angular parameters, a set of individual detectors was created, associated to the different angular sectors and coplanar with the projection screen. In fact, detecting the transmitted flux directly on screen sectors allows moreover an accurate estimation of the experimental error induced by the camera's calibration procedures (spectral, photometric, spatial, additional corrections).

Practically, in order to have only one tracing session (and not six), all the six screen positions were simulated at once by the way of six virtual screens. To avoid inter-reflections between the different detection surfaces, they were defined as perfect absorbers.

Each screen is split into sectors using cones of half angles $\frac{1}{2}\Delta\theta_2 + N \cdot \Delta\theta_2$ (see Figure 6.19(a)) and planes of azimuths $\frac{1}{2}\Delta\phi_2 + N \cdot \Delta\phi_2$ (Figure 6.19(b)) to determine the intersection lines of the sectors. With an output resolution $(\Delta\theta_2, \Delta\phi_2)$ respectively equal to $(5^\circ, 5^\circ)$ and $(10^\circ, 15^\circ)$ for the prisms and blind, about 1400, respectively 300, different detection surfaces were created. Figures 6.19(c) and 6.19(d) show the resulting simulation models with the 45° prismatic panel and 0° tilt blind configuration respectively.

Because of the samples physical dimensions, the illuminated area for the symmetric prism was restricted experimentally to a disk of 6 cm diameter with an opaque diaphragm, whereas the asymmetric panel and blind were measured with 10 cm and 15 cm diaphragms respectively. Hence, virtual opaque (100% absorbing) diaphragms were placed in front of the sample, of aperture diameters respectively 6 cm, 10 cm and 15 cm for the symmetric, asymmetric prisms and venetian blind. They are shown on Figures 6.19(c) and 6.19(d) as well.

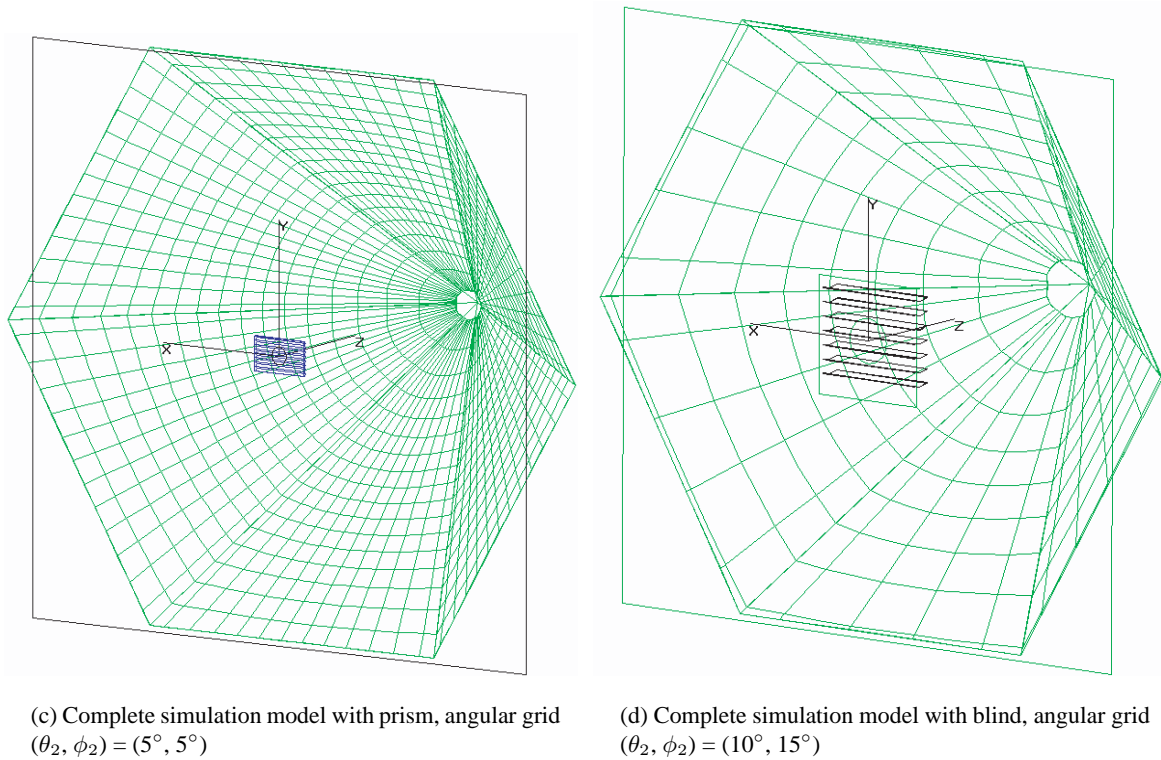
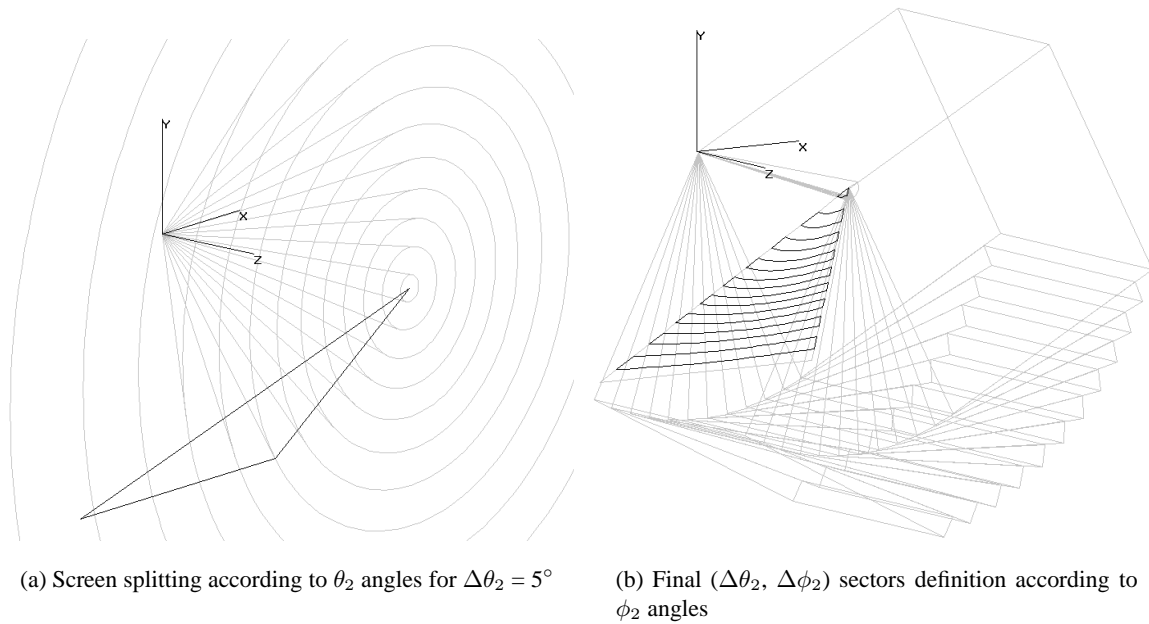


Figure 6.19: Simulation model composed of an opaque diaphragm, the analyzed sample, a non-interacting incident flux detection surface and six absorbing detection screens split into angular sectors of intervals $(\Delta\theta_2, \Delta\phi_2)$.

Ray-tracing simulation parameters

The rays were emitted from an annular grid, composed of 45 rings and sending about 200,000 rays ($\sim 6,000$ rays at each wavelength). The flux threshold (fractional value of starting flux for which a ray will be terminated) was set to 0.05 for the prisms characterization, and lowered to 0.001 for the blind, to keep sufficient track of the diffused rays for the BTDF estimation.

It was checked that a larger number of rays (e.g. 15,000 per wavelength) or a lower cut-off value (e.g. 0.001 for the prisms, 0.0005 for the blind) did not significantly affect the results: both induced differences lower than 1% whereas computer simulation time was considerably increased. It must be noted that the source does not appear as a separate model object: it sends rays according to particular grid and beam specifications, but has no physical (optical) properties.

Ray-tracing plot examples are displayed on Figure 6.20 for the asymmetric prism for incidence $(\theta_1, \phi_1) = (30^\circ, 270^\circ)$ and for the blind with horizontal slats for incidence $(12^\circ, 90^\circ)$. Only a few (about a thousand) of the 200,000 traced rays are shown on the plot, to get a readable transmitted light distribution.

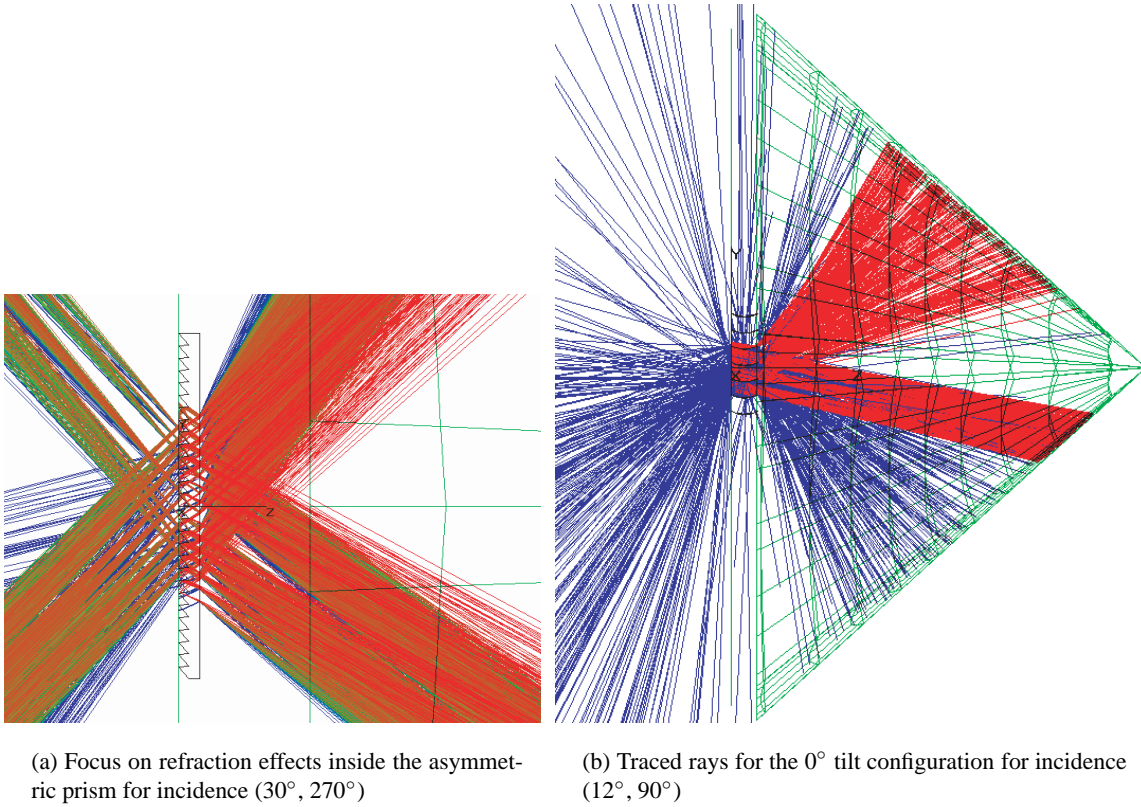


Figure 6.20: Ray-tracing plots for prism and blind characterization (only a few of the traced rays are displayed; towards the left appears the reflected part of the incident beam, not considered in this study).

Conversion into BT(R)DF data

As mentioned above, the considered quantitative output is the total photometric flux collected by each angular sector on the projection screens, summed up according to $V(\lambda)$ for all traced wavelengths. Dividing each of these individual fluxes by the incident flux to get the normalized fluxes $\phi_{2\text{norm}}(\theta_2, \phi_2)$ (%), one can calculate the corresponding BTDF values through Equation (6.14), directly deduced from Equation (6.11):

$$BTDF(\theta_1, \phi_1, \theta_2, \phi_2) = \frac{\phi_{2\text{norm}}}{\Delta\theta_2^{\text{rad}} \cdot \Delta\phi_2^{\text{rad}} \cdot \sin\theta_2 \cos\theta_2} \quad (6.14)$$

Once converted into the corresponding BTDF data, the ray-tracing-based data were compared to the experimental ones. The results are presented and discussed in Section 6.5.5 for both types of materials.

6.5.3 Virtual model of ideal set-up

Verifying experimental BTDF data by reproducing the measurement conditions as faithfully as possible allows to estimate the error due to the detection technique. Fortunately, the results presented on Figures 6.23 and 6.24 in Section 6.5.5 confirm that these procedures are appropriate and that the results assessed thanks to this digital imaging-based methodology are reliable.

To complement this study, an additional analysis made possible by the flexibility of virtual models was carried out: an ideal set-up was modeled, whose results were compared to the experimental conditions.

The simulations were achieved for the following set of incidences: $(40^\circ, 45^\circ)$ for the symmetric prism (flat face on incident side), $(0^\circ, 0^\circ)$, $(10^\circ, 90^\circ)$ and $(40^\circ, 90^\circ)$ for the asymmetric one (gratings on incident side for the first two directions, flat face for the third).

Sun as the light source

In our case, the ideal light source is of course the sun, of spectrum given on Figure 6.21 and showing a perfect collimation.

The parameterisation of a virtual sun was realized by approximating its continuous spectrum with a discrete set of values, pointed out on the continuous curve on Figure 6.21. A new TracePro[®] version allowing weighted wavelengths having been released, the laborious method of spectrum approximation described in Section 6.5.2 was replaced by a simple wavelengths list, of weights proportional to the corresponding radiance of the sun spectrum.

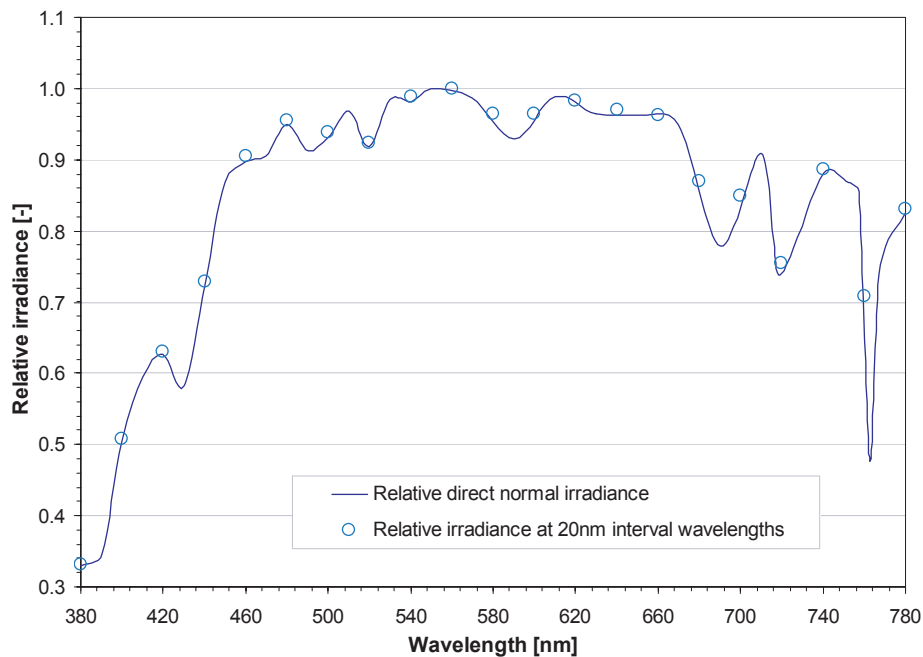


Figure 6.21: Relative solar spectrum and approximation by a set of discrete values at regular wavelengths intervals, providing the weights to be assigned to each considered wavelength.

Hemispherical detector

As far as the detection surface is concerned, even though a flat projection screen is preferable experimentally to avoid inter-reflections, a virtual hemisphere subdivided in the same way makes up a more ideal detection surface, the light being collected at a constant distance from the sample and with normal rays.

Moreover, as explained in Section 5.4.2, if the source is sufficiently far away from the sample compared to the sample-to-screen distance $d(\theta_2, \phi_2)$ (which is of course the case for the sun), the reception area S (or more generally $S \cos \alpha$ for surfaces that would not be normal to the rays) has to be comparable to the apparent illuminated area of the sample, i.e. to $A \cos \theta_1$. As A is fixed by the experimental conditions and as the angular grid $(\Delta\theta_2, \Delta\phi_2)$ must be equal to $(5^\circ, 5^\circ)$, the only parameter that can be adjusted to fit this condition is the hemispherical detector's radius d_{hemis} (distance to hemisphere).

Of course, the sectors' areas vary over the hemisphere according to $d_{\text{hemis}}^2 \sin \theta_2 \Delta\theta_2^{\text{rad}} \Delta\phi_2^{\text{rad}}$, where $\Delta\theta_2^{\text{rad}}$ and $\Delta\phi_2^{\text{rad}}$ are both equal to 0.0873 rad (i.e. to 5°). The calculation of d_{hemis} for the 6 and the 10 cm diaphragm diameters was therefore made by taking the average discretization sector surface over the whole hemisphere: the obtained radii are respectively 53.5 and 89.1 cm.

It must be observed that for the default sample diaphragm diameter (10 cm), the hemisphere radius is extremely close to the actual average distance from the sample to the projection screen in the experimental facility, equal to 90.5 cm.

As mentioned in Section 5.4.2, in order that a surface detection becomes equivalent to a directional analysis of rays emerging from a non-punctual surface, the distance between the sample and the detector should be at least ten times larger than the sample diameter, which is about the case for the determined "ideal" hemisphere radii (as well as for the experimental set-up). The output referential being linked to the emerging face of the sample, the detection hemisphere was modeled with a base plane merged with the latter.

The resulting hemispherical detector is shown on Figure 6.22(a). As the transmitted light is only distributed on a small number of angular sectors, only some of them were isolated on the hemisphere to facilitate their assignment to the corresponding angular couples (θ_2, ϕ_2) and reduce the processing time. A ray-tracing plot is displayed on Figure 6.22(b) for the asymmetric panel for incidence $(40^\circ, 90^\circ)$. The figure clearly outlines the spread of transmitted rays induced by the variation of the refractive index with the wavelength, also observed for other incidence directions (and for the experimental conditions model).

The transmission peaks, revealed by Figures 6.23 and 6.24, cannot always be identified on these ray-trace plots. Indeed, the sensitivity of the human eye (photopic curve $V(\lambda)$) is taken into account for photometric flux estimations, and thus assigns varying weights to rays of different wavelengths. Also, the plots cannot provide quantitative information on the weight of each ray, which are all shown in the same way even though representing very different flux values.

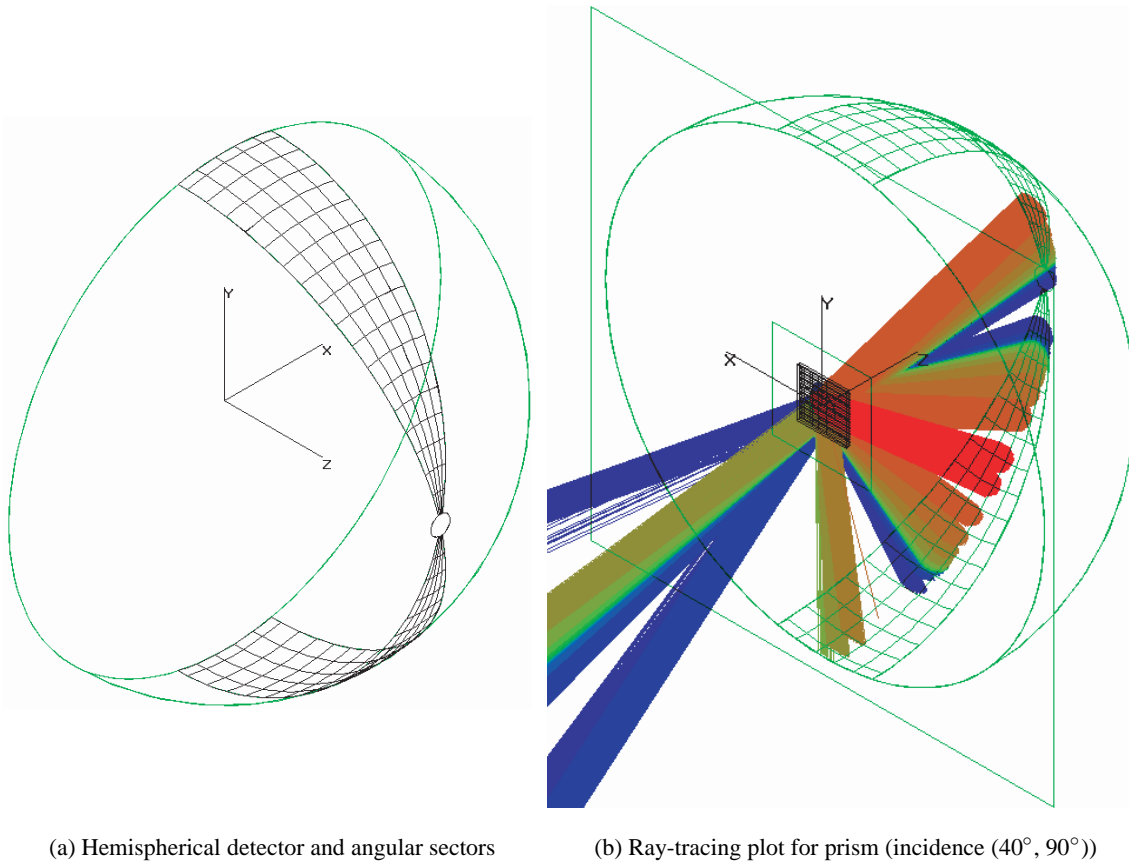
6.5.4 Simulation error estimation

Ray-tracing calculations

The statistical error due to the number of traced rays can be assessed using the theory of sampling: the probability of obtaining a result P with less than a given error ς and with a determined confidence C is related to the size of the sample (i.e. the number of rays N_R) by Equation (6.15):

$$\varsigma = \sqrt{\frac{1}{N_R \cdot (1 - C)} \cdot \frac{1 - P}{P}} \quad (6.15)$$

P is the normalized emerging light flux reaching each averaging sector. Admitting a confidence level of 95% and tracing 200,000 rays per incident direction, we obtain a statistical error comprised between 4% and 0.5%: its exact value depends on the simulation model threshold (0.001 for the venetian blinds but 0.05 was sufficient for the prisms) and the emerging direction (the lower the value, the greater the error). An statistical error ς of 1% was thus considered.



(a) Hemispherical detector and angular sectors

(b) Ray-tracing plot for prism (incidence $(40^\circ, 90^\circ)$)

Figure 6.22: Ideal set-up model configuration: hemispherical absorbing detector and virtual sun.

The performance of the chosen software TracePro[®] was verified by comparing achieved BTDF data with results obtained with the validated *Radiance* programme for the laser cut panel described in Sections C.2.1 and 5.5.1.

For this purpose, it was modeled in both simulation programs with the same geometrical characteristics (Greenup et al., 2000) and using the same simplification hypotheses, in particular a null diffuse component on the parallel cuts. This hypothesis actually revealed a too strong approximation compared to reality, but allowed consistent results from one program to the other.

The chosen incidence direction was $(\theta_1, \phi_1) = (60^\circ, 90^\circ)$ and the corresponding BTDF was assessed according to adjacent hemisphere sectors of same intervals $(\Delta\theta_2, \Delta\phi_2) = (5^\circ, 5^\circ)$ for both models. Although the ray-tracing techniques were completely different (forward versus backwards ray-tracing), the obtained results agreed exceptionally well, only differing by 1% in relative terms: a strong confidence in the accuracy of the ray-tracing program was brought as a consequence.

Model sensitivity study

The error assumed for experimental BTDF data, represented by the corresponding error bars on Figures 6.23 to 6.27 (“BTDF_{meas}” curves), was deduced from the study conducted in Section 6.1, and thus set to 10% for the three analyzed systems (Equation (6.6)).

To determine a relative error associated to the prismatic glazing model, the impact of the simplification hypotheses (Section 6.5.1) was assessed by modifying slightly certain simulation parameters and examining how these changes affected the BTDF data.

Several altered models were thus created for both panels and each modification was analyzed individually:

- average variations of ± 0.01 were imposed on the acrylic refraction indexes (close to 1.49 over most of the visible spectrum);
- the sample position was shifted half a period;
- the gratings edges were rounded at 0.25 mm off the theoretical summits;
- a diffuse component of 2% was added on the surfaces of the prisms to create an equivalent of surface wearing.

The relative differences on BTDFs generated by these modifications were averaged, for each studied parameter, over the set of incident and transmitted directions; only BTDF data greater than 5% of the curve maxima were considered.

This led to relative inaccuracies of about 19%, 4%, 16% and 8% associated respectively to the refraction index, the sample position, the gratings sharpness and the diffuse component, this last parameter only affecting the results in one way (lower peaks).

A global error of 26% was then obtained from calculating the Root Sum Square (RSS) of the relative individual errors, including those due to the limits of the model: threshold ($\sim 1\%$ error), number of emitted rays ($\sim 1\%$), discretized source spectrum ($\sim 2\%$), mentioned in Section 6.5.2.

As far as the accuracy of the blind model results is concerned, it was estimated likewise by observing the impact of the following modifications of the simulation model parameters:

- small difference in the slats tilt (3° anticlockwise when seen from $\phi_i = 0^\circ$, each slat being hence shifted 0.6 mm to keep the interface at the same position);
- half a period slats position shift (37 mm further down);
- variation of the curvature radius (± 1.8 cm, the slats width being fixed);
- neutral mirror coating (constant reflectance of 83.7% over the spectrum, no diffuse component);
- neutral paint coating (constant reflectance of 28.6% over the spectrum, no specular component); this last parameter only affected the results significantly for the incident direction $(\theta_1, \phi_1) = (40^\circ, 270^\circ)$ shown on Figure 6.27(d).

As mentioned in Section 6.5.1, the edges of the venetian blind's slats were rounded in the simulation model, to be as close as possible to reality and to avoid aberrant ray paths. Nonetheless, sharp edges were proven to be of negligible influence on BTDF data.

A different simulation model was created for each parameter, the modification's impact being evaluated for two different incident directions: $(31^\circ, 30^\circ)$ and $(68^\circ, 45^\circ)$. Only the transmitted directions where BTDF data were greater than 5% of the curve maxima were considered for determining the resulting variations of BTDF data.

In this study, the data corresponding to direct transmission peaks were separated from those corresponding to light transmitted after reflection on the mirrored side of the slats, so that errors could be associated individually to each of them. The $(40^\circ, 270^\circ)$ incidence was analyzed apart from the others, in order to assess the effect of the paint coating specifications when the diffuse transmission becomes significant compared to the other components.

The relative differences on BTDFs generated by these modifications were gathered by parameter and averaged over the incident and transmitted directions. This led to relative inaccuracies of 14%, 5%, 4% and 0.3% for the regular peaks and 22%, 8%, 33% and 19% for the mirror reflected peaks, respectively associated to the slats tilt angle, position and curving radius and mirror coating's specifications. The paint coating parameter's effect was estimated to 58%, which shows how sensitive low BTDFs were to even slight model differences.

In the end, global errors of 16%, 45% and 58% were obtained respectively for regular, mirror and paint reflected transmission applying the same RSS method as for the prisms and including the errors due to the model's limits.

Their large values show that the model's adequacy to provide a copy of the physical blind could rapidly be lowered with a slightly inappropriate choice of simulation parameters, or with flawed or irregularly manufactured slats. However, as shown by the close agreement between the "BTDF_{meas}" and "BTDF_{sim}" curves for nearly all the studied situations in Figures 6.26 and 6.27, the blind's model can be considered as very satisfactory to conduct a reliable assessment of transmission performances on the basis of on ray-tracing simulations.

The relative errors found for the prisms and blind are to be added to the statistical error associated to the number of traced rays. The resulting error bars are represented on Figures 6.23 to 6.27 and associated to "BTDF_{sim}" curves.

6.5.5 Results comparisons

In order to point out differences between experimental and ray-tracing-based data with high accuracy, two-dimensional plots for varying altitudes ϕ_2 along given azimuths θ_2 were chosen instead of the more intuitive 3D representations in spherical coordinates presented in Section 5.5.1.

As the transmission features were generally sharp for both types of systems, only small solid angles were covered, thus requiring only few 2D plots per incident direction.

For each analyzed situation, the relevant outgoing azimuth planes (i.e. the angles ϕ_2 for which the transmission is non-zero) were determined. Both measured and calculated BTDF data were reported along these outgoing planes as functions of altitude θ_2 for all selected incident directions.

The azimuth planes next to the most relevant ones were also checked (planes $\phi_{2m} \pm \Delta\phi_2$ and $\phi_{2m} \pm 2\Delta\phi_2$, where ϕ_{2m} is the azimuth angle for which the BTDFs reach a local maximum); they generally revealed the same kinds of behaviours as the main plane (but with lower values), as shown on Figures 6.24(e), 6.24(f), 6.25(b), 6.25(f), 6.26(c), 6.26(f), 6.27(c) and 6.27(f). For the prismatic elements, main and secondary maxima can appear in different azimuth planes ϕ_2 for the same incident direction; in such cases, the corresponding peaks are shown on separate graphics, as in Figures 6.23(f), 6.24(b) and 6.24(i). For conciseness, some section views show ϕ_2 planes in pairs (90° and 270° , 75° and 255°), the latter being then plotted with negative values for θ_2 (Figures 6.24(c), 6.25(e), 6.26(a), 6.26(b), 6.26(c), 6.26(d), 6.27(a), 6.27(b) and 6.27(c)).

Prismatic glazing

The results obtained for the two prismatic panels for the faithful experimental set-up model are shown on Figures 6.23 and 6.24 with an output resolution ($\Delta\theta_2$, $\Delta\phi_2$) of (5° , 5°).

These figures illustrate the good agreement achieved between the real and virtual BTDF data: even though the transmission features are extremely sharp (high gradients increase the risk of having significant discrepancies between two assessment methods), the relative discrepancies remain reasonable: their average value is of 18.6%, by far inferior to the assumed errors on the simulation results. Furthermore, a similar qualitative light behaviour was revealed, the peaks corresponding exactly to the same directions, for the main as well as the secondary maxima.

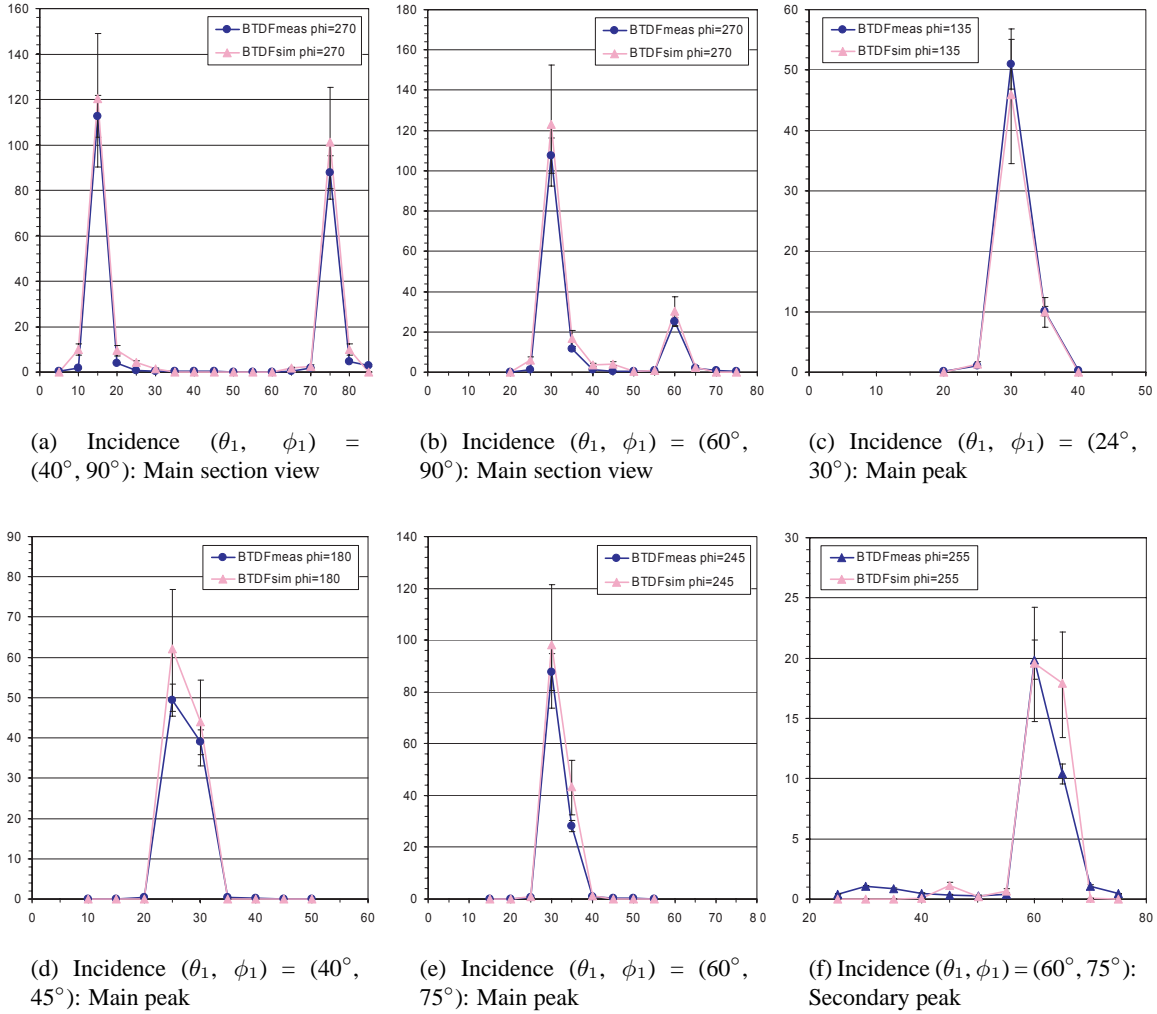


Figure 6.23: BTDF (sr^{-1}) vs. θ_2 ($^\circ$) along ϕ_2 planes: comparison of measurements ($\text{BTDF}_{\text{meas}}$) and calculations (BTDF_{sim}) for the symmetric prism (45° gratings, flat face on incident side).

The comparison of BTDF values obtained by measurement and by simulation with ideal conditions is given on Figure 6.25. In order to appreciate the effect of the model changes, the results provided by the simulation of experimental conditions were added on the graphs as well.

The observed discrepancies remain very low when comparing experimental with ideal simulation results and show coherent behaviours: the peaks appear exactly along the same directions and BTDFs differ only by about 11.4% in relative terms for the four analyzed configurations. The differences are thus even lower than for the faithful model, which tends to prove that the new parameters (source spectrum, beam spread, detector) compensate each other's effects, and that the light distribution assessment can only be improved in a slight way if using a more ideal set-up than the actual experimental facility.

One can notice that the hemisphere radius for the asymmetric panel (89.1 cm) is very close to the average sample to screen distance for the measurement facility (90.5 cm), leading to comparable average dimensions for the discretization sectors. This distance being on the other hand significantly smaller for the symmetric panel hemisphere (53.5 cm), one can expect slightly poorer results for the latter, confirmed by Figures 6.25(a) and 6.25(b) where discrepancies between measurement and ideal set-up model are of about 14.1%, whereas they are of only 10.7% for the $42^\circ/5^\circ$ prism. Fortunately, the 6 cm diaphragm is a rather exceptional dimension, chosen because of the physical sample's size; 10 cm is the default diaphragm for experimental assessment.

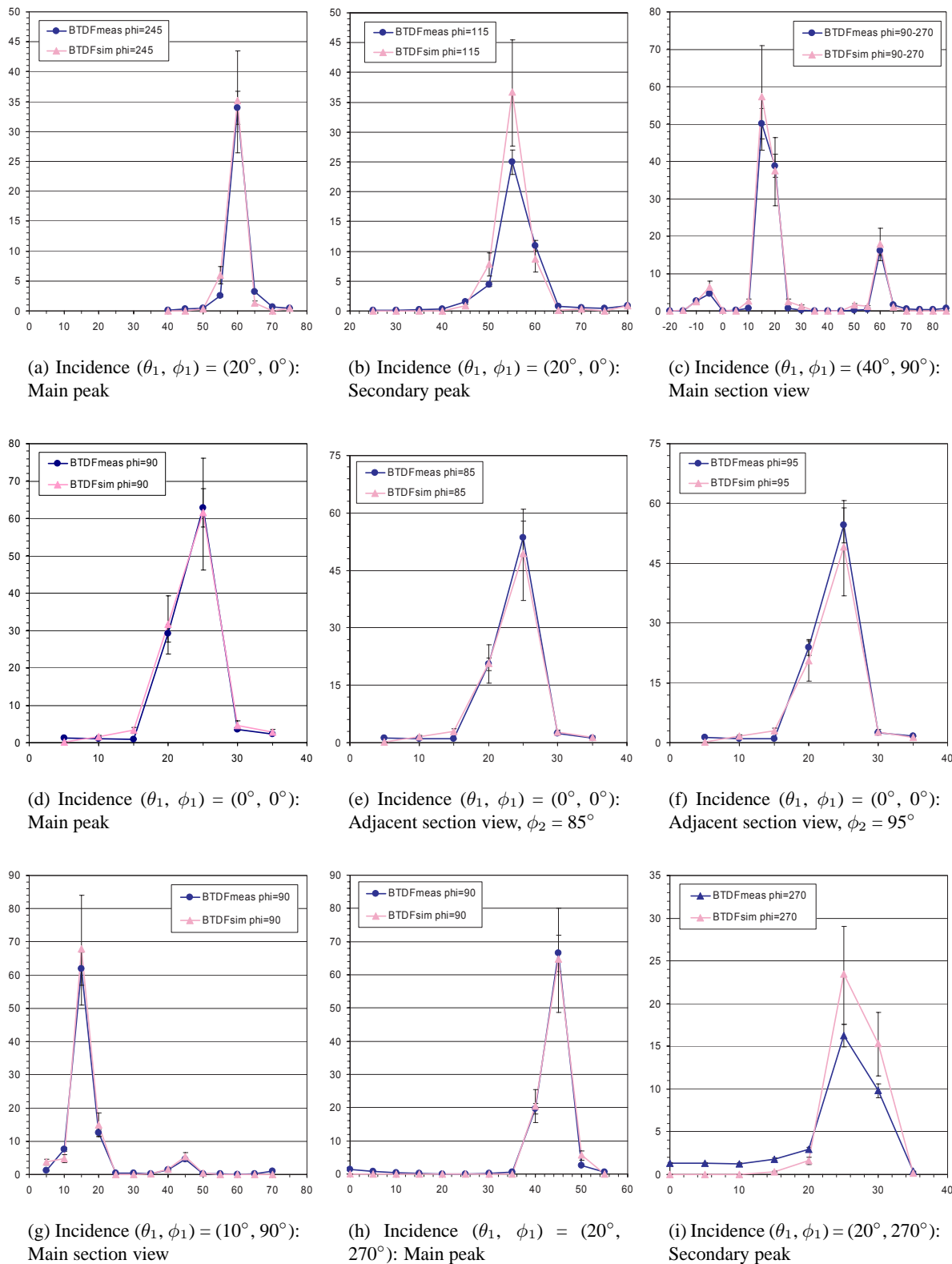


Figure 6.24: BTDF (sr^{-1}) vs. θ_2 ($^\circ$) along ϕ_2 planes: comparison of measurements ($\text{BTDF}_{\text{meas}}$) and calculations (BTDF_{sim}) for the asymmetric prism ($42^\circ 5'$ gratings, (a) to (c) with flat face on incident side, (d) to (h) with gratings on incident side).

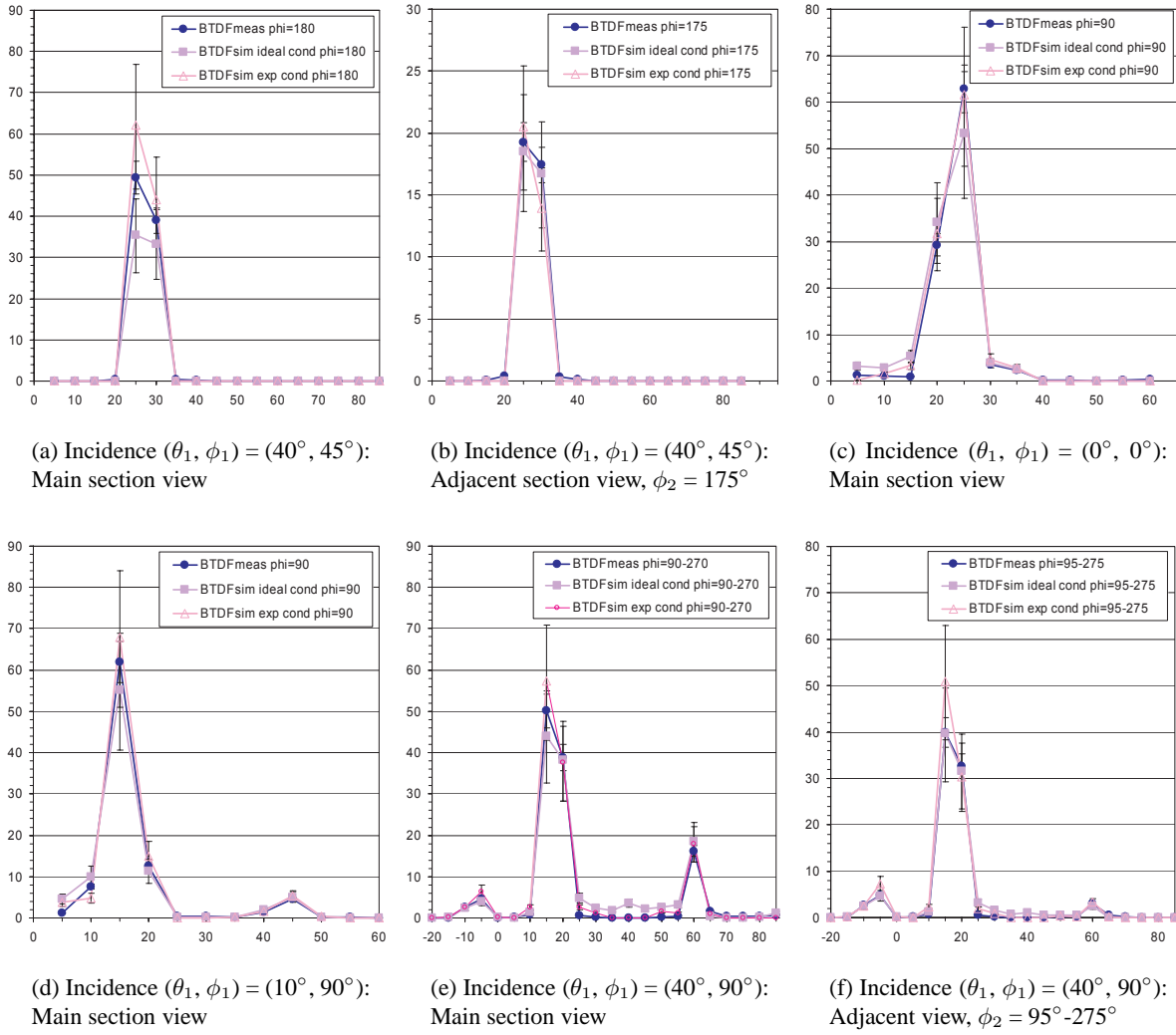


Figure 6.25: BTDF (sr^{-1}) vs. θ_2 ($^\circ$) along ϕ_2 planes: comparison of measurements ($\text{BTDF}_{\text{meas}}$) and calculations with ideal ($\text{BTDF}_{\text{sim ideal}}$) and experimental ($\text{BTDF}_{\text{sim exp}}$) conditions for the two prismatic panels.

Venetian blind

The results are shown on Figures 6.26 and 6.27; as mentioned in Section 6.5.2, the grids for BTDF averaging fit ($10^\circ, 15^\circ$) intervals.

Overall, the obtained results show a remarkable agreement between real and virtual BTDF data: although the transmission features are sharp in most configurations, the qualitative light behaviour is analogous for the experimental and computational methods; this is true as well for the light transmitted regularly (rays passing between the slats) as for the rays that were redirected after reflection on the curved slats surfaces.

On the quantitative level, the observed discrepancies are generally comprised within the error bars, making up an average value of 20% in relative terms; more specifically, relative errors of 15.3% 23.4% and 43.7% are observed for the direct, mirror and paint reflected peaks respectively (i.e. again smaller than the assumed simulation model errors).

The few situations where the curves differ by more than the error bars range (Figures 6.26(a), 6.26(d) and especially 6.27(d)) are generally associated to lower BTDF values, where the sensitivity to the simulation conditions is higher. If we consider the results of Figure 6.27(d) in particular,

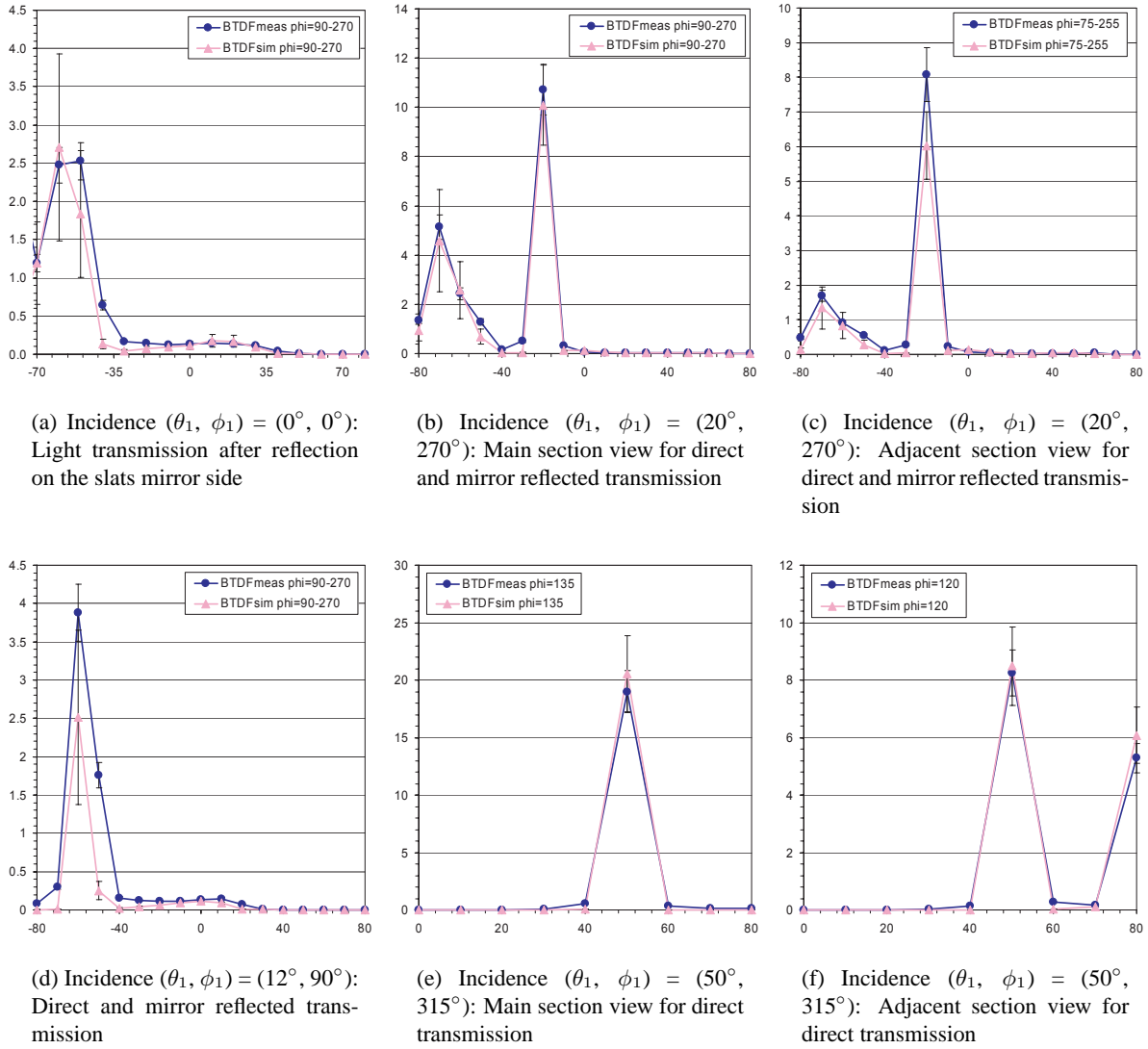


Figure 6.26: BTDF (sr^{-1}) vs. θ_2 ($^\circ$) along ϕ_2 planes: comparison of measurements (BTDF_{meas}) and calculations (BTDF_{sim}) for the 45° slats tilt configuration.

we can observe that they correspond to a light distribution where practically all the transmitted rays have undergone a reflection on the paint side of the slats (diffuse surface), which explains the low transmission value: a direct-hemispherical transmittance of 3% was found with both assessment methods. It will thus be considerably influenced by the model parameters, and more specifically by the paint coating specular component and reflection coefficient variations over the spectrum.

Overall, the results shown on Figures 6.23 to 6.27 make up a positive reciprocal validation, strengthened by the fact that the experimental and computational methods are based on very different parameters and assessment approaches and that the modeling of the selected samples was complex, requiring additional measurements and a careful modeling of their geometrical properties.

This validation applies at two levels: on one hand, it supports the quality of the experimental set-up, and more specifically of the adopted detection technique and the calibration and correction procedures; on the other hand, it proves that ray-tracing simulations provide a reliable and operational tool for complex fenestration systems assessment.

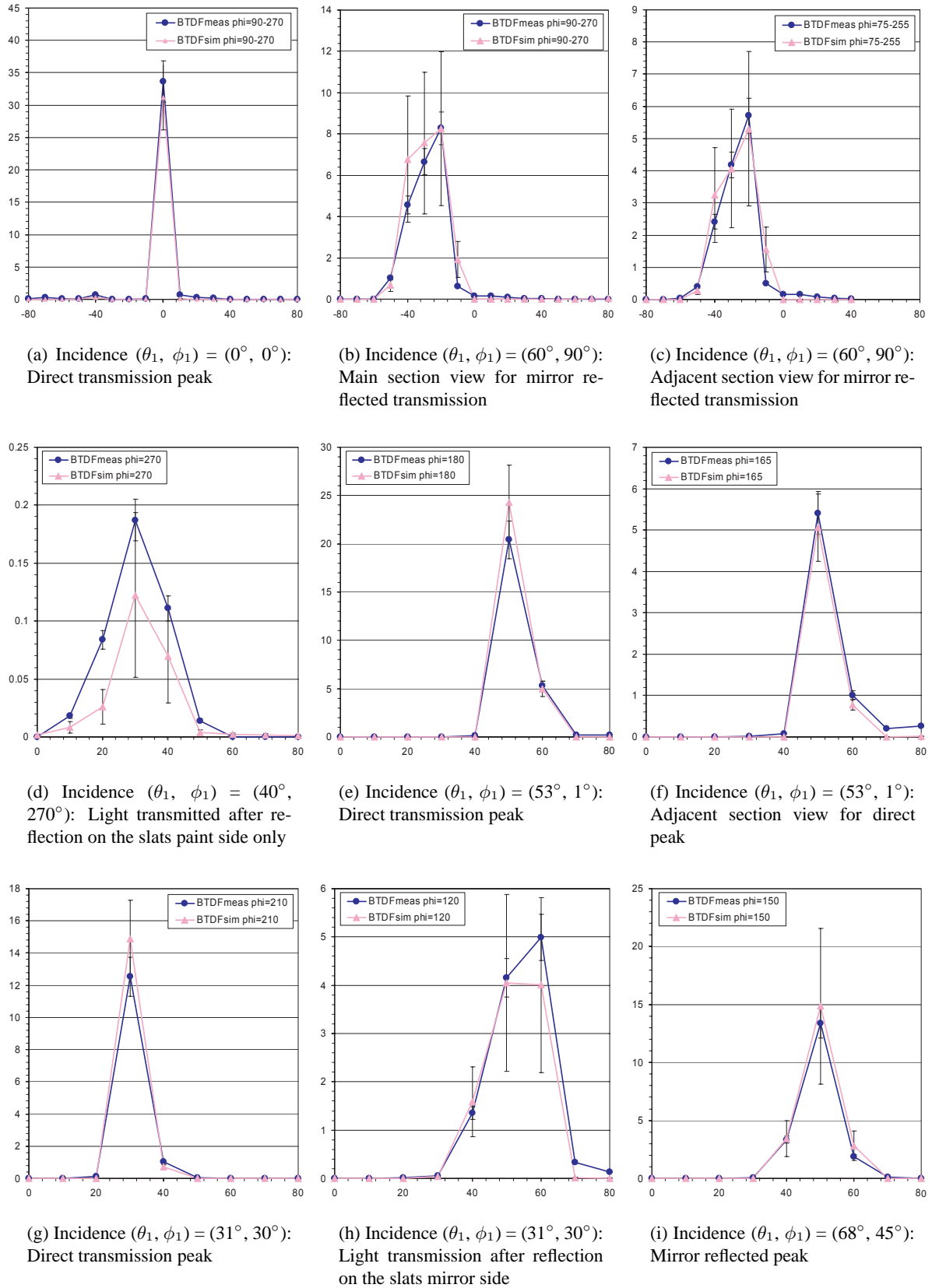


Figure 6.27: BTDF (sr^{-1}) vs. θ_2 ($^\circ$) along ϕ_2 planes: comparison of measurements ($\text{BTDF}_{\text{meas}}$) and calculations (BTDF_{sim}) for the 0° slats tilt configuration.

Chapter 7

Conclusion

“There is a great satisfaction in building good tools for other people to use.” (Freeman Dyson)

7.1 Achievements

Advanced fenestration systems, which include solar blinds, new glazing materials and daylight redirecting devices, can contribute to reduce significantly energy consumption of buildings, while simultaneously improving visual comfort conditions for users. Full knowledge of the light distribution characteristics through such systems is, however, required to control the propagation of daylight deeper in rooms and to allow larger solar gains in winter and lower solar loads in summer.

These rather variable features of fenestration materials can be formulated physically in terms of Bidirectional Transmission (Reflection) Distribution Functions - BT(R)DFs -, that need to be assessed experimentally through an appropriate goniophotometric equipment.

A novel bidirectional goniophotometer was designed and set up for this purpose, based on an innovative measurement technique: instead of moving a sensor from one position to the other in order to scan the whole transmission or reflection hemisphere, the emerging light flux is reflected by a flat diffusing screen towards a calibrated CCD camera, used as a multiple-points luminance-meter.

A complete investigation of the emerging light flux distribution is thus obtained within only six positions of the screen and camera system, reducing the monitoring time by a factor of about three hundred when compared to conventional approaches. As a consequence, the determination of a complete set of BT(R)DF data for one incident direction indeed only requires a few minutes, while several hours are needed for a sufficient set of emerging directions to be scanned.

Furthermore, thanks to the combination of a projection screen and of digital imaging techniques, luminance mappings of the emerging light flux are created with a pixel level spatial resolution; at the same time, saturation and under-exposure effects are avoided by combining several integration intervals to analyze a given situation, which greatly enhances the luminance dynamic.

A complete and continuous information about the emerging light flux distribution is thus obtained, that can be split into adjacent sectors of appropriate angular intervals.

The development of this device took place in four major phases, whose main achievements are summarized below.

Goniophotometer for reflection and transmission measurements

The realized bidirectional goniophotometer presents three major components:

- a fixed light source providing, as far as possible, a collimated and spectrally optimal light beam that shows an appropriate uniformity over the sample area;
- a computer controlled movable mechanical support that allows modifying the incident light direction on the material sample;
- a computer controlled “light detection device” made of a triangular flat projection screen - diffusing and spectrally neutral - associated to an image capturing CCD video camera.

The major structural components were first designed and constructed for measurements in transmission: main platform, rotating ring, supporting structure and light-proof cap.

The final design of the goniophotometer for BTDF characterization took place as the first stages of the present work and was realized thanks to several additional developments.

Appropriate command routines were developed for all motors. An accuracy of about 0.2° was achieved for the positioning of the main platform, the sample holder and the rotating ring supporting the “light detection device”, guaranteeing a high accuracy in the determination of both the incident direction (θ_1, ϕ_1) and the emerging directions (θ_2, ϕ_2) .

An optimal sample holder was designed, ensuring the coplanarity of the external sample surface with the rotation axis of the main platform and reducing obstructed light rays to a minimum: at worst, only 10% of the emerging hemisphere is lost, moreover in the region of least interest (grazing outgoing angles of altitude θ_2 greater than 85°).

A diffusing detection screen was fixed on the rotating ring opposite to the camera at an inclination angle fitting the theoretical value with a 0.05° accuracy; its coating properties were verified to be of constant reflectance over the visible wavelengths with only 1.5% relative fluctuations, and of directional diffusing properties satisfying the lambertian model within a 2.6% relative range.

The CCD camera was set up for a full view of the detection screen for any configuration and calibrated into an accurate multiple-points luminance-meter, as detailed in the next part.

For reflection measurements, the device envelope and mechanical components were carefully revised, as the incident and emerging light fluxes are in this configuration on the same side of the sample. Therefore, a controlled passage of the incident beam into the measurement space was created, minimizing parasitic reflections around the sample. Openings in the detection screen for the situations where it obstructs the incoming light flux were also required, made as small as possible to restrict the produced blind zones.

The practical answer to these constraints proved successful and reliable, for both the light beam penetration into the measurement space and the passage through the obstructing screen.

A static metal sheet was perforated with a set of elliptic openings of dimensions given by the apparent sample area, accounting for tilt angle θ_1 and cut out at the corresponding positions on a quarter circle arc; it was fixed on a supporting frame and designed to serve as a gliding support for an unrolling, motorized synthetic strip covering all elliptic apertures but one, in order to target the incident beam on the sample surface precisely.

A new incident light source was selected to answer the more severe constraints in illumination value and collimation of the novel device; the metal sheet ellipses were then adjusted to the incident light beam’s properties, to ensure a uniform sample illuminance (1.4% relative variations) and restrict parasitic reflections around it to a negligible value.

Removable covers were cut out of the detection screen, for which a motorized extraction and repositioning system was developed: the covers were of shape and dimensions determined by the projection of the apparent sample area on the screen plane, in order to ensure the passage of impinging light but minimize the blinded region; permanent electro-magnets (PEMs) were mounted on a motorized wagon for their removal and repositioning, with an additional mechanical extractor using screw-like pins.

Command routines for the two new motors were developed, for a precise positioning of the synthetic strip's unique aperture and for a reliable screen covers handling process, at all device configurations.

Experimental accuracy of the goniophotometer

The use of digital video techniques proved very fruitful for this novel approach. The overall video system was calibrated in a detailed and exhaustive manner to achieve an appropriate accuracy for the BT(R)DF measurements. These calibration procedures were focused on three main issues and required to implement some additional corrections.

The spectral response of the CCD camera was corrected to fit the human eye's spectral sensitivity $V(\lambda)$ with a 10.2% accuracy, which, however, influences the determined luminance values by less than 1%, as it only appears as a second order error.

The photometric calibration allowed to convert pixel greyscale values (0 to 255) into luminances (in $\text{Cd}\cdot\text{m}^{-2}$) for different integration intervals ranging from 40 ms to 2.56 s with a mean relative error of 1%.

The spatial calibration determined the relationship between image pixel coordinates and the hemispherical polar angles (θ_2, ϕ_2) of the corresponding emerging direction. Matrix-based referential adaptations were thus developed to ensure a flexible investigation of the emerging light flux distribution, applied at a pixel level resolution (i.e. at an angular resolution of about 0.1° to 0.3° in altitude and azimuth) and accounting for the current sample thickness and incident azimuth ϕ_1 .

Several additional calibration procedures were necessary. The imperfect collimation of the incident beam asked for a correction factor to be applied on the sample diameter, determined with a 1.4% relative accuracy. The darkening effect observed on raw images (that could reach 6% close to its edges) was compensated by the way of a correction figure applied on the digit values directly, thus achieving a 99% uniformity. Finally, the slight parasitic effects caused by the incident beam penetration into the measurement space were subtracted from the captured images.

The command software developed for this device was tested successfully for both the transmission and reflection modes; the advanced imaging techniques combined to the matrix-based approach for spatial analysis and gathering of BT(R)DF data into adjacent angular sectors ($\Delta\theta_2, \Delta\phi_2$) proved their usefulness to speed up the data acquisition process, improve the resolution in luminance and ensure a continuous and accurate investigation of the emerging light flux distribution.

By choosing only optimal integration intervals for the conversion of image pixels into luminances, over and under-exposure effects were prevented and an equal and accurate resolution over the whole luminance dynamic was achieved. The adequacy of the considered sample illuminance values $E_1(\theta_1)$ was guaranteed by its simultaneous measurement at each image capture.

Once digital maps of the $\frac{L_{\text{screen}}}{E_1(\theta_1)}$ ratios were determined, the corresponding BT(R)DF maps were created by compensating distance and light tilt effects at a pixel level accuracy, as well as the screen reflection coefficient and the apparent sample area.

These maps were then subdivided into adjacent averaging sectors according to a regular grid of emerging directions (θ_2, ϕ_2) for an easier handling of data. The optimal angular intervals $\Delta\theta_2$ and $\Delta\phi_2$ of these sectors were determined by the sample area, to fulfill the required conditions for assessing specular and diffuse components of emerging light flux together, and to account for the possible divergence of emerging rays reaching a given point on the screen, the sample being non-punctual.

An adequate graphical formatting of the heavy data files in spherical co-ordinates was also realized to provide a synthetic and intuitive visualization of the system's transmission or reflection features. Three types of representations complementing one another were developed: the projection of BT(R)DF data on a virtual hemisphere (allowing their precise directional analysis), the so-called photometric solid (a three-dimensional equivalent of the luminous intensity characteristics provided for artificial lighting fixtures) and a selection of the most relevant cross-section views of this photometric solid, that allows a detailed study of the numerical values along azimuth planes.

A detailed assessment of the experimental accuracy of the goniophotometer was carried out using different approaches.

The many intermediate calibration stages necessary to extract BT(R)DF data from raw digital images were reviewed and an experimental error associated to each of them: CCD camera calibrations, spatial accuracy, correction factors, processing restrictions, material and mechanical constraints. A global error on BT(R)DF data equal to 10% was deduced from this study and thereafter verified with detailed comparisons at different levels. This value corresponds to a very satisfactory accuracy for figures as complex as BT(R)DFs.

Different materials presenting a known symmetry were characterized in either transmission or reflection; the expected features or the theoretical bidirectional functions were duly verified against measured data, with discrepancies varying from 1% to 8%.

Within the framework of international projects, several systems were characterized with various goniophotometers. Whenever possible, the respectively obtained bidirectional measurements were thus compared for diffuse transmission with the present device; these comparisons outlined differences lower than 8%, which proves that the BT(R)DF data were reliable for the different instruments, but also that the averaging method chosen for this one did not alter the results quality.

The more commonly used method for validating BT(R)DF data was also applied to cross-check the reliability and accuracy of the novel goniophotometer. It consists of integrating numerically the bidirectional data in order to deduce the directional-hemispherical transmittance or reflectance; this value is then compared to an Ulbricht sphere measurement made with the same sample. To consolidate this comparison, the considered integrating sphere values resulted from measurements carried out by various European laboratories.

Several fenestration systems were selected for this study: diffusing materials, laser cut and prismatic glazings, fabric blinds. Overall, the agreement between the two assessment methods proved excellent, the observed discrepancies remaining lower than the assumed measurement errors.

In addition to this, a different approach for directional-hemispherical comparisons was chosen, resorting to ray-tracing simulations for prismatic panels and a mirror coated venetian blind. The same conclusion was reached, as the resulting differences were always comprised within the two methods own errors.

These results, together with an analysis performed in the absence of any sample, allowed to determine a reliable value of 15% for the relative error to assume on τ_{dh} and similarly ρ_{dh} values deduced from the present BT(R)DF assessment.

The high quality of these measurements was also confirmed by an original and extensive comparative study of experimental bidirectional data with computer simulations.

A virtual model of the goniophotometer was constructed for this purpose and two types of fenestration systems were modelled as faithfully as possible: acrylic prisms with either symmetric (45°) or asymmetric ($42^\circ/5^\circ$) gratings, and a venetian blind presenting curved slats with a mirror coating on the upper side, either horizontal (0°) or tilted (45°).

This study represented a first and successful attempt of validating detailed bidirectional properties of complex fenestration systems in a roundabout approach with ray-tracing simulations. The comparisons between simulations and measurements showed a remarkably close agreement, despite the sharpness of the transmission features, the very different assessment methods and the important number of parameters that had to be taken into consideration. The discrepancies between BTDF data were indeed always lower than the estimated errors on the simulation results alone, for both the prismatic panels and the venetian blind.

Overall, these different validation approaches led to fulfilling results for the achieved bidirectional goniophotometer, placing reliance on the assumptions made in the construction of the instrument and on the various calibration and correction procedures that were necessary to convert the CCD camera into a reliable multiple-points luminance-meter.

7.2 Perspectives of application and use

Once a fenestration system is characterized according to its BT(R)DF, the way it redistributes the impinging light flux inside a room is precisely known, which can lead to a better use of these elements in building construction and allow progress in research and industrial applications.

A substantial set of BTDF and BRDF measurements was achieved for a large variety of fenestration systems (about fifty different types), listed in Appendix C: diffusing panels and sunlight redirecting glazings, as well as fabric and venetian blinds with different coatings and shapes.

An important part of this considerable database was already used by the industrial partners of this project, and by the solar blinds manufacturer Baumann-Hüppe AG in particular. The quality and competitiveness of their products could thus be improved, by optimizing their visual comfort performances and energy savings potential.

The growing interest shown by practitioners and the window components industry in this kind of data confirms the adequacy of this measurement device to their needs. It allows them to benefit from an easy, rapid - and therefore cheap - access to a reliable and accurate characterization of their products and prototypes; it also provides them with objective guidelines to improve their performances, as suitable adjustments of shapes and/or coatings (reflection coefficients, texture, etc.) can be pointed out, and thereafter verified for further optimization.

A special attention was paid to provide an easy and synthetic graphical representation of the light transmission (reflection) properties of materials: these representations offer an efficient way to clearly present product features to practitioners in the building construction sector according to a common physical description of their photometric transmission (reflection) properties. Architects will then be able to judiciously select the most suitable fenestration system for their particular project, basing their choice on objective and precise criteria.

In the field of building simulation tools, the potentialities of daylighting performances assessment programs will be considerably increased if they can benefit from an accurate and objective characterization database of the new fenestration systems and include their bidirectional properties in the calculation routines.

Such programs include the image rendering software *Radiance* (Ward Larson and Shakespeare, 1998) and its derivatives (Reinhart and Herkel, 2000), as well as ADELINÉ (Roy, 2000) and WIS (van Dijk, 2001); commercial softwares, such as RELUX[®] developed by Relux Informatik (associated as a partner to this project), also show a strong interest in this field of development.

The achieved bidirectional data actually found an additional application opportunity in a matrix-based calculation tool, that is still at an early stage of development (Fernandes and Papamichael, 2003). Instead of assessing the daylight distribution in a room for a specific complex fenestration system, this tool opts for the opposite approach: it searches for the optimal system to achieve given daylighting performance goals, basing the selection on the largest available bidirectional database.

Of course, to include complex glazings in daylighting simulation tools (as described in Section 5.5.4 or in Mitanchey et al. (2002); De Boer (2003)), the BT(R)DF data need first to be processed for a directional function in emergence to be associated to a given sky luminance distribution. The latter can be typically based on the subdivision of the sky hemisphere defined by Tregenza (1987) for the International Daylighting Measurement Program (IDMP), applying the all-weather model by Perez et al. (1993) to recreate a realistic distribution or the partial daylight factor method developed for scale model measurements under artificial sky by Michel and Scartezzini (2002).

7.3 Outlook

This work has led to the full achievement of an innovative measurement device for the assessment of the bi-directional light transmission (BTDF) and reflection (BRDF) properties of complex fenestration systems, using digital video techniques. The established methodology proved to be efficient and reliable, providing an accurate set of BT(R)DF data within an extremely reasonable time interval, about three hundred times shorter than for conventional characterizations based on a scanning process.

To further improve its efficiency and extend its applicability, several enhancement possibilities can be considered.

Replacing the actual black and white CCD camera by a color camera, already used for instance for the color and luminance uniformity testing of displays (Jenkins et al., 2001) but asking for a more elaborate spectral calibration (Ohno and Hardis, 1997; Pattanaik and Torrance, 1998; Michel et al., 2001), would allow a more accurate assessment of the daylight distribution inside a building equipped with complex glazing or shading systems. Typically, the occurrences of color separation would be pointed out (observed for holographic films and prismatic elements) and both the visual performance and agreeableness factors could be better taken into account (Chain et al., 2001).

Yet to allow the characterization of the spectral distribution of the emerging light flux, necessary for solar heat gains assessments to be possible, a further step would be required, either using wavelength-selective filters in front of the camera's objective or separating the incident light flux into a set of monochromatic beams.

Obviously, technical improvements such as using a more powerful computer, or even two communicating computers to separate the pure image acquisition and movements driving from the data processing, would allow the characterization time to be further reduced; on the other hand, considerable progress having been made in the field of digital imaging since the beginning of this work, CCD video cameras with much higher pixel resolutions are now available, and would significantly refine the angular resolution in emergence, probably by a factor four or more.

The ray-tracing comparisons conducted in Section 6.5 revealed that simulation methods prove to be a valuable tool for parametric studies. The agreement between experimental and computational approaches remains very sensitive to the accuracy of the system's model though, slight differences between the latter and the real system leading to important results discrepancies, as shown by the simulation error study presented in Section 6.5.4. .

When the involved materials or coatings are of well-known properties, the creation of a sufficiently precise model can be relatively easy: in the case of prismatic panels, the geometry and wavelength-dependent refractive index were simply taken from the manufacturer's data, and a very close agreement was still achieved for most situations, as shown in Section 6.5.5. For many fenestration systems prototypes, however, some components will require a preliminary measurement for their transmission and reflection properties to be implemented faithfully in the model. Typically, the mirror and paint coatings of the studied venetian blind slats had to be characterized beforehand and fortunately proved almost perfectly specular and diffusing, respectively. Yet for more complex materials, a detailed BT(R)DF might be required for the calculation results to be reliable.

In consequence, combining both experimental and computational aspects appears as a very promising niche: flexibility and data accessibility can be considerably increased with the ray-tracing approach, while accurate and detailed measurements of new coatings or materials are still essential for results to be reliable, as well as to provide reference data for validating the characterization of whole systems.

Finally, an essential issue in the assessment and use of bidirectional functions is certainly their simplification, that is to be understood at two very different levels.

Since the early 90's, numerous models for bidirectional reflectance functions based on spherical harmonics (Mohlenkamp, 1997), wavelets (Stollnitz et al., 1995a,b) or other analytic functions were developed for computer graphics applications and photo-realistic rendering of anisotropic objects (Poulin and Fournier, 1990; Sillion et al., 1991; Ward, 1992; Schlick, 1994b,a; Lafortune et al., 1997; Lalonde and Fournier, 1997; Rusinkiewicz, 1997; Collins, 1998; Neumann et al., 1999; Noé, 1999; Noé and Péroche, 2000; Koudelka et al., 2001; Drago and Myszkowski, 2001; Deniel, 2002). These analytical models could be extended to fenestration systems applications, in order to allow BT(R)DF figures to be classified into a finite number of transmission or reflection types (Baker et al., 1997; van Dijk, 2001), and, for this categorization to be systematic, associate them to analytic functions.

Some models have actually taken shape in this field already: in the REVIS project (van Dijk, 2001), bidirectional functions were separated into five components, named specular, diffuse, specular redirected, scattered specular and scattered redirected portions; in the appendix of Scartezzini et al. (1997b), a development of BTDFs based on spherical harmonics is proposed, that would require further inquiries to be applicable.

On the other hand, to ensure that these data are used by a large number of protagonists in the building industry, more concise expressions of bidirectional functions are needed.

A more synthetic and building oriented approach would then be preferable to describe fenestration systems and window components, like a BT(R)DF representation providing average values over the group of directions pointed towards each wall, floor and ceiling, or thanks to a systematic link between a BT(R)DF type and the luminous atmosphere it induces in a room according to architects criteria and qualifications.

This research project hence offers diverse and interesting perspectives for improving the luminous performances in buildings, and opens a wide range of encouraging development possibilities.

Thanks to accurate and time-efficient bidirectional measurements, such as provided by the present goniophotometer, a more intensive and appropriate use of advanced fenestration systems will be possible. In addition to decisive improvements in visual comfort, energy savings will be enhanced significantly by reducing electric demand for lighting, heating and cooling loads through a more focused control of solar gains.

In this way, goniophotometry appears as one of the many important tools to take into consideration in the conception of sustainable buildings.

Appendix A

Mechanical components specifications

A.1 Main platform and rotating ring

The plane view of the bidirectional goniophotometer's mechanical concept is shown on Figure A.1, where the rotating system for the sample holder and the ring supporting the camera and detection screen are apparent.

On Figure A.2, a cross-section of the main platform is provided, with the initial configuration of the light-proof cap.

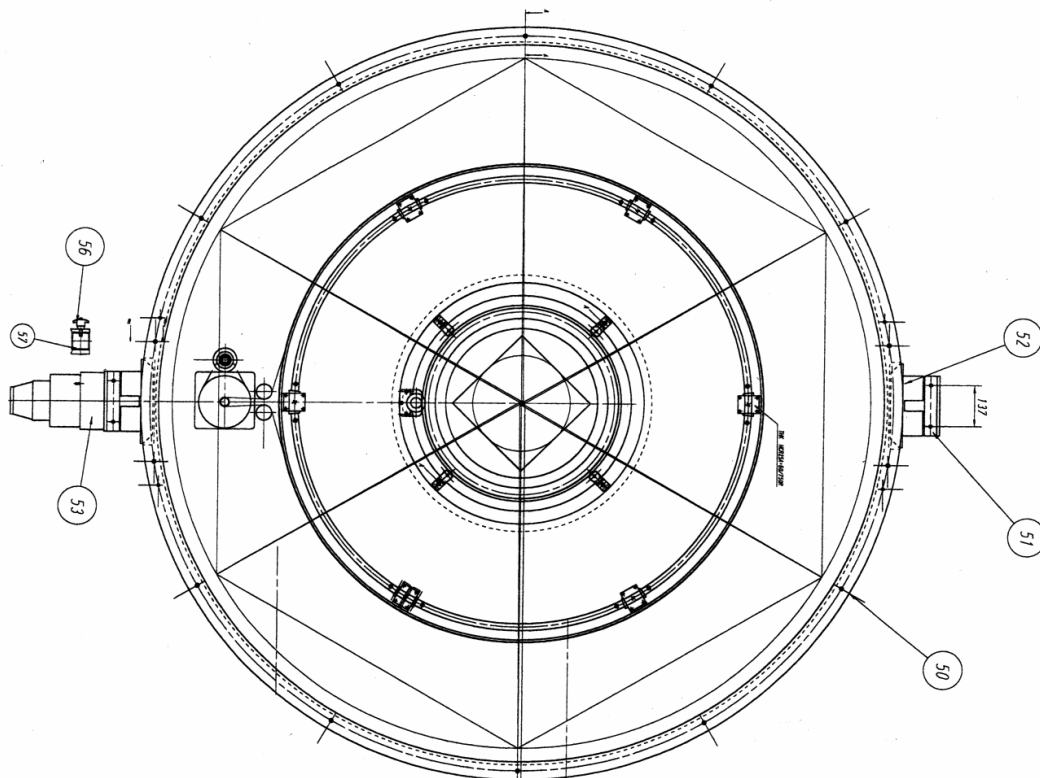


Figure A.1: Plane view of the major structural components of the bidirectional goniophotometer (Consultant: D. Glauser).

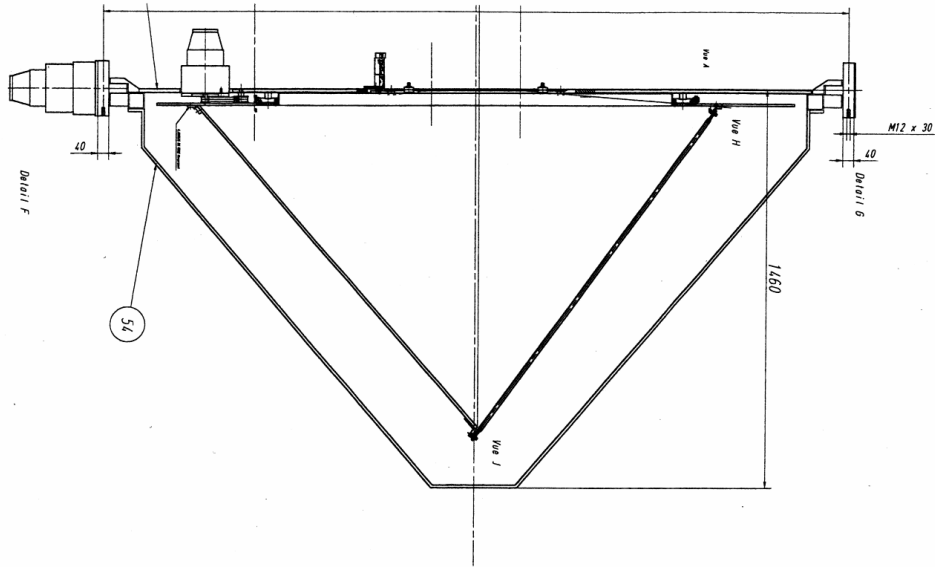


Figure A.2: Cross-section view of the major structural components of the bidirectional goniophotometer (Consultant: D. Glauser).

A.2 Quarter-circular support frame

A structural metallic frame was added on the main platform to support the static perforated sheet for the final reflection goniophotometer configuration. Its geometrical characteristics are shown on Figure A.3.

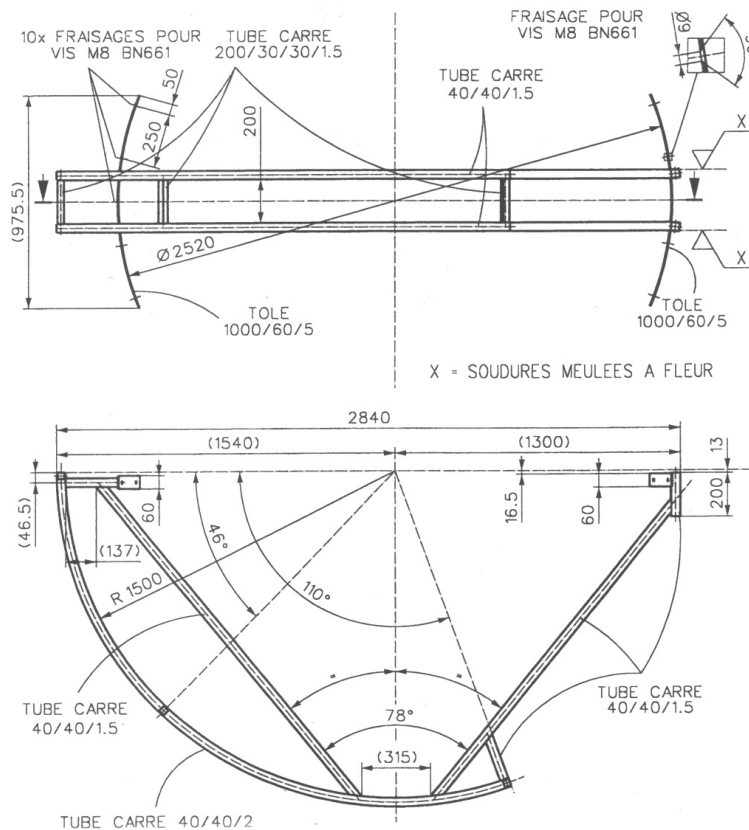
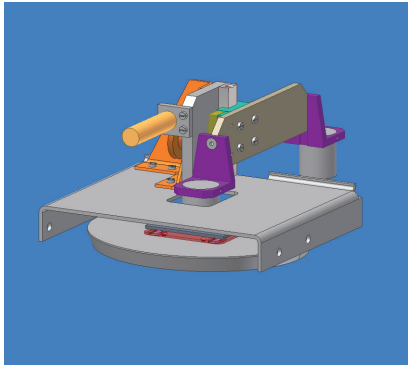


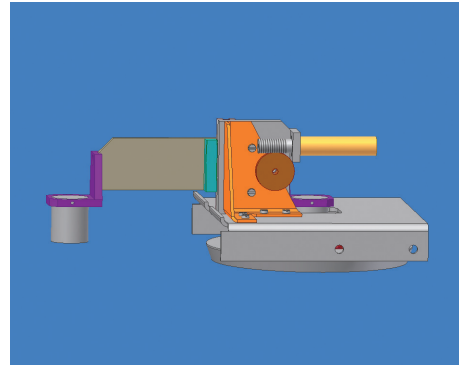
Figure A.3: Plane and cross-section views of the quarter-circular support frame for BRDF measurements (Consultant: S. Bringolf).

A.3 Motorized screen

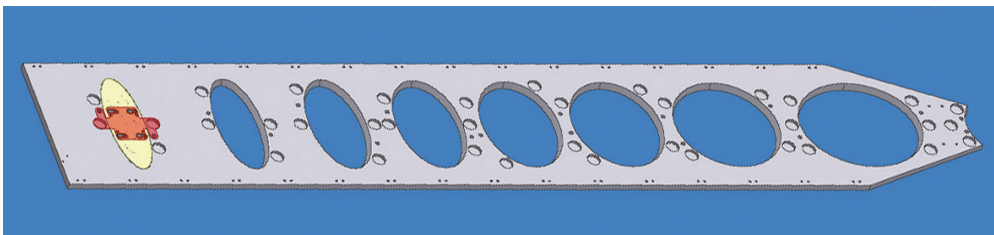
Schematic representations of the motorized screen concept for reflection measurements are shown on Figure A.4: the different mechanical components necessary for the screen covers extraction by the moving wagon are visible on Figures A.4(a) and A.4(b); the aluminium insert on the central axis of the screen is illustrated on Figure A.4(c), and the whole system shown on Figure A.4(d).



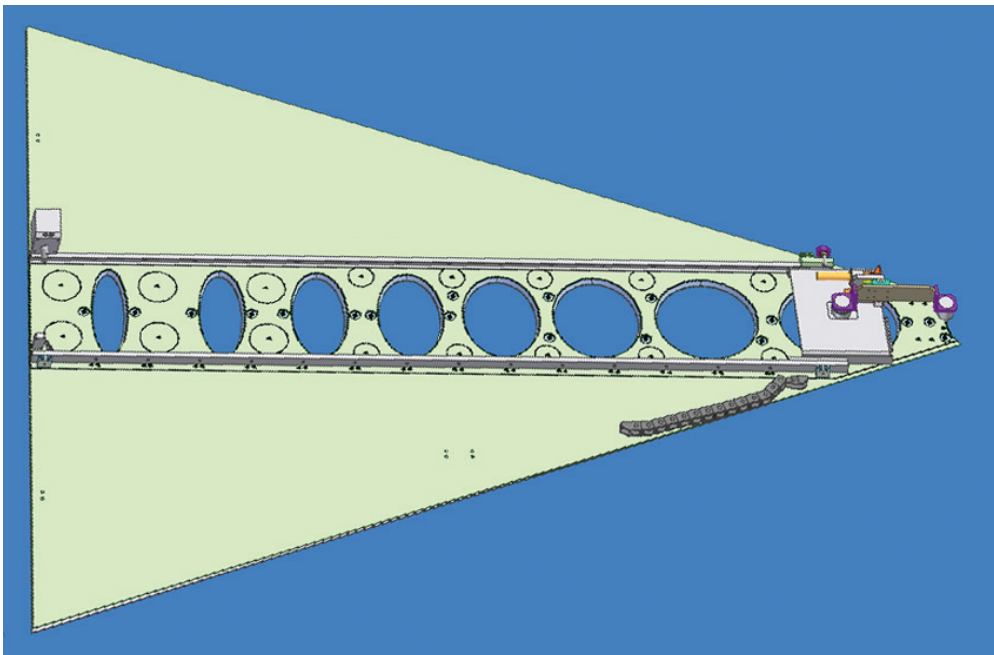
(a) Wagon, axonometric view



(b) Wagon, side view



(c) Aluminium insert with cut-out ellipses



(d) Complete screen system

Figure A.4: Design of the motorized screen with removable covers.

A.4 Sample mounting

The relative position of the sample to the co-ordinate system has a huge impact on the measurement results. Its orientation must therefore be defined according to a well-established convention for BT(R)DF measurement comparisons to be pursued.

Within the framework of Task 21 (“Daylighting in Buildings”) of the International Energy Agency (2000), a common format was determined and several rules established to guarantee a consistent information from one dataset to the other.

The origin axes $\phi_i = 0^\circ$ ($i = 1, 2$), whose vectors are collinear for incidence and transmission, are bound up with the sample itself. As illustrated by Figure A.5, placing the latter in a vertical plane and observing it from the incident source side, the $\phi_i = 0^\circ$ axes point horizontally at the right hand side. This direction therefore corresponds to the one indicated by slats or gratings in case of samples presenting parallel features. The only difference between the origin axes for ϕ_1 and ϕ_2 is that they belong to different planes in case the sample is of non-zero thickness.

As for the origin axes $\theta_1 = 0^\circ$ and $\theta_2 = 0^\circ$, they are given by the vectors normal to the external, respectively internal (towards emergence) sample interfaces, pointing towards the incident, respectively emerging directions.

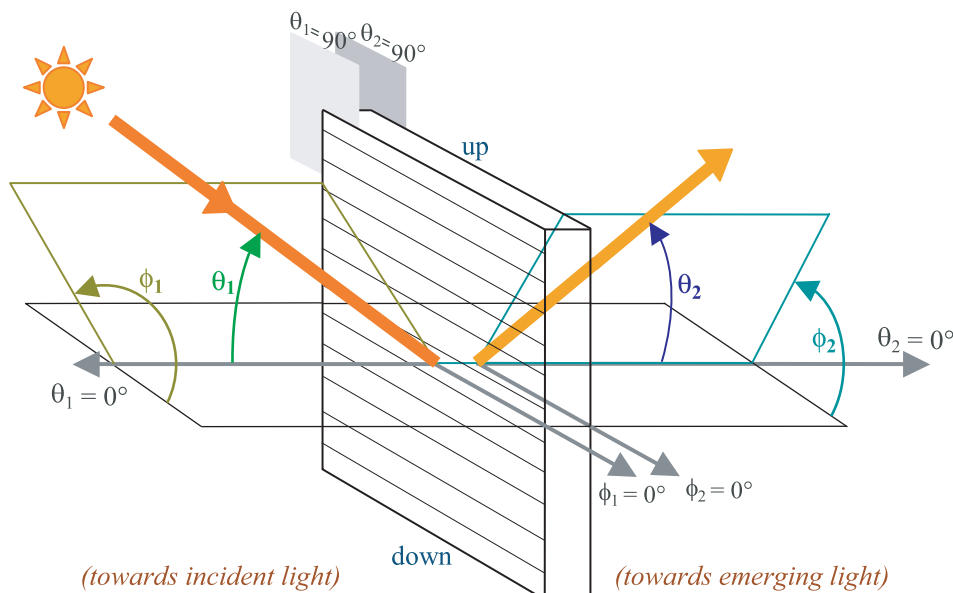


Figure A.5: Orientation of a characterized system with regard to the coordinate system.

To be mounted properly on the sample holder, any fenestration system must fulfill certain requirements, illustrated in Figure A.6:

- the system must be mounted in a square frame of exterior dimensions 40×40 cm, and of thickness 1.5 cm, painted in mat black;
- the system's plane facing the incident light must be exactly on a level with the frame's border (see Figure A.6(b));
- For BRDF measurements, in case the sample is not perfectly opaque (or it is significantly smaller than the frame), a highly absorbing material (e.g. black velvet) must be placed and fixed on or around all sides, as illustrated in Figure A.6(b), in order to collect the light that would otherwise be transmitted and that could cause inter-reflections.

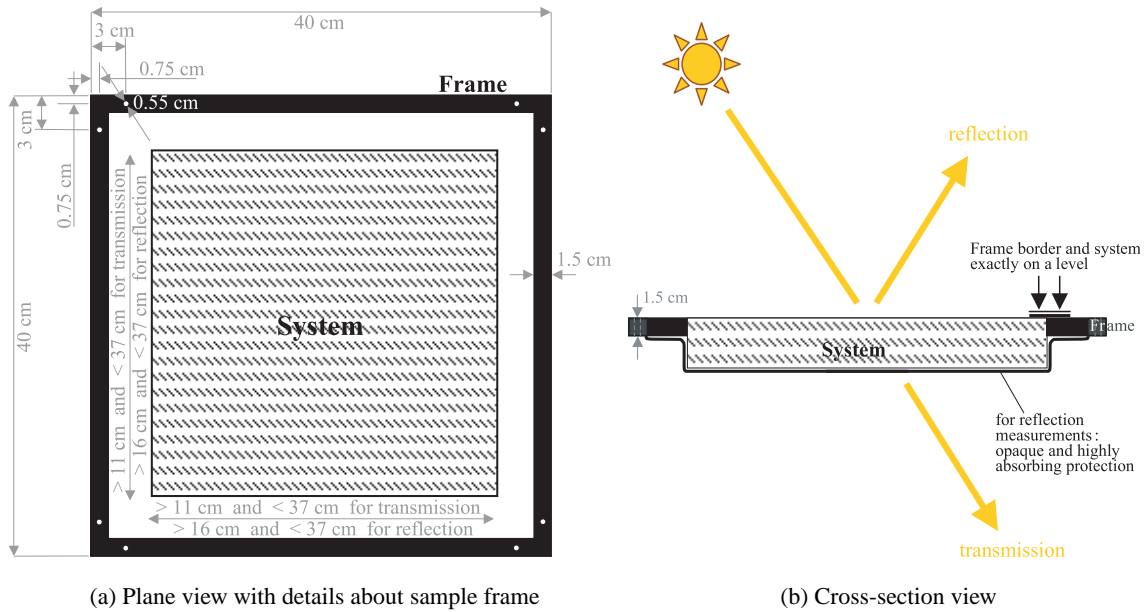


Figure A.6: Specifications for the sample dimensions and framing.

Diaphragms are prepared to restrict the illuminated area to a disk of diameter 10, 15, 20 or 30 cm for transmission, the choice depending on the system's parameters and heterogeneity; for reflection, the maximal diameter is of 15 cm due to the penetration of the incident beam into the measurement space.

Appendix B

Command interface and monitoring procedure

The functionalities of the command interface and the monitoring procedure from the user's point of view are here described in more details than in Chapter 5.

The complete command interface is shown on Figure B.1. On the main interface designed for the selection of incidence and emergence parameters in transmission or reflection mode, additional side frames appear on the right and bottom, used to drive the mechanical movements of the device independently. They allow a status control (right frame) and individual axes movements (bottom part). The small frame on the bottom-right corner allows to select only specific characterization phases to be running: device movements, averaging grid construction, image capture and/or processing, recomposed image, final data file creation.

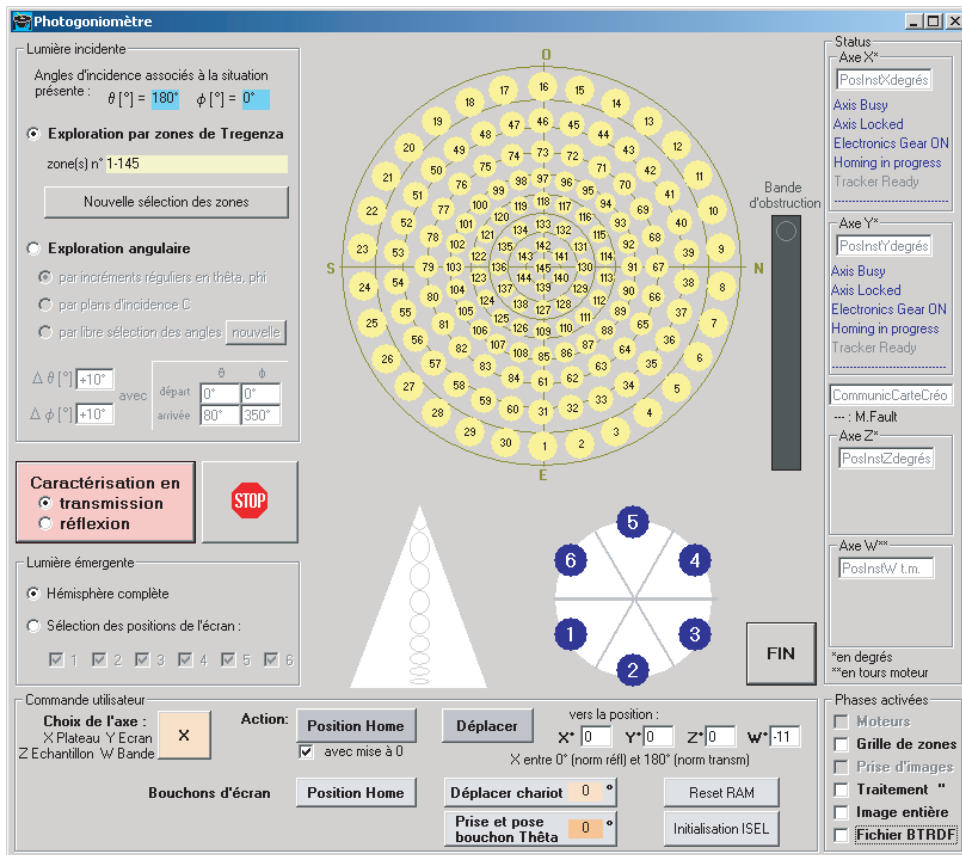


Figure B.1: Complete driving software interface for BT(R)DF characterizations.

At startup, the Creonics card variables for the main platform and rotating ring axes are first initialized, as well as the COM ports axes (sample holder and unrolling synthetic strip) and the screen wagon ISEL micro-controller. In the same order, a homing command is executed for these five axes, that are thereafter moved to their respective zero positions before a picture is taken to locate the LED's position for the exact screen detection area determination (see Section 4.2.1).

The BT(R)DF characterization parameters can then be chosen, according to different investigation options in incidence and emergence, as explained below.

B.1 Determination of the BT(R)DF monitoring parameters

B.1.1 Incident directions set

Two types of exploration in incidence are proposed, represented by their respective stereographic projections on Figure B.2, either based on a sky vault coverage or on polar angles, as detailed below. For the latter, the incident directions set can be either created according to regular steps in altitude and azimuth, or along azimuth planes, or according to freely chosen incident angles.

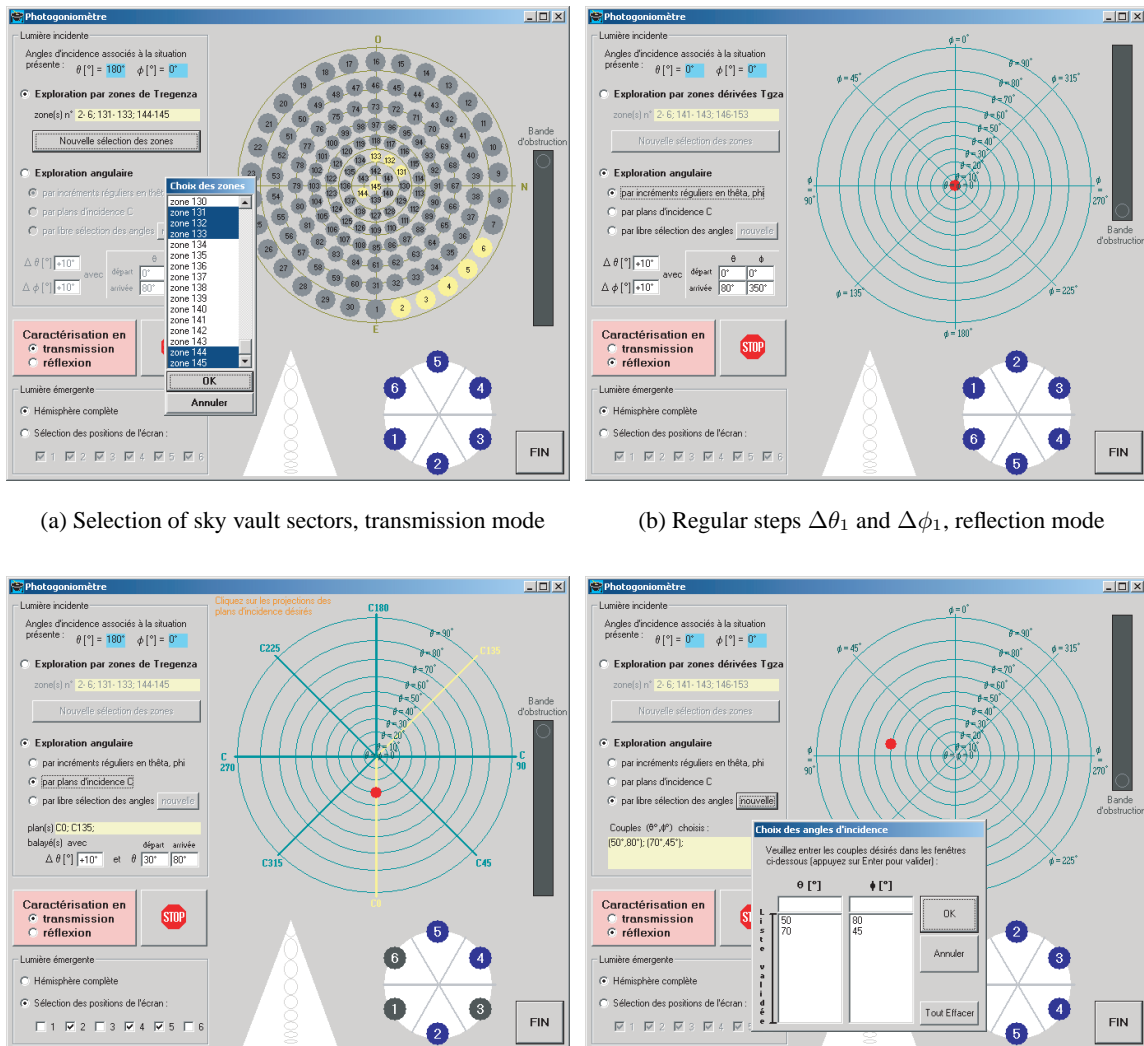


Figure B.2: Graphical interface for the different investigation options.

As mentioned in Section 4.2.3, a reversal of the referential occurs both in incidence and emergence when the characterization mode changes from transmission (BTDF) to reflection (BRDF).

When comparing Figures B.2(a) and 5.1(b), it can be observed that the incident directions set based on a sky vault coverage differs whether it is the transmission or reflection mode that is selected. Their specifications are explained below.

In both cases, a specific set of directions can be selected either by mouse-clicking on the stereographic view directly, or by choosing the desired ones amongst the list displayed in the popping-up window when the "Nouvelle sélection des zones" command is activated.

Subdivision of the incident hemisphere according to solid angles

145 directions in transmission

In transmission mode, the default set of incident directions matches the subdivision of the sky hemisphere for luminance measurements defined by Tregenza (1987) for the International Daylighting Measurement Program (IDMP), as agreed within Task 21 of the International Energy Agency (2000). This subdivision determines 145 sectors on the incident vault, illustrated on Figure B.3, whose respective centers provide the considered 145 incident directions (θ_1, ϕ_1) for BTDF characterization.

In altitude, these 145 directions, listed in Figure B.6, are distributed according to 12° steps; in azimuth, their gap increases from 15° for grazing θ_1 values (84°) to 60° for the arrangement around the normal direction (i.e. for $\theta_1 = 12^\circ$), in order to make up a hemisphere coverage rate of 79% with 12° opening angle disks, 68% with 11° and 55% with 10° disks.

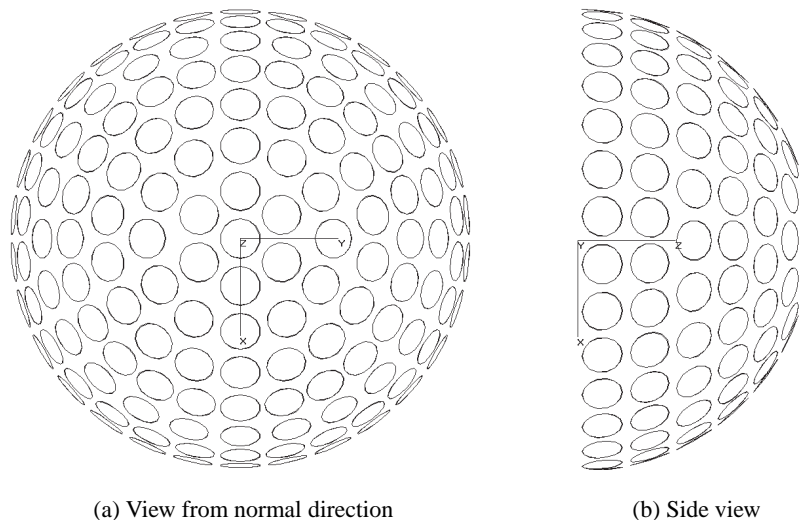


Figure B.3: Subdivision of the incident hemisphere (sky dome) into 145 sectors of 10° opening.

Very recently, the Berlin University of Technology (TUB) proposed a revision of this default incident directions set (Herrmann et al., 2003), as the actual configuration is in fact more suitable for zenithal openings than for lateral windows, that are however the most common ones today.

To adapt it to realistic sun courses, they suggest to convert the (θ_1, ϕ_1) co-ordinates into sun co-ordinates, and to use a hybrid distribution based on the above configuration, close to rotating both top and bottom halves of Figure B.3(a) by 84°, respectively downwards and upwards around a horizontal axis.

163 directions in Reflection

For reflection measurements, the set of incident directions is free in azimuth, but the altitude

angle θ_1 has to be a multiple of 10° due to the controlled penetration of the impinging beam (see Section 3.3.3). A set of 163 sectors of 10° opening was therefore determined, closely matching the configuration in transmission to get a similar exploration in reflection and determining the 163 default incident directions for BRDF characterization, listed in Figure B.7.

The resulting configuration is shown on Figure B.4, making up a 68% coverage rate for the used incident hemisphere (i.e. 62% for the complete (up to 90°) hemisphere).

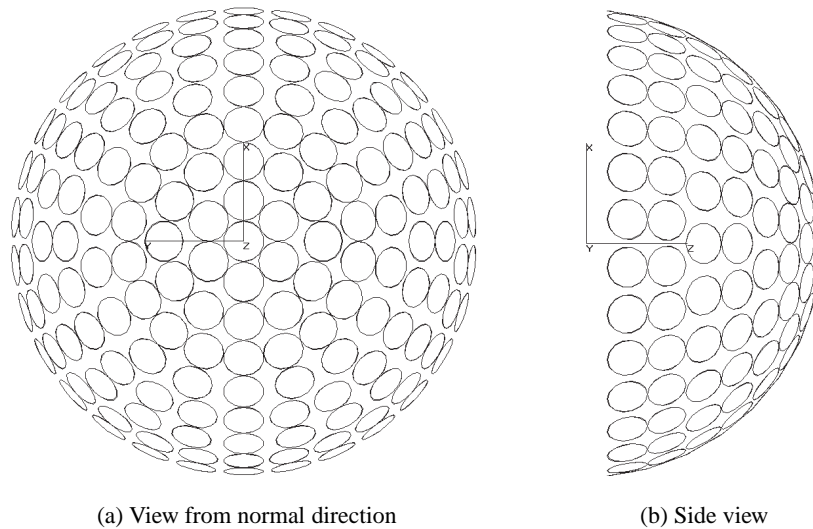


Figure B.4: Subdivision of the incident hemisphere (sky dome) into 163 sectors of 10° opening.

If in the future an exact match between investigations in transmission and reflection turns out to be necessary, a second projection screen and perforated metal sheet with 12 steps ellipses will be developed.

Reduced set with symmetries

For a sample presenting a well-known symmetry, the set of 145 (resp. 163) directions is reduced in a way described by Table B.6 (resp. B.7). These tables are separated into sections of backgrounds corresponding to the greyscale pattern appearing on Figure B.5.

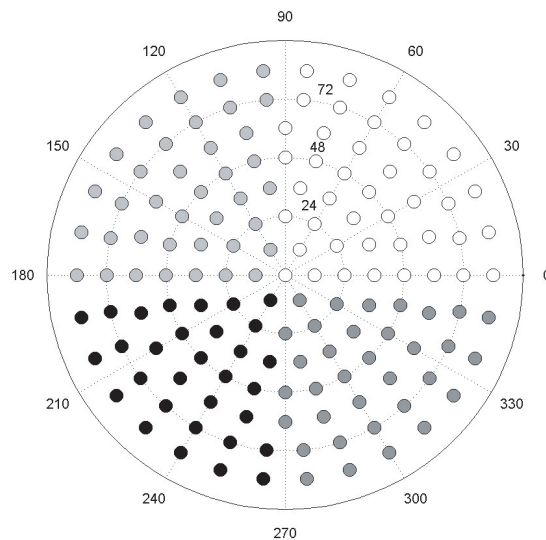


Figure B.5: Stereographic view of the 145 light incidence directions for BTDF measurements, with greyscale levels relating to the backgrounds of Figures B.6 (and similarly of Figure B.7).

θ_1	ϕ_1 -step	ϕ_1	Light incidents must be measured for:
0°	-	0°	All samples
12°	60°	0°, 60°	All samples
24°	30°	0°, 30°, 60°, 90°	All samples
36°	20°	0°, 20°, 40°, 60°, 80°	All samples
48°	15°	0°, 15°, 30°, 45°, 60°, 75°, 90°	All samples
60°	15°	0°, 15°, 30°, 45°, 60°, 75°, 90°	All samples
72°	12°	0°, 12°, 24°, 36°, 48°, 60°, 72°, 84°	All samples
84°	12°	0°, 12°, 24°, 36°, 48°, 60°, 72°, 84°	All samples
For rotational symmetry, only measurements for $\theta_1 = 0^\circ, 12^\circ, 24^\circ, 36^\circ, 48^\circ, 60^\circ, 72^\circ$ and 84° need to be done.			
Additional Measurements, if the sample is asymmetric to:			
12°	60°	120°, 180°	$\phi_1 = 90^\circ / 270^\circ$
24°	30°	120°, 150°, 180°	$\phi_1 = 90^\circ / 270^\circ$
36°	20°	100°, 120°, 140°, 160°, 180°	$\phi_1 = 90^\circ / 270^\circ$
48°	15°	105°, 120°, 135°, 150°, 165°, 180°	$\phi_1 = 90^\circ / 270^\circ$
60°	15°	105°, 120°, 135°, 150°, 165°, 180°	$\phi_1 = 90^\circ / 270^\circ$
72°	12°	96°, 108°, 120°, 132°, 144°, 156°, 168°, 180°	$\phi_1 = 90^\circ / 270^\circ$
84°	12°	96°, 108°, 120°, 132°, 144°, 156°, 168°, 180°	$\phi_1 = 90^\circ / 270^\circ$
12°	60°	300°	$\phi_1 = 0^\circ / 180^\circ$
24°	30°	270°, 300°, 330°	$\phi_1 = 0^\circ / 180^\circ$
36°	20°	280°, 300°, 320°, 340°	$\phi_1 = 0^\circ / 180^\circ$
48°	15°	270°, 285°, 300°, 315°, 330°, 345°	$\phi_1 = 0^\circ / 180^\circ$
60°	15°	270°, 285°, 300°, 315°, 330°, 345°	$\phi_1 = 0^\circ / 180^\circ$
72°	12°	276°, 288°, 300°, 312°, 324°, 336°, 348°	$\phi_1 = 0^\circ / 180^\circ$
84°	12°	276°, 288°, 300°, 312°, 324°, 336°, 348°	$\phi_1 = 0^\circ / 180^\circ$
12°	60°	240°	$\phi_1 = 0^\circ / 180^\circ$ and $\phi_1 = 90^\circ / 270^\circ$
24°	30°	210°, 240°	$\phi_1 = 0^\circ / 180^\circ$ and $\phi_1 = 90^\circ / 270^\circ$
36°	20°	200°, 220°, 240°, 260°	$\phi_1 = 0^\circ / 180^\circ$ and $\phi_1 = 90^\circ / 270^\circ$
48°	15°	195°, 210°, 225°, 240°, 255°	$\phi_1 = 0^\circ / 180^\circ$ and $\phi_1 = 90^\circ / 270^\circ$
60°	15°	195°, 210°, 225°, 240°, 255°	$\phi_1 = 0^\circ / 180^\circ$ and $\phi_1 = 90^\circ / 270^\circ$
72°	12°	192°, 204°, 216°, 228°, 240°, 252°, 264°	$\phi_1 = 0^\circ / 180^\circ$ and $\phi_1 = 90^\circ / 270^\circ$
84°	12°	192°, 204°, 216°, 228°, 240°, 252°, 264°	$\phi_1 = 0^\circ / 180^\circ$ and $\phi_1 = 90^\circ / 270^\circ$

Figure B.6: Incident directions based on the 145 sectors configuration for BTDF measurements, accounting for sample symmetries.

The symmetries that can be accounted for are of four different types:

- rotational symmetry, restricting the required incident directions to a single, arbitrary azimuth plane, chosen as the $\phi_1 = 0^\circ$ plane;
- axial symmetry along $\phi_1 = 0^\circ$ -180°;
- axial symmetry along $\phi_1 = 90^\circ$ -270°;
- axial symmetry along both $\phi_1 = 0^\circ$ -180° and 90° -270° (symmetry of order 4).

If the sample is specified symmetric according to one of these types, the incident directions set is automatically reduced consequently, as illustrated by Figure B.8(b).

θ_1	ϕ_1 -step	ϕ_1	Light incidents must be measured for:
0°	-	0°	All samples
10°	60°	0°, 60°	All samples
20°	30°	0°, 30°, 60°, 90°	All samples
30°	20°	0°, 20°, 40°, 60°, 80°	All samples
40°	20°	0°, 20°, 40°, 60°, 80°	All samples
50°	15°	0°, 15°, 30°, 45°, 60°, 75°, 90°	All samples
60°	15°	0°, 15°, 30°, 45°, 60°, 75°, 90°	All samples
70°	12°	0°, 12°, 24°, 36°, 48°, 60°, 72°, 84°	All samples
80°	12°	0°, 12°, 24°, 36°, 48°, 60°, 72°, 84°	All samples
For rotational symmetry, only measurements for $\theta_1 = 0^\circ, 10^\circ, 20^\circ, 30^\circ, 40^\circ, 50^\circ, 60^\circ, 70^\circ$ and 80° need to be done.			
Additional Measurements, if the sample is asymmetric to:			
10°	60°	120°, 180°	$\phi_1 = 90^\circ / 270^\circ$
20°	30°	120°, 150°, 180°	$\phi_1 = 90^\circ / 270^\circ$
30°	20°	100°, 120°, 140°, 160°, 180°	$\phi_1 = 90^\circ / 270^\circ$
40°	20°	100°, 120°, 140°, 160°, 180°	$\phi_1 = 90^\circ / 270^\circ$
50°	15°	105°, 120°, 135°, 150°, 165°, 180°	$\phi_1 = 90^\circ / 270^\circ$
60°	15°	105°, 120°, 135°, 150°, 165°, 180°	$\phi_1 = 90^\circ / 270^\circ$
70°	12°	96°, 108°, 120°, 132°, 144°, 156°, 168°, 180°	$\phi_1 = 90^\circ / 270^\circ$
80°	12°	96°, 108°, 120°, 132°, 144°, 156°, 168°, 180°	$\phi_1 = 90^\circ / 270^\circ$
10°	60°	300°	$\phi_1 = 0^\circ / 180^\circ$
20°	30°	270°, 300°, 330°	$\phi_1 = 0^\circ / 180^\circ$
30°	20°	280°, 300°, 320°, 340°	$\phi_1 = 0^\circ / 180^\circ$
40°	20°	280°, 300°, 320°, 340°	$\phi_1 = 0^\circ / 180^\circ$
50°	15°	270°, 285°, 300°, 315°, 330°, 345°	$\phi_1 = 0^\circ / 180^\circ$
60°	15°	270°, 285°, 300°, 315°, 330°, 345°	$\phi_1 = 0^\circ / 180^\circ$
70°	12°	276°, 288°, 300°, 312°, 324°, 336°, 348°	$\phi_1 = 0^\circ / 180^\circ$
80°	12°	276°, 288°, 300°, 312°, 324°, 336°, 348°	$\phi_1 = 0^\circ / 180^\circ$
10°	60°	240°	$\phi_1 = 0^\circ / 180^\circ$ and $\phi_1 = 90^\circ / 270^\circ$
20°	30°	210°, 240°	$\phi_1 = 0^\circ / 180^\circ$ and $\phi_1 = 90^\circ / 270^\circ$
30°	20°	200°, 220°, 240°, 260°	$\phi_1 = 0^\circ / 180^\circ$ and $\phi_1 = 90^\circ / 270^\circ$
40°	20°	200°, 220°, 240°, 260°	$\phi_1 = 0^\circ / 180^\circ$ and $\phi_1 = 90^\circ / 270^\circ$
50°	15°	195°, 210°, 225°, 240°, 255°	$\phi_1 = 0^\circ / 180^\circ$ and $\phi_1 = 90^\circ / 270^\circ$
60°	15°	195°, 210°, 225°, 240°, 255°	$\phi_1 = 0^\circ / 180^\circ$ and $\phi_1 = 90^\circ / 270^\circ$
70°	12°	192°, 204°, 216°, 228°, 240°, 252°, 264°	$\phi_1 = 0^\circ / 180^\circ$ and $\phi_1 = 90^\circ / 270^\circ$
80°	12°	192°, 204°, 216°, 228°, 240°, 252°, 264°	$\phi_1 = 0^\circ / 180^\circ$ and $\phi_1 = 90^\circ / 270^\circ$

Figure B.7: Incident directions based on the 163 sectors configuration for BRDF measurements, accounting for sample symmetries.

Exploration according to polar angles

The different options available for an exploration based on polar angles are illustrated on Figures B.2(b) to B.2(d).

For the first two options, the starting and ending values of θ_1 and ϕ_1 as well as their respective steps $\Delta\theta_1$ and $\Delta\phi_1$ (only $(\Delta)\theta_1$ for the second option) can be defined with the corresponding text boxes appearing on the left-hand side of the interface. The C planes are selected by clicking on the stereographic view.

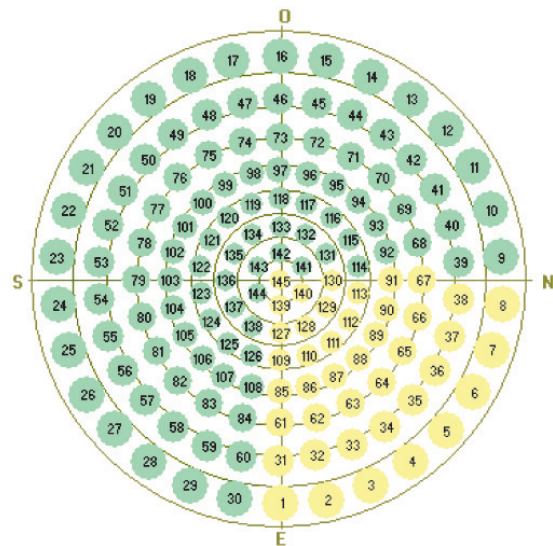
When clicking on the “nouvelle” command button for the third option, a window pops-up where any set of (θ_1, ϕ_1) directions can be chosen.

B.1.2 Sample properties

The sample characteristics are registered thanks to the window shown on Figure B.8(a), that appears at the beginning of a characterization. They will be reported in the final BT(R)DF data file (see Section B.2.1).

Naming the sample is mandatory, as well as providing the thickness of the latter and the diameter of the diaphragm chosen to restrict its illuminated area, that will be corrected in the data processing according to Section 4.3.1; in addition to this, the sample manufacturer and known symmetries can be specified, and additional comments can be added.

(a) Sample properties window



(b) Reduction of incident directions set according to sample symmetry

Figure B.8: Sample characteristics and known symmetries.

B.1.3 Emergence parameters

Screen positions

Generally, an investigation at all six screen positions is preferable to allow a full knowledge of the transmission or reflection properties of the characterized material.

At calibration or testing stages, however, or to reduce the measurement time when the emergence features are known to be restricted to only certain hemisphere portions, specific screen positions can be selected individually either by mouse-clicking on their orthogonal projection or by checking the corresponding numbers on the left-hand side of the interface.

Averaging grid resolution

The averaging grid intervals $\Delta\theta_2$ and $\Delta\phi_2$ are to be chosen according to the sample illuminated area for a consistent BT(R)DF assessment. These intervals are determined by the user thanks to Input boxes that appear right after the sample properties are defined.

The optimal values for $\Delta\theta_2$ and $\Delta\phi_2$ are proposed by default in these Input boxes, as well as limits within which these values should remain. In altitude, the possible averaging intervals range from 0.5° to 90° with a minimal increment of 0.1° ; in azimuth, only divisors of 60° between 1° and 60° are allowed, with a minimal increment of 0.5° .

The determination of the optimal intervals $\Delta\theta_2$ and $\Delta\phi_2$ is based on several criteria that cannot be fulfilled altogether, leading to a necessity of compromises.

The most important requirement is to verify Equation (5.17) in Section 5.4.2, especially if the emerging light distribution presents a significant regular (specular) component.

On the other hand, the illuminated area A has to be considered as a point compared to the observation distance d with the BT(R)DF formalism. As the distance from the sample to a given point on the screen is fixed, an increase in A must be coupled to larger averaging sectors ($\Delta\theta_2$, $\Delta\phi_2$) in order to compensate the growing divergence of emitted rays that can reach this same point (see Equations (6.3) and (6.4) in Section 6.1.2). $\Delta\theta_2$ and $\Delta\phi_2$ should at the same time respect a certain interdependence (no fine resolution in altitude combined to a coarse one in azimuth, or vice-versa).

In addition to this, the illuminated diameter of the sample should be significantly larger than its thickness to avoid edge effects (and the physical sample itself larger than the diaphragm aperture for the same reasons). The sample thickness is here understood in a large sense, as well applied for the slats inclination of a venetian blind as for a compact sample.

B.2 BT(R)DF assessment deliverables

Once the exploration parameters are fully defined in both incidence and emergence, the characterization process is started by clicking on “Caractérisation en transmission / réflexion”, and the sequence of actions described in Section 5.1.2 takes place. If the image capture option is checked, the Image-Pro Plus[®] program is automatically launched if not yet open.

Several tests are first applied on the incidence and emergence parameters: at least one incident direction and one screen position must be selected, the starting and ending points for θ_1 and ϕ_1 must suit the chosen angular steps $\Delta\theta_1$ and $\Delta\phi_1$, 10° steps (or multiples of 10°) must be guaranteed in altitude in reflection mode, the chosen averaging intervals $\Delta\theta_2$ and $\Delta\phi_2$ must match the restrictions given in Section B.1.3.

If the sample name was used before, a warning message appears to ask for a deletion or keeping of the prior measurements; in the second case, a consistency in the chosen diameter and averaging grid is checked.

The necessary new averaging grids are constructed via a DDE protocol with Matlab[®]. Simple instructions intended for the user appear explicitly in a sequence of message windows during this process.

The measurement procedure itself is then started. Files containing the list of positions to be reached by the different motorized axes are created to be read in loop sequences.

At each axis movement, the graphical interface is actualized for the measurement process to be followed easily:

- coloring of incident vault sectors (yellow = still to be investigated, red = currently investigated, green = already investigated) or positioning of circular patch on the stereographic view (if the C planes option is selected, the latter follow the same coloring convention as the vault sectors);
- in emergence, a similar coloring convention is applied at each new screen position: blue = still to be investigated for the current incident direction, red = currently investigated, green = already investigated, grey = not selected;
- as illustrated in Figure 5.1(b), when a screen cover is removed to let the incident beam pass through in reflection mode, the corresponding screen patch on the graphical interface turns orange; likewise, when the synthetic strip opens the passage through one of the metal sheet ellipses, the corresponding ellipse on the interface turns yellow;
- on the opened Image-Pro Plus[®] window, the progressive creation of the recomposed image can be observed.

B.2.1 Format of BT(R)DF data files

The achieved BTDF or BRDF dataset is saved in ASCII format on an electronic file denominated after the sample name and including the institute's designation as well as the considered incident direction. This leads to BTDF files named after `lesoT_SampleName_θ1-φ1.txt` and BRDF files named after `lesoR_SampleName_θ1-φ1.txt`.

These files contain the following data, in agreement with the common format for bidirectional measurements defined within Task 21 of the International Energy Agency (2000):

- the sample characteristics: name, manufacturer, measurement type (transmission or reflection), symmetry indicator, area, thickness, additional comments, date of measurement and institute denomination;
- the measurement parameters: incident direction (θ_1, ϕ_1) , averaging grid intervals $(\Delta\theta_2, \Delta\phi_2)$, limit altitude $\theta_{2\text{lim}}$;
- the directional-hemispherical light transmittance or reflectance τ_{th} or $\rho_{\text{th}}(\theta_1, \phi_1)$, based on Equation (6.12);
- the *BTDF* or *BRDF* values, expressed in $\text{Cd}\cdot\text{m}^{-2}\cdot\text{luxe}^{-1}$ and associated to the regular set of emerging directions (θ_2, ϕ_2) (the triplets $\phi_2, \theta_2, BT(R)DF$ are given in three columns separated by a tab character of ASCII code 9); for BRDF files, the angular sectors corresponding to the blind area around the incident direction will be associated to *NaN* values (Not a Number).

The angular co-ordinates (θ_1, ϕ_1) and (θ_2, ϕ_2) of the final file follow the format and sample orientation convention described in Figure A.5.

However, in order to avoid any confusion between BTDF and BRDF datasets, the altitude angle appearing in the file is defined as the angle between the normal to the sample on the incident interface and the emerging light flux direction; it remains therefore equal to θ_2 in reflection (comprised between 0° and 90°), but becomes equal to $180^\circ - \theta_2$ in transmission (comprised between 90° and 180°). No additional convention is needed for ϕ_1 and ϕ_2 , comprised between 0° and 360° .

The graphical representations of BT(R)DFs (and more specifically the sections views, only figures where altitude angles appear explicitly) are modified accordingly for consistency (see

Appendix C). For simplification reasons, real θ_2 angles were displayed in Sections 5.5.1 (Figure 5.17), 6.2.1 (Figure 6.2(a)) and 6.3.1 (Figure 6.6).

An example of file contents is given below for BTDF and BRDF values, which would be named “lesoT_Example_48_90.txt” and “lesoR_Example_50_90.txt” respectively.

BTDF measurements:

```
#material: Example
#manufacturer: Unknown
#measurement type: Transmission
#Isym = 0 ! symmetry indicator: 0 no symmetry (phi_1 = 0°...360°)
#
#           1 rotational symmetry (only for one phi_1)
#           2 symmetry to phi=0° and phi=180° (phi_1 = 0°...180°)
#           3 symmetry to phi=90° and phi=270° (phi_1 = -90°...90°)
#           4 symmetry to phi=0° and phi=180° & to phi=90° and phi=270° (phi_1 = 0°...90°)
#considered area [cm2]: 78.54
#thickness [cm]: 2.65
#comments: additional comments about the sample or the characterisation parameters
#measurements done at the Solar Energy and Building Physics Laboratory, LESO-PB/EPFL
#measurements and processing by Marilyne Andersen
#date of measurement: 08.03.00
#contact marilyne.andersen@epfl.ch for details
#light incidence :
#phi_1: 90° (azimuth)
#theta_1: 48° (altitude)
#BTDF values averaged over output directions from (phi_2 - 2.5) to (phi_2 + 2.5) in azimuth
#and from (theta_2 - 2.5) to (theta_2 + 2.5) in altitude
#measurements not performed for theta_2 < 94.2
#light transmittance: 0.09
#light transmittance calculated from BTDF values, with extrapolated values for 90 < theta_2 < 94.2
#data
#phi_2 theta_2 BTDF
0    95    0.030
5    95    0.028
...  ...  ...
350  95    0.016
355  95    0.028
0    100   0.030
5    100   0.030

a.s.o.

355  175   0.048
0    180   0.052
END
```

BRDF measurements:

```

#material: Example
#manufacturer: Unknown
#measurement type: Reflection
#Isym = 0 ! symmetry indicator: 0 no symmetry (phi_1 = 0°...360°)
#
#           1 rotational symmetry (only for one phi_1)
#           2 symmetry to phi=0° and phi=180° (phi_1 = 0°...180°)
#           3 symmetry to phi=90° and phi=270° (phi_1 = -90°...90°)
#           4 symmetry to phi=0° and phi=180° & to phi=90° and phi=270° (phi_1 = 0°...90°)
#considered area [cm2]: 176.71
#thickness [cm]: 0
#comments: additional comments about the sample or the characterisation parameters
#measurements done at the Solar Energy and Building Physics Laboratory, LESO-PB/EPFL
#measurements and processing by Marilyne Andersen
#date of measurement: 08.03.03
#contact marilyne.andersen@epfl.ch for details
#light incidence :
#phi_1: 90° (azimuth)
#theta_1: 50° (altitude)
#BRDF values averaged over output directions from (phi_2 - 7.5) to (phi_2 + 7.5) in azimuth
#and from (theta_2 - 5.0) to (theta_2 + 5.0) in altitude
#blind zone around output direction (theta_2,phi_2) = (50,90), where BRDFs are put to NaN
#measurements not performed for theta_2 > 84.0
#light reflectance: 0.67
#light reflectance calculated from BRDF values, with extrapolated values for 84.0 < theta_2 < 90
#data
#phi_2 theta_2 BRDF
0      80      0.230
15     80      0.128
...    ...    ...
330    80      0.116
345    80      0.128
0      70      0.230
15     70      0.230

a.s.o.

60     50      0.241
75     50      NaN
90     50      NaN
105    50      NaN
120    50      0.269

a.s.o.

345    10      0.348
0      0       0.452
END

```

B.2.2 Recombined image and photometric solids

In addition to the final BT(R)DF text file, an integral view gathering the six calibrated screen images is provided in TIF format (see Section 5.3.3). To produce the graphical representations described in Section 5.5.1 from the numeric data file, a simple Visual Basic[®] interface was developed, shown in Figure B.9 and allowing to automate the construction or opening of the 3D figures by Matlab[®] for any selection of BT(R)DF files.

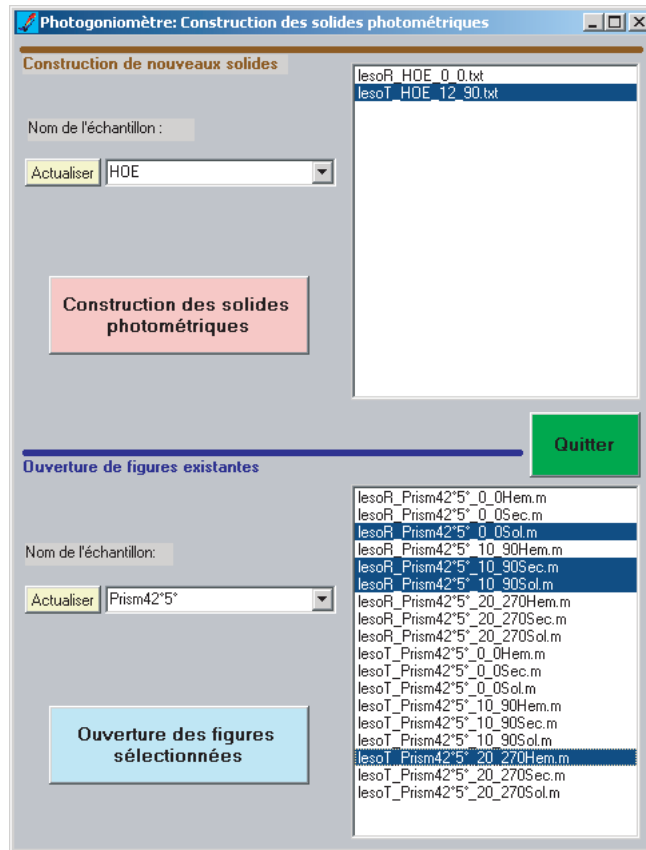


Figure B.9: Interface for an automated construction of the BT(R)DFs graphical representations.

Appendix C

List of BTDF and BRDF measurements

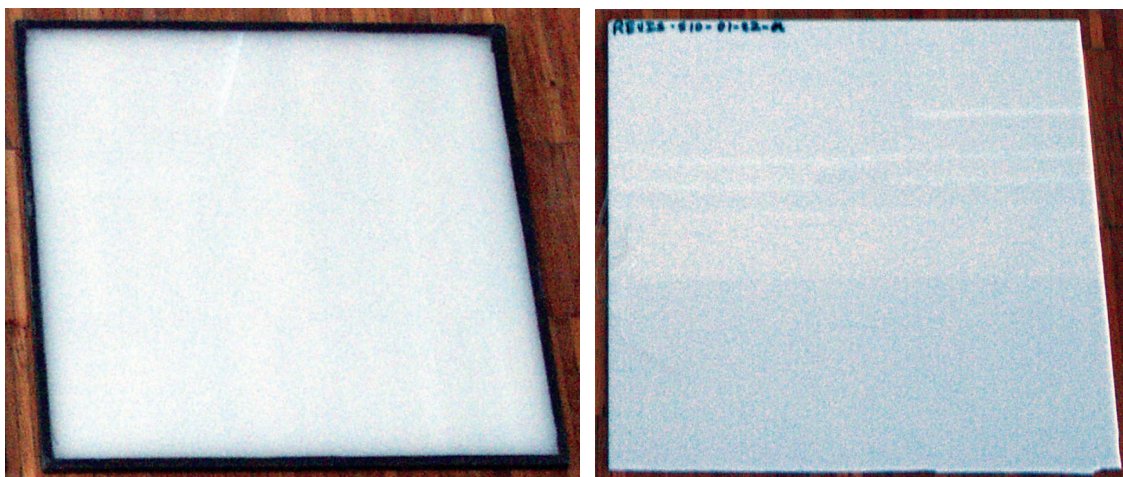
Bidirectional measurements were realized on a large number of complex glazings and shading devices with the present goniophotometer, both in transmission and reflection. The number of investigated incident directions varies from 3 to about 80 amongst the different systems. Some optical materials were characterized on both faces; most of the venetian blinds were analyzed with various slats tilt angles.

The illuminated areas were generally of diameter 10 or 15 cm, and the averaging grid intervals ($\Delta\theta_2$, $\Delta\phi_2$) equal either to $(5^\circ, 5^\circ)$, $(5^\circ, 15^\circ)$ or $(10^\circ, 15^\circ)$.

The achieved BTDF and BRDF measurements are listed in this appendix, the systems being gathered by type: diffusing, sunlight redirecting or prismatic materials, fabric and venetian blinds. For each group of similar systems within these different types, a detailed result is provided in the most appropriate graphical form.

C.1 Diffusing materials

Three diffusing samples were studied: pictures of the two opalescent materials characterized in transmission are shown in Figure C.1 (the one illustrated in Figure C.1(a) was also analyzed in reflection); the BRDF was determined for the diffusing white paint used for the detection screen. The BT(R)DF measurement details are given below for each material.



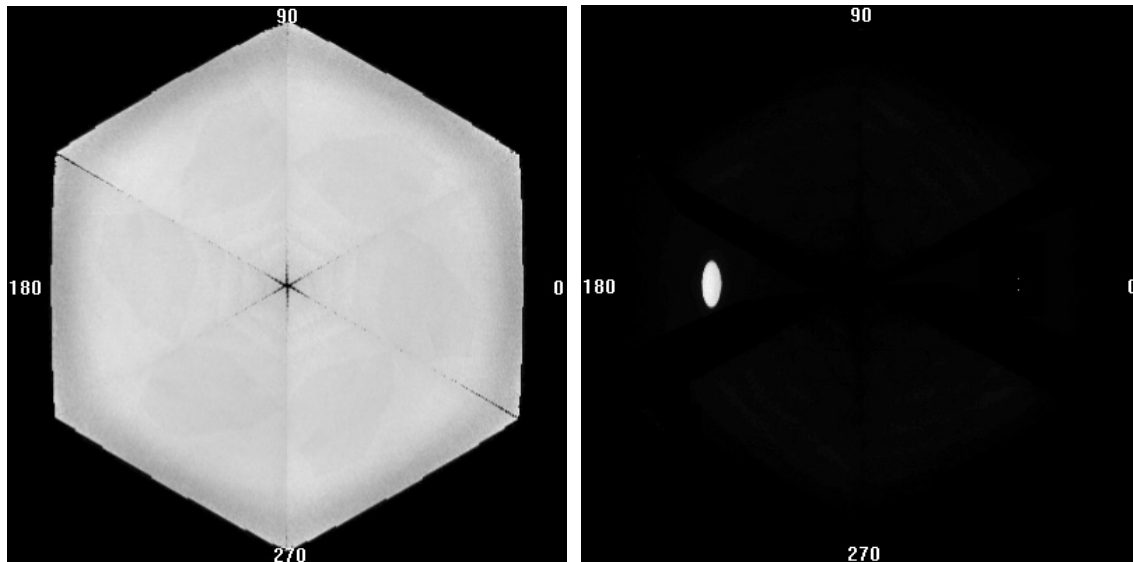
(a) White opalescent plexiglas

(b) White opalescent plastic

Figure C.1: Diffusing samples.

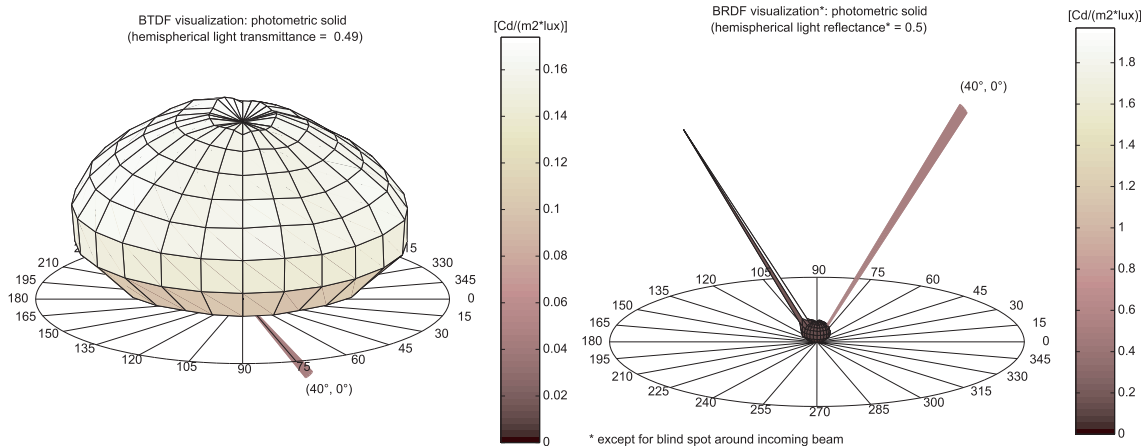
C.1.1 White opalescent plexiglas

The material is manufactured by Roehm. The sample thickness is equal to 6 mm. Its BTDF was determined every 10° and 12° in altitude along the 0° azimuth plane ($C0$ plane) (only one plane because of the rotational symmetry), with a $(10^\circ, 15^\circ)$ averaging grid and a diaphragm diameter of 20 cm. Its BRDF was determined every 20° in altitude along the $C0$ plane, for a 15 cm diameter and the same averaging grid. Examples of BT(R)DF data are displayed in Figure C.2.



(a) BTDF, recombined image

(b) BRDF, recombined image



(c) BTDF, photometric solid

(d) BRDF, photometric solid

Figure C.2: BTDF and BRDF representations for the white opalescent plexiglas for incidence $(\theta_1, \phi_1) = (40^\circ, 0^\circ)$.

C.1.2 White opalescent plastic

The white diffusing plastic material (2.5 mm thick) was characterized within the framework of the European project REVIS (van Dijk, 2001). Its BTDF was determined for incidences $(0^\circ, 0^\circ)$, $(30^\circ, 90^\circ)$ and $(60^\circ, 90^\circ)$, with a $(10^\circ, 15^\circ)$ averaging grid and a diaphragm diameter of 20 cm. Examples of BTDF data are shown in Figure C.3.

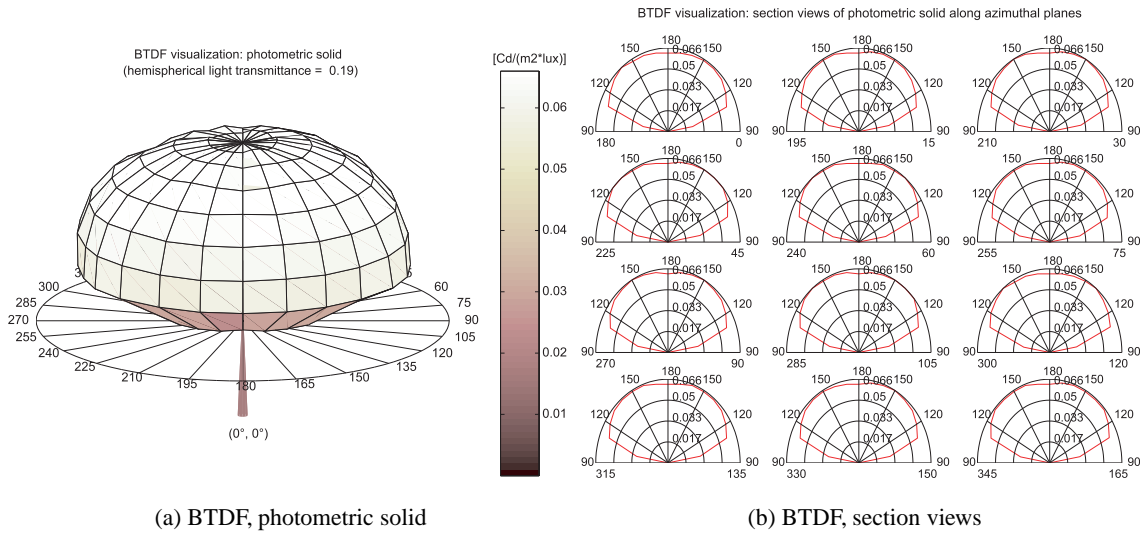


Figure C.3: BTDF representations for the white opalescent plastic for incidence $(\theta_1, \phi_1) = (0^\circ, 0^\circ)$.

C.1.3 Diffusing paint

The BRDF was determined for the LMT photometer paint for incidence $(10^\circ, 0^\circ)$ for validation purposes, with a $(5^\circ, 15^\circ)$ averaging grid and a diaphragm diameter of 15 cm. The resulting photometric solid is given in Figure C.4 with the corresponding section views along $C\phi$ planes.

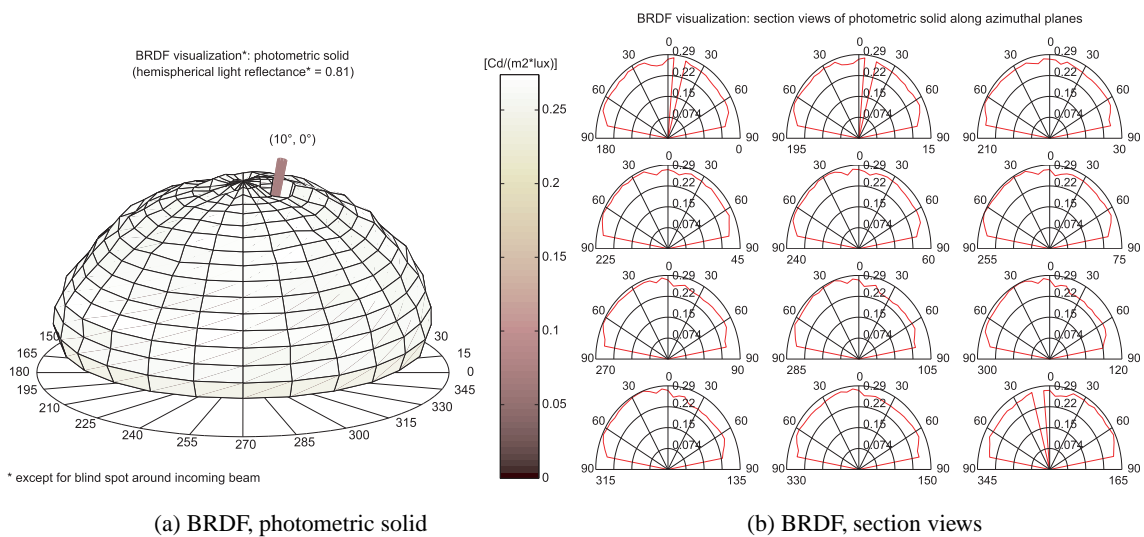


Figure C.4: BRDF representations for the LMT photometer paint covering the detection screen for incidence $(\theta_1, \phi_1) = (10^\circ, 0^\circ)$.

C.2 Sunlight redirecting systems

Four types of sunlight redirecting systems were studied: laser cut panels, a sun-directing glass, a holographic film and a combination of curved mirror squares. Their pictures are shown in Figure C.5.

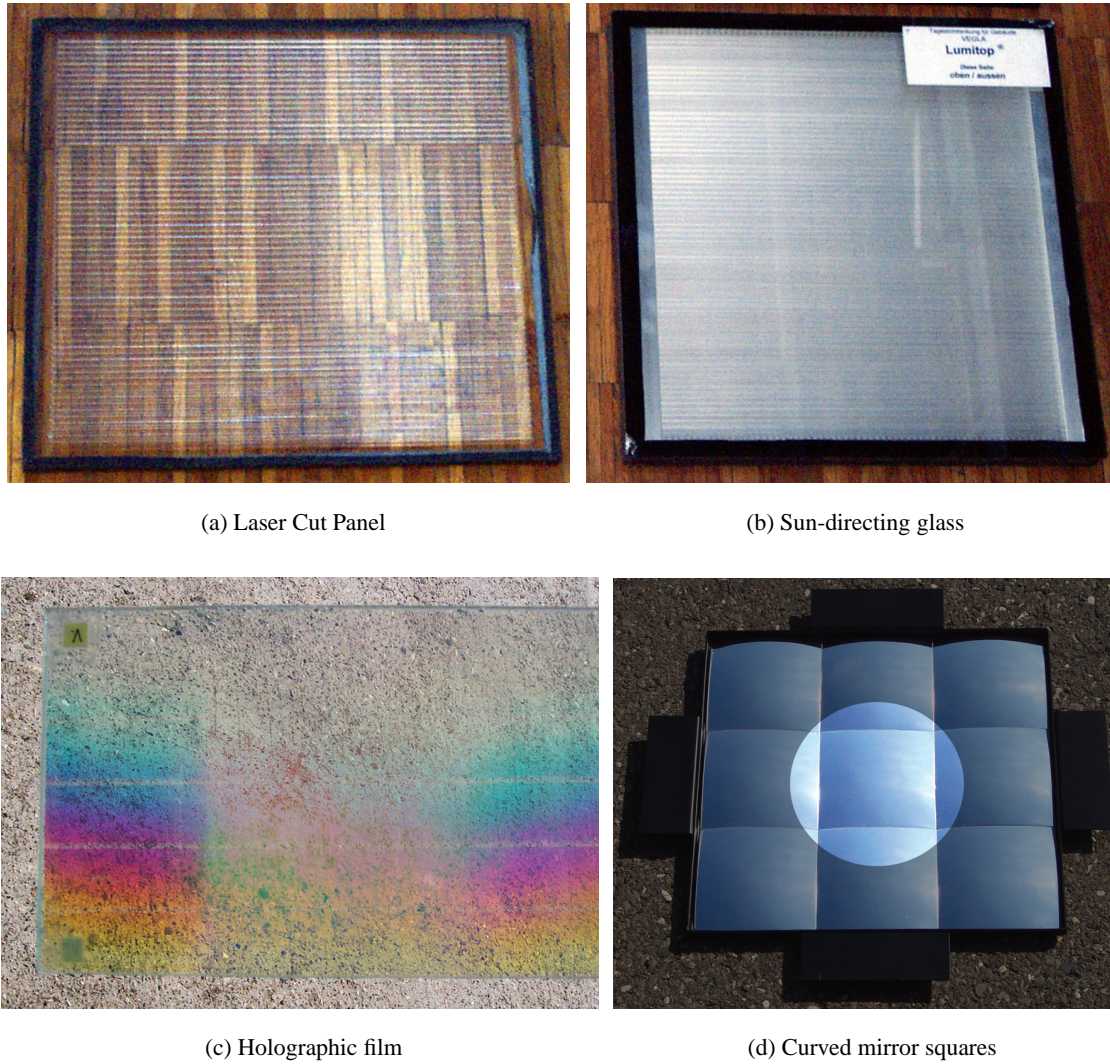


Figure C.5: Sunlight redirecting systems.

C.2.1 Laser Cut Panel

Two acrylic panels with parallel stripes were studied: the so-called laser cut panel (Edmonds, 1993), cut through the entire material (6 mm thick), and a similar sample of thickness 8 mm, whose cuts remain within the acrylic core.

The incident directions set for the first sample consisted of the 145 directions matching the sky vault subdivision by Tregenza (1987), in practice reduced to 42 thanks to the quadratic symmetry (see Section B.1.1), in addition to every 10° in altitude along azimuth planes $C0$ and $C90$.

For the second, incident directions every 12° along the $C90$ plane and every 30° along the $C270$ plane were considered, as well as a set of directions based on realistic sun positions at given times of the day: solar time 8h, 10h, 12h at spring/autumn equinox (March 21/September 21) and at summer and winter solstices (June 21 and December 21), for a South-oriented façade at latitude 47°N . This lead to the following polar angles (θ_1, ϕ_1) : $(43^\circ, 90^\circ)$, $(52^\circ, 50^\circ)$, $(69^\circ, 21^\circ)$, $(20^\circ, 90^\circ)$, $(31^\circ, 30^\circ)$, $(53^\circ, 1^\circ)$, $(66^\circ, 90^\circ)$, $(72^\circ, 61^\circ)$ and $(86^\circ, 37^\circ)$.

For both materials, the averaging grid intervals $(\Delta\theta_2, \Delta\phi_2)$ were equal to $(5^\circ, 5^\circ)$, and the diaphragm diameter 10 cm. Examples of BTDF data are given in Figure C.6.

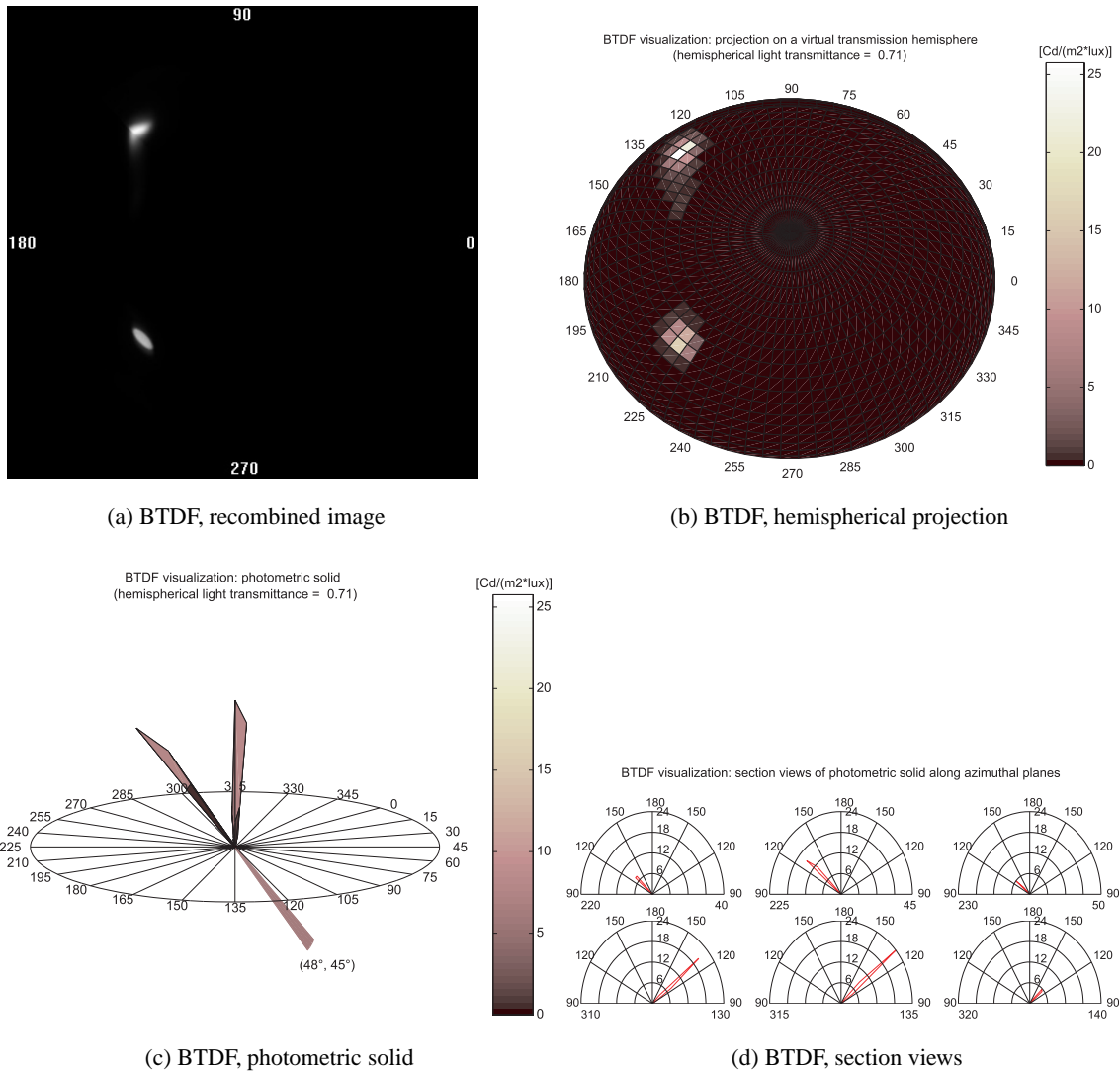


Figure C.6: BTDF representations for the laser cut panel for incidence $(\theta_1, \phi_1) = (48^\circ, 45^\circ)$.

C.2.2 Sun directing glass

The sun-directing glass, named “Lumitop™” is manufactured by Vegla. The sample thickness is equal to 25 mm. Its BTDF was determined according to the 145 default directions in transmission, reduced to 76 as it presents an axial symmetry along axis $\phi_1 = 90^\circ\text{-}270^\circ$. The averaging grid was $(5^\circ, 5^\circ)$, and the diaphragm diameter 10 cm. Examples of BTDF data are shown in Figure C.7.

C.2.3 Holographic film

The holographic film (or HOE for Holographical Optical Element) was placed within two glass layers, making up a 7 mm thick sample. This kind of glazing can be used either for a vertical opening, or for a 45° tilted orientation, in which case it must be rotated 180° .

In its vertical use, it was characterized in transmission according to the same set of incident directions as for the second acrylic panel with parallel cuts: every 12° along the $C90$ plane and every 30° along the $C270$ plane, in addition to the nine directions based on realistic sun positions: $(43^\circ, 90^\circ)$, $(52^\circ, 50^\circ)$, $(69^\circ, 21^\circ)$, $(20^\circ, 90^\circ)$, $(31^\circ, 30^\circ)$, $(53^\circ, 1^\circ)$, $(66^\circ, 90^\circ)$, $(72^\circ, 61^\circ)$ and $(86^\circ, 37^\circ)$.

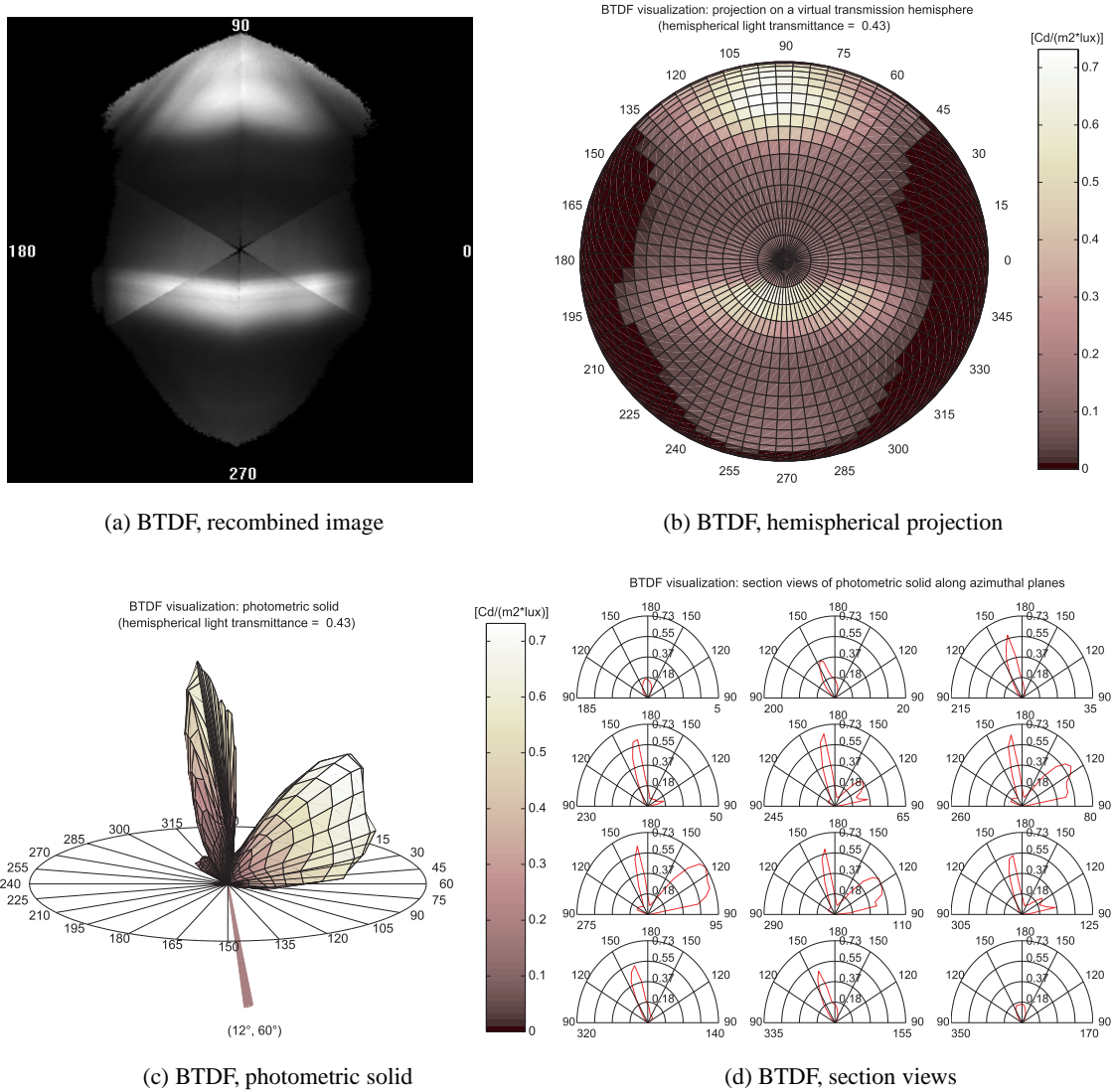


Figure C.7: BTDF representations for the sun-directing glass “Lumitop” for incidence $(\theta_1, \phi_1) = (12^\circ, 60^\circ)$.

This whole set of virtual sun positions (fictitious for the two “negative” positions $(30^\circ, 270^\circ)$ and $(60^\circ, 270^\circ)$) was kept for the 45° tilt configuration of the HOE, and the corresponding polar angles (θ_1, ϕ_1) for a 45° tilted façade deduced from Equation (C.1):

$$\begin{aligned} \theta_{1_{\text{HOE } 45^\circ}} &= \arccos(\cos \theta_1 \cdot \cos 45^\circ + \sin \theta_1 \cdot \sin \phi_1 \cdot \sin 45^\circ) \\ \phi_{1_{\text{HOE } 45^\circ}} &= \frac{\sin \theta_1 \cdot \sin \phi_1 \cdot \cos 45^\circ - \cos \theta_1 \cdot \sin 45^\circ}{\sin \theta_{1_{\text{HOE } 45^\circ}}} \end{aligned} \quad (\text{C.1})$$

This led to the following directions: $(45^\circ, 270^\circ)$, $(33^\circ, 270^\circ)$, $(21^\circ, 270^\circ)$, $(9^\circ, 270^\circ)$, $(3^\circ, 90^\circ)$, $(15^\circ, 90^\circ)$, $(27^\circ, 90^\circ)$, $(75^\circ, 270^\circ)$, $(2^\circ, 270^\circ)$, $(30^\circ, 359^\circ)$, $(25^\circ, 270^\circ)$, $(38^\circ, 316^\circ)$, $(64^\circ, 332^\circ)$, $(21^\circ, 90^\circ)$, $(36^\circ, 39^\circ)$ and $(62^\circ, 25^\circ)$.

The vertical configuration of the HOE was also analyzed according to the 145 default directions in transmission, reduced to 76 because of its axial symmetry along $\phi_1 = 90^\circ$ - 270° .

In addition to this, BTDF and BRDF measurements were performed every 30° in altitude along azimuth planes $C0$, $C45$ and $C90$.

The averaging grid was $(5^\circ, 5^\circ)$ for all BT(R)DF measurements, and the diaphragm diameter 10 cm. Examples of BT(R)DF data are shown in Figure C.8.

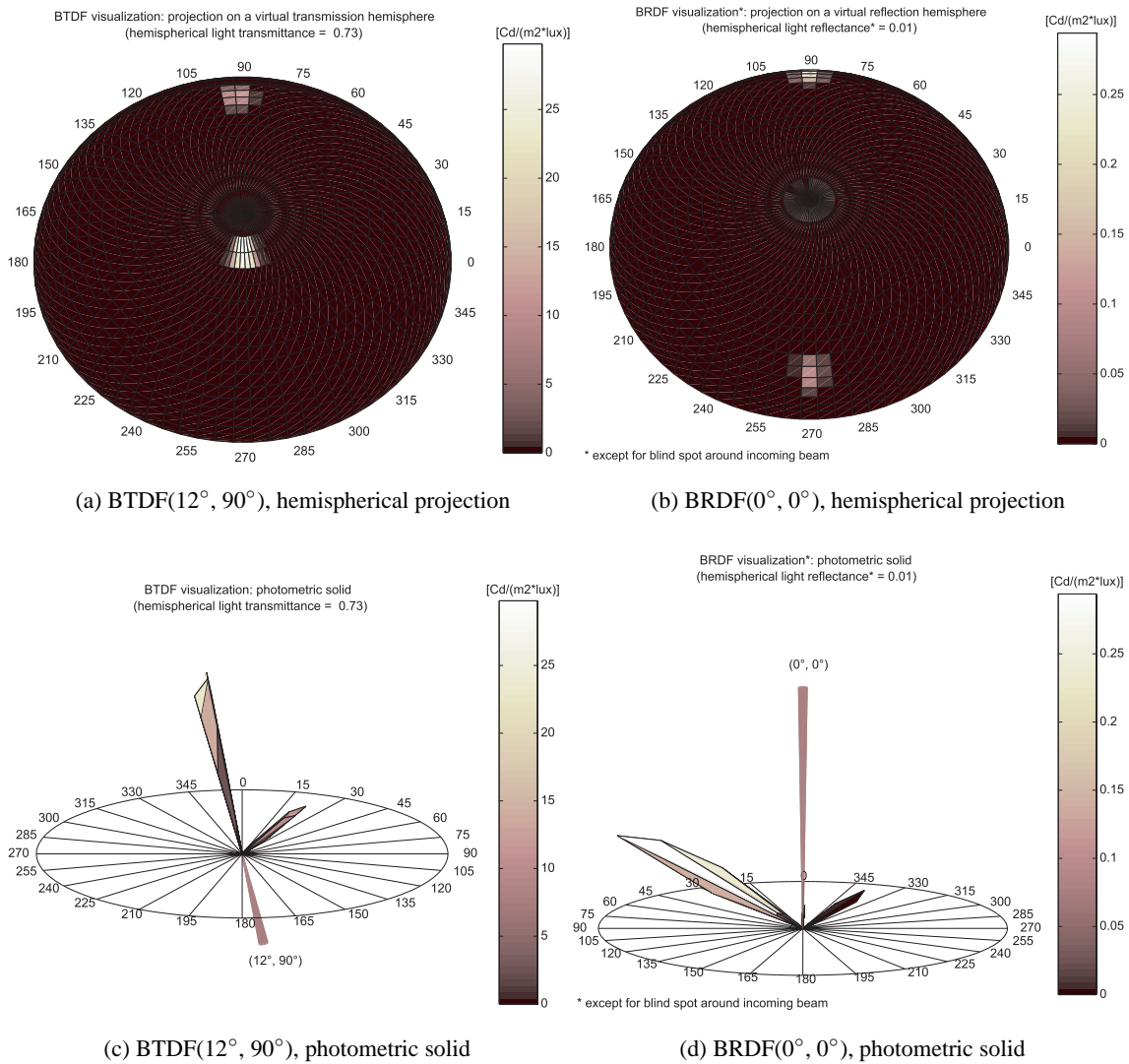


Figure C.8: BTDF and BRDF representations for the HOE for incidences $(\theta_1, \phi_1) = (12^\circ, 90^\circ)$ and $(0^\circ, 0^\circ)$ respectively.

C.2.4 Adjacent curved mirrors

The combination of curved mirror squares consists of nine adjacent elements, of dimensions 10×10 cm each and of 1 cm curvature amplitude. The illuminated area was restricted to a disk of diameter 15 cm centered on the central piece, as illustrated in Figure C.5(d).

BRDF measurements were realized every 10° in altitude along azimuth planes $C0$ and $C45$; two examples are shown on Figure C.9.

C.3 Prismatic panels

Two acrylic prismatic panels, presenting 45° and $42^\circ/5^\circ$ gratings respectively, were characterized in transmission, the second one being analyzed in reflection as well for a few incidences. An axonometric perspective is shown for both of them on Figures C.10(a) and C.10(b). In addition to this, an extensive set of BTDF measurements was performed on a prismatic film from 3M, illustrated in Figure C.10(c).

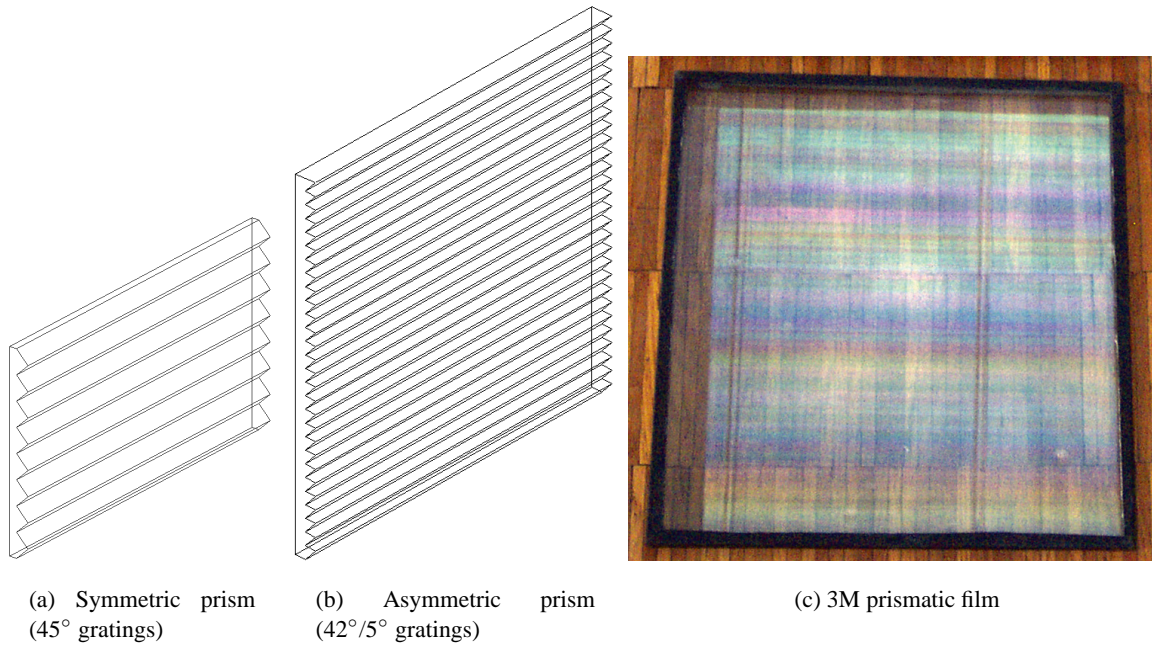


Figure C.10: Prismatic panels.

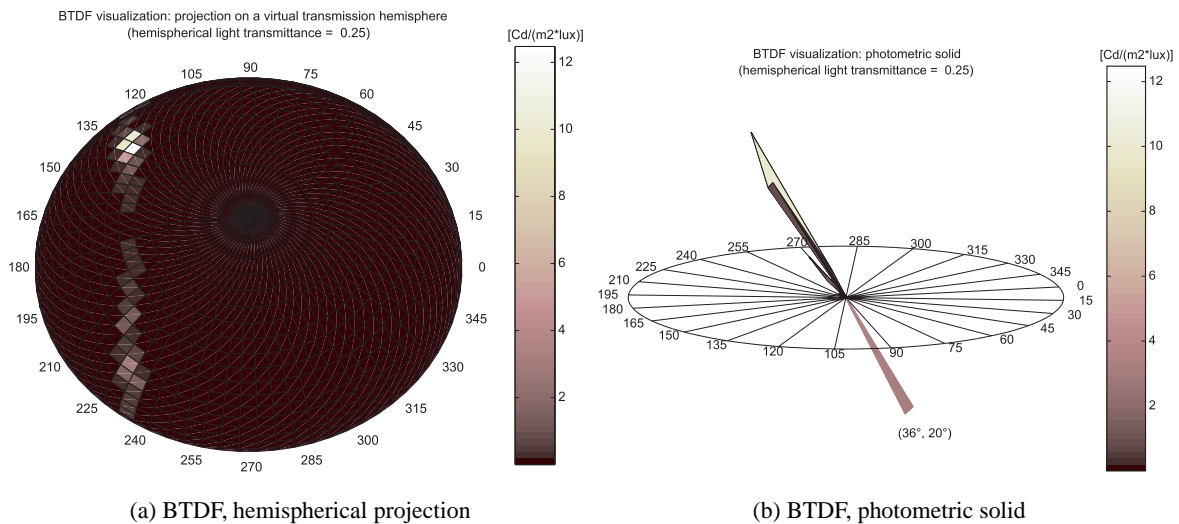


Figure C.11: BTDF representations for the symmetric prism (45° gratings, flat face on incident side) for incidence $(\theta_1, \phi_1) = (36^\circ, 20^\circ)$.

The asymmetric prism was characterized both in transmission and reflection with an illuminated diameter of 10 cm. Two configurations were studied: either flat side or $42^\circ/5^\circ$ gratings facing the incident light.

For the first configuration, the incident directions set for BTDF measurements consisted of the 76 directions based on the sky vault subdivision accounting for symmetry along axis $\phi_1 = 90^\circ - 270^\circ$, and of altitudes θ_1 every 20° along azimuth planes $C0, C90$ and $C270$. For BRDF measurements, the following set of directions was considered: $(0^\circ, 0^\circ), (0^\circ, 20^\circ), (10^\circ, 90^\circ), (40^\circ, 90^\circ)$ and $(20^\circ, 270^\circ)$. An example of resulting BTDF and BRDF for the same incident direction $(\theta_1, \phi_1) = (20^\circ, 0^\circ)$ is illustrated in Figure C.12.

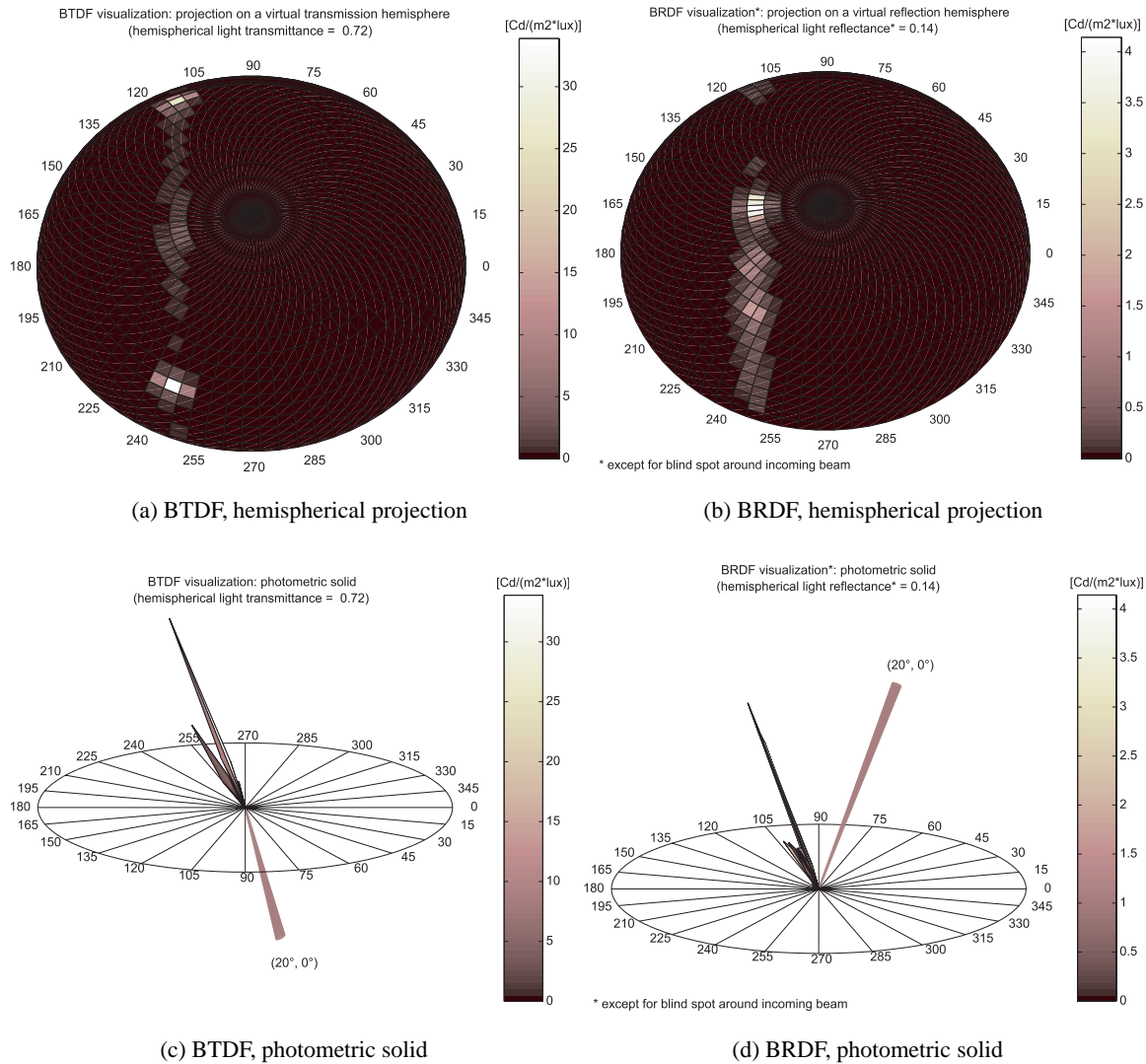


Figure C.12: BTDF and BRDF representations for the asymmetric prism ($42^\circ/5^\circ$ gratings, flat face on incident side) for incidence $(\theta_1, \phi_1) = (20^\circ, 0^\circ)$.

The second configuration, with gratings on the incident side, was analyzed in transmission every 10° in altitude along azimuth planes $C0$, $C90$ and $C270$ for a convenient comparison to integrating sphere data (see Section 6.4.2). Reflection measurements were performed for incident directions $(0^\circ, 0^\circ)$, $(10^\circ, 90^\circ)$ and $(20^\circ, 270^\circ)$. An example of resulting BTDF and BRDF for $(\theta_1, \phi_1) = (10^\circ, 90^\circ)$ is illustrated in Figure C.13.

C.3.2 3M prismatic film

A Scotch Optical Lighting Film (“SOLFTM” film) manufactured by 3M and applied on a 6 mm thick glass pane was characterized in transmission, with either the gratings or the flat face on the incident side.

The illuminated area was of diameter 10 cm and the averaging grid was $(5^\circ, 5^\circ)$. For both orientations of the sample, the incident directions set comprised the 42 directions matching the sky vault subdivision accounting for quadratic symmetry, in addition to every 10° in altitude along azimuth planes $C0$ and $C90$. Examples of BTDF data are shown in Figure C.14.

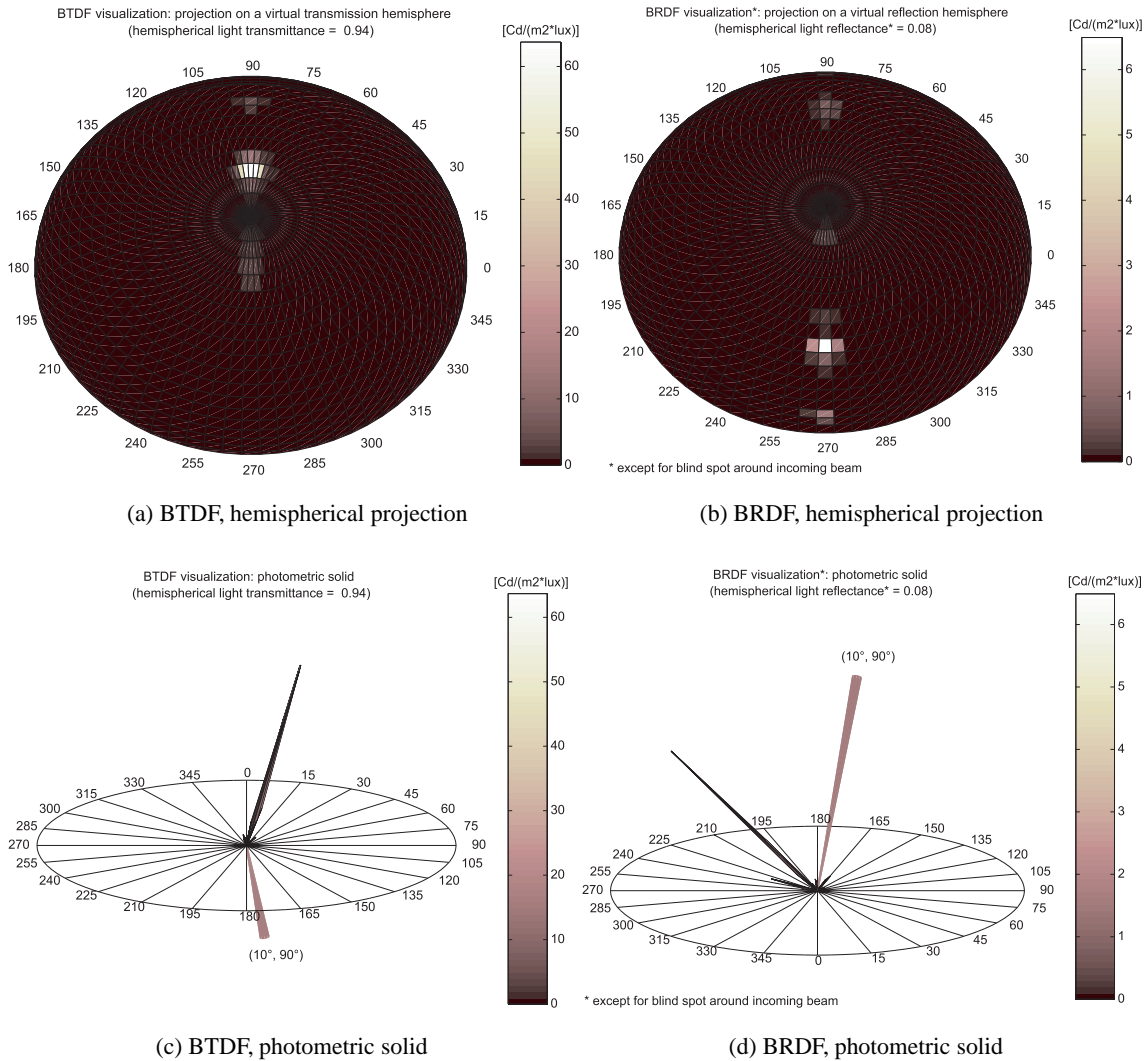


Figure C.13: BTDF and BRDF representations for the asymmetric prism ($42^\circ/5^\circ$ gratings on incident side) for incidence $(\theta_1, \phi_1) = (10^\circ, 90^\circ)$.

C.4 Fabric blinds

Ten types of fabric blinds were studied. Six were manufactured by Baumann-Hüppe AG; for each one of these, BTDF measurements were performed on two to five different models. The four others were analyzed within the European project REVIS (van Dijk, 2001), mainly in transmission as well. Their pictures and some BTDF data are provided in the next two sections.

C.4.1 Baumann-Hüppe prototypes

The Baumann-Hüppe's fabric blind prototypes were characterized at an early stage of calibration, in September 1999. The achieved BTDF data are therefore approximate values (assumed error of about 20%).

Incident directions were analyzed every 30° in altitude and along azimuth planes $C0$, $C90$ and $C270$. The averaging grid was $(10^\circ, 15^\circ)$ and the diaphragm diameter 17 cm (former sample holder). The different fabric blind models, illustrated in Figures C.15(a)(b) to C.17(a)(b), are listed below, gathered by type; the resulting BTDF for incidence $(30^\circ, 0^\circ)$ is provided for each of the six types in the hemispherical projection graphical form.

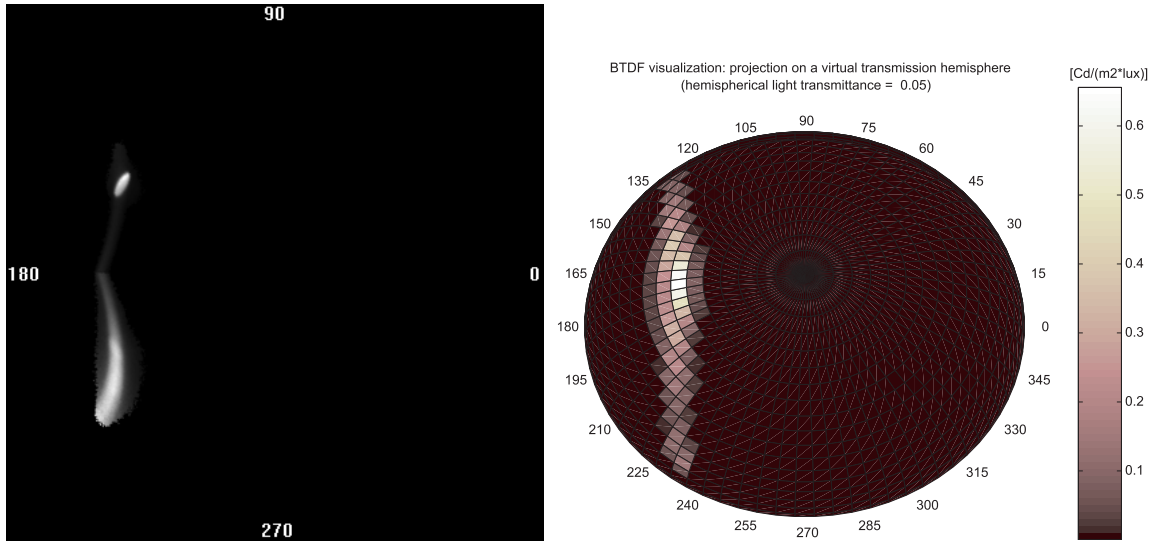
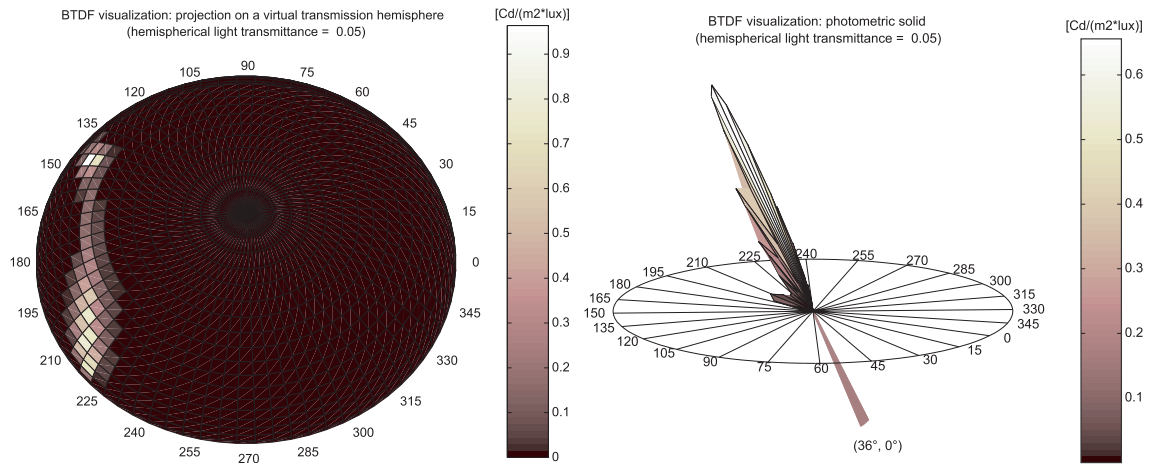
(a) BTDF($60^\circ, 30^\circ$) gratings out, recombined image(b) BTDF($36^\circ, 0^\circ$) gratings in, hemispherical projection(c) BTDF($60^\circ, 30^\circ$) gratings out, photometric solid(d) BTDF($36^\circ, 0^\circ$) gratings in, photometric solid

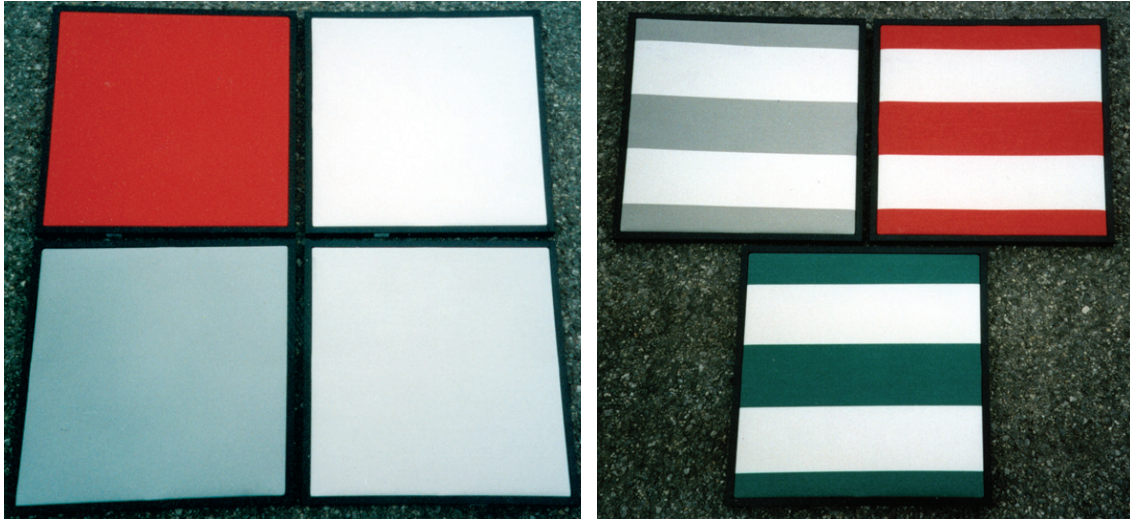
Figure C.14: BTDF representations for the 3M prismatic film for incidences $(\theta_1, \phi_1) = (60^\circ, 30^\circ)$ (gratings on incident side) and $(36^\circ, 0^\circ)$ (flat face on incident side).

Fabric blind type DOLAN (Figures C.15(a) and C.15(c)):

- DOLAN 1111, red
- DOLAN 1127, white
- DOLAN 1128, silver grey
- DOLAN 1134, pearl grey

Fabric blind type DOLAN DUO COLOR, with colored stripes (Figures C.15(b) and C.15(d)):

- DOLAN DUO COLOR 1234, silver / white
- DOLAN DUO COLOR 1245, cherry / white
- DOLAN DUO COLOR 1247, green / white



(a) DOLAN models

(b) DOLAN DUO COLOR models

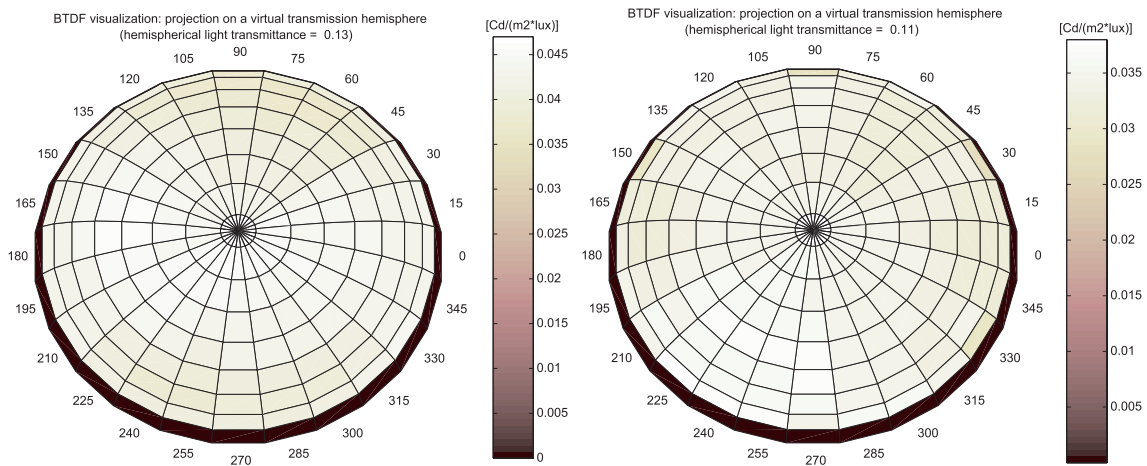
(c) BTDF($30^\circ, 0^\circ$) for DOLAN, hemispherical projection(d) BTDF($30^\circ, 0^\circ$) for DOLAN DUO COLOR, hemispherical projection

Figure C.15: DOLAN and DOLAN DUO COLOR models: picture and BTDF representation for incidence $\theta_1, \phi_1 = (30^\circ, 0^\circ)$.

Fabric blind type PANAMA (Figures C.16(a) and C.16(c)):

- PANAMA 4201, paloma (white)
- PANAMA 4205, strada (pearl grey)

Fabric blind type PLISSEE, pleated (Figures C.16(b) and C.16(d)):

- PLISSEE 1109, standard, semi-transparent (mat silver grey)
- PLISSEE 3014, coating of vaporised aluminium, semi-transparent (shiny pearl grey)
- PLISSEE 3141, standard, not transparent (shiny silver grey)
- PLISSEE 4041, coating of vaporised aluminium, not transparent (shiny pearl grey)
- PLISSEE 4042, coating of vaporised aluminium, opaque (shiny pearl grey)

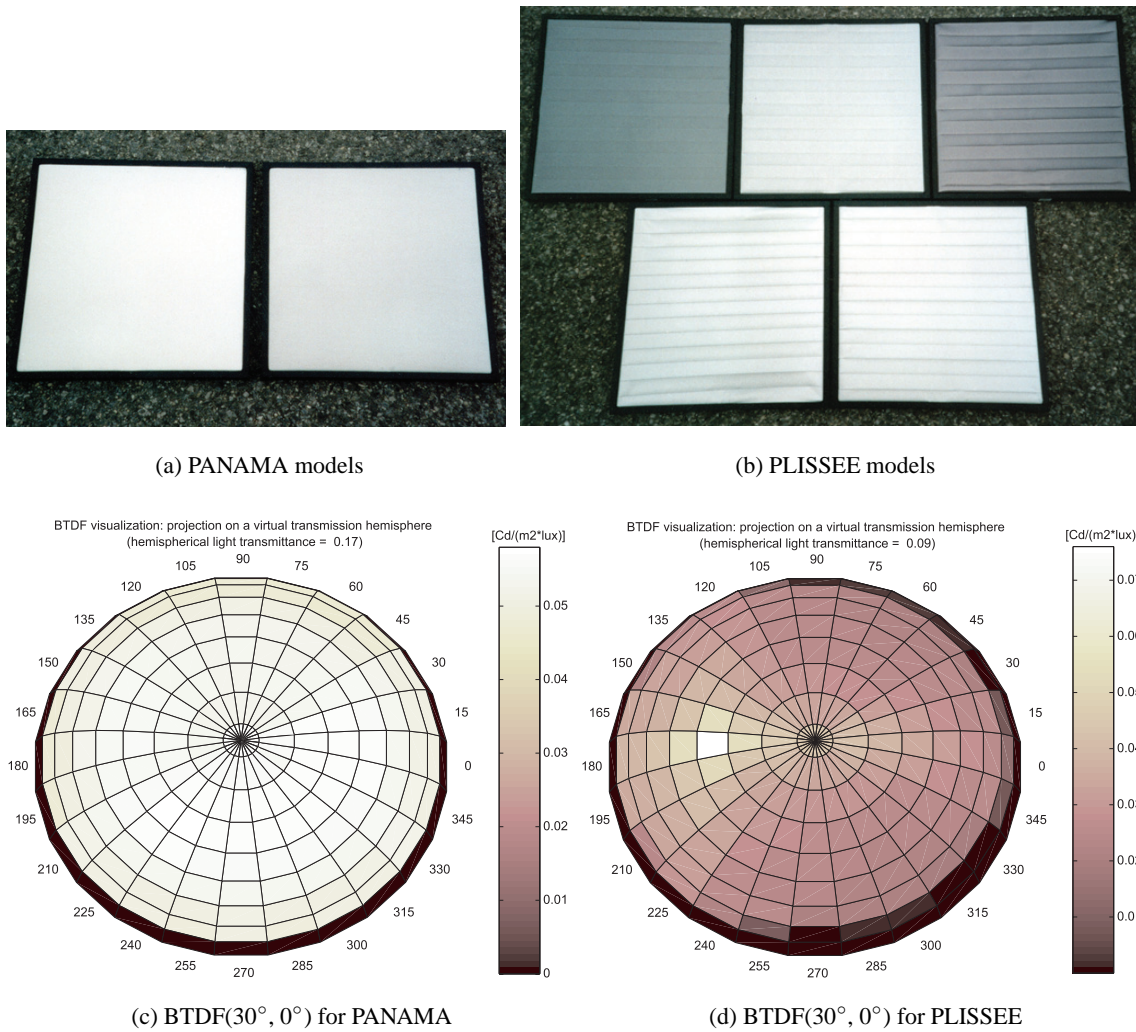


Figure C.16: PANAMA and PLISSEE models: picture and BTDF representation (hemispherical projection) for incidence $\theta_1, \phi_1 = (30^\circ, 0^\circ)$.

Fabric blind type ROLLO, thick (Figures C.17(a) and C.17(c)):

- ROLLO 7520, coating of vaporised aluminium (grey)
- ROLLO 9451, coating of vaporised aluminium, opaque (pearl grey)
- ROLLO 9563, foil (dark grey)

Fabric blind type SHADOW, hatched with colored stripes (Figures C.17(b) and C.17(d)):

- SHADOW 4120, mirabel / white
- SHADOW 4123, grey / white

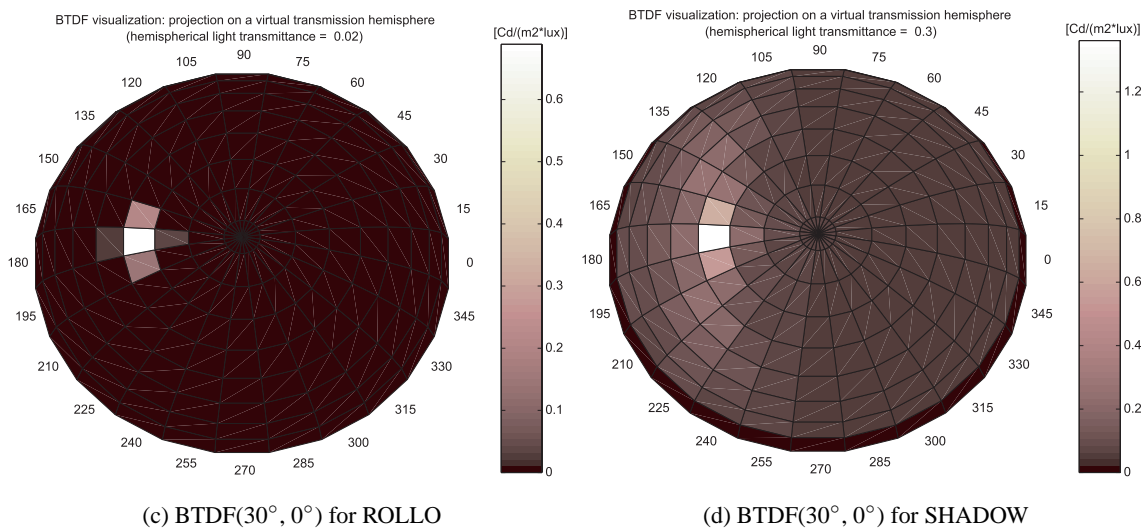
C.4.2 Fabric blinds with reflective coating

All four solar shading fabrics studied within the framework of the REVIS project (van Dijk, 2001) and manufactured by Verosol present a shiny grey front side (towards incident light), as shown by Figure C.18(a). Their inner side, illustrated in Figure C.18(b), varies in appearance from one fabric type to the other.



(a) ROLLO models

(b) SHADOW models



(c) BTDF(30°, 0°) for ROLLO

(d) BTDF(30°, 0°) for SHADOW

Figure C.17: ROLLO and SHADOW models: picture and BTDF representation (hemispherical projection) for incidence $\theta_1, \phi_1 = (30^\circ, 0^\circ)$.

These materials were characterized in transmission every 30° in altitude along the azimuth plane $C90$, with an averaging grid ($10^\circ, 15^\circ$) and a diaphragm diameter of 20 cm.

The four types of fabrics, used as a flat or roller blinds, are named by numbers:

- S06- is transparent, shiny grey on its external side, soft and sparkling steel grey (316/00) on its inner side;
- S07- is semi-transparent, very shiny grey on its external side, bright red (312/359) on its inner side; it was characterized both in transmission and reflection according to the three mentioned incident directions, for the same ($10^\circ, 15^\circ$) averaging grid and for illuminated areas of diameter 15 cm and 20 cm; an example of BT(R)DF result is given in Figure C.19 for incidence ($30^\circ, 90^\circ$);

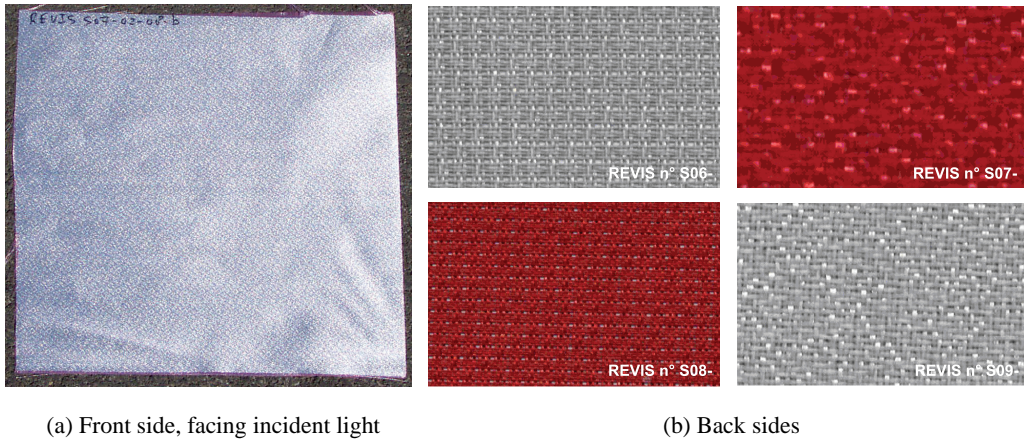


Figure C.18: Verosol[®] solar shading fabric samples.

- S08- is transparent, shiny grey on its external side, soft red (816/278) on its inner side;
- S09- is semi-transparent, very shiny grey on its external side, soft light steel grey (312/000) on its inner side.

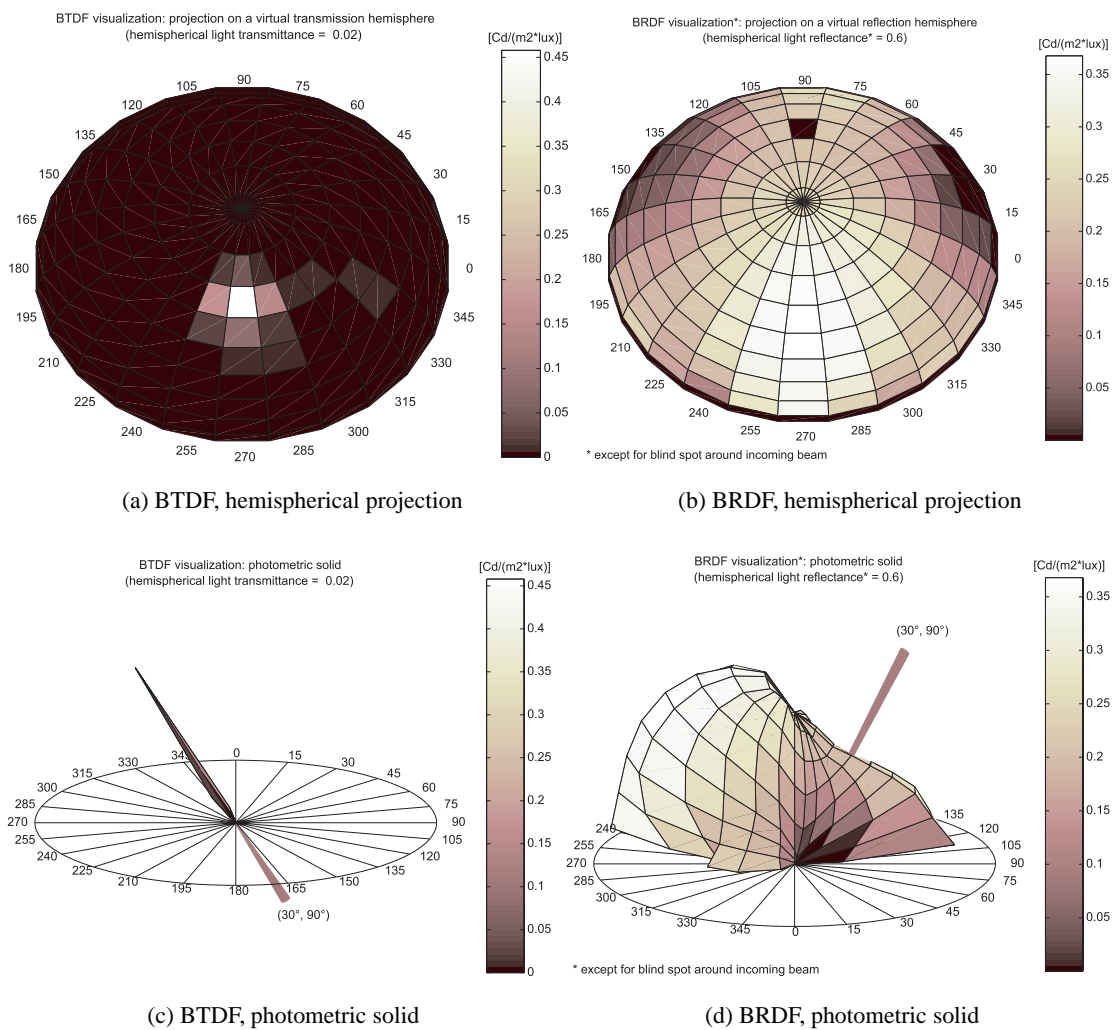


Figure C.19: BTDF and BRDF for the S07- fabric for incidence $(\theta_1, \phi_1) = (30^\circ, 90^\circ)$.

C.5 Venetian blinds

Four major types of venetian blinds (mainly manufactured by Baumann-Hüppe AG) were analyzed, amongst which up to nine different models were considered: mirror slats between glass layers (“OKASolarTM” prototype on Figure C.20(a)), mirror slats half, entirely or not perforated (Figures C.20(a) and C.20(c)), blinds with special slats shape and coating (Köster blinds, see Figures C.20(d) and C.20(e)) and four different painted metallic blinds (Figure C.20(f)).



Figure C.20: Different models of venetian blind prototypes.

For each model, BTDF measurements were performed for one or several slats configurations, detailed below. Except for the metallic slats, the incident directions set was defined as follows:

- a solar time based set of incidences was determined for an arbitrary south-oriented façade at latitude 47°N and the same dates and times as for the laser cut panel and the holographic film (Sections C.2.1 and C.2.3), leading to polar angles (θ_1, ϕ_1) equal to: $(43^\circ, 90^\circ)$, $(52^\circ, 50^\circ)$, $(69^\circ, 21^\circ)$, $(20^\circ, 90^\circ)$, $(31^\circ, 30^\circ)$, $(53^\circ, 1^\circ)$, $(66^\circ, 90^\circ)$, $(72^\circ, 61^\circ)$ and $(86^\circ, 37^\circ)$;
- to have an idea of the transmission properties’ evolution with a growing altitude angle of the sun, incident directions every 12° along the $C90$ plane were added;
- even if non-realistic, some “negative” (under horizon) sun positions were considered too, to provide a better information about the samples behaviour: every 20° in altitude along the ϕ_1 plane $C270$;

- finally, additional measurements were performed for the mirror and Köster blinds (Sections C.5.2 and C.5.3) to verify to what extent BTDF figures associated to different incident directions (θ_1, ϕ_1) but corresponding to similar profile angles α_p were comparable, α_p being defined in Duffie and Beckman (1991) as “the angle through which a plane that is initially horizontal must be rotated about an axis in the plane of the surface in question in order to include the sun”; expressing α_p as a function of θ_1 and ϕ_1 , Equation (C.2) is obtained:

$$\alpha_p = \arctan \left(\frac{\tan \left(\operatorname{sgn}(\sin \phi_1) \cdot \arccos \left(\frac{\cos \theta_1}{\cos(\arctan(-\tan \theta_1 \cdot \cos \phi_1))} \right) \right)}{\cos \left(\arctan(-\tan \theta_1 \cdot \cos \phi_1) \right)} \right) \quad (\text{C.2})$$

Based on Equation (C.2), the four incident directions $(17^\circ, 45^\circ)$, $(46^\circ, 45^\circ)$, $(68^\circ, 45^\circ)$ and $(50^\circ, 315^\circ)$ were added as they induced profile angles α_p approximately equal (with a $\pm 0.2^\circ$ margin) to the already chosen incidences $(12^\circ, 90^\circ)$, $(36^\circ, 90^\circ)$, $(60^\circ, 90^\circ)$ and $(40^\circ, 270^\circ)$ respectively. As a matter of fact, it was found that the profile angle parameter alone was not determining in the resulting BTDF figure.

These considerations led to the set of incident directions given in Table C.1.

θ_1 ($^\circ$)	43	52	69	20	31	53	66	72	86	0	12	24
ϕ_1 ($^\circ$)	90	50	21	90	30	1	90	61	37	90	90	90
θ_1 ($^\circ$)	36	48	60	72	20	40	60	17	46	68	50	
ϕ_1 ($^\circ$)	90	90	90	90	270	270	270	45	45	45	315	

Table C.1: Incident directions set for the BTDF characterization of the venetian blinds with mirror and Köster slats.

C.5.1 Mirror blind between glass layers

The optimized sun shading system “OKASolarTM” illustrated in Figure C.20(a) and manufactured by Okalux AG consists of an optically adjusted solar protective blind sandwiched between two insulated glass panes. It was characterized in transmission for the incident directions set defined in Table C.1, except for the four directions added for the angle profile study, for an averaging grid $(5^\circ, 5^\circ)$ and a diaphragm diameter of 10 cm. An example of BTDF result is shown on Figure C.21.

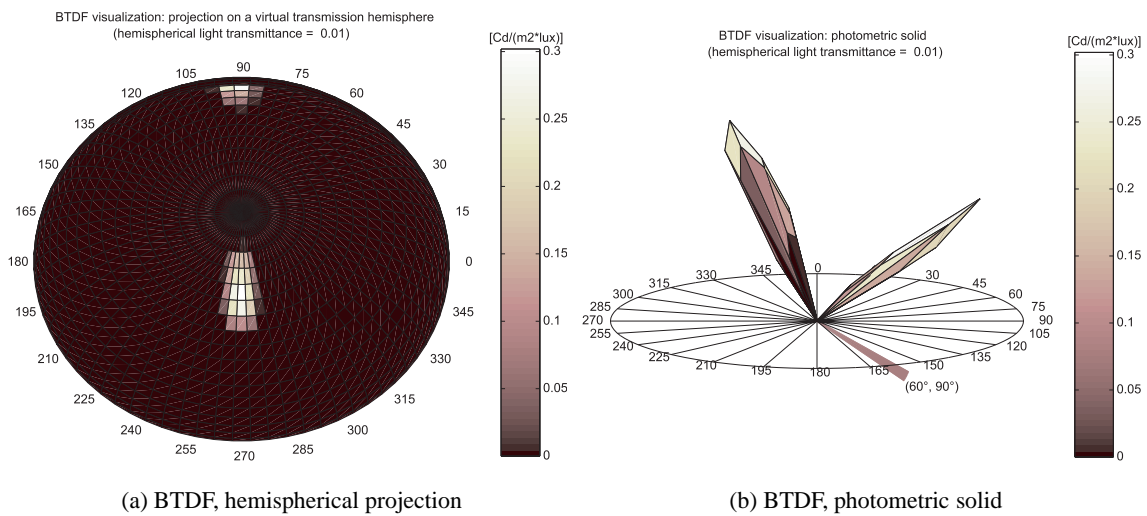


Figure C.21: BTDF for the “OKASolarTM” sandwiched mirror blind for incidence $(\theta_1, \phi_1) = (60^\circ, 90^\circ)$.

C.5.2 Curved slats with mirror coating

Nine venetian blind prototypes with curved slats and mirror coating on the upper side, beige and mat paint coating on the lower side were characterized in transmission, all of them manufactured by Baumann-Hppe AG. They present slats of different sizes, either half perforated (with the perforation towards the inside of the building), entirely or not, and were analyzed according to the three slats tilt configurations illustrated in Figure C.22: 0° (horizontal), 45° and closed.

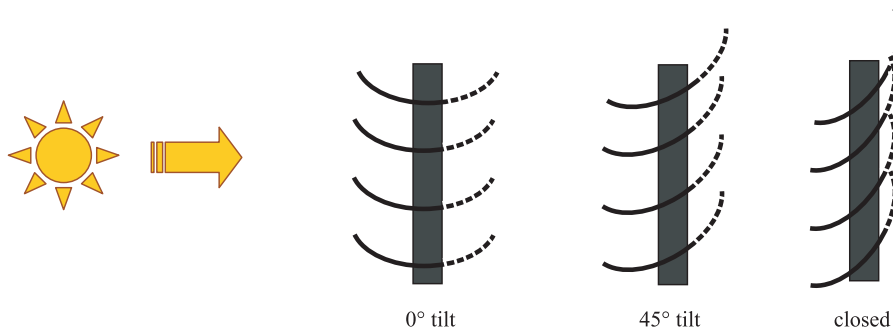


Figure C.22: Three slats tilt configurations: 0° tilt, 45° tilt and closed. For half perforated slats, the holes are on the inside.

Gathered by size, they can be listed as follows:

- 25 mm large; three types: full, half, entirely perforated slats; slats tilt angles: 0° , 45° , closed;
- 50 mm large; three types: full, half, entirely perforated slats; slats tilt angles: 0° , 45° , closed;
- 80 mm large; two types: half and entirely perforated slats; slats tilt angles: 0° , 45° ;
- 90 mm large; one type: half perforated slats; slats tilt angles: 0° , 45° .

Their BTDF was determined for the complete incident directions set of Table C.1 with an illuminated area of 15 cm diameter and an averaging grid (10° , 15°). A BTDF comparison example between full and half perforated slats for the same incident direction is given in Figure C.23 for two slats tilt configurations.

C.5.3 Köster blinds

Three models of Köster blinds were analyzed, all 35 mm large and presenting either indented, mirrored slats or a reflective white coating with a special slats profile.:

- indented and mirror reflective surface on upper side, mat reflective coating on lower side; slats tilt angles: 0° , 45° , closed;
- slats profile: curved (spoon-like), then serrated (∇ shape) towards the inside of the building; mat reflective coating on upper side, mat white paint on lower side; slats tilt angle: 0° ;
- improved version of the previous blind, curved then $\nabla\nabla$ shaped profile; slats tilt angle: 0° .

They were characterized in transmission with an illuminated area of 15 cm diameter and an averaging grid ($\Delta\theta_2$, $\Delta\phi_2$) = (10° , 15°); a result example is given in Figure C.24, where the BTDFs obtained for these three Köster blind types are compared for the same incident direction as in Figure C.23.

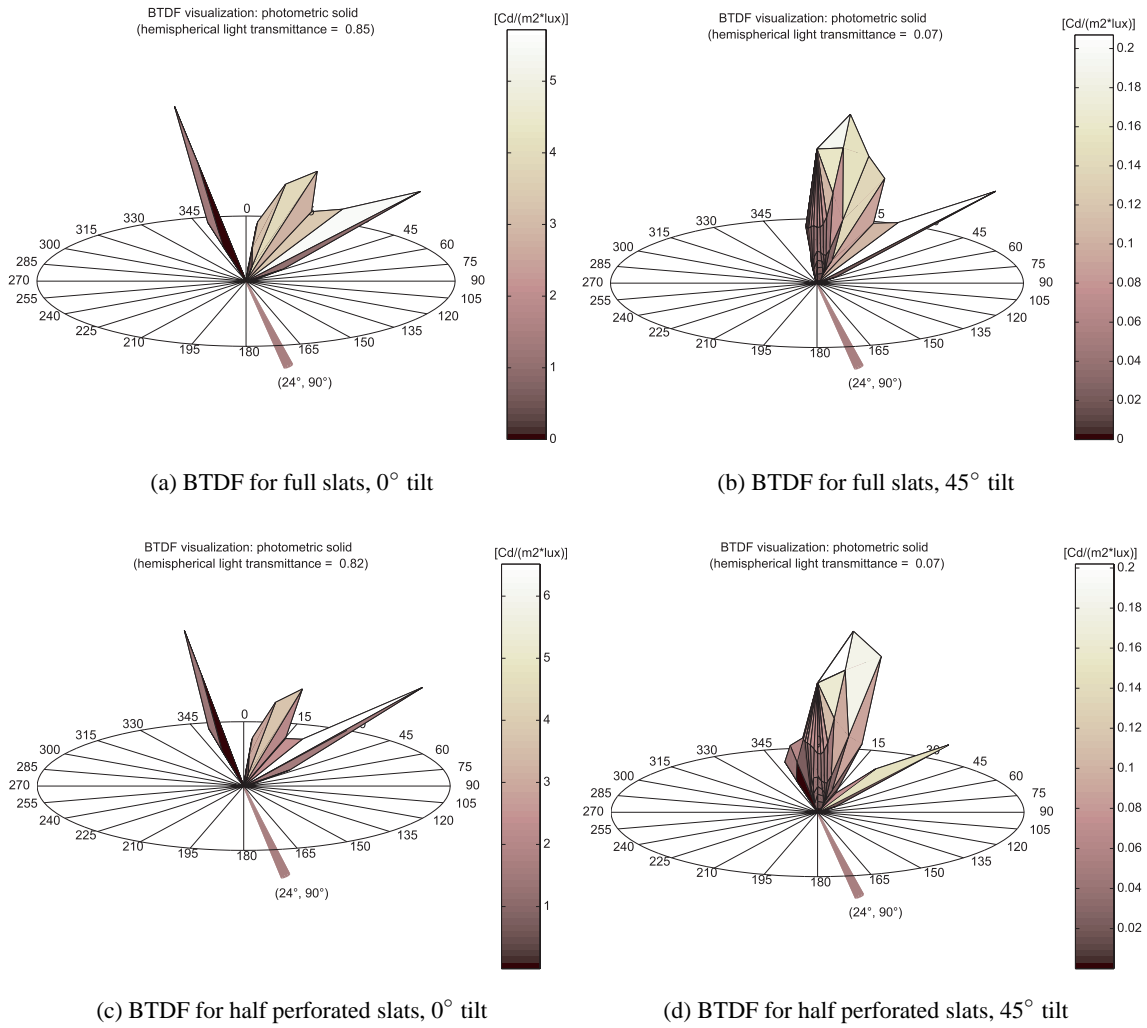


Figure C.23: BTDF (photometric solids) for the 50 mm large mirror blind, either half perforated or not, for incidence $(\theta_1, \phi_1) = (24^\circ, 90^\circ)$.

C.5.4 Metallic slats

As for the fabric blinds described in Section C.4.1, the Baumann-Hüppe's metallic blind prototypes were characterized at an early stage of calibration; a larger relative error (of about 20%) is thus to be assumed on the achieved BTDF data.

Three prototypes present conventional slats profiles, with varying paint coatings: brown, black and white. The fourth, named "Shine", is of special profile shape (spoon-like) and covered with a car body manufacturing quartz-based paint of pearl grey color.

All four have equal dimensions (10 cm large, 34 cm long, 8 cm between neighbor slats), with a slats tilt angle fixed to 60° according to the format of Figure C.22 (30° in regard to the window plane).

The same set of incident directions as for the fabric blinds of Section C.4.1 was used, i.e every 30° in altitude, along azimuth planes $C0$, $C90$ and $C270$; the averaging grid was $(10^\circ, 15^\circ)$ and the diaphragm diameter 17 cm (former sample holder).

Two BTDF result examples are shown on Figure C.25 for the incident direction $(30^\circ, 90^\circ)$.

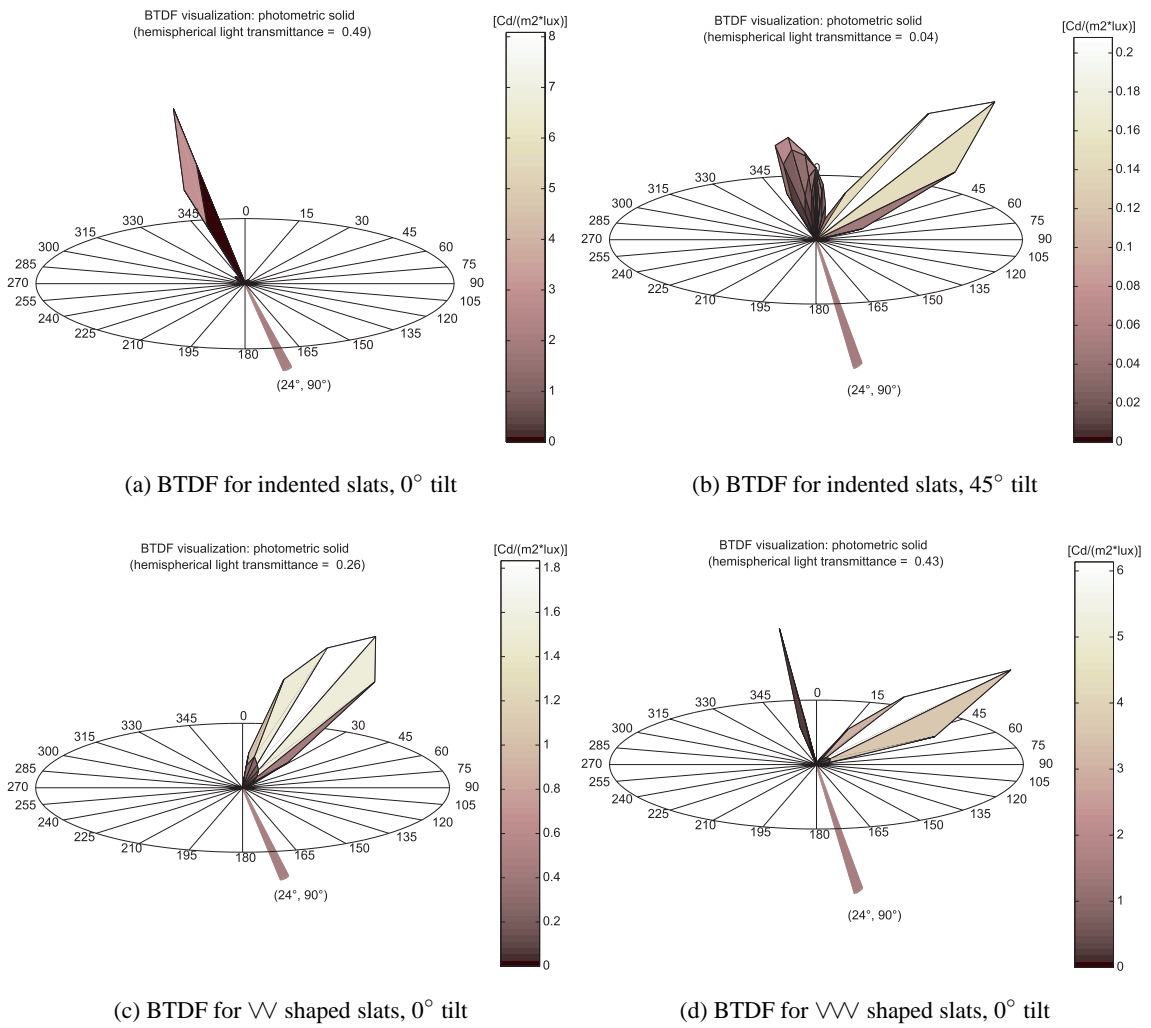


Figure C.24: BTDF (photometric solids) for the Köster blinds for incidence $(\theta_1, \phi_1) = (24^\circ, 90^\circ)$.

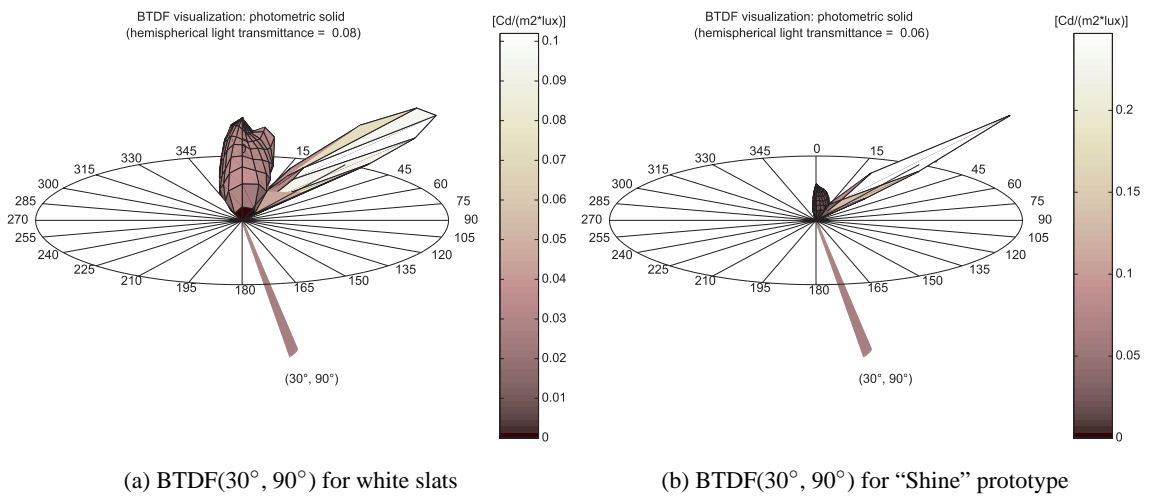


Figure C.25: BTDF (photometric solids) for two metallic blinds for incidence $(\theta_1, \phi_1) = (30^\circ, 90^\circ)$.

Appendix D

Nomenclature

All the symbols relating to parameters and variables used throughout the thesis are here gathered as a nomenclature list.

Photometric quantities

BTDF Bidirectional Transmission Distribution Function ($\text{Cd}\cdot\text{m}^{-2}\cdot\text{lux}^{-1}$) or (sr^{-1})

BRDF Bidirectional Reflection Distribution Function ($\text{Cd}\cdot\text{m}^{-2}\cdot\text{lux}^{-1}$) or (sr^{-1})

q luminance coefficient ($\text{Cd}\cdot\text{m}^{-2}\cdot\text{lux}^{-1}$) or (sr^{-1})

E_1 illuminance on the sample plane due to the incident light flux (lux)

E_{\perp} illuminance on a plane perpendicular to the incident beam (lux)

E_{screen} illuminance on the screen plane (lux)

$E_{\text{screen}_{\text{spec}}}$ screen illuminance due to regularly (specularly) transmitted (reflected) light (lux)

$E_n(\theta_2, \phi_2)$ illuminance on the hemispherical surface element ΔS_n (lux)

I_1 intensity emitted from the source within a solid angle element $d\omega_1$ (Cd)

I_2 intensity emitted from the sample within a solid angle element $d\omega_2$ (Cd)

L_1 luminance of an element of incident light flux ($\text{Cd}\cdot\text{m}^{-2}$)

L_2 luminance of an element of emerging light flux ($\text{Cd}\cdot\text{m}^{-2}$)

L_{screen} screen luminance ($\text{Cd}\cdot\text{m}^{-2}$)

$L_{\text{screen}_{\text{diff}}}$ screen luminance due to diffuse emerging light ($\text{Cd}\cdot\text{m}^{-2}$)

$L_{\text{screen}_{\text{spec}}}$ screen luminance due to regularly (specularly) transmitted (reflected) light ($\text{Cd}\cdot\text{m}^{-2}$)

Φ_1 total incident light flux (lumen)

Φ_2 total emerging light flux (lumen)

$d\Phi_2$ element of light flux emitted within $d\omega_2$ (lumen)

ρ_{screen} directional/diffuse screen reflection factor (-)

τ_{dir} direct (regular) transmission factor (-)

ρ_{dir} direct (specular) reflection factor (-)

$\tau_{\text{dir}} | \rho_{\text{dir}}$ combined symbol to express either τ_{dir} or ρ_{dir} (-)

τ_{dh} directional-hemispherical light transmittance of sample, for a given incident direction (-)

ρ_{dh} directional-hemispherical light reflectance of sample, for a given incident direction (-)

$\tau_{\text{dh}} | \rho_{\text{dh}}$ combined symbol to express either τ_{dh} or ρ_{dh} (-)

λ wavelength (nm)

$\Delta\lambda_n$ wavelength interval between measured data ($n - 1$) and n (nm)

$V(\lambda)$ normalized human eye's spectral sensitivity (-)

$S_{\text{raw}}(\lambda)$ raw (uncorrected) spectral sensitivity of the CCD camera (-)

$S(\lambda)$ (corrected) spectral sensitivity of the CCD camera (-)

τ_i filter's internal transmittance (i.e. after surface reflection losses are accounted for) (-)

τ_{i_0} filter's internal transmittance at thickness e_0 (-)

R_l filter's reflection loss factor (-)

T total filter transmittance (-)

T_0 total filter transmittance at measured thickness e_0 (-)

T_{comb} total transmission factor resulting from the combination of the three correcting filters (-)

F_{min} function to minimize for best $V(\lambda)$ fit of $S(\lambda)$ curve (-)

f'_1 quantity to express the matching of $S(\lambda)$ with $V(\lambda)$ (-)

ϵ photometric error for assessing the impact of the spectral calibration (-)

$\Gamma_{\text{meas}}(\lambda), \Gamma_{\text{calib}}(\lambda)$ radiometric spectra of the light source used respectively for BT(R)DF measurements and photometric calibration ($\mu\text{W}\cdot\text{cm}^{-2}\cdot\text{sr}^{-1}$)

$\epsilon_{\text{BT(R)DF}}$ relative error on final BT(R)DF values (-)

$\epsilon_{\tau_{\text{dh}}|\rho_{\text{dh}}}$ relative error on τ_{dh} or ρ_{dh} values (-)

$M_{C_{\text{BT(R)DF}}}$ correction matrix to convert $\frac{L_{\text{screen}}}{E_1}$ ratios into $BT(R)DF$ values

Polar and solid angles

θ_1, ϕ_1 polar co-ordinates of the incident light flux (°)

$\Delta\theta_1$ incident altitude step for BRDF measurements (°)

θ_2, ϕ_2 polar co-ordinates of the emerging (either transmitted or reflected) light flux (°)

$\Delta\theta_2, \Delta\phi_2$ angular intervals determining the BT(R)DF averaging grid (°)

$\Delta\theta_2^{\text{rad}}, \Delta\phi_2^{\text{rad}}$ angular intervals determining the BT(R)DF averaging grid (rad)

$\theta_{2\text{lim}}$ limit emerging altitude at which no obstruction occurs(°)

$\theta_{2\text{max}}$ maximal altitude of averaging sectors (°)

$\theta_{2\text{Ref}}$ altitude angle between the considered direction and the normal to the sample plane, for the reference situation (°)

ϕ_{2m} azimuth angle for which a BT(R)DF reaches a local maximum (°)

ψ_2 azimuth angle projected on the sample plane and comprised between -30° and $+30^\circ$ (null along the central axis of the screen), for an arbitrary screen position (°)

ψ_{20} ψ_2 value on screen position p_0 at which the origin axis for ϕ_2 is projected (°)

S_ψ minimal azimuth shift of averaging grid (°): $S_\psi = \phi_1 \bmod \Delta\phi_2$

ψ'_2 resulting ψ_2 angles after averaging grid shift (°): $\psi'_2 = \psi_2 + S_\psi$

$L_{\psi'_2-}, L_{\psi'_2+}$ limit values of ψ'_2 groups on an arbitrary screen position for a shift S_ψ (°)

$d\omega_1, d\omega_2$ solid angle subtended by the incident, emerging light flux (sr)

Ω_2 solid angle aiming at averaging sector around emerging direction (θ_2, ϕ_2) (sr)

Θ_0 projection screen inclination angle regarding the sample plane (°): $\Theta_0 = \arctan \frac{2}{\sqrt{3}} \cong 49.1^\circ$

α angle between direction (θ_2, ψ_2) and normal to the screen plane (or more generally impinging angle on screen surface) (°)

η angular divergence of rays reaching the characterized region of the sample (°)

γ_a, γ_b angles between normal to sample and directions pointing at D_p 's edges (°)

γ'_a, γ'_b angles between normal to sample and directions pointing at D_p 's edges (°)

$\Upsilon_{\theta_2}, \Upsilon_{\psi_2}$ maximal divergence of emerging rays reaching a same point on the projection screen (°)

$M_{\theta_{2\text{Ref}}}$ matrix of dimensions the (duplicated) digital image, of coefficients $\theta_{2\text{Ref}}(X, Y)$

M_{θ_2} matrix of dimensions the (duplicated) digital image, of coefficients $\theta_2(X, Y)$

M_{ψ_2} matrix of dimensions the (duplicated) digital image, of coefficients $\psi_2(X, Y)$

$M_{\{\theta\}}(\theta_2)$ binary matrix of dimensions the (duplicated) digital image, of coefficients 1 when corresponding to values within $\theta_2 \pm \frac{1}{2}\Delta\theta_2$ in the M_{θ_2} matrix, 0 elsewhere

$M_{\{\psi\}}(\psi'_2, S_\psi)$ binary matrix of dimensions the (duplicated) digital image, of coefficients 1 when corresponding to values within $\psi'_2 \pm \frac{1}{2}\Delta\phi_2$ in the $M_{\psi_2} + S_\psi$ matrix, 0 elsewhere

M_α matrix of dimensions the (duplicated) digital image, of coefficients $\alpha(X, Y)$

Surface and distance parameters

A sample area (cm²)

dA surface element on sample (cm²)

D illuminated sample diameter (on incident interface) (cm)

D_{out} emitting sample diameter (on emerging interface) (cm)

D_p diameter of the projected sample disk on the screen plane along direction $(\theta_1, 0^\circ)$ (cm)

D' required sample disk diameter to be projected as D'_p along direction $(\theta_1, 0^\circ)$ (cm)

D'_p direct spot diameter measured on the projection screen for incidence $(\theta_1, 0^\circ)$ (cm)

l_p distance between center of D_p and screen detection area apex (cm)

h distance from equivalent point source to sample (cm)

d distance between screen and sample center (on emerging interface) (cm)

d_\perp minimal distance between sample center and screen plane (cm)

d_{Ref} distance between referential origin and screen plane along direction $(\theta_{2\text{Ref}}, \psi_2)$ (cm)

H difference in level between screen detection area base and apex (cm): $H = 115$ cm

g gap between detection area base and external sample interface (cm)

S averaging sector area on the projection screen (cm²)

dS surface element on screen (cm²)

ΔS averaging sector area on the emerging hemisphere (cm²)

x, y cartesian coordinates on projection screen (cm)

X, Y pixel co-ordinates on digital image (-)

d_{obst} distance of the first obstacle to the emerging light path (cm)

h_{obst} height of the first obstacle to the emerging light path (cm)

e_s sample thickness (cm)

e filter thickness (mm)

e_0 measured filter thickness (mm)

R_{slat} curvature radius of venetian blind slats (mm)

ξ thickness of venetian blind slats (mm)

l_{slat} width of venetian blind slats (mm)

e_{slat} curvature amplitude of venetian blind slats (mm)

$M_{d_{\text{Ref}}}$ matrix of dimensions the (duplicated) digital image, of coefficients $d_{\text{Ref}}(X, Y)$

M_d matrix of dimensions the (duplicated) digital image, of coefficients $d(X, Y)$

Numbering variables

p screen position number (-): $p = 1 \dots 6$

p_0 screen position number on which the origin axis for ϕ_2 is projected (-)

Δp_0 number of screen positions separating p_0 from the current position p , according to the screen numbering order shown in Figure 4.12 (-)

κ normalization factor in F_{\min} (-)

N_λ number of considered wavelengths for spectral calibration (-)

N_i total number of incident directions (-)

N_{im} number of selected integration intervals for a given luminous situation ($1 \leq N_{\text{im}} \leq 7$) (-)

N_{out} total number of averaging sectors (-)

N_G number of new averaging grids required for the current characterization (-)

$N_{\theta\psi'}$ averaging sectors numbering following an angular logic (decreasing θ_2 , increasing ψ'_2) (-)

$N_{\text{IP}+}$ averaging sectors numbering following an Image-Pro Plus[®] count (-)

N_{subZ} superior to 1 if and only if the corresponding averaging sector contains more than one sub-sectors (-)

$N_{\text{non}\exists}$ superior to 1 for all (sub-)sectors associated to a same averaging sector (-)

N_{blind} set to θ_1 if the considered sub-sector is eliminated when the elliptic cover around θ_1 is removed in reflection mode, to -1 if it is never affected (-)

Other symbols

I_{heating} energy consumption index for heating ($\text{MJ}\cdot\text{m}^2\cdot\text{year}^{-1}$)

$I_{\text{electricity}}$ energy consumption index for electricity ($\text{MJ}\cdot\text{m}^2\cdot\text{year}^{-1}$)

γ correction factor of CCD camera response ($\gamma = 1$ for a linear response) (-)

ς statistical error on ray-tracing calculations induced by the number of traced rays (-)

NaN defines that a variable is “Not A Number” (-)

Bibliography

- American Society for Testing and Materials (1997a). Standard guide for selection of geometric conditions for measurement of reflection and transmission properties of materials. Annual Book of ASTM Standards E 179-96, Pennsylvania.
- American Society for Testing and Materials (1997b). Standard practice for angle resolved optical scatter measurements on specular or diffuse surfaces. Annual Book of ASTM Standards E 1392-96, Pennsylvania.
- Andersen, M. (1998). Dispositif de mesure de la distribution de luminance du ciel basé sur des techniques d'imagerie numérique : développement et validation expérimentale. Master's thesis, EPFL, Lausanne. Published under author's maiden name (Thys).
- Andersen, M. (2001). Use of matrices for the adaptation of video-based photogoniometric measurements to a variable referential. In *Proceedings Solar Energy in Buildings CISBAT 2001*, pages 193–198, Lausanne, Oct. 3-4. EPFL.
- Andersen, M. (2002). Light distribution through advanced fenestration systems. *Building Research and Information*, 30(4):264–281.
- Andersen, M. (In Press). Matrix-based analysis of digital images: application to photogoniometric measurements with variable referential. *Optics and Lasers in Engineering*. Special issue "Optics in Switzerland".
- Andersen, M., Michel, L., Roecker, C., and Scartezzini, J.-L. (2001). Experimental assessment of bi-directional transmission distribution functions using digital imaging techniques. *Energy and Buildings*, 33(5):417–431.
- Andersen, M., Rubin, M., Powles, R., and Scartezzini, J.-L. (2003a). Bi-directional light transmission properties assessment for venetian blinds: computer simulations compared to photogoniometer measurements. In *Proceedings ISES Solar World Congress 2003 - Solar Energy for a Sustainable Future*, page paper O2 35, Gothenburg, Sweden, June 14-19. International Solar Energy Society.
- Andersen, M., Rubin, M., and Scartezzini, J.-L. (2003b). Comparison between ray-tracing simulations and bi-directional transmission measurements on prismatic glazing. *Solar Energy*, 74(2):157–173.
- Andersen, M. and Scartezzini, J.-L. (2003). Including of specular component in a BTDF or BRDF assessment based on digital imaging. In *Proceedings CISBAT 2003*, pages 223–228, Lausanne, Oct. 8-9. EPFL.
- Andersen, M., Scartezzini, J.-L., Roecker, C., and Michel, L. (2000). Bi-directional Photogoniometer for the Assessment of the Luminous Properties of Fenestration Systems. CTI Project 3661.2, LESO-PB/EPFL, Lausanne.

- Apian-Bennowitz, P. (1994). Designing an apparatus for measuring bidirectional reflection/transmission. In *Proceedings SPIE Vol. 2255, Optical Materials Technology for Energy Efficiency and Solar Energy Conversion XIII*, pages 697–706.
- Apian-Bennowitz, P. (2003). Pab gonio-photometer. Internet WWW page at URL: <<http://www.optic-simulation.com/gonio-photometer/>> (Accessed 01.10.03).
- Apian-Bennowitz, P. and von der Hardt, J. (1998). Enhancing and calibrating a goniophotometer. *Solar Energy Materials and Solar Cells*, 54(1-4):309–322.
- Apian-Bennowitz, P., von der Hardt, J., and Goller, M. (1994). Characterization of aerogels for computer simulations.
- Arney, J. and Hung-Tran (1998). Design of a Photogoniometer to Measure Angular Dependent Optical Properties. In *Proceedings of 51st annual Imaging Science & Technology's PICS Conference*, pages 179–182, Springfield, VA. IS&T.
- Ashdown, I. (1993). Near-Field Photometry: A new approach. *Journal of the Illuminating Engineering Society*, 22(1):163–180.
- Ashdown, I. (2000). Comparing Photometric Distributions. *Journal of the Illuminating Engineering Society*, 29(1):25–33.
- Ashdown, I. and Rykowski, R. (1998). Making Near-Field Photometry Practical. *Journal of the Illuminating Engineering Society*, 27(1):67–79.
- Association Française de l'Éclairage (1991). *La photométrie en éclairage*. Société d'Éditions Lux, Paris.
- Aydinli, S. (1996). Short description of the spiral goniophotometer for bi-directional measurements (TU Berlin). Report for IEA SHC Task 21, ECBCS Annex 29, Subtask A, Technische Universität Berlin (TUB), Berlin.
- Baker, N., Fanchiotti, A., and Steemers, K. (1997). *Daylighting in Architecture - A European Reference Book*. James & James, London.
- Bakker, L. and van Dijk, D. (1995). Measuring and processing optical transmission distribution functions of TI-materials. Private Communication, TNO Building and Construction Research, Delft.
- Ballinger, J. and Lyons, P. (1998). Advanced glazing and associated materials for solar and building applications. Report for IEA SHC Task 18, Draft Final Report for Subtask A.
- Barthel, J., Comblen, A., Flamant, G., and Eugène, C. (2002). Goniospectrophotometric characterisation of advanced daylighting materials. In *Proceedings of the 3rd European Conference on Energy Performance & Indoor Climate in Buildings EPIC 2002*, pages 841–846, Lyon, France, Oct. 23-26. ENTPE.
- Beck, A., Körner, W., Gross, O., and Fricke, J. (1999). Making better use of natural light with a light-redirecting double-glazing system. *Solar Energy*, 66(3):215–221.
- Becker, M. (1998). Evaluation and characterization of display reflectance. *Displays*, 19:35–54.
- Bellia, L., Cesarano, A., Minichiello, F., and Sibilio, S. (2002). Setting up a CCD photometer for lighting research and design. *Building and Environment*, 37:1099–1106.

- Beltran, L., Lee, E., and Selkowitz, S. (1997). Advanced Optical Daylighting systems: Light Shelves and Light Pipes. *Journal of the Illuminating Engineering Society*, 26(2):91–106.
- Berrutto, V. (1996). *Métriologie de la qualité visuelle des ambiances lumineuses: Application à l'éclairage des bureaux*. PhD thesis, Université de Savoie, Chambéry.
- Berrutto, V. and Fontoynt, M. (1995). Applications of CCD cameras to lighting research: Review and extension to the measurement of glare indices. In *Proceedings CIE 119, 23rd Session*, pages 192–195, New Delhi.
- Bicheron, P., Leroy, M., Hautecoeur, O., and Breon, F. (1997). Enhanced discrimination of boreal forest covers with directional reflectances from the airborne polarization and directionality of Earth reflectances (POLDER) instrument. *Journal of geophysical research*, 102(D24):29517–29528.
- Bläsi, B., Bühler, C., Georg, A., and Gombert, A. (2003). Microstructured surfaces in architectural glazings. In *Proceedings ISES Solar World Congress 2003 - Solar Energy for a Sustainable Future*, Gothenburg, Sweden, June 14-19. International Solar Energy Society.
- Bodart, M. and De Herde, A. (2002). Global energy savings in offices buildings by the use of daylighting. *Energy and Buildings*, 34:421–429.
- Boyce, P. (1998). Why Daylight ? In *Proceedings of Daylight'98 International Conference on Daylighting Technologies for Energy Efficiency in Buildings*, pages 359–365, Ottawa, Ontario, Canada.
- Breitenbach, J., Lart, S., Längle, I., and Rosenfeld, J. (2001). Optical and thermal performance of glazing with integral venetian blinds. *Energy and Buildings*, 33(5):433–442.
- Breitenbach, J., Lart, S., and Rosenfeld, J. (1999). Optical properties and total solar energy transmittance of double glazing with solar control film. In *North Sun Conference*, Edmonton, Canada.
- Breitenbach, J. and Rosenfeld, J. (1998). Design of a Photogoniometer to Measure Angular Dependent Optical Properties. In *Proceedings of International Conference on Renewable Energy Technologies in Cold Climates*, pages 386–391, Ottawa, Canada. Solar Energy Society of Canada Inc.
- Breitenbach, J. and Rosenfeld, J. (2000). Goniospectrometer measurements of the optical performance of a holographic optical element. *Solar Energy*, 68(5):427–437.
- Brunold, S. (2000). Investigations of the influence of the surface texture of low-iron glasses on the transmittance of the solar radiation. SPF Report for INTERFLOAT CORP., Hochschule Rapperswil.
- Campbell, N. (1998). *A Monte Carlo approach to thermal radiation distribution in the built environment*. PhD thesis, University of Nottingham, Nottingham.
- Chain, C., Dumortier, D., and Fontoynt, M. (2001). Consideration of daylight's colour. *Energy and Buildings*, 33(3):193–198.
- Chevalier, B., Hutchins, M., Maccari, A., Olive, F., Oversloot, H., Platzer, W., Polato, P., Roos, A., Rosenfeld, J., Squire, T., and Yoshimura, K. (1998). Solar energy transmittance of translucent samples: A comparison between large and small integrating sphere measurements. *Solar Energy Materials and Solar Cells*, 54(1-4):197–202.

- Collins, S. (1998). Monte Carlo Methods and the Challenge of Photo-Realism in Computer Graphics. External Technical Report TCD-CS-1998-14, Computer Science Department, Trinity College, Dublin.
- Commission Internationale de l'Eclairage (1932). *CIE Proceedings, 1931*. Cambridge University Press, Cambridge.
- Commission Internationale de l'Eclairage (1977). Radiometric and photometric characteristics of materials and their measurement. *CIE*, 38(TC-2.3).
- Commission Internationale de l'Eclairage (1983a). The basis of physical photometry. *CIE*, 18.2(TC-1.2).
- Commission Internationale de l'Eclairage (1983b). Discomfort glare in the interior working environment. *CIE*, 55(TC-3.4).
- Commission Internationale de l'Eclairage (1987). Methods of characterizing illuminance meters and luminance meters - Performance, characteristics and specifications. *CIE*, 69.
- Commission Internationale de l'Eclairage (1989). The Measurement of Luminous Flux. *CIE*, 84.
- Commission Internationale de l'Eclairage (1996). The photometry and goniophotometry of luminaires. *CIE*, 121.
- Commission Internationale de l'Eclairage (1998). Practical methods for the measurement of reflectance and transmittance. *CIE*, 130.
- Compagnon, R. (1994). *Simulations numériques de systèmes d'éclairage naturel à pénétration latérale*. PhD thesis, Ecole Polytechnique Fédérale de Lausanne, Lausanne.
- Coulomb, J.-M. and Brusque, C. (1996). Propriétés de réflexion des surfaces: Le gonioreflectomètre du LCPC - Performances et perspectives d'études. *Bulletin des Laboratoires des Ponts et Chaussées*, 204:25–36.
- Council for Sustainable Development (1997). Sustainable Development: Action Plan for Switzerland. Technical Report BUWAL, Swiss Federal Office for Environment, Forest and Landscape, Bern.
- Courret, G. (1999). *Systèmes anidoliques d'éclairage naturel*. PhD thesis, EPFL, Lausanne.
- Dana, K., van Ginneken, B., Nayar, S., and Koenderink, J. (1999). Reflectance and Texture of Real-World Surfaces. *ACM Transactions on Graphics*, 18(1):1–34.
- De Boer, J. (2003). Incorporation of numerical goniophotometry into daylighting design. In *Proceedings CISBAT 2003*, pages 229–234, Lausanne, Oct. 8-9. EPFL.
- Demircan, A., Schuster, R., Radke, M., Schnermark, M., and Rser, H. (2000). Use of a wide angle CCD line camera for BRDF measurements. *Infrared Physics & Technology*, 41(1):11–19.
- Deniel, J.-M. (2002). *Modélisation des luminaires et des BRDF: réalisation, mesure et compression*. PhD thesis, Université de Rennes 1, Rennes.
- Dennis, M. (2003). Automated solar shading analysis. In *Proceedings ISES Solar World Congress 2003 - Solar Energy for a Sustainable Future*, Gothenburg, Sweden, June 14-19. International Solar Energy Society.

- Dittmar, C., Schuster, H., Oetzel, M., and Müller, H. (2003). Validation process of daylighting test facilities at the University of Dortmund. In *Proceedings CISBAT 2003*, pages 235–240, Lausanne, Oct. 8-9. EPFL.
- Drago, F. and Myszkowski, K. (2001). Validation proposal for global illumination and rendering techniques. *Computers & Graphics*, 25(3):511–518.
- Dubois, M.-C. (1997). Solar Shading and Building Energy Use - A Literature Review, Part 1. Technical Report TABK-97/3049, Lund Institute of Technology, Lund, Sweden.
- Dubois, M.-C. (2000a). A method to define shading devices considering the ideal total solar energy transmittance. In *Proceedings Eurosun 2000*, Copenhagen, Denmark, June 19-22.
- Dubois, M.-C. (2000b). A simple chart to design shading devices considering the window solar angle dependent properties. In *Proceedings Eurosun 2000*, Copenhagen, Denmark, June 19-22.
- Duffie, J. and Beckman, W. (1991). *Solar Engineering of Thermal Processes*, chapter 1, pages 13–21. John Wiley & Sons Inc., 2nd edition.
- Edmonds, I. (1993). Performance of laser-cut deflecting panels in daylighting. *Solar Energy Materials and Solar Cells*, 29:1–26.
- Fernandes, L. and Papamichael, K. (2003). Automating the selection of fenestration systems to best meet daylighting performance goals. In *Proceedings Building Simulation 2003*, Eindhoven The Netherlands, Aug. 11-14. IBPSA.
- Fontoynt, M. (1995). Properties of glazings for daylighting applications. Final Report JOU2-CT940404, ENTPE, Lyon, France.
- Fontoynt, M. (2002). Perceived performance of daylighting systems: lighting efficacy and agreeableness. *Solar Energy*, 73(2):83–94.
- Foo, S. (1997). A gonioreflectometer for measuring the bidirectional reflectance of material for use in illumination computation. Master's thesis, Cornell University, Ithaca, NY.
- Francioli, D. and Meyer, J.-J. (2003). Etude de l'éblouissement au moyen d'un photoluminancemètre numérique. In *Proceedings CISBAT 2003*, pages 265–270, Lausanne, Oct. 8-9. EPFL.
- Friedman, A. and Cammalleri, V. (1997). Selection criteria for energy-efficient windows. *Building Research and Information*, 25(4):234–238.
- Fusco, G., Macrelli, G., Polato, P., and Rossi, G. (1999). Variable angle photometric characterization of a laminated glass embedding a lamellae system. *Solar Energy*, 66(6):423–438.
- Georg, A., Graf, W., Schweiger, D., Wittwer, V., Nitz, P., and Wilson, H. (1998). Switchable glazing with a large dynamic range in total solar energy transmittance (TSET). *Solar Energy*, 62(3):215–228.
- Georgiev, G. and Butler, J. (2002). Bi-directional reflectance distribution function and hemispherical reflectance of JSC Mars-1. In *Proceedings Conference on Surface Scattering and Diffraction for Advanced Metrology II*, pages 165–175, July 9.
- Glassner, A. (1995). *Principles of digital image synthesis*, volume 1, chapter 7. Morgan Kaufmann Publishers, Inc., San Francisco, CA.

- Glenn, J., Dodds, G., and Robinson, R. (1999). Practical limitations and measurements for camera based road luminance / lighting standards assessment. *Journal of the Illuminating Engineering Society*, 28(1):64–70.
- Goesele, M., Heidrich, W., Lensch, H., and Seidel, H.-P. (2000). Building a photo studio for measurement purposes. In *Proceedings of the 5th Conference on Vision, Modeling, and Visualization (VMV-00)*, pages 165–175.
- Greenberg, C. (1994). Optically switchable thin films: a review. *Thin Solid Films*, 251(2):81–93.
- Greenup, P., Bell, J., and Moore, I. (2001). The importance of interior daylight distribution on overall energy performance. *Renewable Energy*, 22:45–52.
- Greenup, P., Edmonds, I., and Compagnon, R. (2000). RADIANCE algorithm to simulate laser-cut panel light redirecting elements. *Lighting Research and Technology*, 32(2):49–54.
- Grundmann, O., Krochmann, E., and Khanh, T. (1993). Accuracy on luminous intensity distribution measurement using goniophotometers with facility of turning the light source with auxiliary detector. In *Proceedings of the VIIth European Lighting Conference*, pages 717–722, Edinburgh, UK, April 4-7. Heriot-Watt University.
- Guillemin, A. (2003). *Using genetic algorithms to take into account user wishes in an advanced building control system*. PhD thesis, EPFL, Lausanne.
- Hammersley, J. and Handscomb, D. (1964). *Monte Carlo Methods*. Methuen & Co Ltd, London.
- Han, J. and Perlin, K. (2003). Measuring Bidirectional Texture Reflectance with a Kaleidoscope. *ACM Transactions on Graphics*, 22(3):741–748.
- Hecht, E. (1987). *Optics*, chapter 8. Addison-Wesley Publishing Company, Inc., USA, second edition.
- Herrmann, B., Rosemann, A., Aydinli, S., and Kaase, H. (2003). EUMELDAT. Technical report, Technische Universität Berlin, Berlin, Germany.
- Holmes, J. (1988). Light reflection by prismatic sheets. *CIBSE Research Note*, 20(3):115–117.
- Hubbard, G., Clanton, N., and Franta, G. (2003). Less is more: lessons learned from the Low Energy Super Store. In *Proceedings ISES Solar World Congress 2003 - Solar Energy for a Sustainable Future*, Gothenburg, Sweden, June 14-19. International Solar Energy Society.
- Hunn, B., Grasso, M., Beaudry, M., and House, P. (1991). Measurement of bidirectional solar-optical properties of shading fabrics. In *ASHRAE Transactions 97 (2)*, page 455.
- Hunn, B., Grasso, M., Rewerts, A., and Beaudry, M. (1996). Evaluation of directional shading fabric composites with application to improved daylighting. *HVAC&R Research*, 2(4):354–375.
- Hüppe-Form (1988). *Beschattung von Bildschirmarbeitsplätzen*. VIS-Broschüre.
- Hutchins, M., Topping, A., Anderson, C., Olive, F., van Nijnatten, P., Polato, P., Roos, A., and Rubin, M. (2001). Measurement and prediction of angle-dependent optical properties of coated glass products: results of an inter-laboratory comparison of spectral transmittance and reflectance. *Thin Solid Films*, 392(2):269–275.
- Huynh, V. and Wong, W. (1993). Optical technique for the measurement of 2-d texture of roller bearing surfaces. In *Proceedings of the 36th Midwest Symposium on Circuits and Systems, Vol. 2*, pages 1464–1466, Detroit, MI. IEEE.

- Illuminating Engineering Society of North America (1984). *Lighting Handbook - Application and Reference Volume*. IESNA, New York.
- Illuminating Engineering Society of North America (1993). *Lighting Handbook*. IESNA, New York.
- Inoue, T. (2003). Solar shading and daylighting by means of autonomous responsive dimming glass: practical application. *Energy and Buildings*, 35:463–471.
- International Energy Agency (2000). *Daylight in Buildings - A source book on daylighting systems and components*. IEA SHC Task 21 / ECBCS Annex 29, Berkeley.
- International Organization for Standardization (2003). Glass in building - determination of light transmittance, solar direct transmittance, total solar energy transmittance, ultraviolet transmittance and related glazing factors. ISO 9050 TC 160/SC 2.
- Jenkins, D., Beuzekom, D., Kollman, G., Wooley, C., and Rykowski, R. (2001). Digital imaging colorimeter for fast measurement of chromaticity coordinate and luminance uniformity of displays. In *Proceedings SPIE Vol. 4295, Flat Panel Display Technology and Display Metrology II*. Edward F. Kelley.
- Jenkins, D. and Mönch, H. (2000). Source Imaging Goniometer Method of Light Source Characterization for Accurate Projection System Design. In *2000 Society for Information Display Conference*, Long Beach, CA. SID.
- Kaempf, J. (2003). Technical Report and User's Manual BTDF2prism2. Draft, LESO-PB/EPFL, Lausanne.
- Karlsson, J., Rubin, M., and Roos, A. (2001). Evaluation of predictive models for the angle-dependent total solar energy transmittance of glazing materials. *Solar Energy*, 71(1):23–31.
- Karner, K., Mayer, H., and Gervautz, M. (1996). An Image based Measurement System for Anisotropic Reflection. *Computer Graphics Forum*, 15(3):119–128.
- Katholieke Hogeschool Sint-Lieven (2002). Technical university - department industrial engineering, research group optical measurements: Photogoniometer. Internet WWW page at URL: <<http://www.kahosl.be/lichtmeting/english/fotogoniometer-engels.htm/>> (Accessed 14.02.02).
- Katholieke Hogeschool Sint-Lieven (2003). Indicatieve en decoratieve verlichting met led's. Internet WWW page at URL: <<http://www.kahosl.be/woep/projectdetail.asp?ID=IWT>> (Accessed 14.10.03).
- Ke, L. (1999). A method of light reflectance measurement. Master's thesis, The University of British Columbia, Vancouver, Canada.
- Kischkoweit-Lopin, M. (1996). Description of the photogoniometer for bi-directional measurements. Report for IEA SHC Task 21, ECBCS Annex 29, Subtask A, Institut für Licht- und Bautechnik an der Fachhochschule Köln (ILB), Cologne, Germany.
- Kischkoweit-Lopin, M. (1998). Goniophotometer for bidirectional measurements (ILB, Köln). Report for IEA SHC Task 21, ECBCS Annex 29, Subtask A, Institut für Licht- und Bautechnik an der Fachhochschule Köln (ILB), Cologne, Germany.
- Kischkoweit-Lopin, M. (2002). An overview of daylighting systems. *Solar Energy*, 73(2):7782.

- Klems, J. (1994). A new method for predicting the solar heat gain of complex fenestration systems - I: Overview and derivation of the matrix layer calculation. In *ASHRAE Winter Meeting*, New Orleans, LA, Jan. 22-26.
- Klems, J. and Warner, J. (1995). Measurement of bidirectional optical properties of complex shading devices. In *ASHRAE Transactions 101 (1)*, pages 791–801, Chicago, IL.
- Klems, J., Warner, J., and Kelley, G. (1997). A comparison between calculated and measured SHGC for complex glazing systems. In *ASHRAE Transactions 102 (1)*, pages 931–939, Atlanta, Feb. 17-21 (1996).
- Klems, J., Yazdanian, M., and Kelley, G. (1995). Measured performance of selective glazings. In *Thermal Performance of the Exterior Envelopes of Buildings VI*, Clearwater Beach, FL, Dec. 4-8.
- Kloss, S.-H. (2001). *Ein Goniophotometer zur Messung des Lichtstromes und der Lichtstrkeverteilung von hohlen Lichtleitern*. PhD thesis, Technische Universität Berlin, Berlin.
- Kondo, T., Iwata, T., and Kimura, K.-I. (1997). Study on the evaluation system of visual environment including daylight. In *Proceedings Right Light 4, Vol. 2*, pages 129–136, Copenhagen, Denmark. IAEEL.
- Köster, H. (1989). Automatic heat control with mirror optics. In *Proceedings of the 2nd Workshop on Transparent Insulation*, Freiburg, Germany.
- Koudelka, M., Belhumeur, P., Magda, S., and Kriegman, D. (2001). Image-based modeling and rendering of surfaces with arbitrary BRDFs. In *Proceedings IEEE Computer Society Conference on Computer Vision and Pattern Recognition, Vol 1*, pages 568–575, Dec. 8-14.
- Kuhn, T., Bühler, C., and Platzer, W. (2001). Evaluation of overheating protection with sunshading systems. *Solar Energy*, 69(Suppl. 6):59–74.
- Lafortune, E., Foo, S.-C., Torrance, K., and Greenberg, D. (1997). Non-linear approximation of reflectance functions. In *Proceedings Siggraph'97 Conference*, pages 117–126. ACM Siggraph, Addison Wesley.
- Lalonde, P. and Fournier, A. (1997). Generating reflected directions from BRDF data. In *Proceedings Eurographics'97, Vol. 16 (3)*.
- Le Corbusier (1923). *Vers une architecture*. Flammarion, Paris, 1999 edition.
- Lee, E., DiBartolomeo, D., and Selkowitz, S. (1999). The effect of venetian blinds on daylight photoelectric control performance. *Journal of the Illuminating Engineering Society*, 28(1):3–23.
- Lensch, H., Kautz, J., and Goesele, M. (2003). Image-Based Reconstruction of Spatial Appearance and Geometric Detail. *ACM Transactions on Graphics*, 22(2):234–257.
- Lewin, I., Laird, R., and Young, J. (1992). Video photometry for quality control - CCD technology produces an all-terrain photometer system. LD&A, pp. 16-20.
- Lewin, I. and O'Farrell, J. (1999). Luminaire Photometry Using Video Camera. *Journal of the Illuminating Engineering Society*, 28(1):57–63.
- Li, D. and Lam, J. (2000). Measurements of solar radiation and illuminance on vertical surfaces and daylighting applications. *Renewable Energy*, 20:389–404.

- Li, D., Lam, J., and Wong, S. (2002). Daylighting and its implications to overall transfer value (OTTV) determinations. *Energy*, 27:991–1008.
- Libby, B. (2003). The evangelists of natural light - Selling architects on the benefits of the sun's illumination. *International Herald Tribune*, June 19:7.
- Lighting Sciences Inc. (1999). Universal mirror goniophotometer. Scottsdale, AZ.
- LMT Lichtmesstechnik GmbH Berlin (1998). Lmt photometer paint - Manual and application instructions. Berlin, Germany.
- Lorenz, W. (2001). A glazing unit for solar control, daylighting and energy conservation. *Solar Energy*, 70(2):109–130.
- Loscos, C. (1999). *Ré-éclairage et Remodélisation Interactifs des Scènes Réelles pour la Réalité augmentée*. PhD thesis, Université Grenoble I, Grenoble.
- Lu, R., Koenderink, J., and Kappers, A. (1998). Optical properties (bidirectional reflectance distribution function) of velvet. *Applied Optics*, 37(25):5974–5984.
- Lu, R., Koenderink, J., and Kappers, A. (2000). Optical properties (bidirectional reflectance distribution function) of shot fabric. *Applied Optics*, 39(31):5785–5795.
- Marschner, S., Westin, S., Lafortune, E., and Torrance, K. (2000). Image-based bi-directional reflectance distribution function measurement. *Applied Optics*, 39(16):2592–2600.
- Marschner, S., Westin, S., Lafortune, E., Torrance, K., and Greenberg, D. (1999). Image-based BRDF measurement including human skin. In *Proceedings Eurographics Workshop on Rendering*, Granada, Spain, June 21-23.
- McCluney, R. (1994). *Introduction to Radiometry and Photometry*. Artech House, Boston.
- McCluney, R. and Sung, J. (1999). Simulation of venetian blind optical properties with monte carlo ray tracing. Technical report, Florida Solar Energy Center, Cocoa, FL.
- Michel, L. (1999). *Méthode expérimentale d'évaluation des performances lumineuses de bâtiments*. PhD thesis, EPFL, Lausanne.
- Michel, L. and Andersen, M. (1999). Réalisation d'un photo-uranotomographe à imagerie numérique. In *Proceedings Solar Energy in Buildings CISBAT'99*, pages 289–294, Lausanne, Sept. 22-23. EPFL.
- Michel, L., Francioli, D., and Meyer, J.-J. (2001). Digital image facilities for visual comfort evaluation. In *Proceedings Solar Energy in Buildings CISBAT 2001*, pages 205–210, Lausanne, Oct. 3-4. EPFL.
- Michel, L., Roecker, C., and Scartezzini, J.-L. (1995). Performance of a new sky scanning simulator. *Lighting Research and Technology*, 27(4):197–207.
- Michel, L. and Scartezzini, J.-L. (2002). Implementing the partial daylight factor method under a scanning sky simulator. *Solar Energy*, 72(6):473–492.
- Milandri, A., Asllanaj, F., and Jeandel, G. (2002). Determination of radiative properties of fibrous media by an inverse method comparison with the Mie theory. *Journal of Quantitative Spectroscopy and Radiative Transfer*, 74(5):637–653.

- Mitanchey, R., Escaffre, L., and Marty, C. (2002). From optical performances characterization of a redirecting daylight material to daylighting simulations. In *Proceedings of the 3^d European Conference on Energy Performance & Indoor Climate in Buildings EPIC 2002*, pages 721–726, Lyon, France, Oct. 23-26. ENTPE.
- Mitanchey, R., Periole, G., and Fontoynt, M. (1995). Goniophotometric measurements: Numerical simulation for research and development applications. *Lighting Research and Technology*, 27(4):189–196.
- Mitchell, R., Kohler, C., Arasteh, D., Carmody, J., Huizenga, C., and Curcija, D. (2003). THERM 5 / WINDOW 5 NFRC Simulation Manual. Window & therm documentation, Lawrence Berkeley National Laboratory, Berkeley, CA.
- Moeck, M. (1998). On daylight quality and quantity and its application to advanced daylight systems. *Journal of the Illuminating Engineering Society*, 27(1):3–21.
- Mohlenkamp, M. (1997). *A Fast Transform for Spherical Harmonics*. PhD thesis, Yale University, New Haven, CT.
- Molina, J., Coronel, J., Maestre, I., and Guerra, J. (1995). Optical and thermal modeling of complex glazing systems. 6th experts meeting of IEA SHC Task 18 / advanced glazing and associated materials for solar and buildings applications, University of Seville, Seville.
- Moore, F. (1985). *Concepts and practice of architectural daylighting*. Van Nostrand Reinhold Company, New York.
- Müller, H. (1994). Application of holographic optical elements in buildings for various purposes like daylighting solar shading and PV power generation. *Renewable Energy*, 5(11):935–945.
- Müller, H. (1996). Tageslicht Beleuchtungsvorsichtung bestehend aus mindestens einer lichtleitenden Platte. Patent DE 4442228 C1, Germany.
- Murray-Coleman, J. and Smith, A. (1990). The Automated Measurement of BRDFs and their Application to Luminaire Modeling. *Journal of the Illuminating Engineering Society*, 19(1):87–99.
- Nadal, M. (2000). Optical measurements and standard materials for color and appearance. Internet WWW page at URL: <<http://slp.nist.gov/appearance/nadal.pdf>> (Accessed 15.10.03). Optical Technology Division, NIST Workshop on Metrology and Modeling of Color and Appearance.
- Nandy, P., Thome, K., and Biggar, S. (1998). Instrument for retrieval of brdf data for vicarious calibration. In *Proceedings of Geoscience and Remote Sensing Symposium IGARSS, Vol. 2*, pages 562–564, Seattle, WA. IEEE International.
- Nazzal, A. (2001). A new daylight glare evaluation method - introduction of the monitoring protocol and calculation method. *Energy and Buildings*, 33:257–265.
- Neumann, L., Neumann, A., and Szirmay Kalos, L. (1999). Reflectance models with fast importance sampling. *Computer Graphics Forum*, 18(4):249–265.
- Nicodemus, F. (1970). Reflectance nomenclature and directional reflectance and emissivity. *Applied Optics*, 9(6):1474–1475.
- Nicodemus, F., Richmond, J., Hsia, J., Ginsberg, I., and Limperis, T. (1977). Geometrical Considerations and Nomenclature for Reflectance. NBS monograph 160, National Bureau of Standards, U.S. Department of Commerce, Washington, DC.

- Noé, N. (1999). *Etude de fonctions de distribution de la réflectance bidirectionnelle*. PhD thesis, Ecole Nationale Supérieure des Mines de Saint-Etienne and Université Jean Monnet de Saint-Etienne, Saint-Etienne, France.
- Noé, N. and Péroche, B. (2000). Hierarchical reconstruction of BRDFs using locally supported functions. *Computer Graphics Forum*, 19(2):173–184.
- Ochi, S. and Lizuka, T. (1996). Charged-Coupled Device Technology. *Japanese Technology Reviews*, 30(A).
- Office Fédéral des Questions Conjoncturelles (1994). Eclairage des bureaux - Programme d'action RAVEL - Utilisation rationnelle de l'électricité. Technical Report 724.329.2f, OCFIM, Bern.
- Ohno, Y. and Hardis, J. (1997). Four-color matrix method for correction of tristimulus colorimeters. In *Proceedings of Imaging Science & Technology's 5th Color Imaging Conference*, pages 301–305. IS&T.
- ORIEL Instruments (2003). Colored glass filters technical discussion. Internet WWW pages at URL: <<http://www.oriel.com/homepage/down/pdf/10004.pdf>> and <<http://www.oriel.com/netcat/VolumeIII/pdfs/colfltttech.pdf>> (Accessed 11.11.03).
- Papamichael, K., Klems, J., and Selkowitz, S. (1988). Determination and Application of Bidirectional Solar-Optical Properties of Fenestration Materials. Technical Report LBL-25124, Lawrence Berkeley National Laboratory, Berkeley.
- Pasini, I. and Transley, B. (1994). Assessing the Luminous Environment with IQ CAM SCENE Video Photometer/Colorimeter. In *Light Wave, IESNA Conference*.
- Pattanaik, S. and Torrance, K. (1998). Light Measurement using the Photometrics-PXL1300L CCD Camera. Technical report, Program of Computer Graphics, Cornell University, Ithaca, NY.
- Perez, R., Seals, R., and Michalsky, J. (1993). All-weather model for sky luminance distribution: preliminary configuration and validation. *Solar Energy*, 50(3):235–245.
- Platzer, W. (2002). Basic data for model calculations of solar shading systems. Report for IEA SHC Task 27, Subtask A T27-A3-FRG-WJP-2001-2, Fraunhofer Institute for Solar Energy Systems, Freiburg, Germany.
- Pohl, W. and Scheiring, C. (1998). Charakterisierung von Tageslichtsystemen. In *Proceedings OTTI 1998 Viertes Symposium Innovative Lichttechnik in Gebäuden*, pages 133–140, Staffeinstein.
- Poulin, P. and Fournier, A. (1990). A model for anisotropic reflection. *SIGGRAPH Computer Graphics*, 24(4):273–281.
- PRC Krochmann GmbH (1996). Goniophotometer 702 with facility for turning the light source. Berlin.
- Proctor, M. (2000). Active multispectral bidirectional distribution function measurement system. Master's thesis, Air Force Institute of Technology, Wright-Patterson Air Force Base, Ohio.
- Programme d'action RAVEL (1995). La lumière naturelle à bon escient / Neuer Komfort mit Tageslicht. Technical report, EDMZ, Bern.

- Ramanath, R. (2000). Interpolation methods for the bayer color array. Master's thesis, North Carolina State University, Raleigh, NC.
- Rea, M. and Jeffrey, I. (1990). A new luminance and image analysis system, for lighting and vision - I. Equipment and calibration. *Journal of the Illuminating Engineering Society*, 19(1):64–72.
- Reim, M., Beck, A., Körner, W., Petricevic, R., Glora, M., Weth, M., Schliermann, T., Fricke, J., Schmidt, C., and Pötter, F. (2002). Highly insulating aerogel glazing for solar energy usage. *Solar Energy*, 72(1):21–29.
- Reinhart, C. and Herkel, S. (2000). The simulation of annual daylight illuminance distributions a state-of-the-art comparison of six RADIANCE-based methods. *Energy and Buildings*, 32(2):167–187.
- Reinhart, C. and Walkenhorst, O. (2001). Validation of dynamic RADIANCE-based daylight simulations for a test office with external blinds. *Energy and Buildings*, 33(7):683–697.
- Rhyner, R., Roecker, C., and Scartezzini, J.-L. (1991). An automated heliodon for daylighting building design. In *Proceedings ISES 91 Solar World Congress*, Denver, CO, Aug. 19-23. International Solar Energy Society.
- Roos, A. (1997). Optical characterization of coated glazings at oblique angles of incidence: measurements versus model calculations. *Journal of Non-Crystalline Solids*, 218:247–255.
- Rosenfeld, J. (1996). On the calculation of the total solar energy transmittance of complex glazings. In *Proceedings of the 8th International Meeting on Transparent Insulation*, Freiburg, Germany.
- Rosenfeld, J., Platzer, W., van Dijk, H., and Maccari, A. (2001). Modelling the optical and thermal properties of complex glazing: overview of recent developments. *Solar Energy*, 69(Suppl. 6):1–13.
- Roy, G. (2000). A comparative study of lighting simulation packages suitable for use in architectural design. Technical report, Murdoch University, Perth, Western Australia.
- Rubin, M. and Powles, R. (2001). Optical properties of glazing materials at normal incidence. In *Revista della Stazione Sperimentale del Vetro (CEN Workshop on Glazing)*, pages 13–16, La Defense, Paris, France, Oct. 5-6 (2000).
- Rubin, M., Powles, R., and von Rottkay, K. (1999). Models for the angle-dependent optical properties of coated glazing materials. *Solar Energy*, 66(4):267–276.
- Rubin, M., von Rottkay, K., and Powles, R. (1998). Window optics. *Solar Energy*, 62(3):149–161.
- Rusinkiewicz, S. (1997). A survey of BRDF representation for computer graphics. Internet WWW page at URL: <<http://www-graphics.stanford.edu/smr/cs348c/surveypaper.html>> (Accessed 10.05.99). CS348c.
- Ryer, A. (1997). Light Measurement Handbook. Internet WWW page at URL: <<http://www.intl-light.com/handbook/registered.html>> (Accessed 11.11.03).
- Rykowski, R. (1994). Illumination System Measurement Using CCD Cameras. In *International Optical Design Conference, Technical Digest*, Washington, DC. Optical Society of America.
- Sandmeier, S. (2000). Acquisition of Bidirectional Reflectance Factor Data with Field Goniometers. *Remote Sensing of Environment*, 73:257–269.

- Sauter, G. (1996). Goniophotometry: new calibration method and instrument design. In *Proceedings of the 1994 5th International Conference on Radiometry NEWRAD*, pages 685–688, Berlin, Germany. Metrologia Vol. 32 (6).
- Scartezzini, J.-L. (2003). Advances in Daylighting and Artificial Lighting. In *Proceedings Research in Building Physics*, Leuven, Belgium, Sept. 14-18. Technologisch Instituut.
- Scartezzini, J.-L., Compagnon, R., Citherlet, S., Courret, G., Michel, L., Paule, B., and Simos, S. (1997a). Daylighting design of European buildings. UE project 93.0015, LESO-PB/EPFL, Lausanne. OFES/BBW.
- Scartezzini, J.-L., Compagnon, R., Roecker, C., and Michel, L. (1997b). Bidirectional photogoniometer for advanced glazing materials based on digital imaging techniques. *Lighting Research and Technology*, 29(4):197–205.
- Scartezzini, J.-L., Compagnon, R., Ward, G., and Paule, B. (1994). Computer daylighting simulation tools. Technical report, University of Geneva / EPFL, Lausanne.
- Scartezzini, J.-L. and Paule, B. (1994). Office Lighting. Technical report, EDMZ, Bern.
- Schlick, C. (1994a). An inexpensive BRDF model for physically-based rendering. *Computer Graphics Forum*, 13(3):233–246.
- Schlick, C. (1994b). A survey of shading and reflectance models. *Computer Graphics Forum*, 13(2):121–131.
- Schmitt Industries (2003). Schmitt Measurement Systems - SMS-Facilities: SMS CASI[®] Scatterometer. Internet WWW page at URL: <<http://www.schmitt-ind.com/products-services-measurement-services-facilities.shtml>> (Accessed 29.09.03).
- Schweizerische Lichttechnische Gesellschaft (1992). *Handbuch für Beleuchtung*. Ecomed Verlag, Landsberg.
- Selkowitz, S. and Lee, E. (1998). Advanced fenestration systems for improved daylight performance. In *Proceedings International Daylighting Conference '98*, Ottawa, Canada, May 11-13.
- Siemens AG (1996). Produktinformation Tageslichtsystems. Technical report, Siemens AG, Traunreut, Germany.
- Sillion, F., Arvo, J., Westin, S., and Greenberg, D. (1991). A global illumination solution for general reflectance distributions. In *SIGGRAPH'91 Conference Proceedings*, page 1.
- Smith, G. (1999). Photogoniometer at the university of technology, sydney. International Daylighting RD&A, 2-99 (8), p. 13. University of Sydney, Australia.
- Smith, G. (2003). Materials and systems for efficient lighting and delivery of light. In *Proceedings ISES Solar World Congress 2003 - Solar Energy for a Sustainable Future*, Gothenburg, Sweden, June 14-19. International Solar Energy Society.
- Smith, G., Green, D., McCredie, G., Hossain, M., Swift, P., and Luther, M. (2001). Optical characterisation of materials and systems for daylighting. *Renewable Energy*, 22(1-3):85–90.
- Song, K., Degelman, L., and Boyer, L. (1994). Determining Daylighting Parameters by a Luminance Mapping System and Scale Models. *Journal of the Illuminating Engineering Society*, 23(1):65–75.

- Stollnitz, E., DeRose, T., and Salesin, D. (1995a). Wavelets for Computer Graphics: A Primer, part I. *IEEE Computer Graphics and Applications*, 15(3):76–84.
- Stollnitz, E., DeRose, T., and Salesin, D. (1995b). Wavelets for Computer Graphics: A Primer, part II. *IEEE Computer Graphics and Applications*, 15(4):75–85.
- Surface Optics (2003). SOC 200 Bidirectional Reflectometer. Internet WWW page at URL: <<http://www.surfaceoptics.com/Products/Reflectometers/200.htm>> (Accessed 12.10.03).
- Swiss Federal Office of Conjonctural Problems (1995). Appropriate daylight. Technical report, EDMZ, Bern.
- Tansley, B., Houser, K., and Pasini, I. (1999). The IQCam Digital Image Photometer System: Principles of Operation and Comparative Performance. *Journal of the Illuminating Engineering Society*, 28(1):182–200.
- TechnoTeam Bildverarbeitung GmbH (2003). Goniofotometer RIGO 801. Internet WWW page at URL: <<http://www.technoteam.de/rigo.html>> (Accessed 17.10.03).
- Tregenza, P. (1987). Subdivision of the sky hemisphere for luminance measurements. *Lighting Research and Technology*, 19:13–19.
- Tsuchida, S., Sato, I., and Okada, S. (1999). Measurement of land surface brdf with spatial instability for vicarious calibration. In *Proceedings of SPIE - The International Society for Optical Engineering Vol. 3870*, pages 254–258.
- van Dijk, D. (2001). Daylighting Products with Redirecting Visual Properties (The project RE-VIS). Final Report JOE3-CT98-0096, TNO Building and Construction Research, Delft.
- van Nijnatten, P. (2002). A spectrophotometer accessory for directional reflectance and transmittance of coated glazing. *Solar Energy*, 73(3):137–149.
- van Nijnatten, P. (2003). An automated directional reflectance/transmittance analyser for coating analysis. *Thin Solid Films*, 442(1-2):74–79.
- Ward, G. (1992). Measuring and modeling anisotropic reflection. *ACM SIGGRAPH Computer Graphics*, 26(2):265–272.
- Ward Larson, G. and Shakespeare, R. (1998). *Rendering with Radiance - The Art and Science of Lighting Visualization*. Morgan Kaufmann Publishers, Inc., San Francisco, CA.
- Weinläder, H., Beck, A., and Fricke, J. (2003). Façade panel with PCM for daylighting and space heating. In *Proceedings ISES Solar World Congress 2003 - Solar Energy for a Sustainable Future*, Gothenburg, Sweden, June 14-19. International Solar Energy Society.
- Welford, W. and Winston, R. (1989). *Non-imaging optics*. Academic Press, New York.
- West, S. and Pearce, N. (1998). NPL's new goniophotometer paves the way to improved measurements of luminous and spectral total flux. *Optical Radiation Measurement newsletter*, Spring 1998 (6), p. 4. National Physical Laboratory, UK.
- Whitehead, L., Kan, P., Lui, K., and Jacob, S. (1999). Near Field Photometry of Prism Light Guide Luminaires Using a CCD Camera. *Journal of the Illuminating Engineering Society*, 28(2):3–9.
- Williams, D. (2003). Sun fact sheet. Internet WWW page at URL: <<http://nssdc.gsfc.nasa.gov/planetary/factsheet/sunfact.html>> (Accessed 02.12.03). National Space Science Data Center (NSSDC), NASA Goddard Space Flight Center.

- Wilson, M., Jacobs, A., Solomon, J., Pohl, W., Zimmermann, A., Tsangrassoulis, A., and Fontoynt, M. (2002). Creating sunlight rooms in non-daylit spaces. In *ECEEE Summer Study Proceedings Right Light 5*, Nice. European Council for an Energy Efficient Economy.
- Wirth, H. (2000). *Richtungsselektive Steuerung von Sonnenstrahlung durch Fenster*. PhD thesis, EPFL, Lausanne.
- Wirth, H., Gombert, A., Wittwer, V., and Luther, J. (1997). Sun Protection and Daylighting with New Angular Selective Structures. In *Proceedings Solar Energy in Buildings CISBAT'97*, Lausanne, Oct. 1-2. EPFL.
- Wolf, E. (1979). Einstein's Researches on the Nature of Light. *Optics News*, 5(1):24–39.
- Wright, H., Sanders, C., and Gignac, D. (1969). Design of Glass Filter Combinations for Photometers. *Applied Optics*, 8(12):2449–2455.
- Zajonc, A. (1993). *Catching the Light - The Entwined History of Light and Mind*. Oxford University Press, New York.

Marilyne ANDERSEN

marilyne@andersen.be
<http://lesowww.epfl.ch/doctorants/andersen/>

Born on September 27, 1974.
Swiss & Belgian citizenships. Married.



Education

- Mar 00 - Apr 04 **PhD, Swiss Federal Institute of Technology (EPFL), Switzerland**
Solar Energy and Building Physics Laboratory (LESO-PB)
Advisor: Prof. Jean-Louis Scartezzini
- Oct 93 - Apr 98 **M. Sc. in Physics, EPFL** (“Diplôme d’ingénieure physicienne EPF”)
1995-96 : Exchange student at **Université Catholique de Louvain (UCL), Belgium**
- Sep 90 - Mar 93 **Certificat de Maturité Fédérale, Collège Champittet, Pully, Switzerland**
Scientific orientation (type C)

Professional Experience

- Jul 04 - **Assistant Professor (tenure-track), Massachusetts Institute of Technology (MIT), USA**
Building Technologies discipline group
Department of Architecture
- May 98 - Jun 04 **Teaching and Research Assistant, LESO-PB, Section of Architecture, EPFL**
PhD research project
Participation in international research projects (IEA Tasks 21, 27, 31; REVIS)
Supervisor of student projects for Teaching Unit “Rehabilitation” (daylighting theme)
Teaching assistant for undergraduate course “Building Physics”
Research project supervisor of postgraduate visiting student
- Sep 01 - Jul 02 **Visiting Scholar, Lawrence Berkeley National Laboratory (LBNL), USA**
Building Technologies Department
- Jul 93 - Aug 93 **Internship, Woodward Clyde (URS Corp.), Lausanne, Switzerland**
Environmental impact study of a service company site (Basel, Switzerland)
- Sep 90 - Jul 97 **Private lessons** in mathematics and physics

Consulting and Services

- Jan 03 – Jan 04 **Consultant for ESTIA, Lausanne, Switzerland**
Development of a generalized calculation method for the sky factor
- Jan 01 - Feb 04 **Baumann-Hüppe AG, Wädenswil, Switzerland**
Performance assessment of solar blinds and solar shading prototypes
- Mar 00 - Jan 03 **Reviewer for “Solar Energy” and “Energy and Buildings” journals**

Fellowships

- Sep 01 - May 02 **Swiss National Science Foundation (SNF) Fellowship**
Granted to prospective researchers
- Sep 95 - Jun 96 **Erasmus Fellowship**
Granted by the European Community